

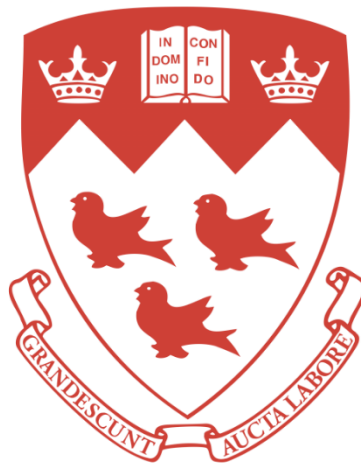
# **Laser Powder Bed Fusion of Precipitation-Hardened Rene 41 and Rene 77 Nickel Base Superalloys**

**Sila Ece Atabay**

Department of Mining and Materials Engineering

McGill University, Montreal, Quebec, Canada

November 2021



A thesis submitted to McGill University in partial fulfillment of the requirements of the degree  
of Doctor of Philosophy

© Sila Ece Atabay 2021

All Rights Reserved

# Abstract

---

Laser powder bed fusion (LPBF) is a promising technology that enables the production of complex parts with unique freedom in design and short lead times. A variety of metallic materials can be processed through LPBF. However, for applications requiring high strength and high temperature resistance, Ni-base superalloys are the primary choice of material. While there are variety of superalloys that can be produced through LPBF, most high-strength alloys are prone to cracking and considered difficult to weld. The main objective of this research is to assess the processability of precipitation hardenable Ni-based superalloys by LPBF. For this purpose, processing two different precipitation hardenable alloys, Rene 41 (R41) having fair weldability and Rene 77 (R77) categorized as difficult to weld, are studied along with their microstructural development and mechanical properties.

First, the R41 alloy was produced by LPBF, and its microstructural evolution was investigated. Crack-free and dense sample having a cube geometry was produced upon parameter optimization. The as-built (AB) microstructure revealed columnar grains with a preferred orientation along the  $\langle 100 \rangle$  direction. Transmission electron microscopy analysis revealed the absence of  $\gamma'$  precipitates in the as-fabricated state due to the high cooling rates experienced during the LPBF process. Afterwards, the samples were subjected to the standard solutionizing and aging heat treatment for precipitation of the main strengthening phase  $\gamma'$ . Even though the grain morphology was similar to the AB sample, the formation of distinct carbide particles at the grain and cell boundaries were observed along with the precipitation of fine and homogeneously distributed  $\gamma'$  after the heat treatment. The size of these  $\gamma'$  precipitates was smaller compared to the reported values in the literature. Mechanical properties of the samples both in AB and heat-treated state was characterized. Hardness and strength showed a significant increase after the heat treatment from the  $\gamma'$  precipitation. Results proved that when standard heat treatment is applied to the LPBF fabricated R41 parts, the measured room temperature strength and elongation meet the Aerospace Materials Specifications (AMS). The effect of build direction on the mechanical properties was also studied. From the orientation of the grains with the loading direction, the vertically built samples displayed higher elongation. Fractography analysis revealed that failure occurred in a ductile manner for both as fabricated and heat-treated samples.

Since the microstructure obtained after LPBF is very different compared to the conventional processing techniques, the suitability of the commercially applied heat treatment cycles has to be studied. Hence, additional heat treatments were applied to understand the effect of different solutionizing temperatures on the development of microstructure and mechanical properties. The microstructural analysis includes grain morphology and texture, volume fraction, distribution, and morphology of the  $\gamma'$  precipitates and carbides. These analyses revealed that for heat treatment above the  $\gamma'$  solvus temperature, a completely different microstructure was obtained. Formation of an equiaxed grain morphology with random orientation was detected. This heat treatment cycle also resulted in the precipitation of  $\gamma'$  and carbide phases similar to the sub-solvus heat treatment but with different size distribution and morphology. Following the microstructural characterization, tensile properties were tested at 760°C. YS and UTS values were obtained for AB, sub-solvus and super-solvus heat-treated samples and these values were on par with the wrought and heat-treated alloys reported in the literature. However, the measured elongation values and deformation behaviors showed significant differences due to their different microstructures. The columnar grain morphology of the sub-solvus heat-treated sample led to the highest elongation at break while the microstructure obtained after super-solvus treatment had the highest work hardening rate during deformation.

Finally, the knowledge gained from R41 was used to study the manufacturability of the R77 alloy. This alloy is more prone to cracking during fabrication due to its higher content of alloying elements. Elimination of cracking in a difficult to weld alloy solely by parameter optimization was proven possible with LPBF of R77. Furthermore, these crack-free structures were maintained upon a modified version of the standard heat treatment. Detailed microstructural characterization of AB and heat-treated samples were conducted similarly to the R41. In this case, the presence of extremely fine  $\gamma'$  precipitates was identified after LPBF, and a bimodal distribution including cuboidal primary and spherical secondary precipitates developed following the heat treatment. Tensile properties for both conditions were tested at room temperature and 810 °C and the results were compared with wrought counterparts and with other difficult to weld alloys fabricated by LPBF. The samples in both conditions showed different room and elevated temperature deformation behaviors. AB sample showed significant hardening whereas, the heat-treated one had improved elongation due to thermally activated microtwinning.

## Résumé

---

La fusion laser sur lit de poudre (LPBF) est une technologie prometteuse qui permet la production de pièces complexes avec une liberté de conception unique et des délais courts. Une variété de matériaux métalliques peut être traitée par LPBF. Cependant, pour les applications nécessitant une résistance élevée et une résistance à haute température, les superalliages à base de Ni sont le premier choix de matériau. Bien qu'il existe une variété de superalliages pouvant être produits par LPBF, la plupart des alliages à haute résistance sont sujets à la fissuration et considérés comme difficiles à souder. L'objectif principal de cette recherche est d'évaluer l'aptitude au traitement des superalliages à base de Ni durcissables par précipitation par LPBF. À cette fin, le traitement de deux alliages durcissables par précipitation différents, Rene 41 (R41) ayant une bonne soudabilité et Rene 77 (R77) classés comme difficiles à souder, sont étudiés ainsi que leur développement microstructural et leurs propriétés mécaniques.

Tout d'abord, l'alliage R41 a été produit par LPBF, et son évolution microstructurale a été étudiée. Un échantillon sans fissure et dense ayant une géométrie cubique a été produit lors de l'optimisation des paramètres. La microstructure telle que construite (AB) a révélé des grains colonnaires avec une orientation préférée le long de la direction  $\langle 100 \rangle$ . L'analyse par microscopie électronique à transmission a révélé l'absence de précipités  $\gamma'$  à l'état brut en raison des vitesses de refroidissement élevées rencontrées pendant le processus LPBF. Ensuite, les échantillons ont été soumis au traitement thermique standard de mise en solution et de vieillissement pour la précipitation de la phase de renforcement principale  $\gamma'$ . Même si la morphologie des grains était similaire à celle de l'échantillon AB, la formation de particules de carbure distinctes aux limites des grains et des cellules a été observée ainsi que la précipitation de  $\gamma'$  fins et répartis de manière homogène après le traitement thermique. La taille de ces précipités  $\gamma'$  était plus petite par rapport aux valeurs rapportées dans la littérature. Les propriétés mécaniques des échantillons à la fois à l'état AB et à l'état traité thermiquement ont été caractérisées. La dureté et la résistance ont montré une augmentation significative après le traitement thermique de la précipitation  $\gamma'$ . Les résultats ont prouvé que lorsqu'un traitement thermique standard est appliqué aux pièces R41 fabriquées par LPBF, la résistance et l'allongement mesurés à température ambiante répondent aux spécifications AMS. L'effet de la direction de fabrication sur les propriétés mécaniques a également été étudié.

À partir de l'orientation des grains avec la direction de chargement, les échantillons construits verticalement présentaient un allongement plus élevé. L'analyse de fractographie a révélé que la rupture s'est produite de manière ductile à la fois pour les échantillons fabriqués et traités thermiquement.

Étant donné que la microstructure obtenue après LPBF est très différente par rapport aux techniques de traitement conventionnelles, l'adéquation des cycles de traitement thermique appliqués commercialement doit être étudiée. Par conséquent, des traitements thermiques supplémentaires ont été appliqués pour comprendre l'effet de différentes températures de mise en solution sur le développement de la microstructure et des propriétés mécaniques. L'analyse microstructurale comprend la morphologie et la texture des grains, la fraction volumique, la distribution et la morphologie des précipités  $\gamma'$  et des carbures. Ces analyses ont révélé que pour le traitement thermique au-dessus de la température de solvus  $\gamma'$ , une microstructure complètement différente a été obtenue. La formation d'une morphologie de grain équiaxe avec une orientation aléatoire a été détectée. Ce cycle de traitement thermique a également entraîné la précipitation des phases  $\gamma'$  et carbure de manière similaire au traitement thermique sous-solvus mais avec une distribution de taille et une morphologie différentes. Suite à la caractérisation microstructurale, les propriétés de traction ont été testées à 760°C. Les valeurs YS et UTS ont été obtenues pour les échantillons traités thermiquement AB, sub-solvus et super-solvus et ces valeurs étaient comparables aux alliages forgés et traités thermiquement rapportés dans la littérature. Cependant, les valeurs d'allongement mesurées et les comportements de déformation ont montré des différences significatives en raison de leurs différentes microstructures. La morphologie des grains colonnaires de l'échantillon traité thermiquement sous-solvus a conduit à l'allongement à la rupture le plus élevé tandis que la microstructure obtenue après traitement super-solvus avait le taux d'écroutissage le plus élevé pendant la déformation.

Enfin, les connaissances acquises grâce au R41 ont été utilisées pour étudier la fabricabilité de l'alliage R77. Cet alliage est plus sujet à la fissuration lors de la fabrication en raison de sa teneur plus élevée en éléments d'alliage. L'élimination de la fissuration dans un alliage difficile à souder uniquement par l'optimisation des paramètres s'est avérée possible avec le LPBF de R77. De plus, ces structures sans fissures ont été maintenues sur une version modifiée du traitement thermique standard. La caractérisation microstructurale détaillée des échantillons AB et traités

thermiquement a été effectuée de la même manière que pour le R41. Dans ce cas, la présence de précipités  $\gamma'$  extrêmement fins a été identifiée après LPBF et une distribution bimodale comprenant des précipités primaires cubiques et secondaires sphériques s'est développée après le traitement thermique. Les propriétés de traction pour les deux conditions ont été testées à température ambiante et à 810 °C et les résultats ont été comparés avec des homologues forgés et avec d'autres alliages difficiles à souder fabriqués par LPBF. Les échantillons dans les deux conditions ont montré différents comportements de déformation à température ambiante et à température élevée. L'échantillon AB a montré un durcissement significatif alors que celui traité thermiquement avait un allongement amélioré grâce au micro-jumelage activé thermiquement.

# Table of Contents

---

Abstract .....	I
Résumé.....	III
Table of Contents .....	VI
List of Figures .....	IX
List of Tables .....	XIV
Acknowledgments.....	XV
Contributions of Authors .....	XVI
Chapter 1: Introduction .....	1
1.1. Background .....	1
1.2. Research Objectives.....	3
1.3. References .....	3
Chapter 2: Literature Review .....	6
2.1. Laser Powder Bed Fusion (LPBF).....	6
2.2. Nickel-Base Superalloys .....	9
2.2.1. Microstructure of Ni-Base Superalloys .....	9
2.2.2. Heat Treatment of Ni-base Superalloys.....	12
2.2.3. Strengthening Mechanisms in Ni-Base Superalloys.....	16
2.3. Microstructure and Properties of R41 .....	19
2.4. Microstructure and Properties of R77 .....	23
2.5. LPBF of Ni-base Superalloys .....	26
2.5.1. Processability\ Weldability of Ni-base Superalloys .....	26
2.5.2. Microstructure of Ni-base Superalloys Processed by LPBF .....	32
2.5.3. Thermal Post Processing of Ni-base Superalloys Processed by LPBF.....	36

2.5.4. Mechanical Properties of Ni-base Superalloys Processed by LPBF .....	39
2.6. References .....	43
Chapter 3: Microstructure and Mechanical Properties of Rene 41 Alloy Manufactured by Laser Powder Bed Fusion .....	61
3.1. Abstract .....	62
3.2. Introduction .....	62
3.3. Experimental Procedure .....	63
3.4. Results & Discussion .....	65
3.4.1 Powder Characterization .....	65
3.4.2 Microstructural Characterization of the As-fabricated Samples .....	67
3.4.3 Microstructural Characterization of the Heat-Treated Samples .....	71
3.4.4. Mechanical Properties .....	75
3.5. Conclusion .....	79
3.6. Acknowledgement .....	80
3.7. References .....	80
Chapter 4: Effect of Heat Treatment on the Microstructure and Elevated Temperature Tensile Properties of Rene 41 Alloy Produced by Laser Powder Bed Fusion .....	86
4.1. Abstract .....	87
4.2. Introduction .....	87
4.3. Experimental Procedure .....	89
4.4. Results and Discussion .....	91
4.4.1. Microstructure .....	91
4.4.2. Grain Morphology and Texture .....	96
4.4.3. Elevated Temperature Tensile Properties .....	99
4.4.4. Hot Deformation Behavior .....	103
4.4.5. Fractography .....	104

4.5. Conclusion .....	107
4.6. Acknowledgement.....	108
4.7. References .....	108
Chapter 5: Microstructure and Mechanical Properties of Difficult to Weld Rene 77 Superalloy Produced by Laser Powder Bed Fusion .....	115
5.1. Abstract .....	116
5.2. Introduction.....	116
5.3. Materials and Methods.....	118
5.4. Results and Discussion .....	120
5.4.1. Density .....	120
5.4.2. Microstructural Comparison of AB and HT Samples.....	121
5.4.3. Room Temperature Tensile Deformation Behavior .....	128
5.4.4. Elevated Temperature Tensile Deformation Behavior .....	133
5.4.5. Fractography .....	140
5.5. Conclusion .....	143
5.6. Acknowledgment .....	145
5.7. References.....	145
Chapter 6: General Discussion.....	152
6.1. Introduction.....	152
6.2. Laser Powder Bed Fusion of R41 .....	153
6.3. Post-processing Heat Treatment of R41 and Its Effects on Elevated Temperature Properties .....	154
6.4. Laser Powder Bed Fusion of R77 .....	156
6.5. References.....	157
Chapter 7: Conclusion.....	160
Chapter 8: Contributions to the Original Knowledge .....	163

# List of Figures

---

Figure 1. 1. Effect of Al and Ti content on cracking susceptibility of Ni-base superalloys.....	2
Figure 2.1. Schematic illustration of an LPBF system. ....	6
Figure 2. 2. Different LPBF scanning strategies.....	8
Figure 2.3. Crystal structure of the (a) $\gamma'$ , and (b) $\gamma''$ phases .....	11
Figure 2.4. Schematic sketch of microstructure showing possible carbide types and morphologies in Ni-base superalloys.....	12
Figure 2.5. Evolution of $\gamma'$ shape with aging heat treatment .....	14
Figure 2.6. Schematic representation of the effect of cooling rate on $\gamma'$ size, and morphology ..	15
Figure 2.7. Schematical representation of an ordered $\gamma'$ precipitate before and after the dislocation cutting leading to the APB formation .....	18
Figure 2.8. Dislocation particle interactions as a function of precipitate size and their relative contribution to the strength .....	19
Figure 2.9. Microstructure of (a) wrought (b) laser melt deposited R41 alloy subjected to the standard heat treatment .....	21
Figure 2.10. Minor phase concentration in R41 alloy as a function of aging time and temperature .....	22
Figure 2.11. Microstructure of cast and heat-treated R77 showing (a) bimodal $\gamma'$ precipitates, (b) grain boundary carbides.....	25
Figure 2.12. Weldability assessment diagram for Ni-based superalloys using the chemical composition.....	27

Figure 2. 13. Schematic illustration of liquid film behavior for (a) attractive, (b) repulsive grain boundaries .....	29
Figure 2.14. (a) Change in melt pool geometry as a function of energy density, and microstructure, and crack density of CM247LC having (b) low heat input, (c) high heat input .....	32
Figure 2. 15. (a) SEM micrograph, (b) EBSD IPF map of as-fabricated CM247LC .....	33
Figure 2. 16. (a) Solidification map showing the effect of G and R on the resulting microstructure, (b) influence of solidification velocity on the microstructure based on interface stability theory. ....	35
Figure 2.17. SEM micrographs of LPBF fabricated CMSX-4 showing (a) remaining defects, (b) $\gamma'$ structure after optimized heat treatment (c) $\gamma'$ structure of a cast sample after conventional heat treatment .....	38
Figure 2.18. Demonstration of the (a) four different build directions and (b) their corresponding tensile properties .....	41
Figure 2.19. Effect of heat treatment on mechanical properties of various superalloys .....	42
Figure 2.20. (a) Yield strength and (b) ductility of various LPBF processed and heat-treated high $\gamma'$ containing Ni-base superalloys at different temperatures.....	43
Figure 3. 1. SEM micrograph showing (a) size and shape (b) morphology of the R41 powder. .	66
Figure 3. 2. (a) particle size distribution (b) cohesive index of R41 powder. ....	67
Figure 3. 3. Optical micrograph of as polished cross-section of the LPBF fabricated sample. ....	67
Figure 3. 4. EBSD analysis of the as fabricated R41 parts. ....	68
Figure 3. 5. SEM micrograph of the R41 parts fabricated by LPBF. ....	69
Figure 3. 6 BF TEM image and corresponding SAED pattern of the as-fabricated samples. ....	71

Figure 3. 7 (a) Lower magnification (b) higher magnification SEM image of the R41 parts after heat treatment.....	72
Figure 3. 8. EBSD analysis of the heat-treated R41 parts. ....	72
Figure 3. 9. EDS elemental maps of R41 after heat treatment. ....	73
Figure 3. 10. BF TEM images of (a) the heat-treated sample and SAED patterns of (b) $\gamma'$ precipitates in the intercellular area and (c) $M_6C$ carbides on cell boundaries.....	75
Figure 3. 11. Tensile stress strain diagram of R41 alloy in as fabricated and heat-treated condition. ....	77
Figure 3. 12. Tensile fracture surface of (a), (c) as fabricated (b), (d) heat treated R41 samples. 79	
Figure 4. 1. (a) Morphology (b) PSD of the R41 powder.....	90
Figure 4. 2. SEM micrographs of the R41 samples in (a) and (b) AB; (c) and (d) HT1; (e) and (f) HT2 condition. ....	93
Figure 4. 3. SEM micrographs and corresponding EDS linescan analysis of R41 samples in (a) HT1, (b) HT2 conditions.....	94
Figure 4. 4. $\gamma'$ precipitates size distribution upon (a) HT1 and (b) HT2 conditions.....	95
Figure 4. 5. IPF orientation maps and the corresponding pole figures for (a)AB, (b)HT1 and (c)HT2 conditions.....	96
Figure 4. 6. (a) Diameter, (b) aspect ratio of the grains in AB, HT1 and HT2 conditions. ....	97
Figure 4. 7. Recrystallized grain distribution in (a) AB, (b) HT1, (c) HT2 conditions. (d) Fraction of recrystallized grains in all conditions. ....	99
Figure 4. 8. Tensile properties of R41 @ 760C in different conditions; (a) UTS and YS, (b) elongation.....	101

Figure 4. 9. (a) True stress-true strain curve for R41 samples at 760°C, (b) IPF orientation map of HT1 condition near fracture surface along with the misorientation map. .... 104

Figure 4. 10. SEM micrographs (a) near fracture region, (b) and (c) fracture surface of the AB condition. .... 105

Figure 4. 11. SEM micrographs (a) near fracture region, (b) and (c) fracture surface of the HT1 condition. .... 106

Figure 4. 12. SEM micrographs (a) near fracture region, (b) and (c) fracture surface of the HT2 condition. .... 107

Figure 5. 1. (a) Morphology, (b) PSD of the starting R77 powder.....118

Figure 5. 2. As-polished micrograph of the (a) entire cross-section of the AB sample along with the higher magnification images from (b) top, (c) middle, and (d) bottom sections. .... 121

Figure 5. 3. IPF orientation maps and the corresponding pole figures for (a) AB and (b) HT samples..... 123

Figure 5. 4. (a) and (b) SEM micrographs; (c) size distribution of  $\gamma'$  precipitates in AB condition. .... 125

Figure 5. 5. (a) and (b) SEM micrographs; (c) size distribution of  $\gamma'$  precipitates in HT condition. .... 125

Figure 5. 6. SEM micrographs and corresponding EDS linescan analysis in (a) and (c) AB; (b) and (d) HT conditions..... 127

Figure 5. 7. (a) YS vs. elongation (b) UTS vs. elongation of R77 in AB and HT conditions and their comparisons to other high  $\gamma'$  containing alloys at RT ..... 129

Figure 5. 8. EBSD analysis of the AB sample tested at RT (a) IPF orientation map and its corresponding inverse pole figure along the LD. (b) Band contrast, (c) IPF orientation map, and (d) misorientation map of the selected enlarged region highlighting the slip bands. .... 131

Figure 5. 9. EBSD analysis of the HT sample tested at RT (a) IPF orientation map and its corresponding inverse pole figure along the LD. (b) Band contrast, (c) IPF orientation map, and (d) misorientation map of the selected enlarged region..... 133

Figure 5. 10. SEM micrographs after testing at 810 °C in (a) and (b) AB, (c) and (d) HT conditions. .... 135

Figure 5. 11. (a) YS vs. elongation (b) UTS vs. elongation of R77 in AB and HT conditions and their comparisons to other high  $\gamma'$  containing alloys at 810 °C ..... 136

Figure 5. 12. EBSD analysis of the AB sample tested at 810°C (a) IPF orientation map and its corresponding inverse pole figure along the LD. (b) Band contrast, (c) IPF orientation map, and (d) misorientation map of the selected enlarged region highlighting the slip bands. .... 138

Figure 5. 13. EBSD analysis of the HT sample tested at 810°C (a) IPF orientation map and its corresponding inverse pole figure along the LD. (b) Band contrast, (c) IPF orientation map, and (d) misorientation map of the selected enlarged region. (e) and (f) misorientation profile of the twins highlighted in (c). .... 140

Figure 5. 14. (a), (b), and (c) The fracture surface of the AB sample, tested at RT. .... 141

Figure 5. 15. (a), (b), and (c) The fracture surface of the AB sample, tested at 810 °C. .... 142

Figure 5. 16. (a), (b), and (c) The fracture surface of the HT sample, tested at RT. .... 143

Figure 5. 17. (a), (b), and (c) The fracture surface of the HT sample, tested at 810 °C. .... 143

## List of Tables

---

Table 2.1. Summary of the phases observed in Ni-base superalloys.....	10
Table 2.2. Lattice misfit and particle size variations for different alloys, resulting in the shift in the morphology of $\gamma'$ precipitates from spherical to cuboidal .....	14
Table 2.3. Tensile properties of a wrought R41 after the standard heat treatment as a function of temperature .....	23
Table 2.4. Room temperature tensile properties of cast and wrought R77 parts after being subjected to the standard heat treatment .....	25
Table 3.1. Chemical composition of the R41 powder. ....	64
Table 3.2. Summary of the mechanical properties of R41 alloy for different processing conditions. ....	78
Table 4.1. Chemical composition of the R41 powder according to certificate of conformity of the manufacturer. ....	89
Table 4.2. Composition of the $\gamma$ matrix for AB, HT1 and HT2 conditions .....	102
Table 5.1. Chemical composition of the R77 powder as per the certificate of conformity. ....	118

## Acknowledgments

---

First of all, I would like to express my gratitude to my supervisor, Prof. Mathieu Brochu, for giving me the opportunity to be a part of his group and for his continuous support and guidance from the beginning of my Ph.D. I am also grateful to him for constantly providing me opportunities and encouraging me to take responsibility to improve myself both academically and personally. It was an honor working with you and being a part of your research group.

I am also thankful to all my friends in the Materials Engineering department and all the members of the Powder Processing and Additive Manufacturing of Advanced Materials (P2[AM]2) research group, including but not limited to: Beto, Oscar, Xianglong, Amit, Ivonne, Tejas, Pierre, Amy, Eileen, and Mohsen. Thank you for providing support in daily struggles and being there whenever I needed it. I would like to express my special thanks to Nicolas, for all the help and discussions regarding scanning electron microscopy. I also have to acknowledge all the administrative and technical staff of the Materials Engineering department, including Barbara, Leslie, Robert, Florence, and June, for all their assistance.

I would like to acknowledge the Natural Sciences and Engineering Research Council (NSERC) of Canada and the McGill Engineering Doctoral Award (MEDA) for the generous financial support that I received for my research.

It wouldn't be possible for me to accomplish any of these without the support of my family. I want to thank my family Semine, Fikret, and Doğa for their heartwarming support, encouragement, and appreciation throughout my entire life. Last but not least, I would like to express my deepest gratitude to my husband Fatih for his unfailing support, continuous encouragement, patience, and love.

## Contributions of Authors

---

This thesis was organized in a manuscript-based style following the guideline from the Graduate and Postdoctoral Studies of McGill University (<https://www.mcgill.ca/gps/thesis/thesis-guidelines>). The thesis contains three manuscripts, which have been published. Chapters 3, 4, and 5 consists of each the individual manuscript. The contributions of the authors of each manuscript are summarized below.

1. **S.E. Atabay**, O. Sanchez-Mata, J.A. Muñiz-Lerma, R. Gauvin, M. Brochu, Microstructure and mechanical properties of Rene 41 alloy manufactured by laser powder bed fusion, *Mater. Sci. Eng. A.* 773 (2020) (Chapter 3)
2. **S.E. Atabay**, O. Sanchez-Mata, J.A. Muñiz-Lerma, M. Brochu, Effect of heat treatment on the microstructure and elevated temperature tensile properties of Rene 41 alloy produced by laser powder bed fusion, *J. Alloys Compd.* (2020) (Chapter 4)
3. **S.E. Atabay**, O. Sanchez-Mata, J.A. Muñiz-Lerma, M. Brochu, Microstructure and mechanical properties of difficult to weld Rene 77 superalloy produced by laser powder bed fusion, *Mater. Sci. Eng. A.* 827 (2021) (Chapter 5)

As the first author of all the manuscripts, Ms. Atabay developed the main idea of the study, conducted all the sample fabrication and characterization, analyzed all the results, and wrote all the manuscripts.

Mr. Oscar Sanchez-Mata provided support with the metallographic sample preparation and participated in the discussion of the results of all the manuscripts.

Dr. Jose Alberto Muñiz-Lerma provided helpful technical and scientific advice and assistance with the sample fabrication using the Renishaw AM400 laser powder bed fusion system.

Prof. Raynald Gauvin offered technical expertise and assisted in the elemental analysis in Chapter 3.

Prof. Mathieu Brochu supervised the entire project as well as supplied technical and scientific advice for each manuscript.

# Chapter 1: Introduction

---

## 1.1. Background

Nickel base superalloys are one of the primary choices of materials for high-temperature applications. They have microstructural and mechanical stability, as well as high corrosion and oxidation resistance at elevated temperatures up to 1000 °C [1]. The unique high-temperature performance of the Ni-base superalloys is strongly dependent on their composition and microstructural constituents [2,3]. Some Ni-base superalloys rely on solid solution strengthening while some gain their strength from precipitation of the  $\gamma'$  and/or  $\gamma''$  phases, along with some hardening through precipitation of carbides and/or other intermetallic phases [1,4].

Rene 41 (R41) and Rene 77 (R77) are both precipitation-hardened superalloys used for hot section parts of the turbine engines. R41 is known to operate at temperatures up to 980 °C and is mostly used in exhaust nozzles in military turbine engines, hot section parts of jet aircraft engines, and divergent seal and flap components [5,6]. R77 is an alloy with a high  $\gamma'$  volume fraction, designed to operate at a temperature range of 730- 930 °C [7]. It is often used in hot gas turbine engine parts, such as vanes blades and discs [8]. Despite their exceptional elevated temperature performance, usage of these alloys has been limited for a variety of reasons. Strain age cracking in the heat-affected zone and/or in the base metal is reported as a primary problem during welding and post-weld heat treatments of R41 [9]. Susceptibility to cracking is associated with the precipitation kinetics of the  $\gamma'$  precipitates, hence the Al and Ti content of the alloys [10]. As shown in Figure 1.1. R41 and R77 have different cracking susceptibilities according to their compositions. The composition of R41 classifies it as an alloy having moderate weldability from the welding metallurgy definition. As such, its processing window is found to be very limited [11]. For alloy R77, a coarse and inhomogeneous grain structure after casting was reported in addition to its hot cracking susceptibility during welding [8,12–14]. Additionally, the Al and Ti content of the R77 classifies it as a difficult to weld alloy. Hence, the utilization of new processing techniques that allows process parameter and microstructural control would enable the broader application of these alloys.

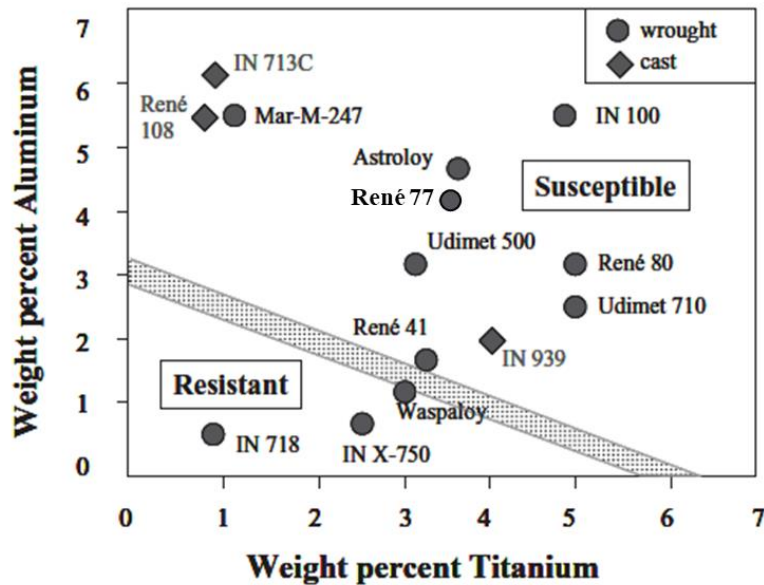


Figure 1. 1. Effect of Al and Ti content on cracking susceptibility of Ni-base superalloys.  
(adapted from [1]).

Laser powder bed fusion (LPBF), one of the main additive manufacturing (AM) processes, involves selective melting and solidification of metal powders by the aid of a laser raster along a pre-defined path. LPBF offers more design flexibility over conventional manufacturing techniques due to its ability to produce complex parts with reduced material waste, production cost, and time [15,16]. Additionally, it enables microstructural control and allows the fabrication of materials having unique microstructural features and superior mechanical properties compared to their cast and/or wrought counterparts. Owing to these advantages, LPBF is attracting more and more attention to fabricate high-temperature components for aerospace and nuclear applications [17,18].

In spite of all the advantages it has to offer, LPBF of precipitation-hardenable Ni-base superalloys remains challenging. The material encounters rapid heating and cooling cycles during fabrication, resulting in the presence of high residual stresses in the finished part. The combination of these residual stresses with the cracking susceptibility of Ni-base superalloys limits their processing and applications [19,20]. Hence, the success of LPBF of precipitation-hardenable Ni-base superalloys remains limited to a few alloys [21–23]. Many alloys having superior elevated temperature properties are overlooked. Even for the alloys that are extensively studied, a knowledge gap exists in terms of their microstructural and mechanical response to the post-processing heat treatments.

## 1.2. Research Objectives

The main objective of this research is to assess the processability of precipitation-hardenable Ni-based superalloys, R41 and R77, by LPBF. This includes process parameter optimization to achieve high-density defect-free parts from cracking susceptible alloys along with investigation of the microstructural development and mechanical properties of the parts both after fabrication and subsequent heat treatments. Specifically, the research will focus on the following aspects:

1. Understand the LPBF processability and microstructural development of R41, an alloy with moderate weldability, and R77, a difficult to weld alloy.
2. Comprehend the microstructure evolution during post-processing heat treatments to design new heat treatments compatible with the LPBF microstructure.
3. Understand the relation between the microstructure and the room and elevated temperature mechanical properties.
4. Understand the transferability of the process parameter and heat treatment design knowledge between different alloy systems having different susceptibilities to cracking.

## 1.3. References

- [1] J.N.D.& J. C.Lippold, *Welding Metallurgy and Weldability of Nickel-Base Alloys*, J. Chem. Inf. Model. 53 (2009) 456. doi:10.1017/CBO9781107415324.004.
- [2] R.C. Reed, *The Superalloys fundamentals and applications*, *Superalloys Fundam. Appl.* 9780521859 (2006) 1–372. doi:10.1017/CBO9780511541285.
- [3] J. Chander, *Hardening Mechanism and Corrosion Resistance of Nickel-Base Alloys: A Review*, *Can. Metall. Q.* 3 (1964) 57–77. doi:10.1179/cmq.1964.3.1.57.
- [4] B. Geddes, H. Leon, X. Huang, *Superalloys: Alloying and Performance*, 2010. doi:10.1016/B978-0-7020-2797-0.00001-1.
- [5] Q.L. Pan, B. Li, Y. Wang, Y.W. Zhang, Z.M. Yin, *Characterization of hot deformation behavior of Ni-base superalloy Rene’41 using processing map*, *Mater. Sci. Eng. A.* 585 (2013) 371–378. doi:10.1016/j.msea.2013.07.066.
- [6] D. Tali, H. Gasan, M. Gulesen, S. Gurgun, M. Cemal, *Turning Operation of Nickel Based Superalloy Rene 41*, (2017) 9–11.
- [7] S. Wang, *Welding and Repair of Single Crystal Ni-based Superalloys*, (2005).

- [8] H.-S. Wang, C.-Y. Huang, K.-S. Ho, S.-J. Deng, Microstructure Evolution of Laser Repair Welded René 77 Nickel-Based Superalloy Cast, *Mater. Trans.* 52 (2011) 2197–2204. doi:10.2320/matertrans.m2011264.
- [9] R. Kayacan, R. Varol, O. Kimilli, The effects of pre- and post-weld heat treatment variables on the strain-age cracking in welded Rene 41 components, *Mater. Res. Bull.* 39 (2004) 2171–2186. doi:10.1016/j.materresbull.2004.08.003.
- [10] S. Kou, *Welding Metallurgy*, 2nd Editio, A John Wiley & Sons, Inc., 2003.
- [11] M.M. Attallah, R. Jennings, X. Wang, L.N. Carter, Additive manufacturing of Ni-based superalloys: The outstanding issues, *MRS Bull.* 41 (2016) 758–764. doi:10.1557/mrs.2016.211.
- [12] R.G. Ding, O.A. Ojo, M.C. Chaturvedi, Laser beam weld-metal microstructure in a yttrium modified directionally solidified Ni<sub>3</sub>Al-base alloy, *Intermetallics*. 15 (2007) 1504–1510. doi:10.1016/J.INTERMET.2007.05.008.
- [13] M. Zielińska, J. Sieniawski, M. Poręba, Microstructure and mechanical properties of high temperature creep resisting superalloy René 77 modified CoAl<sub>2</sub>O<sub>4</sub>, *Arch. Mater.* 28 (2007) 629–632.
- [14] M. Zielinska, J. Sieniawski, Surface modification and its influence on the microstructure and creep resistance of nickel based superalloy René 77, *Arch. Metall. Mater.* 58 (2013) 95–98. doi:10.2478/v10172-012-0157-6.
- [15] D. Herzog, V. Seyda, E. Wycisk, C. Emmelmann, Additive manufacturing of metals, *Acta Mater.* 117 (2016) 371–392. doi:10.1016/j.actamat.2016.07.019.
- [16] W.E. Frazier, Metal additive manufacturing: A review, *J. Mater. Eng. Perform.* 23 (2014) 1917–1928. doi:10.1007/s11665-014-0958-z.
- [17] A.S. Shaikh, F. Schulz, K. Minet-Lallemand, E. Hryha, Microstructure and Mechanical Properties of Haynes 282 Superalloy Produced by Laser Powder Bed Fusion, *Mater. Today Commun.* (2021) 102038. doi:10.1016/j.mtcomm.2021.102038.
- [18] B. Peter, Development in Additive Manufacturing for High Temperature Alloys, DOE/NETL Crosscutting Res. Progr. Annu. Rev. Meet. 2015. (2015).
- [19] L.N. Carter, M.M. Attallah, R.C. Reed, Laser powder bed fabrication of nickel-base superalloys: influence of parameters; characterisation, quantification and mitigation of cracking, *Proc. 12th Int. Symp. Superalloys*, Champion, PA, 9–13 Sept. 2012. (2012) 577–

586. doi:10.1002/9781118516430.ch64.
- [20] W.E. King, A.T. Anderson, R.M. Ferencz, N.E. Hodge, C. Kamath, S.A. Khairallah, A. Rubenchik, Laser powder bed fusion additive manufacturing of metals; physics, computational, and materials challenges, *Appl. Phys. Rev.* 2 (2015). doi:10.1063/1.4937809.
- [21] Y. Gao, D. Zhang, M. Cao, R. Chen, Z. Feng, R. Poprawe, J.H. Schleifenbaum, S. Ziegler, Effect of  $\delta$  phase on high temperature mechanical performances of Inconel 718 fabricated with SLM process, *Mater. Sci. Eng. A.* 767 (2019) 138327. doi:10.1016/J.MSEA.2019.138327.
- [22] H.E. Helmer, C. Körner, R.F. Singer, Additive manufacturing of nickel-based superalloy Inconel 718 by selective electron beam melting: Processing window and microstructure, *J. Mater. Res.* 29 (2014) 1987–1996. doi:10.1557/jmr.2014.192.
- [23] Y. Tian, J.A. Muñoz-Lerma, M. Brochu, Nickel-based superalloy microstructure obtained by pulsed laser powder bed fusion, *Mater. Charact.* 131 (2017) 306–315. doi:10.1016/j.matchar.2017.07.024.

## Chapter 2: Literature Review

---

### 2.1. Laser Powder Bed Fusion (LPBF)

Laser powder bed fusion (LPBF), as one of the main additive manufacturing techniques defined by the ASTM committee F42, has driven significant research, and found applications in many areas such as aerospace, automobile, and nuclear industries [1–3]. LPBF offers great design flexibility by allowing complex part production with reduced material waste, production cost, and time [4–6].

A schematical illustration of an LPBF system is shown in Figure 2.1. The process involves selective melting and solidification of certain areas on the powder bed by a focused laser beam. The laser scanning path is defined by the part geometry and the selected scan strategy. After completion of a layer, the build plate is lowered by a thickness equivalent to the layer thickness, and a fresh layer of the powder is spread by the recoater. This process continues until the part is completed. The built chamber is protected with the flow of an inert gas (argon, nitrogen) during the process to avoid oxidation [5,7]

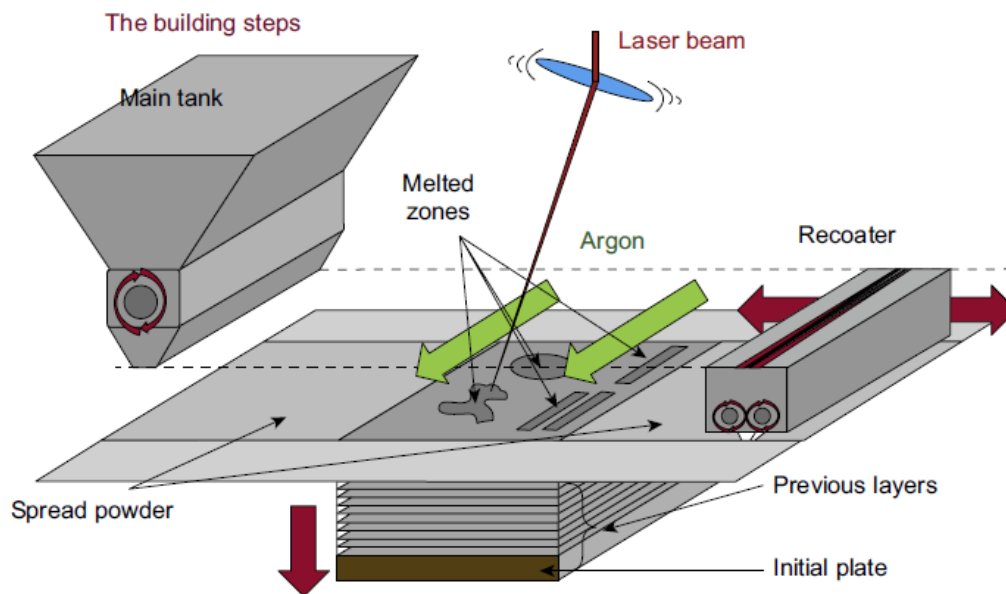


Figure 2.1. Schematic illustration of an LPBF system [5].

Control of various process parameters is required to achieve the desired microstructure and properties for the manufactured components. The basic processing parameters in the LPBF include layer thickness ( $t$ ), laser power ( $P$ ), hatch spacing ( $h$ ), and scanning speed ( $v$ ) in the case of a continuous laser. If the used laser type is pulsed the scanning speed parameter is replaced by the ratio of the point distance between each pulse ( $pd$ ) to the exposure time of a single pulse ( $ET$ ). To characterize the process, a combination of these key variables defined as volumetric energy density is used. The volumetric energy densities for a continuous laser ( $E_c$ ) and a pulsed laser ( $E_p$ ) can be calculated by using the following equations [5];

$$E_c = \frac{P}{v \cdot h \cdot t} \quad (2.1)$$

$$E_p = \frac{P \cdot ET}{pd \cdot h \cdot t} \quad (2.2)$$

In addition to the parameters included in the volumetric energy density equation, the particle size distribution of powder, and laser scanning strategy, play an important role in the finished part quality [8].

Gas atomized powders with spherical shapes are widely used as the feedstock material for the LPBF process to improve powder bed packing density and flowability. These factors are determined by the morphology, size, and distribution of the powder particles. Non-spherical morphologies tend to interlock mechanically and entangle, limiting the flowability of the powder and causing a non-homogenous layer. This may lead to the formation of defects such as porosity and/or incomplete melting in the finished part [9]. Usually, a wide particle size distribution ranging between 10-60  $\mu\text{m}$  is preferred over a monomodal size distribution for LPBF. The wide size distribution improves the packing density as the smaller particles fill the gaps between the larger particles [5,10]. On the other hand, most of the LPBF powders are prone to contamination by gas or moisture adsorption due to their high surface area per unit volume. These contaminants may cause poor powder layer quality resulting in the degradation of the overall properties of the part [10].

Scanning strategy in LPBF can be defined as the scanning directions (e.g., unidirectional, or bidirectional) and arrangement of the scan sequences [8]. After the direction of the laser tracks is determined, various scanning strategies can be employed to fill the pre-defined area. These

strategies include but are not limited to meander, stripe, chessboard, and spiral scanning. Representation of the different scanning strategies is shown in Figure 2.2. Furthermore, the rotation between each layer can be adjusted to modify the grain morphology. The overlapping of the beads and scanning patterns affects the grain orientation and texture as well as the cooling rate. Hence, refined control over the overall material properties of the component can be achieved by modifying the scanning strategies [11,12]

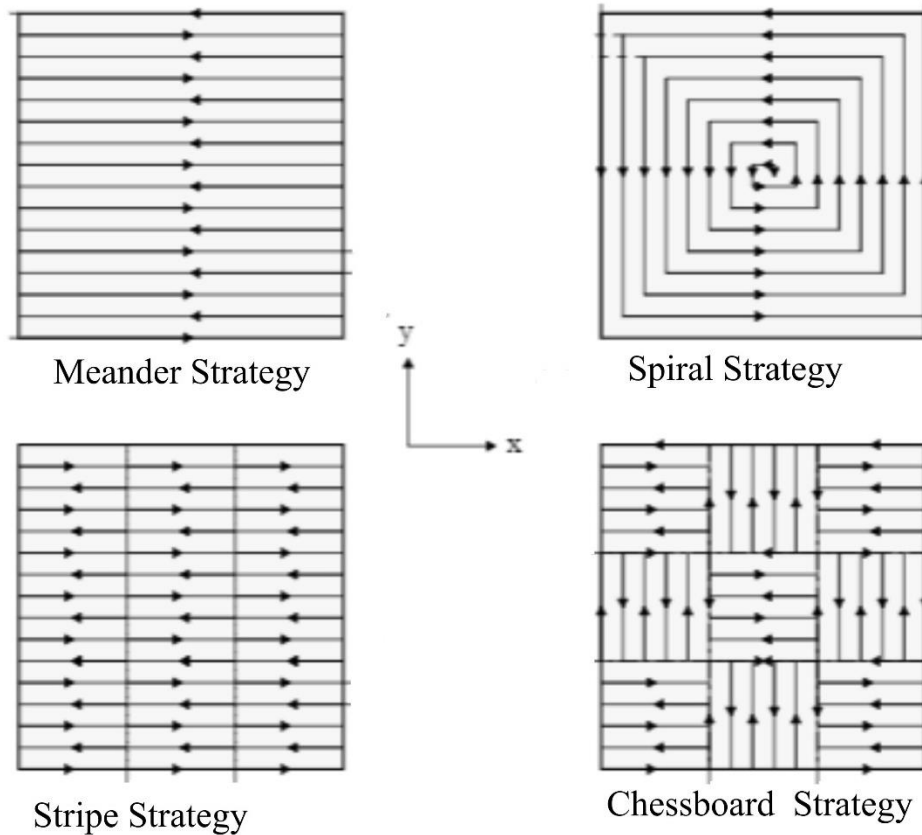


Figure 2. 2. Different LPBF scanning strategies (Adapted from [13]).

LPBF is used to process a variety of metals and their alloys including nickel-base superalloys [14–18], stainless steels [19–22], titanium alloys [8,23,24], aluminum alloys [25–27], high entropy alloys [28,29], copper alloys [30,31]. Among these alloys, Ni-base superalloys are one of the primary choices of materials for aerospace and nuclear application due to their superior properties during high-temperature service [32,33].

## **2.2. Nickel-Base Superalloys**

Ni-base superalloys were first introduced in the late nineteenth century and were developed to a high level of sophistication since then. They are one of the most important classes of engineering materials due to their properties that enables them to be used in a wide range of environments and applications [34]. These alloys can be used for applications that require aqueous and/or high-temperature corrosion resistance, high strength at ambient and high temperature. They are also widely used high-temperature materials in aerospace and power plant applications due to their resistance to fatigue, creep, and environmental degradation at temperatures up to 1000°C [35]. Unlike aluminum or steel alloys Ni-base superalloys don't have a systematic classification. They are most widely classified depending on their composition, hence the constituent phases [34]. If the properties of the alloy are mainly derived by the alloying elements that are in solid solution in the nickel ( $\gamma$ ) matrix, they are classified as solid solution strengthened alloys. When the alloys are hardened by the precipitation of the secondary phases  $\gamma'$  or  $\gamma''$ , they are classified as a precipitation strengthened alloy. Another sub-category is the oxide dispersion strengthened Ni-based superalloys. These alloys gain their properties via the fine oxide particles dispersed in the  $\gamma$  matrix. [35,36].

### **2.2.1. Microstructure of Ni-Base Superalloys**

Ni-base superalloys contain a wide range of alloying elements with relatively high concentrations. Therefore, their microstructure is highly complex with a large number of intermetallics and other phases that determine the properties of the alloy through their fraction, morphology, composition, and location. Table 2.1. gives an overview of the notable phases and the general effects of various alloying elements on phase stability [37].

Table 2.1. Summary of the phases observed in Ni-base superalloys (adapted from [35]).

Matrix Phase:		
<b><math>\gamma</math> (FCC)</b> Solid Solution Strengtheners: Co, Cr, Mo, W, (Fe, Ru, Re)		
Precipitate Phases:		
<b><math>\gamma'</math> Ni<sub>3</sub>(Al,Ti) (L1<sub>2</sub>)</b> Al, Ti	<b><math>\gamma''</math> Ni<sub>3</sub>Nb (BCT)</b> Nb	
Carbides:		
<b>MC</b> W, Mo, Ti, Ta, Nb, Hf	<b>M<sub>23</sub>C<sub>6</sub></b> W, Mo, Cr	<b>M<sub>6</sub>C</b> Mo, W, Nb

The microstructure of superalloys is a face-centered cubic (FCC)  $\gamma$  matrix that contains various secondary phases. Due to the high solubility of nickel, this phase may contain significant concentrations of alloying elements. The addition of substitutional alloying elements such as Cr, Co, Mo, Fe, W, Ru, and Re, within the solubility limit of the matrix phase, contributes to the solid solution strengthening of the  $\gamma$  matrix.

When the composition of Al, Ti in the alloys reaches up to the solubility limit of the  $\gamma$  phase, they form a precipitate phase called  $\gamma'$  coherent with the matrix due to their similar lattice parameters and crystal structures [34]. This phase has a chemical formula of Ni<sub>3</sub>(Al, Ti) with an L1<sub>2</sub> crystal structure with Ni atoms on the faces and either Al or Ti atoms at the corner as shown in Figure 2.3(a) [38].  $\gamma'$  precipitates are the primary strengthening phase at room and elevated temperatures for precipitation strengthened alloys [39].  $\gamma'$  precipitates can have various morphologies such as spherical, cuboidal, and arrays of cubes. The amount of strengthening provided by these precipitates is determined by their size, fraction, and morphology. The volume fraction of these precipitates is determined by the composition of the alloy, yet it can be modified through heat treatments along with their size and morphology [40–42].

When the alloy is rich in Fe and Nb, coherent BCT  $\gamma''$  precipitates form instead of  $\gamma'$ .  $\gamma''$  precipitates have ordered, D0<sub>22</sub> crystal structure shown in Figure 2.3(b) with a disc-shaped morphology

[43,44]. Alloys strengthened by the  $\gamma''$  precipitates have a lower service temperature, caused by the loss of strength at temperatures above 650 °C. This rapid loss in strength is associated with the transformation of  $\gamma''$  to  $\delta$  [37,45].

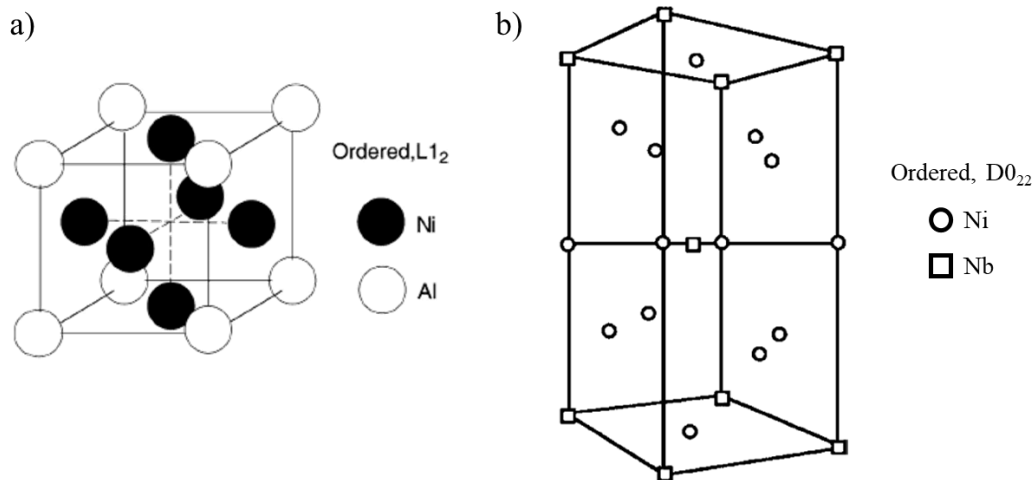


Figure 2.3. Crystal structure of the (a)  $\gamma'$ , and (b)  $\gamma''$  phases (adapted from [34]).

Carbon is present in superalloys as a minor alloying element. Depending on the composition, solidification conditions, and thermal history of the alloy, various carbides are observed in all superalloy groups [46]. The most common types of carbides observed are MC,  $M_{23}C_6$ ,  $M_6C$  where M corresponds to metal atoms such as Mo, Ti, Cr, W, Nb, Ta, Hf [34]. Carbides with globular, blocky, and script morphologies were reported [47,48]. Figure 2.4 shows a representative micrograph sketch showing different types and morphologies of carbides observed in Ni-base superalloys. In most of the superalloys, MC carbides were observed to form in the liquid phase due to the segregation of C during solidification and thus are often present in the inter-dendritic region [49]. MC carbides are found to be very stable at low temperatures but tend to transform into secondary carbides like  $M_{23}C_6$  and  $M_6C$  at intermediate temperatures around 750 °C.  $M_{23}C_6$  carbides mainly contain Cr and Mo and are usually observed at the high angle grain boundaries. They may form discrete particles as well as a grain boundary film. Discontinuous particles were proven to have a significant role in the strengthening whereas a continuous film is detrimental in terms of ductility and rupture life.  $M_6C$  carbides are more stable at elevated temperatures compared to the  $M_{23}C_6$  carbides, due to the higher concentration of refractory elements such as W and Mo.

These carbides can be present both within the grains and at grain boundaries and they usually have a blocky morphology [49–52].

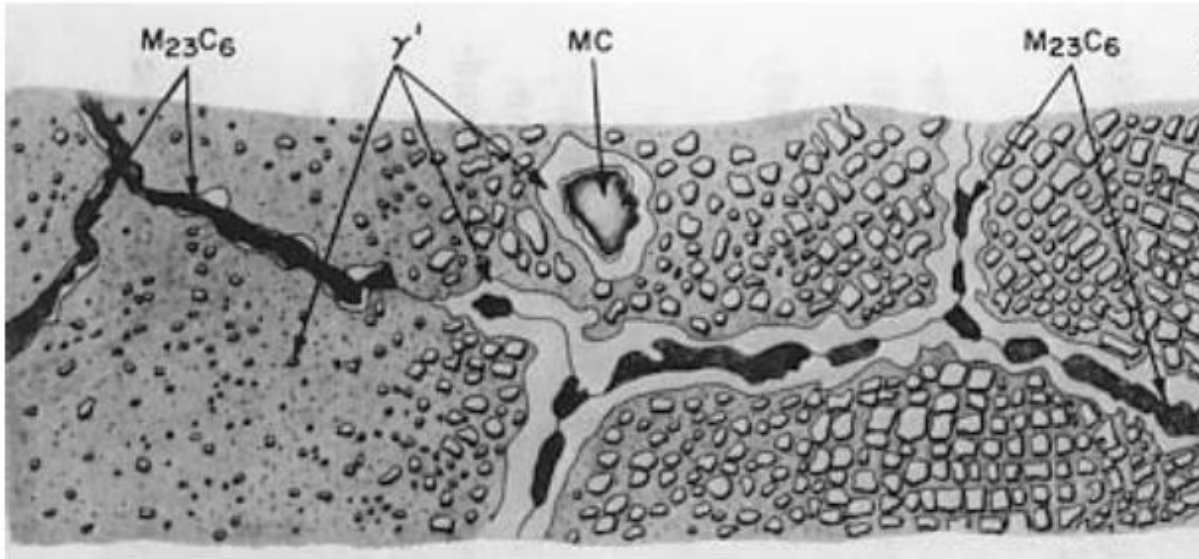


Figure 2.4. Schematic sketch of microstructure showing possible carbide types and morphologies in Ni-base superalloys (adapted from [53]).

The high concentration in refractory metals like W, Mo, Cr, and Re in superalloys leads to the formation of intermetallic phases with high and uniform packing density [54]. Those phases are called topologically closed packed (TCP) phases and generally have a complex crystal structure [34]. The presence of TCP phases is usually known to be detrimental for alloy properties since they reduce the concentration of solid solution elements in the matrix causing a loss in strength and corrosion resistance. They are brittle phases and act as a crack initiation site due to their lath or plate-like morphology, resulting in a reduction in ductility and fatigue life of the alloy [55].

### 2.2.2. Heat Treatment of Ni-base Superalloys

Ni-base superalloys are often subjected to post-processing heat treatments to relieve residual stresses, modify the surface morphology, or modify the microstructure to obtain desired properties [56,57]. The microstructure of the alloys is most commonly modified by homogenization, solutionizing, and aging heat treatments [40,58,59].

Due to their complex chemistries, segregation of alloying elements is observed during solidification. Homogenization heat treatment is used to reduce the compositional gradients and

homogenize the microstructure [60,61]. For precipitation-hardenable superalloys, a solutionizing heat treatment is used followed by an aging treatment. The solutionizing heat treatment involves heating the alloy to a temperature between 1040-1230 °C to dissolve the precipitates formed during solidification. This treatment is followed by rapid cooling of the part to ambient temperature to prevent further precipitation. Then the sample is aged at a temperature below the solvus temperature of  $\gamma'$  to allow the formation of  $\gamma'$  precipitates.

The mechanism leading to  $\gamma'$  precipitation involves diffusion of solute, which might be either classical nucleation and growth or spinodal decomposition [62]. In classical nucleation, a nucleus of a different phase forms to reduce the total free energy of the system  $\Delta G$  given by equation (2.3), where  $V$  is the volume of the nucleus,  $\Delta G_v$  is volumetric free energy change,  $A$  is the surface area,  $\gamma_i$  is interfacial energy and  $\Delta G_s$  is the strain energy change [63]. The nucleation process involves an activation barrier  $\Delta G^*$  defined by equation (2.4). On the other hand, spinodal decomposition occurs by a mechanism where there is no activation barrier for the formation of the precipitates. This process occurs when the small compositional fluctuations spontaneously grow into equilibrium phases to lower the total free energy of the system [64]. Such decomposition is expected to take place in systems that are undercooled to a large extent below their equilibrium transformation temperature [65].

$$\Delta G = -V\Delta G_v + A\gamma_i + V\Delta G_s \quad (2.3)$$

$$\Delta G^* = \frac{16\pi\gamma_i^3}{3(\Delta G_v - \Delta G_s)^2} \quad (2.4)$$

At the early stages of the aging treatment, precipitates have a spherical shape to minimize the interfacial energy therefore, strain energy contribution is minimal. As the precipitates grow, they induce deformation in the surrounding  $\gamma$  matrix lattice creating a stress field. When the magnitude of this stress field is enough to deform the  $\gamma'$  particles, the morphology of the precipitates changes into a cuboidal shape [59,66]. This transition is directly dependent on the size of the precipitate and the lattice parameter misfit ( $\delta$ ) between  $\gamma$  and  $\gamma'$  phases, as per equation (2.5) [34]. Ricks et.al experimentally proved that the critical size that leads to this change in morphology from spherical to cuboidal is different for different alloys and it is dependent on the lattice misfit. Table 2.2. shows that as the lattice misfit between the  $\gamma/\gamma'$  increases, critical particles size to reach the strain field for the morphological transformation decreases [67]. When the material is aged further, coherency

strains are in tension parallel to the faces of the cubes and compressive normal to the faces. This creates a region of low strain on the corners; hence particles continue to grow at the corners. Growth continues on the corners until they also transform into cuboidal morphology. This results in a cuboidal array of  $\gamma'$  precipitates generally observed in the over-aged alloys [34,35,39]. The transition of the morphology of the  $\gamma'$  is shown schematically in Figure 2.5.

$$\delta = 2 \times \left[ \frac{a_{\gamma'} - a_{\gamma}}{a_{\gamma'} + a_{\gamma}} \right] \quad (2.5)$$

Table 2.2. Lattice misfit and particle size variations for different alloys, resulting in the shift in the morphology of  $\gamma'$  precipitates from spherical to cuboidal (adapted from [67]).

Alloy	Lattice Misfit (%)	Critical particle size for spherical/cuboidal transition ( $\mu\text{m}$ )
Udimet 720	<0.2	0.7
Nimonic 105	-0.04	0.7
Nimonic 115	- 0.18	0.5
Nimonic 80A	+ 0.32	0.3
Nimonic 90	+ 0.34	0.3

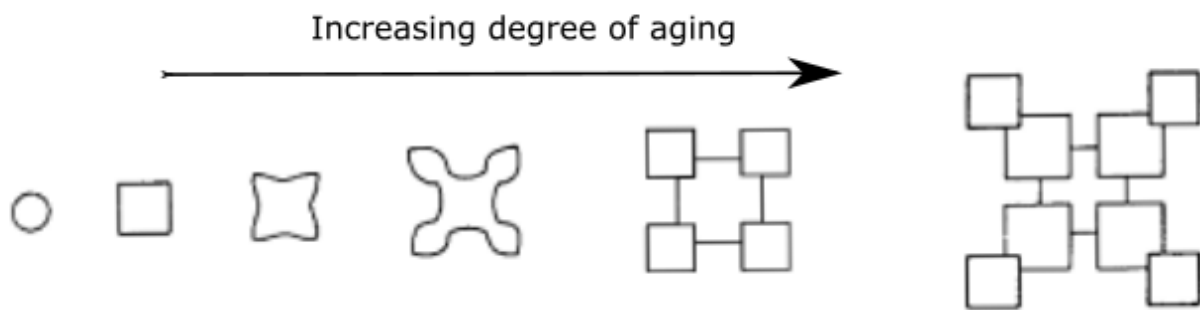


Figure 2.5. Evolution of  $\gamma'$  shape with aging heat treatment (adapted from [34]).

The size, distribution, and morphology of these precipitates have an important impact on the final properties of the part and are highly dependent on the cooling rates during the processing route and applied heat treatments. The studies on the cooling rate effect showed the formation of a monomodal precipitate distribution for high cooling rates such as the ones achieved in water quenching. This is explained by the relatively high nucleation density and limited growth of the

precipitates when they are exposed to such cooling rates [65,68,69]. However, slowly cooled samples revealed a microstructure consisting of multiple  $\gamma'$  size ranges and morphologies [70]. The resulting  $\gamma'$  morphologies caused by different cooling rates and possible size distributions are shown in Figure 2.6 along with the representative micrographs showing spherical unimodal, cuboidal unimodal, and bimodal distributions. In reality, a concentration gradient exists between the cells and cell boundaries in the solidified microstructure of superalloys. The solutionizing heat treatment temperature is selected below the solvus temperature of the  $\gamma'$  to prevent liquation due to these compositional fluctuations. Therefore, a multimodal distribution of  $\gamma'$  particles is generally observed after the heat treatment [34,71,72].

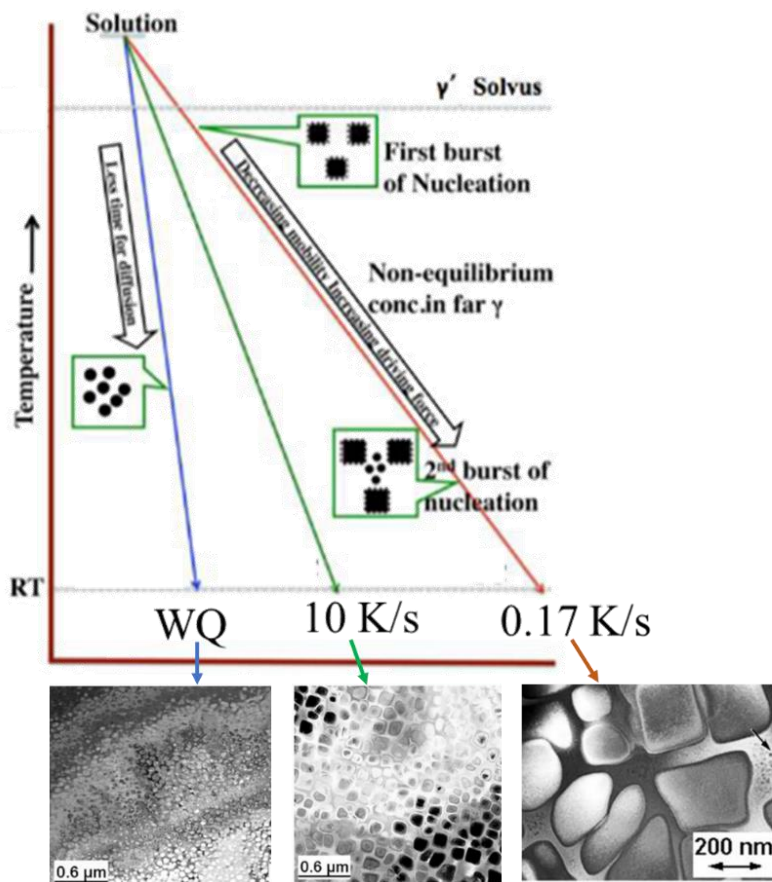


Figure 2.6. Schematic representation of the effect of cooling rate on  $\gamma'$  size, and morphology (adapted from [62,69]).

Although the combined contribution of this multimodal size distribution to the mechanical properties is still not fully understood, it is known that a critical primary  $\gamma'$  particle size has to be reached to have the optimum amount of strengthening through precipitation. Furthermore, a shape

parameter can be used to define the optimal precipitate shape for good high-temperature creep properties. This parameter is directly related to the  $\gamma/\gamma'$  lattice mismatch [73]. Studies also suggest that the presence of small secondary  $\gamma'$  particles, forming in the channels between the primary precipitates improves the creep resistance of the parts [39,74].

### 2.2.3. Strengthening Mechanisms in Ni-Base Superalloys

Ni-based superalloys are the primary choice of material for high-temperature applications due to their exceptional strength both at room and elevated temperatures. A variety of strengthening mechanisms are identified and have been known to contribute to the overall strength of Ni-base superalloys. The main strengthening mechanisms observed in a polycrystalline precipitation-hardenable superalloys are grain boundary strengthening, dislocation strengthening, solid solution strengthening, and precipitation strengthening.

One of the most commonly encountered strengthening mechanisms is grain boundary strengthening. It has been attributed to the presence of high angle grain boundaries acting as a barrier to dislocation motion. The amount of strengthening is directly related to the number of grain boundaries. Hence, grain boundary strengthening is more effective in fine-grained materials. [75]. This is explained by the Hall-Petch relationship given by equation 2.6 [76], where  $D$  is the grain size and  $k_y$  is the constant that has been determined to be  $750 \text{ MPa } \mu\text{m}^{-1/2}$  for superalloys [77,78].

$$\Delta\sigma_{gb} = \frac{k_y}{\sqrt{D}} \quad (2.6)$$

Dislocation strengthening is also a widely accepted mechanism contributing to the strength of superalloys. It is expressed by Taylor and denoted by equation 2.7, where  $M$  is the Taylor factor,  $\beta$  is a constant equal to  $1/3$  for Ni-based superalloys,  $G$  is the shear modulus,  $b$  is burgers vector and  $\rho_d$  is the dislocation density [79,80].

$$\Delta\sigma_d = M\beta Gb\sqrt{\rho_d} \quad (2.7)$$

Another mechanism contributing to the overall strength is solid solution strengthening. Ni-based superalloys contain many different alloying elements that are in solid solution with the  $\gamma$  matrix. The difference in the atomic size of Ni and these substitutional solute atoms distorts the Ni crystal

lattice. This creates a strain field and impedes the dislocation motion resulting in the strengthening [77]. The theory of solid solution strengthening is based on the model proposed by Gypen and Deruyettere [81,82] and is given by equation 2.8, where  $\frac{d\sigma}{\sqrt{dC_i}}$  is a strengthening coefficient that is developed by studying the effect of ternary and higher-order alloying addition to the  $\gamma$  matrix [75,83].

$$\Delta\sigma_{SSS} = \sum_i \left( \frac{d\sigma}{\sqrt{dC_i}} \sqrt{C_i} \right) \quad (2.8)$$

Precipitation hardenable Ni-based superalloys also gain a significant amount of strength due to the interaction of dislocations with  $\gamma'$  particles.  $\gamma'$  precipitates have the ordered L<sub>12</sub> structure. To maintain this ordered structure, dislocations have to travel in pairs while moving through these particles [84]. This particular strengthening mechanism is also named ‘order strengthening’. When the leading dislocation shears the ordered  $\gamma'$  precipitate, it creates an antiphase boundary (APB) across the slip plane, the passage of the trailing dislocation removes it and restores the order [34,64]. Schematic representation of the APB formation is shown in Figure 2.7. Studies show that order strengthening is the most effective strengthening mechanism in precipitation hardenable superalloys, and its effect increases with increasing  $\gamma'$  volume fraction. The amount of strengthening depends upon the dislocation particle interactions determined by the size of the precipitate and APB energy (hence, the equilibrium spacing of paired dislocations) [39,77]

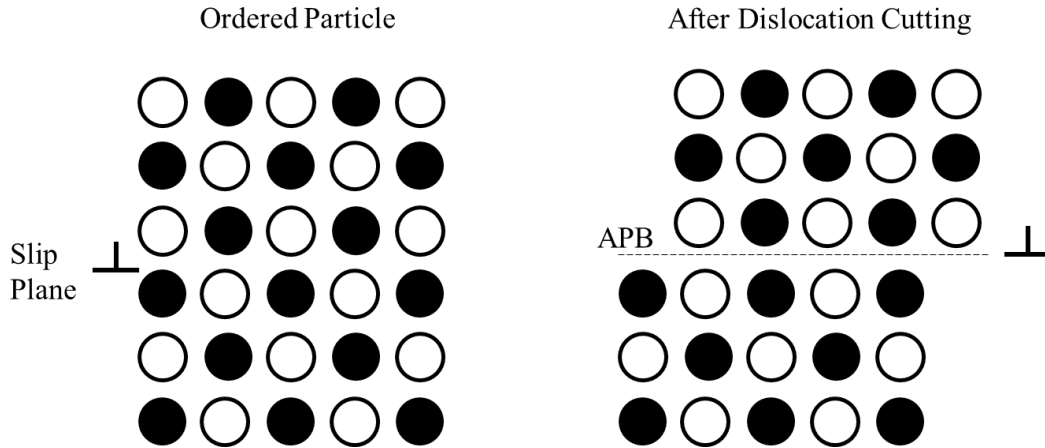


Figure 2.7. Schematical representation of an ordered  $\gamma'$  precipitate before and after the dislocation cutting leading to the APB formation (adapted from [35]).

A distinction was made between weak and strong pair coupling of the dislocation pairs and their interaction with  $\gamma'$  precipitates. In the case of weak pair coupling, each dislocation in the pair is located within a different particle. This case is usually observed when the precipitate size is extremely fine (less than 20 nm). For larger precipitates, the dislocation pair is held together by a higher APB energy and found within the same particle. This situation is called strong pair coupling [75,77]. Kozar et.al. reported that the active mechanism changes from weak pair coupling to strong pair coupling as the size of the  $\gamma'$  precipitates increases. Studies show that the peak material strength is achieved at the transition between the weak and strong pair coupling. However, the critical diameter at which this change occurs depends on the APB energy [75,85,86]. When the particle size is even larger (approximately more than 400nm) the stress required to shear the particles are greater than the stress required to bow between precipitates. In this case, the Orowan looping mechanism is observed. However, Preuss et al. suggested that Orowan looping is not commonly seen in polycrystalline Ni-based superalloys due to the small values of misfit or the complexity of the bi- or tri-modal  $\gamma'$  particle size distributions [77,87,88]. All possible particle dislocation interactions and their contribution to the strength are summarized in Figure 2.8.

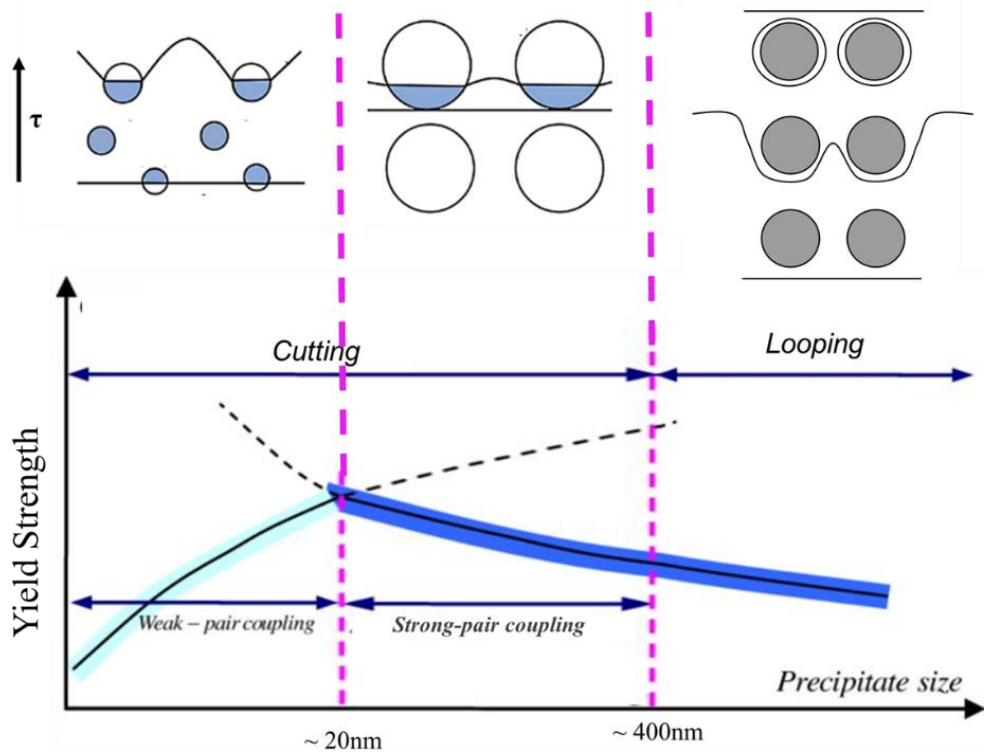


Figure 2.8. Dislocation particle interactions as a function of precipitate size and their relative contribution to the strength (adapted from [72,75,76]).

Evidently, many underlying mechanisms add to the strength of Ni-based superalloys. Individually all the mechanisms are well understood and studied in detail. A comprehensive understanding of the operative strengthening mechanisms enables the design of solidification and heat treatment conditions for desired microstructure.

### 2.3. Microstructure and Properties of R41

R41 is a precipitation strengthened alloy developed in the mid-1950s. It possesses an excellent combination of corrosion and oxidation resistance along with high mechanical and microstructural stability at temperatures up to 980 °C [89,90]. Due to these properties, it is widely used in hot section parts of jet aircraft engines and divergent seal and flap components, and exhaust nozzles in military turbine engines [91,92].

R41 contains Mo, Cr, Co, Fe, Ti, and Al as main alloying elements. Mo, Cr, Co, and Fe are in solid solution in Ni, providing matrix strengthening by creating lattice strain. Cr and Mo also provide

high-temperature corrosion and oxidation resistance. Al and Ti form the  $\gamma'$  phase that provides the main strengthening. Co also makes  $\gamma'$  precipitation more favorable by decreasing the solubility of Al and Ti in Ni. R41 gains its properties both through solid solution strengthening and precipitation hardening [93–95].

Independently from their purpose, distribution of these alloying elements during solidification plays a significant role in the resultant microstructure. The elemental segregation behavior is determined by the segregation coefficient ( $k$ ) and diffusivity ( $D$ ) for the alloying element of interest. Elements with partition coefficient value close to unity like Cr, Co, Fe go into solid solution in Ni while elements with  $k$  value smaller than unity partition in the liquid and segregate in the interdendritic region [96].

Since R41 encounters high temperatures service conditions, stability of the precipitates against coarsening has utmost importance. Coarsening is driven entirely by minimization of the interfacial energy hence, low  $\gamma/\gamma'$  interfacial energy is required for interfacial stability. Heat treatment cycles were optimized for wrought R41 alloy to minimize the interfacial energy between the matrix and the  $\gamma'$  precipitates [34,38].

The standard heat treatment cycle for R41 involves solutionizing at 1065 °C for 4 hours then air cooling to room temperature followed by an aging treatment at 760 °C for 16 hours [97]. Figure 2.9(a) shows the microstructure obtained after aging heat treatment for a wrought [97] and laser melt deposited [94] R41 alloy. Both micrographs consist of  $\gamma'$  precipitates in  $\gamma$  matrix along with a mixture of  $M_6C$  (white),  $MC$  (gray), and  $M_{23}C_6$  carbides at grain boundaries.

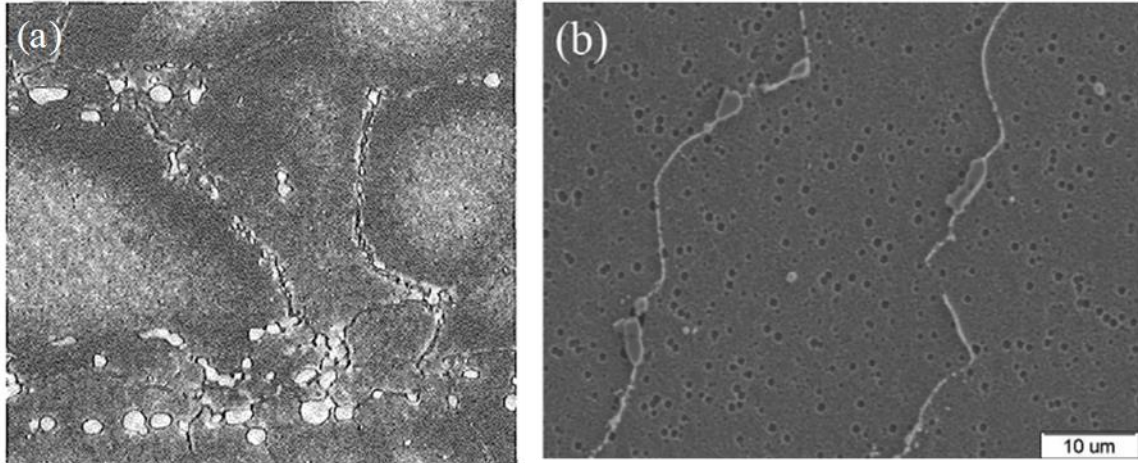


Figure 2.9. Microstructure of (a) wrought (b) laser melt deposited R41 alloy subjected to the standard heat treatment (adapted from [94,97]).

In addition to the  $\gamma'$  precipitates, morphology and type of carbides are also strictly dependent on aging temperature and time as well as the processing condition of the alloy. Figure 2.10 shows the concentration of possible phases as a function of aging time and temperature which can be used as a reference to predict the microstructural change during heat treatments as well as the service life [98,99]. Previous studies identified the formation of MC carbides of Mo and Ti in the grains and at grain boundaries [94,100]. These carbides are stable and abundant at temperatures between 760-870 °C [101]. At higher temperatures, they transformed into  $M_{23}C_6$  and  $M_6C$  carbides.  $M_{23}C_6$  carbides are enriched in Cr but also contain Mo, Fe, and Co [89]. They were observed as grain boundary films in the wrought alloys and a combination of films and blocky particles in both cast and wrought samples.  $M_6C$  carbides containing Mo, Co, and Cr were observed as blocky particles both within the grains and on the grain boundaries [49,89,101].

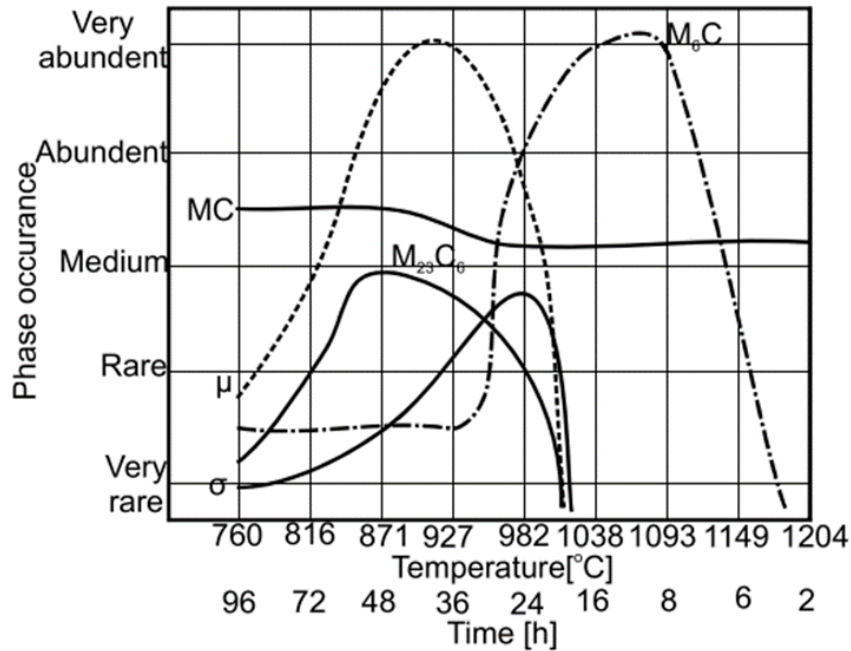


Figure 2.10. Minor phase concentration in R41 alloy as a function of aging time and temperature [102].

Table 2.3 shows the range of ultimate tensile strength (UTS), yield strength (YS), and elongation values for a wrought R41 alloy after being subjected to the mentioned standard heat treatment. As shown, R41 maintains its strength over a wide range of temperatures from -250 to 871 °C. At higher temperatures, it is used for oxidation resistance even though a reduction in strength is observed [103]. Studies also show that R41 experiences a dip in ductility in the temperature range of 760 to 871 °C. Despite the exceptional properties of the wrought alloy, Li et.al reported that standard heat treatment was not appropriate for a laser melt deposited alloy and caused a reduction in the strength [94]. On the other hand, in the work of Atxaga et.al, cast and heat-treated R41 showed superior creep performance, exceeding even the forged parts [104]. These results suggest that heat treatments may require modifications according to the initial microstructure.

Table 2.3. Tensile properties of a wrought R41 after the standard heat treatment as a function of temperature (adapted from [101]).

Temperature (°C)	UTS (MPa)	%0.2 YS (MPa)	Elongation (%)
-250	1324 – 1427	1138 – 1269	2 – 7
-200	1234 – 1372	1110 – 1186	5 – 10
-75	1262 – 1324	1000 – 1048	10 – 13
25	1110 – 1416	793 – 1104	9 – 25
427	1110 – 1207	876 – 931	16 – 24
650	972 – 1138	779 - 876	8 – 19
760	869 – 1048	696 – 938	2 – 20
815	855 – 931	758 – 814	3
871	655 – 827	359 – 745	5 – 18
927	407	310	18 – 22
982	228 – 531	103 – 434	14 – 23
1038	110	69	36 – 40
1093	97 - 186	90 - 165	25 - 51

Despite the good high-temperature properties, this alloy has limited usage due to its cracking tendency during production. Strain age cracking in the heat-affected zone and/or in the base metal has been commonly reported during welding and post-weld heat treatments [53,89,105,106]. Therefore, literature on R41 is mostly focused on conventional fabrication techniques such as casting and forging [89,91,107].

## 2.4. Microstructure and Properties of R77

R77 is another precipitation-hardenable Ni-base superalloy containing high volume fractions of  $\gamma'$  precipitates. It is designed to operate in a temperature range between 730- 900 °C [108]. R77 is known to have remarkable hot corrosion resistance and excellent high-temperature strength and is often used to produce hot gas turbine engine parts, such as vanes blades and discs. [109]. These parts are usually fabricated with investment casting [110].

The composition of R77 is similar to R41 except for its higher Al + Ti content, leading to a higher volume fraction of  $\gamma'$ . It is also solid solution strengthened by Cr, Co, and Mo. The higher Co content compared to R41 favors the precipitation of  $\gamma'$  in this alloy [109].

Just like all other superalloys, the properties of R77 parts are determined by the microstructural features such as grain size and morphology, size and distribution of the  $\gamma'$  and carbide phases [36,41,111]. Hence, control of the microstructure is crucial for the production of parts that fulfill the requirements for aerospace applications. Standard heat treatment applied to cast R77 parts involves two solutionizing and two aging steps leading to a bimodal distribution of  $\gamma'$  precipitates as shown in Figure 2.11(a). This heat treatment consists of a 4 h hold at 1163 °C, 4 h soak at 1080 °C, 24 h hold at 843 °C, and 16 h hold at 760 °C with air cooling between each step [112]. In addition to the  $\gamma'$ , carbides at the grain boundaries are also developing and shown in Figure 2.11(b). The types and morphologies of carbides that can be observed in R77 are very similar to the ones in R41. Even though their stability temperatures and volume fractions are different, the observed carbides are found to be enriched in the same elements due to their similar compositions [109,113].

Previous studies show the presence of Mo and Ti enriched MC carbides in the as-cast microstructure. The first stage of the solutionizing heat treatment is above the solvus temperature of  $\gamma'$  and  $M_{23}C_6$  carbides, respectively. In this stage, all phases were solutionized except the Ti-rich MC carbides. The following step is still above the solvus temperature of  $\gamma'$  but below the  $M_{23}C_6$  solvus temperature. Hence, this stage is applied to stabilize the  $M_{23}C_6$  carbides and improve the oxidation resistance of the part. Then a two-step aging treatment is applied to obtain a bimodal  $\gamma'$  distribution. The primary particles are known to be beneficial for high temperature creep resistance, whereas secondary precipitates improve strength [114,115]. When subjected to the standard heat treatment, a stable microstructure at elevated temperature was reported for cast R77 parts during creep and low cycle fatigue deformation [114,116]. The minimum room temperature tensile properties for a cast and wrought alloy after the standard heat treatment were given in Table 2.4. Both cast and wrought alloys demonstrate similar room temperature strength however, the elongation of the wrought part is significantly higher compared to its cast counterpart.

Table 2.4. Room temperature tensile properties of cast and wrought R77 parts after being subjected to the standard heat treatment (adapted from [116–118]).

Condition	UTS (MPa)	YS(MPa)	Elongation (%)
Cast + Heat Treated	861	755	4
Wrought + Heat Treated	885	760	40

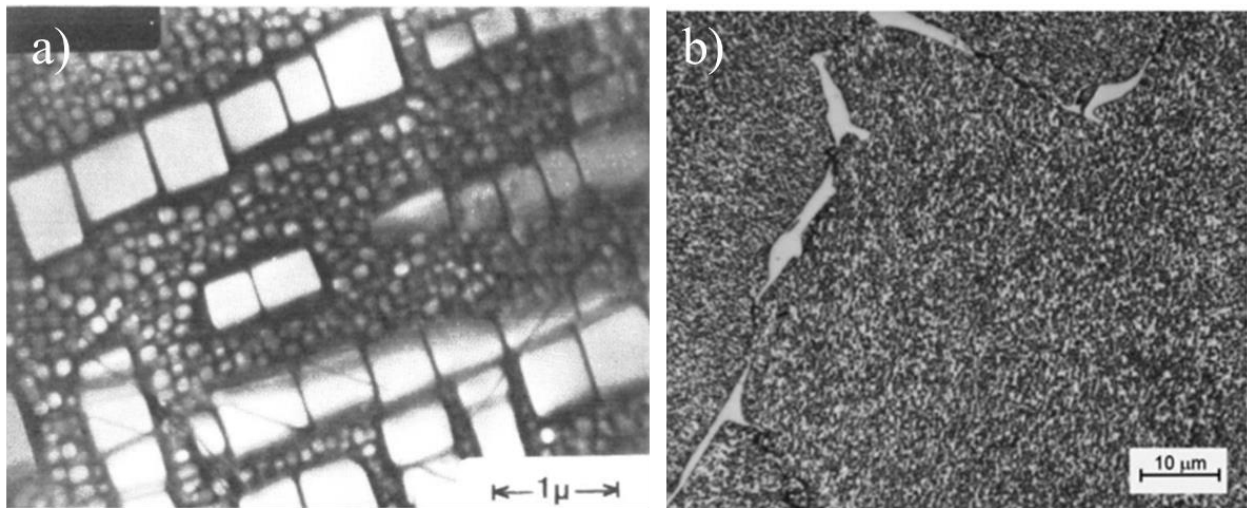


Figure 2.11. Microstructure of cast and heat-treated R77 showing (a) bimodal  $\gamma'$  precipitates, (b) grain boundary carbides (adapted from [113,114]).

Two main issues are reported to be limiting the processing of R77. The first one is the coarse and inhomogeneous grain structure observed in the turbine blades fabricated by investment casting [113,116]. Such microstructure does not fulfill the engineering requirements for the mechanical properties of an aerospace part. The composition of the alloy was modified by adding cobalt aluminate as an inoculant to refine the grain structure. An improvement in creep and tensile properties was observed as a result of this addition [110,113,116]. R77 is also known to be difficult to join or repair by welding due to its susceptibility to hot cracking. Even though few studies indicated that modification and control of process parameters might create a defect and crack-free joints, welding of R77 remains to be challenging [109,119].

## **2.5. LPBF of Ni-base Superalloys**

Specific application of LPBF to fabricate parts made out of Ni-base superalloys has been driven by energy, aerospace, automotive, and medical applications. Excellent properties of the superalloys combined with the design flexibility and near net shape part fabrication ability of LPBF made this particular area especially attractive for the production of high-value parts [120]. Nevertheless, the application of LPBF for the production of mission-critical parts is very challenging due to several reasons. Of particular concern, are the microstructural inhomogeneities and processing-related defects, particularly microcracks [121,122]. So far, LPBF production of various Ni-base superalloys is explored yet the majority of the research is focused on the alloys that are not susceptible to microcrack formation such as IN718 and IN625 [33].

### **2.5.1. Processability\ Weldability of Ni-base Superalloys**

The processability of Ni-base superalloys with LPBF has proven to be challenging. Due to the repetitive heating and cooling cycles the material encounters during LPBF, significant amount of residual stresses are generated, which results in the formation of microcracks. It is well documented that precipitation-hardenable alloys with high content of alloying elements are particularly more susceptible to cracking. Figure 2.12. shows a plot illustrating the classification of selected superalloys as a function of the composition of Al, Ti ( $\gamma'$  forming elements) and Cr, Co (carbide forming elements) [123]. It can be seen that, among the alloys of interest in this work, R41 is classified to have fair weldability whereas R77 is in the difficult to weld region. The weldability of alloys can be used as an indication of their processability by LPBF since LPBF resembles a multilayer laser welding process. Many of the alloys that are considered difficult to weld have been studied to understand the cracking mechanisms and to find protocols to eliminate cracking. The most researched alloys in this field include, but are not limited to, CM247LC [124], IN738 [125], and CMSX-4 [126]. The extensive crack formation was observed in these alloys both in, as-fabricated state and after heat treatment. Four potential cracking mechanisms can be identified during LPBF processing of Ni-based superalloys, namely; solidification cracking, liquation cracking, strain age cracking(SAC), and ductility dip cracking (DDC) [34,35].

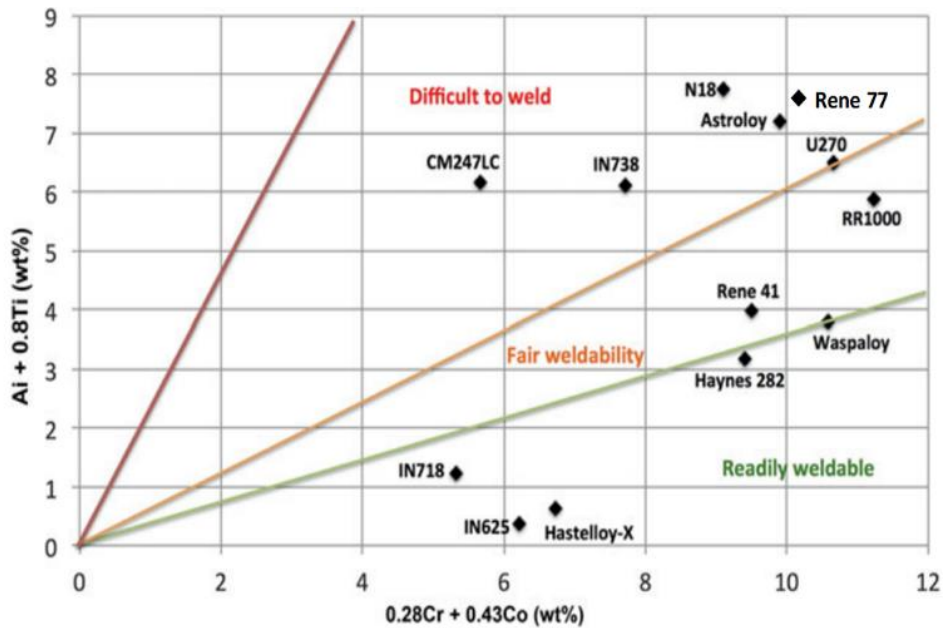


Figure 2.12. Weldability assessment diagram for Ni-based superalloys using the chemical composition (adapted from [123]).

Both solidification and liquation cracking are known to occur due to the presence of a thin continuous liquid film interlocked within a coherent network of solid [34,53,127]. When this liquid film is unable to accommodate the thermal and mechanical stresses during cooling, cracks form along the grain boundaries [128,129]. Hence both of these cracking mechanisms occur with an intergranular manner. Solidification cracking is observed at the terminal stage of the solidification when the fraction of solid,  $f_s$ , is close to 1, due to the presence of a liquid film in the inter-dendritic region [130]. On the other hand, liquation cracking is observed during reheating/cooling. During rapid heating, low melting point phases such as eutectics cannot go into solid solution and cause liquation at the grain boundaries [131]. Another proposed mechanism for liquation cracking is the formation of a liquid film due to constitutional liquation caused by the solute-rich phases such as carbides and intermetallics [132]. Crack susceptibility is mostly determined by the grain boundary area, solidification temperature range, and liquid film behavior [34,128,133]. Finer grain size is reported to reduce the susceptibility to cracking. Since the total grain boundary area is increased, stress accommodated by grain boundaries and triple points is reduced [34,53]. Solidification temperature range and liquid volume fraction are determined by the solute redistribution. Due to the very high cooling rates experienced during LPBF, a mismatch between the actual solidus temperature and the predicted one from the equilibrium phase diagram exists.

Hence, solidification models that are dependent on the partition coefficient ( $k$ ), such as Scheil-Gulliver, are typically used to predict those temperatures [134]. The Scheil equation describes the solute redistribution assuming the solid/liquid interface is in equilibrium, where there is negligible diffusion in solid and complete diffusion in liquid. Alloys having a larger freezing range were proven to be more susceptible to solidification cracking. It is observed that the application of larger thermal gradients increased the hot cracking during LPBF of superalloys, which are generally associated with high energy densities of the laser [135–137].

Grain boundary characteristics play an important role in the prediction of liquid film behavior. According to the grain boundary coalescence theory proposed by Rappaz, the presence of attractive and repulsive grain boundaries can be used to explain the behavior of the liquid film [138]. When two adjacent dendrites form an attractive boundary, as shown in Figure 2.13(a) [130], the liquid film transforms into individual liquid droplets and this type of microstructure is not susceptible to cracking. On the contrary, if the boundary is repulsive, the liquid film is preserved at the terminal stage of solidification as illustrated in Figure 2.13(b) [130,139]. Several researchers calculate a critical misorientation angle for solidification cracking to occur by considering the grain boundary characteristics. Rong et. al. reported a critical misorientation value of  $16^\circ$  whereas Wang et al observed a value of  $13^\circ$  [133,140]. Although the value of the critical misorientation angle varies with alloy composition, studies showed that the high angle grain boundaries are more susceptible to crack formation [141,142].

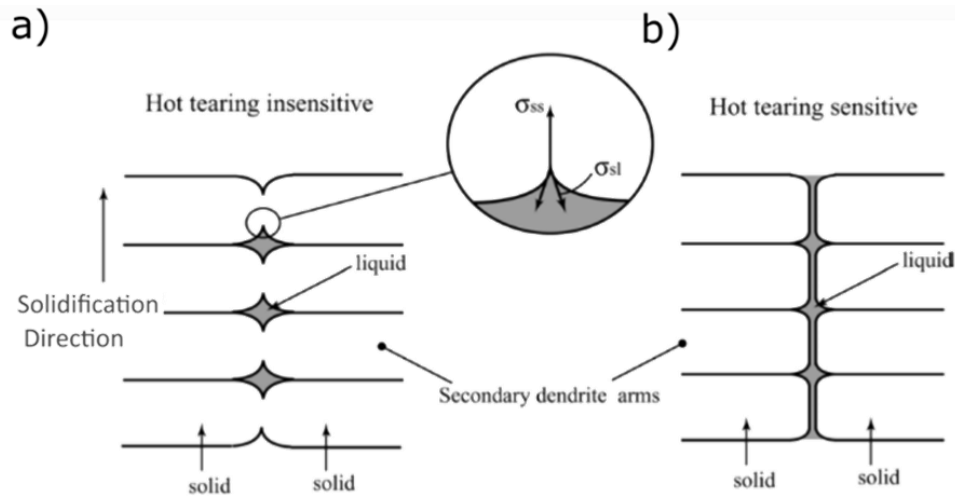


Figure 2. 13. Schematic illustration of liquid film behavior for (a) attractive, (b) repulsive grain boundaries [138].

DDC and SAC are generally observed during the post-processing heat treatments and they both occur during reheating in the solid-state. DDC is defined as cracking due to the reduction in ductility occurring in precipitation hardenable superalloys at intermediate temperatures [39]. The suggested mechanism for DDC is a creep-like mechanism, resulting in void formation at triple points of boundaries or around the phases on grain boundaries, resulting from grain boundary sliding [34]. SAC cracking occurs due to  $\gamma'$  precipitation during reheating. This transformation occurs faster than stress relief. Reduction of ductility due to the presence of these precipitates combined with the residual stress and strain induced by the precipitation results in cracking in the alloy [34,105,106]. The rate of  $\gamma'$  precipitation is increased by the composition (Al+Ti content) and the stored energy in the part. Hence, alloys with a higher volume fraction of  $\gamma'$  are more susceptible to this type of cracking [89,105,106,143]. Both of these cracking mechanisms are typically observed in high angle grain boundaries of precipitation-hardenable alloys and it is reported that reduction of cracking is possible with a reduction in grain size [34,37,128].

Although cracking is still an outstanding issue during LPBF of Ni-based superalloys, previous research proved that its mitigation or elimination is possible by modification of process parameters, and/or alloy composition or preheating the base plate [12,144,145].

One of the most common approaches to mitigate crack formation is via alloy design. As the current alloy systems are designed for conventional manufacturing techniques, there is a possibility that the compositions are not suitable for the LPBF solidification regimes. Various studies demonstrated that solidification cracking is observed as a result of the extensive segregation of the minor alloying elements at the end stage of solidification ( $f_1 < 0.01$ ). Engeli et.al studied the effect of Si on the solidification cracking of IN738LC alloy. A significant reduction in the crack density was observed when the Si content is decreased [9]. Tomus et.al also investigated the effect of C, Mn and, Si content on the hot cracking tendency of Hastelloy X. They observed that alloys with low Si and C content show considerably less cracking, whereas Mn had no significant effect [146]. B and Zr were also found to be detrimental to the crack formation in IN738LC alloy. Segregation of these two elements was observed in the vicinity of microcracks and alloys with low B and Zr content showed significantly low crack density and average crack length [147]. Additionally, Hf was reported as a significant element in terms of susceptibility to cracking. When processed under the same conditions Hf-free CM247LC was less prone to cracking compared to a Hf containing one [16].

Regardless of if the alloy is subjected to compositional modification or not, there is a certain processing window for each alloy system. Therefore, process parameters need to be modified in combination with the composition in many cases [16]. One of the main factors affecting microcracking, as a result of the LPBF process parameters, is the melt pool geometry. Variation in the melt pool geometry is investigated as a function of the process parameter. Linear energy density is used to express a combination of LPBF processing parameters. Figure 2.14(a) shows that as the energy density increases, the depth to width ratio of the melt pools is also increased. As a result, melt pool geometry transforms from conduction mode to keyhole mode. It is observed that the application of larger thermal gradients increases the hot cracking during (LPBF) of superalloys, which are generally associated with high energy densities [135–137]. Zhang et.al established a critical energy density range for a low Mn, Si-containing IN738LC alloy, using melt pool shape correlation, to fabricate crack-free samples [148]. A similar phenomenon is also observed for CM247LC. As seen in Figure 2.14(b) and (c), different melt pool geometries were obtained with different process parameters. A significant reduction in cracking was observed when the melt pool geometry is adjusted to be in conduction mode [16].

Another approach to reduce the crack susceptibility of superalloys during LPBF is to modify the grain structure and grain boundary misorientation. A variety of research showed fine, equiaxed grain structures with low grain boundary misorientations are less prone to cracking. When fabricated using an island scan strategy, bimodal grain morphology and texture were observed for a CM247LC alloy. The microcracks were preferentially located at the boundaries having high misorientations. The possibility of changing the grain structure by changing the scanning strategy was also introduced [136]. Wan et.al has also reported that the scanning strategy can be used to control the grain structure and texture of the Ni-base superalloys [12]. Kontis et.al has successfully processed and fabricated crack-free samples of an alloy with a cracking susceptible composition by using such grain structure modifications. They were able to eliminate cracking by adjusting the melt pool geometry to transform a coarse-grained columnar microstructure that was susceptible to liquation cracking into either small-grained equiaxed (grain width approximately 20  $\mu\text{m}$ ) or fine columnar microstructures (grain width approximately 50  $\mu\text{m}$ ) [149]. Similar results were also reported for IN738LC. The scanning strategy is changed to modify the grain structure from columnar to refined equiaxed one. This modification successfully eliminated cracking in this alloys system [150]. The addition of TiC nanoparticles was also reported as an effective way of eliminating cracking in Hastelloy X. Han et.al suggests that these nanoparticles decreased effectively the number of high angle grain boundaries, eliminating crack formation [151].

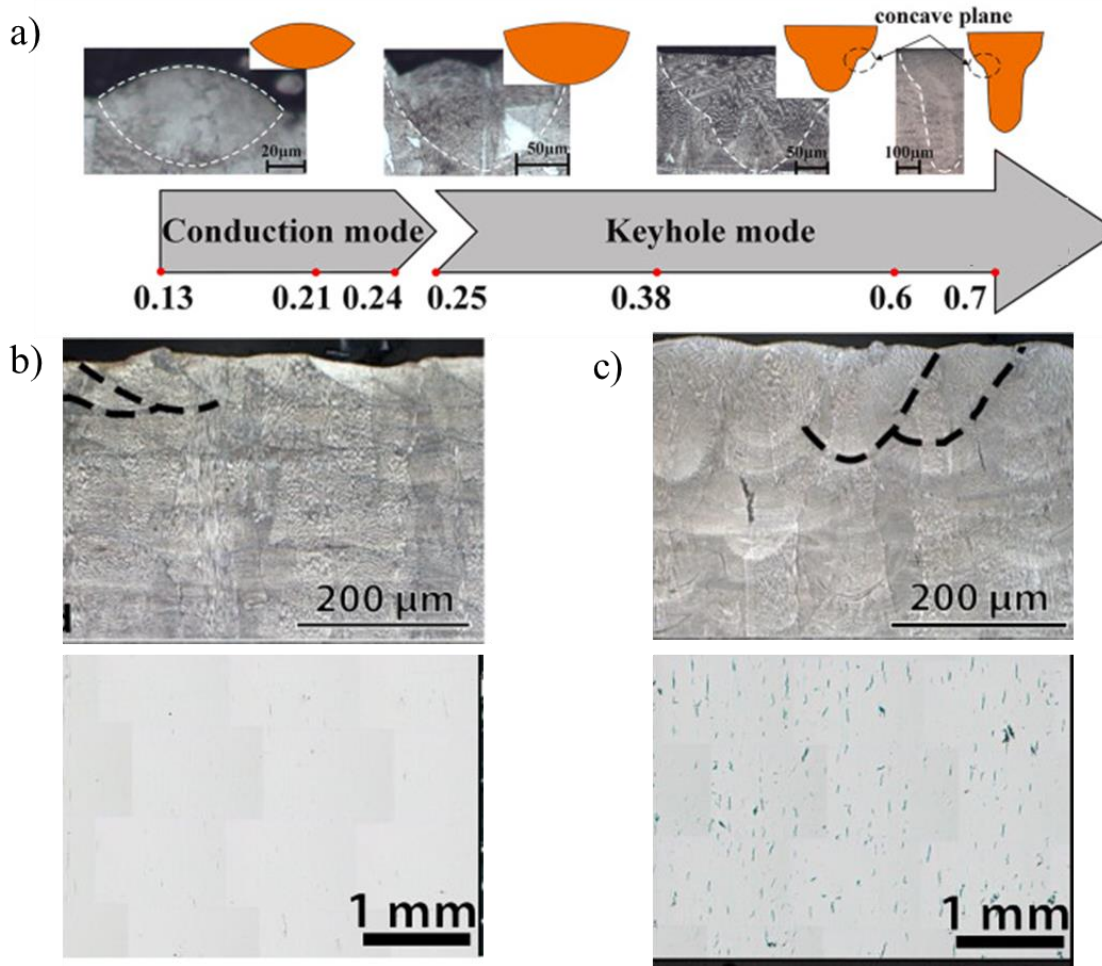


Figure 2.14. (a) Change in melt pool geometry as a function of energy density, and microstructure, and crack density of CM247LC having (b) low heat input, (c) high heat input (adapted from [16,148]).

### 2.5.2. Microstructure of Ni-base Superalloys Processed by LPBF

The thermal cycle in the LPBF process includes rapid heating above melting temperature and rapid solidification of the molten metal with continuous re-heating and re-cooling processes. This results in a finer microstructure compared to conventional casting regardless of the alloy used for manufacturing [6,152]. Usually, a microstructure similar to directionally solidified alloys was observed for LPBF fabricated Ni-base superalloys consisting of fine columnar grains, with a preferred orientation, and their long axis aligned with the building direction is reported. The direction of heat flow plays a very important role in the grain structure. The substrate acts as a heat sink and creates a large heat flux parallel to the build direction causing grains to grow along

the direction of the highest thermal gradient [2,121]. The grains in the newly deposited layer grow on the same crystallographic orientation as the  $\gamma$  grains in the previous layers due to epitaxial solidification. Partial re-melting of the previous layers in the LPBF process facilitates the grain growth from an existing grain, which acts as nuclei for crystal growth in the same orientation [153,154]. As a representation of the typical grain structure of an as-fabricated CM247LC, a micrograph and an EBSD map showing their corresponding orientations are displayed in Figure 2.15. Observation on the cross-section parallel to the building direction revealed grains having their width to length ratio of at least 1:3, and mainly oriented along the  $\langle 100 \rangle$  crystallographic direction for precipitation-hardenable superalloys such as IN625[155], CM247LC[18], IN738LC[156], and IN718[157]. Several studies reported that it is possible to disrupt the epitaxial growth of the grains by changing the scanning strategy. For IN718, when the scan strategy is changed from meander to island, the grain structure of the sample has been replaced with grains having smaller aspect ratios. The orientation of the grains remain in  $\langle 100 \rangle$  direction but the texture intensity was reduced [157]. Similarly, Geiger et.al reported a change in the dominant grain orientation from  $\langle 100 \rangle$  to  $\langle 110 \rangle$  when the rotation angle between the layers is changed [158].

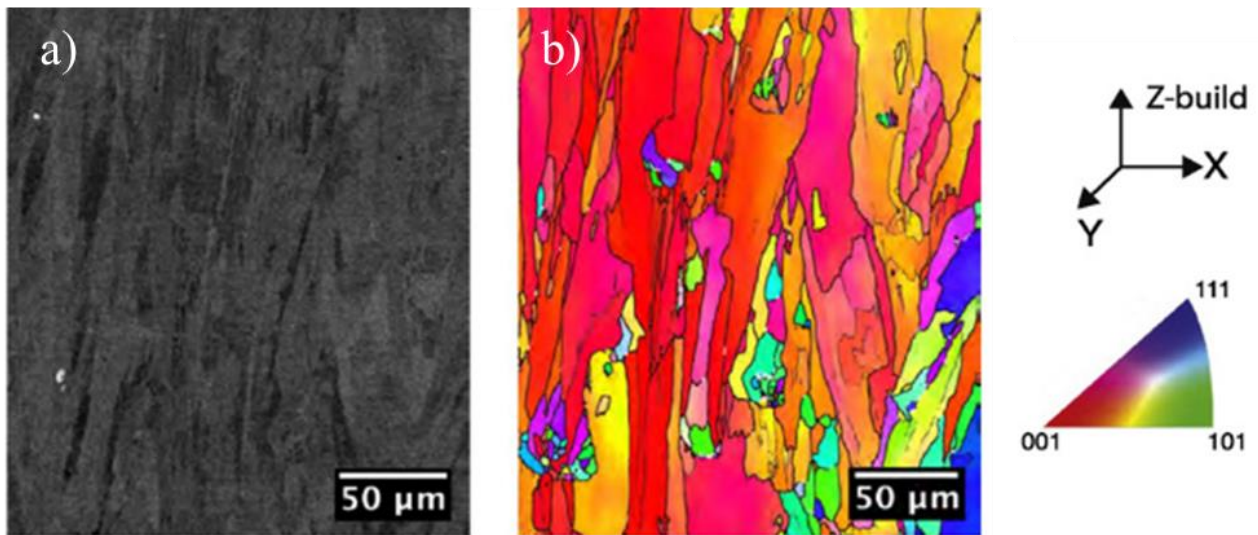


Figure 2. 15. (a) SEM micrograph, (b) EBSD IPF map of as-fabricated CM247LC (adapted from [18]).

The observed columnar grains were usually reported to have a cellular sub-grain morphology, either with no or extremely small secondary arms [12,143,159]. The solidification microstructure in the LPBF fabricated parts is determined by the thermal gradient ( $G$ ) and solidification front

velocity (R). The ratio of G/R is used to predict whether the microstructure will be planar, cellular, columnar dendritic, or equiaxed dendritic whereas cooling rate (G\*R) is used to predict the size of the microstructural features [53,160,161]. The G/R ratio defines the stability of the solidification interface by equation (2.9), in which  $\Delta T$  is the equilibrium freezing range,  $D_L$  is the diffusion coefficient in liquid. As shown in the solidification map in Figure 2.16(a) when the G/R value decreases (ea. constitutional undercooling increases) solidification structure changes from planar to cellular, columnar dendritic, and equiaxed dendritic. Typically, in LPBF very high thermal gradients are observed. Hence, conditions do not favor equiaxed grain formation due to the large degree of undercooling required.

$$\frac{G}{R} \geq \frac{\Delta T}{D_L} \quad (2.9)$$

Although the constitutional supercooling theory has been widely used to explain the solidification microstructures in LPBF, it neglects the surface tension effect and the variation of partition coefficient with solidification front velocity. Hence, interface stability theory is more suitable for predicting microstructural development in the case of rapid solidification. As shown in Figure 2.16(b), for a fixed thermal gradient, the solidification microstructure changes from dendritic to cellular and finally to planar with an increasing solidification rate. The solidification rate where the planar morphology is observed is called the absolute stability and is not sensitive to the thermal gradient [162,163]. Even though the possibility of microstructure modification by parameter optimization has been proven possible, most of the studies reported solidification conditions in LPBF are more suitable to form columnar structures [18,164].

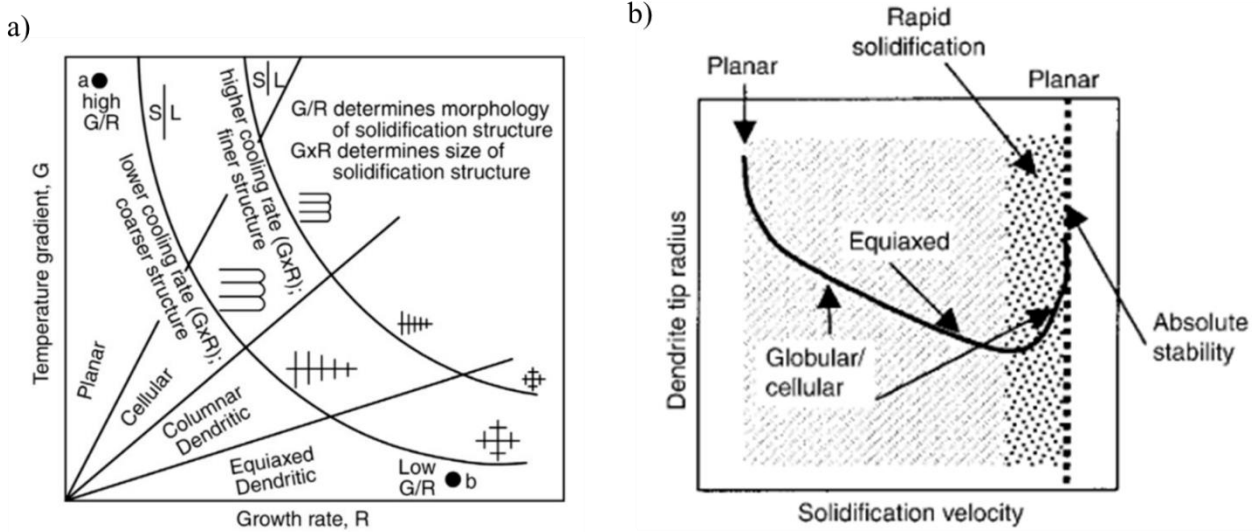


Figure 2. 16. (a) Solidification map showing the effect of G and R on the resulting microstructure, (b) influence of solidification velocity on the microstructure based on interface stability theory (adapted from [53,165]).

Rapid cooling rates reaching up to  $10^8$  °C/s are observed during the LPBF process [44]. The primary dendrite arm spacing (PDAS) is reported to be directly correlated with the cooling rate [163]. Therefore, the cooling rate of the parts can be estimated by using equation (2.10), where  $\epsilon$  represents the cooling rate, a and b are the material constants. Specifically, for Ni-based superalloys  $a = 50 \mu\text{m}(\text{K/s})$  and  $b = 1/3$  [155]. Solidification rates encountered in LPBF are generally in the order of  $10^5$ -  $10^6$  °C/s [166,167].

$$\text{PDAS} = a\epsilon^{-b} \quad (2.10)$$

The phases obtained during the LPBF of Ni-base superalloys are also substantially affected by these high cooling rates. The presence of fine particles decorating the cell boundaries was reported by many researchers. These particles are mainly identified as oxides or carbides [168]. Divya et.al reported the presence of MC-type carbides enriched in Ti, Hf, Ta, and Mo for CM247LC [18]. Similarly Marches et.al reported Mo-rich carbides on the cell boundaries of Hastelloy X [14]. The observed phases are similar to the ones observed in the cast alloys however, their size and distribution showed distinct differences. Carbides observed in the LPBF fabricated IN939 alloy were extremely fine compared to the cast one [169]. It is suggested that C is distributed over a

larger grain boundary area due to the fine grain structure obtained in LPBF [170], resulting in the very fine and highly dispersed carbide morphology in the AB condition.

As discussed before, the size and distribution of the  $\gamma'$  phase are highly dependent on the cooling rate. Observed cooling rates in LPBF can suppress the precipitation: as a result, either very little or no  $\gamma'$  presence is reported for the as-fabricated samples. No  $\gamma'$  was observed in the microstructural analysis of the LPBF processed CMSX-4 alloy. However, the authors suggest that the presence of small nuclei is possible [126]. Similarly, the absence of  $\gamma'$  precipitates is reported for IN738LC [171]. On the other hand,  $\gamma'$  precipitates with sizes ranging between 5-50 nm were identified by transmission electron microscopy (TEM) analysis for CM247LC alloy [18,122]. There is no doubt that the precipitation can be suppressed by the high cooling rates, yet the precipitation kinetics and size distribution are strictly dependent on the alloy composition. Therefore, post-processing heat treatments are critical for LPBF processed precipitation-hardenable Ni-base superalloys in order to obtain desired microstructure and material properties.

### **2.5.3. Thermal Post Processing of Ni-base Superalloys Processed by LPBF**

Heat treatments and/or hot isostatic pressing (HIP) are the most commonly used thermal post-processing techniques for LPBF processed superalloys, to modify the microstructure, reduce or eliminate the defects and residual stresses [21]. The applied heat treatments usually consist of a solution treatment and an aging step while the HIP is conducted in an inert atmosphere under a pressure of 100MPa or more, within the temperature range of 1100 to 1200 °C and up to 4 hours [33]. HIPing was reported to be beneficial for ductility and toughness by reducing the porosity and microcracking for IN738 [156] and CM247LC [122]. However, in some cases, it can be detrimental. It has been proven inefficient in healing the surface-connected cracks, and large residual stresses may lead to macrocracking during the HIP process [124,143]. It should also be noted that most of the applied heat treatments were standardized for the conventionally fabricated parts. Nevertheless, the microstructure obtained after the LPBF process is completely different from the cast/wrought. Cracking during the post-processing heat treatment was one of the most common issues, especially for difficult to weld alloys [143]. Additionally, non-uniform grain morphologies were observed due to partial recrystallization of this microstructure along with a multimodal  $\gamma'$  distribution that are not at their optimal size [169,172]. Compositional variation across the inter-dendritic regions and grain boundaries were also reported [17,173]. These

variations resulted in excessive precipitation of secondary phases such as carbides and TCP phases during the solutionizing heat treatment of the LPBF fabricated parts [44,174,175]. Although, for some alloys, the heat treatment improved the yield and ultimate tensile strength in most of the studies while a reduction in the elongation was observed [175]. Ultimately, the use of standard heat treatments tailored for conventional processing techniques may not translate effectively for LPBF and has to be studied and modified if necessary.

Lopez-Galilea et.al [126] compared the optimization of post-processing heat treatment for LPBF fabricated CMSX-4 alloy with a cast sample. The aim of the heat treatments was to minimize the segregation and optimize the  $\gamma/\gamma'$  structure. Various solutionizing heat treatments were applied to dissolve the Laves phase observed in the as-fabricated condition. They found a short holding time of 15min at 1300 °C was sufficient to homogenize the microstructure. The initial microstructure of the LPBF fabricated alloy was  $\gamma'$  free and application of an aging heat treatment resulted in the formation of fine  $\gamma'$  precipitates with unimodal size distribution. Authors note that a shorter aging time compared to the conventional heat treatment was sufficient to obtain a similar  $\gamma'$  morphology. An integrated HIP and aging heat treatment were also applied. This heat treatment resulted in the formation of TCP phases, which are detrimental in terms of mechanical properties. HIP was not effective in closing the cracks and pores in this sample, furthermore, the presence of large cracks was observed. Figure 2.17 reveals defects observed after the applied post-processing heat treatment as well as the  $\gamma'$  morphology of the LPBF sample with optimized heat treatment with a comparison with the conventionally heat-treated cast sample. It is concluded that once the sample is fully homogenized the aging heat treatment temperature and time should be selected as such to facilitate  $\gamma'$  precipitation but avoid the formation of TCP phases.

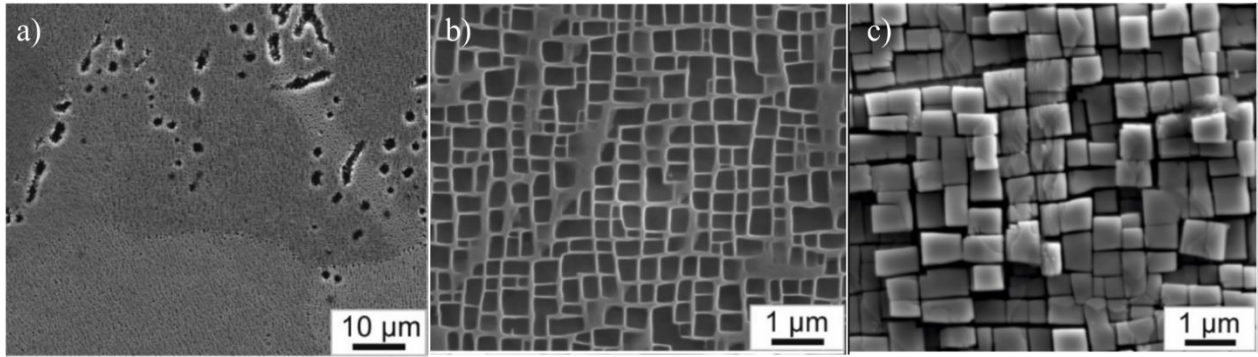


Figure 2.17. SEM micrographs of LPBF fabricated CMSX-4 showing (a) remaining defects, (b)  $\gamma'$  structure after optimized heat treatment (c)  $\gamma'$  structure of a cast sample after conventional heat treatment (adapted from [126]).

In another study, the effect of the solutionizing step on the final microstructure was investigated for an LPBF processed CM247LC alloy [172]. The authors reported that the as-fabricated grain morphology of elongated grains with strong texture along the  $\langle 100 \rangle$  direction was maintained up to 1230 °C. Samples heat treated up to this temperature underwent recovery by coalescence of the cells of the as-fabricated microstructure. Growth of cell boundary carbide particles and  $\gamma'$  precipitates were also observed.  $\gamma'$  size distribution was ranging between 5-50 nm. When solution treated at 1230 °C, partial recrystallization of certain regions was identified. In the partially recrystallized microstructure, a bimodal distribution of irregularly shaped  $\gamma'$  precipitates was reported, with smaller precipitates around 150 nm in size and larger precipitates of approximately 455–570 nm in size. Samples solution treated above this temperature showed recrystallization with a random orientation. The recrystallized samples showed a finer and more uniform  $\gamma'$  distribution due to the dissolution and reprecipitation of the  $\gamma'$ . As a result of this homogenized microstructure, the anisotropy in the elastic properties was also reduced. Therefore, the authors concluded that in practical application, there is a critical temperature for solution treatment. This temperature should be high enough to allow only recrystallization or low enough to allow only recovery, rather than an intermediate temperature.

Gallmeyer [44] et.al. studied a variety of different heat treatment regimes for LPBF fabricated IN718 alloy to develop a better understanding of the process-structure-property relationship. Through detailed characterization of microstructure and tensile properties resulting from different post-processing heat treatments, the authors proved that it is possible to design heat treatments

improving both strength and ductility beyond the properties observed in the wrought and conventionally heat-treated parts. The main modifications made to the standard heat treatment was to increase the solutionizing temperature to dissolve the TCP phases. Solution treatment for only 15 min was sufficient to homogenize the segregated elements while preserving the cellular structure obtained during solidification. Conventionally a two-step aging treatment was applied to this alloy. However, in the case of LPBF, a single step aging was used to obtain a microstructure similar to the one having superior creep performance.

Overall, literature shows it is possible to design a post-processing heat treatment to obtain a microstructure that resembles the one optimized for conventional processing techniques. However, a combination of ductility dip and strain age cracking mechanisms were observed during the post-processing of various alloys having high  $\gamma'$  volume fraction [124,143]. This shows that further optimization of heat treatments is required, especially for the alloys that are susceptible to cracking.

#### **2.5.4. Mechanical Properties of Ni-base Superalloys Processed by LPBF**

Quantification of the mechanical properties of LPBF fabricated Ni-base superalloys is essential before they can be implemented in service. Currently, most of the studies determine the mechanical properties via tensile testing and hardness measurements. Creep and fatigue properties are also studied for LPBF parts, but not as extensively. Usually, the standard testing methods developed for the conventionally fabricated parts are followed. However, it is also common for researchers to modify these standards according to their individual needs [33].

Tensile testing revealed that dislocation strengthening plays a significant role in the mechanical properties of Ni-base superalloys in the as-built state. Generation of dense dislocation forest in cell boundaries and high dislocation densities within the cells are reported after fabrication as a result of the rapid heating and cooling cycles [44]. The presence of this dislocation structure was found to result in a significant improvement in the strength value without sacrificing the elongation [44,171]. Additionally, due to the rapid cooling rates, an extremely fine microstructure is observed after LPBF processing. Hence, the grain boundary strengthening effect is higher compared to cast or wrought parts with coarser grain structures [176]. Even though  $\gamma'$  precipitation is suppressed during the LPBF processing, in some cases, their room temperature strength was even exceeding the wrought or cast and heat-treated parts as a result of the unique LPBF microstructure [122,125].

Elevated temperature tensile properties of various LPBF fabricated superalloys were also investigated by many researchers. When subjected to elevated temperatures even for a short time, microstructural changes were observed for the as-fabricated samples. Rapid precipitation and/or growth of  $\gamma'$  precipitates along with the change in the carbide morphology is possible during elevated temperature exposure. As a result of the microstructural modifications, a rapid hardening response and loss of ductility after a short soaking at elevated temperature were reported for various precipitation-hardenable superalloys [124,177,178].

The directional microstructure of the Ni-base superalloys fabricated via LPBF was reported to result in anisotropy in the mechanical properties [18,156]. Building direction is one of the main factors determining the grain growth direction, hence, it has a great significance on the observed tensile properties. Chlebus [179] et. al fabricated samples in 4 different orientations and investigated their tensile properties (Figure 2.18). They concluded that the orientation of the grains according to the loading direction during tensile testing affects the deformation behavior as well as the fracture mode. The highest strength was observed for the sample built in the  $45^\circ \times 45^\circ$  orientation shown in Figure 2.18. The anisotropy in the mechanical properties is highest in the vertically built samples due to its microstructure being very similar to the directionally solidified samples. The strength of these samples was also lower compared to the horizontally built ones. The authors related this difference to the presence of molten pool boundaries perpendicular to the loading direction, even though the grain orientation was parallel to the testing direction. However, Yadroitsev et.al reported that the molten pool boundaries between the layers are not the weakest point and the strength difference between the build directions was related to the presence of defects transverse to the loading direction [180]. Other studies reported higher strength values for longitudinally built samples compared to transverse ones [181]. Although there is no solid explanation existing on the different mechanical behaviors as a function of building direction, many studies reported that this anisotropy in the mechanical properties is reduced by the heat treatments as they homogenize the microstructure [58,172,179].

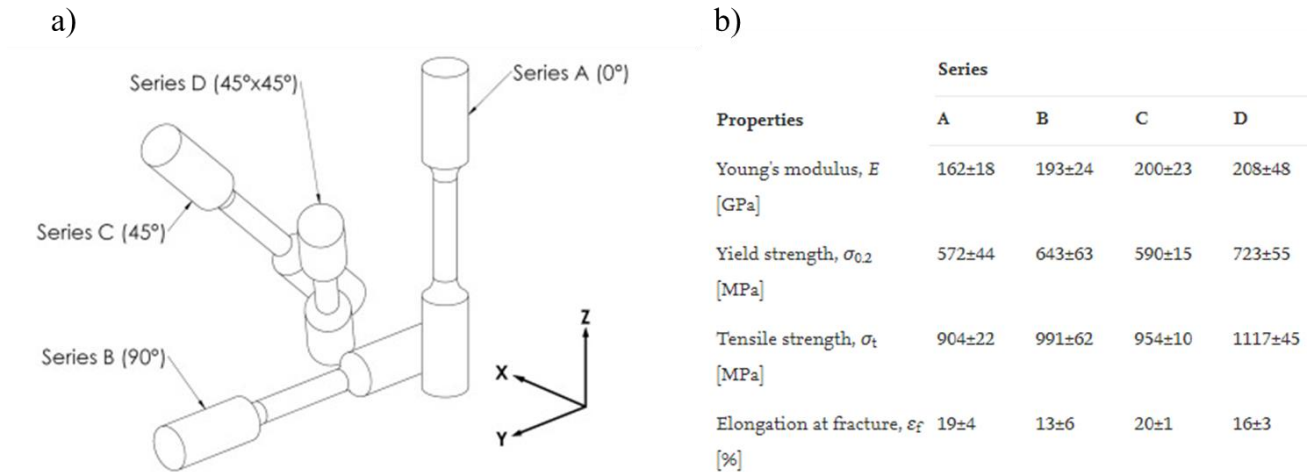


Figure 2.18. Demonstration of the (a) four different build directions and (b) their corresponding tensile properties (adapted from [179]).

Heat treatments are commonly applied to LPBF fabricated superalloys, to homogenize the microstructure and to improve the mechanical properties of the parts. Figure 2.19 summarizes the effect of heat treatment on the tensile properties of various alloys subjected to different heat treatments. In most cases, heat treatments result in an increase in strength and loss in elongation [175]. This mechanical response is mostly related to the strengthening resulting from the precipitation of  $\gamma'$  precipitates. The increase in  $\gamma'$  volume fraction results in a significant increase in the strength value in precipitation hardenable superalloys [44,182]. The application of direct aging heat treatment was found to increase the strength the most due to the presence of fine precipitates. However, the segregation in the as-built sample is not homogenized in this case. As a result formation of carbides and/or TCP phases is accelerated and a significant loss in ductility might be observed [174]. Deshpande [182] *et.al* reported recrystallization of columnar grains after heat treatment. Even with the increased volume fraction of  $\gamma'$  precipitates, these samples showed similar tensile properties to the as-built samples due to the recrystallization. Recrystallization was also observed in the IN939 alloy after being subjected to a solutionizing and aging heat treatment. However, in this case, the newly formed grains were still very fine compared to a cast alloy. Hence, the mechanical properties of the heat-treated samples were still higher compared to the as-built ones and cast counterparts [183].

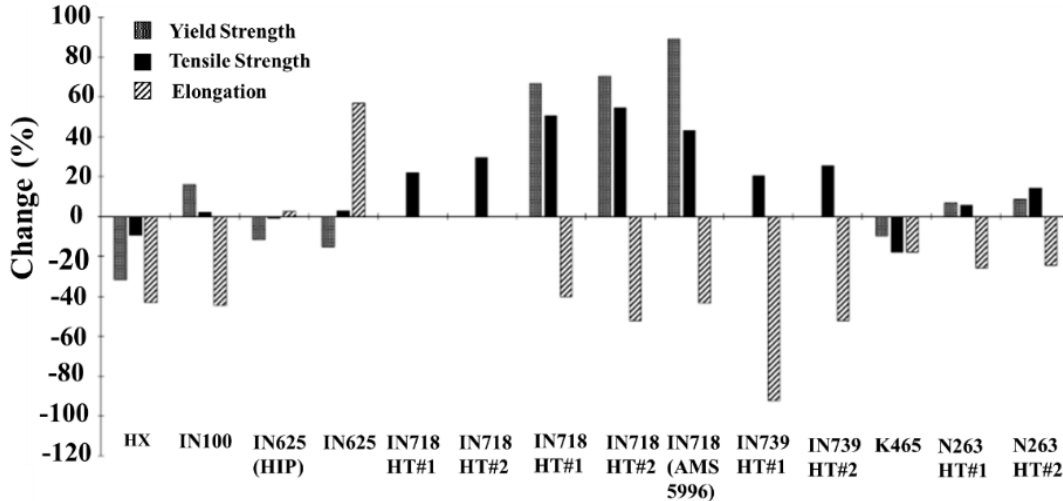


Figure 2.19. Effect of heat treatment on mechanical properties of various superalloys [175].

Ni-base superalloys are high-temperature materials; hence determination of their elevated temperature behavior also has significant importance. Tang et.al [124] studied the room and elevated temperature behavior of various high  $\gamma'$  containing superalloys. Obtained tensile properties at various temperatures for heat-treated alloys having a bimodal  $\gamma'$  distribution is presented in Figure 2.20. Even though the size distribution of the  $\gamma'$  precipitates are slightly different for each alloy, almost all of the alloys preserved high strength values up to 700 °C. The difference between the obtained strength values was associated with the difference in their  $\gamma'$  volume fractions. Another phenomenon that should be noted here is the ductility dip, a significant loss in ductility, occurring in the temperature regime between 760-1000 °C. Studies show that the columnar grain morphology with discrete carbide particles would be beneficial to delay this phenomenon due to its higher resistance to grain boundary sliding [34]. There is certainly a ductility minimum observed approximately around 800 °C for most of the alloys and at 1000 °C for the CM247LC. This difference in the ductility dip temperatures in this study is related to the difference in their  $\gamma'$  solvus temperatures.

Microhardness measurements are also frequently used as a mechanical property test to assess the material condition. Similar to the strength, hardness is also strongly affected by the microstructure of the sample. In some cases, an inhomogeneous structure throughout the sample height was reported, as a result, variation in the hardness value was observed [184]. Wang et.al stated that the finer microstructures lead to higher hardness values. Hence, the cooling rate plays a significant

role in the hardness of the as-built samples. For the heat-treated samples, the size and fraction of the  $\gamma'$  phase have a considerable effect on the hardness of the part. Similar to the strength values, an increase in the hardness value is observed after heat treatment even after short exposure times. Higher volume fraction and finer particle size were found to increase the hardness value more [182]. In some cases, a loss in the hardness was observed due to either grain growth or overaging of the  $\gamma'$  precipitates [185].

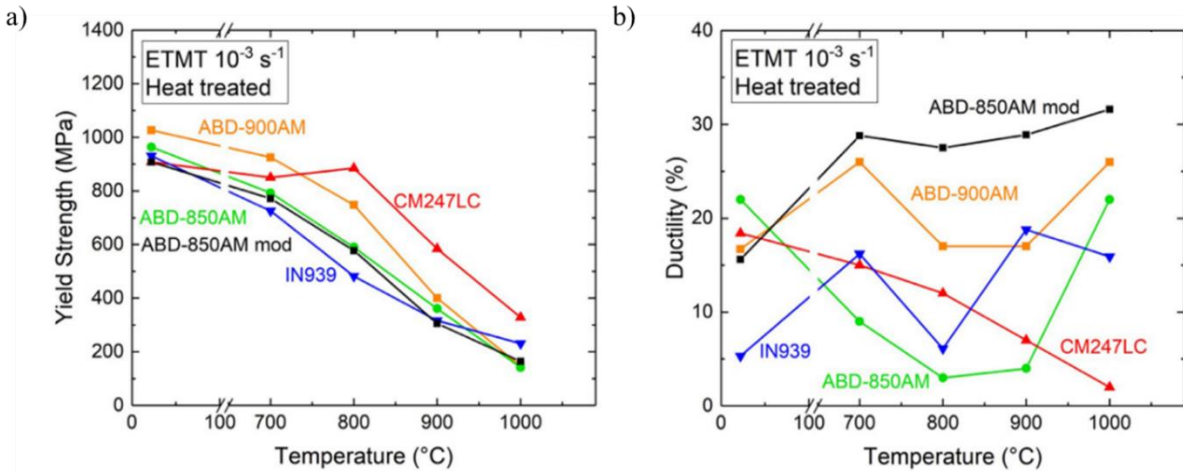


Figure 2.20. (a) Yield strength and (b) ductility of various LPBF processed and heat-treated high  $\gamma'$  containing Ni-base superalloys at different temperatures (adapted from [124]).

## 2.6. References

- [1] W.E. Frazier, Metal additive manufacturing: A review, *J. Mater. Eng. Perform.* 23 (2014) 1917–1928. doi:10.1007/s11665-014-0958-z.
- [2] V. Martinez, A.D. Neely, G. Ren, A. Smart, A.I. of M.R. <London>, *High Value Manufacturing*, 2008.
- [3] F. Froes, R. Boyer, *Additive manufacturing for the aerospace industry*, (2019). <https://search.ebscohost.com/login.aspx?direct=true&scope=site&db=nlebk&db=nlabk&AN=1805939>.
- [4] L. Yang, K. Hsu, B. Baughman, D. Godfrey, F. Medina, M. Menon, S. Wiener, *The additive manufacturing supply chain*, 2017. doi:10.1007/978-3-319-55128-9.
- [5] M. Brandt, ed., *Laser Additive Manufacturing Materials, Design, Technologies, and Applications*, Woodhead Publishing, n.d.

- [6] D. Herzog, V. Seyda, E. Wycisk, C. Emmelmann, Additive manufacturing of metals, *Acta Mater.* 117 (2016) 371–392. doi:10.1016/j.actamat.2016.07.019.
- [7] D. Gu, *Laser Additive Manufacturing (AM): Classification, Processing Philosophy, and Metallurgical Mechanisms*, 2015. doi:10.1007/978-3-662-46089-4\_2.
- [8] P.V. Cobbinah, R.A. Nzeukou, O.T. Onawale, W.R. Matizamhuka, Laser powder bed fusion of potential superalloys: A review, *Metals (Basel)*. 11 (2021) 1–37. doi:10.3390/met11010058.
- [9] R. Engeli, T. Etter, S. Hövel, K. Wegener, Processability of different IN738LC powder batches by selective laser melting, *J. Mater. Process. Technol.* 229 (2016) 484–491. doi:10.1016/j.jmatprotec.2015.09.046.
- [10] S. Vock, B. Klöden, A. Kirchner, T. Weißgärber, B. Kieback, Powders for powder bed fusion: a review, *Prog. Addit. Manuf.* 4 (2019) 383–397. doi:10.1007/s40964-019-00078-6.
- [11] S.H. Sun, K. Hagihara, T. Nakano, Effect of scanning strategy on texture formation in Ni-25 at.%Mo alloys fabricated by selective laser melting, *Mater. Des.* 140 (2018) 307–316. doi:10.1016/j.matdes.2017.11.060.
- [12] H.Y. Wan, Z.J. Zhou, C.P. Li, G.F. Chen, G.P. Zhang, Effect of scanning strategy on grain structure and crystallographic texture of Inconel 718 processed by selective laser melting, *J. Mater. Sci. Technol.* 34 (2018) 1799–1804. doi:10.1016/J.JMST.2018.02.002.
- [13] J. Jhabvala, E. Boillat, T. Antignac, R. Glardon, On the effect of scanning strategies in the selective laser melting process, *Virtual Phys. Prototyp.* 5 (2010) 99–109. doi:10.1080/17452751003688368.
- [14] G. Marchese, G. Basile, E. Bassini, A. Aversa, M. Lombardi, D. Ugues, P. Fino, S. Biamino, Study of the microstructure and cracking mechanisms of hastelloy X produced by laser powder bed fusion, *Materials (Basel)*. 11 (2018). doi:10.3390/ma11010106.
- [15] R.C. Benn, R.P. Salva, Additively Manufactured Inconel Alloy 718, *Superalloy 718 Deriv.* (2012) 455–469. doi:10.1002/9781118495223.ch35.
- [16] S. Griffiths, H. Ghasemi Tabasi, T. Ivas, X. Maeder, A. De Luca, K. Zweiacker, R. Wróbel, J. Jhabvala, R.E. Logé, C. Leinenbach, Combining alloy and process modification for micro-crack mitigation in an additively manufactured Ni-base superalloy, *Addit. Manuf.* 36 (2020) 101443. doi:https://doi.org/10.1016/j.addma.2020.101443.

- [17] O. Sanchez-Mata, X. Wang, J.A. Muñiz-Lerma, M. Attarian Shandiz, R. Gauvin, M. Brochu, Fabrication of Crack-Free Nickel-Based Superalloy Considered Non-Weldable during Laser Powder Bed Fusion, *Materials (Basel)*. 11 (2018). doi:10.3390/ma11081288.
- [18] V.D. Divya, R. Muñoz-Moreno, O.M.D.M. Messé, J.S. Barnard, S. Baker, T. Illston, H.J. Stone, Microstructure of selective laser melted CM247LC nickel-based superalloy and its evolution through heat treatment, *Mater. Charact.* 114 (2016) 62–74. doi:10.1016/j.matchar.2016.02.004.
- [19] I. Yadroitsev, A. Gusarov, I. Yadroitsava, I. Smurov, Single track formation in selective laser melting of metal powders, *J. Mater. Process. Technol.* 210 (2010) 1624–1631. doi:10.1016/j.jmatprotec.2010.05.010.
- [20] X. Wang, J.A. Muñiz-Lerma, O. Sánchez-Mata, M. Attarian Shandiz, M. Brochu, Microstructure and mechanical properties of stainless steel 316L vertical struts manufactured by laser powder bed fusion process, *Mater. Sci. Eng. A*. 736 (2018) 27–40. doi:10.1016/j.msea.2018.08.069.
- [21] J.J. Lewandowski, M. Seifi, Metal Additive Manufacturing: A Review of Mechanical Properties, *Annu. Rev. Mater. Res.* 46 (2016) 151–186. doi:10.1146/annurev-matsci-070115-032024.
- [22] A.L. Vyatskikh, T.B. Slagle, S. Jiang, S.A. El-Azab, U.S. Bertoli, L. Valdevit, E.J. Lavernia, J.M. Schoenung, Thickness-Dependent Microstructure in Additively Manufactured Stainless Steel, *J. Mater. Eng. Perform.* 30 (2021) 6606–6617. doi:10.1007/s11665-021-05931-w.
- [23] M.A. Macias-Sifuentes, C. Xu, O. Sanchez-Mata, S.Y. Kwon, S.E. Atabay, J.A. Muñiz-Lerma, M. Brochu, Microstructure and mechanical properties of  $\beta$ -21S Ti alloy fabricated through laser powder bed fusion, *Prog. Addit. Manuf.* (2021) 1–14.
- [24] C. Xu, F. Sikan, S.E. Atabay, J.A. Muñiz-Lerma, O. Sanchez-Mata, X. Wang, M. Brochu, Microstructure and mechanical behavior of as-built and heat-treated Ti–6Al–7Nb produced by laser powder bed fusion, *Mater. Sci. Eng. A*. (2020). doi:10.1016/j.msea.2020.139978.
- [25] Y. Ding, M. Trask, S. Chou, A. Walker, M. Brochu, Microstructure and mechanical property considerations in additive manufacturing of aluminum alloys, (2017) 745–751. doi:10.1557/mrs.2016.214.
- [26] Y. Li, D. Gu, Parametric analysis of thermal behavior during selective laser melting additive

- manufacturing of aluminum alloy powder, *Mater. Des.* 63 (2014) 856–867. doi:10.1016/j.matdes.2014.07.006.
- [27] C. Brice, R. Shenoy, M. Kral, K. Buchannan, *Materials Science & Engineering A* Precipitation behavior of aluminum alloy 2139 fabricated using additive manufacturing, *Mater. Sci. Eng. A.* 648 (2015) 9–14. doi:10.1016/j.msea.2015.08.088.
- [28] Y. Hou, H. Su, H. Zhang, X. Wang, C. Wang, Fabricating homogeneous fcc-based high-entropy alloys via slm in situ alloying, *Metals (Basel)*. 11 (2021). doi:10.3390/met11060942.
- [29] C. Zhang, J. Zhu, H. Zheng, H. Li, S. Liu, G.J. Cheng, A review on microstructures and properties of high entropy alloys manufactured by selective laser melting, *Int. J. Extrem. Manuf.* 2 (2020). doi:10.1088/2631-7990/ab9ead.
- [30] I. Raffeis, F. Adjei-Kyeremeh, U. Vroomen, E. Westhoff, S. Bremen, A. Hohoi, A. Bührig-Polaczek, Qualification of a Ni-Cu alloy for the laser powder bed fusion process (LPBF): Its microstructure and mechanical properties, *Appl. Sci.* 10 (2020). doi:10.3390/APP10103401.
- [31] M. Bonesso, P. Rebesan, C. Gennari, S. Mancin, R. Dima, A. Pepato, I. Calliari, Effect of Particle Size Distribution on Laser Powder Bed Fusion Manufacturability of Copper, *BHM Berg- Und Hüttenmännische Monatshefte*. 166 (2021) 256–262. doi:10.1007/s00501-021-01107-0.
- [32] S. Seetharaman, M. Krishnan, F. Goh, C. Wen, N.A. Khan, G. Ng, K. Lai, Research Updates on the Additive Manufacturing of Nickel Based Superalloys, *Solid Free. Fabr. 2016 Proc. 27th Annu. Int. Solid Free. Fabr. Symp. – An Addit. Manuf. Conf.* (2016) 469–486. <http://sffsymposium.engr.utexas.edu/sites/default/files/2016/034-Seetharaman.pdf>.
- [33] S. Sanchez, P. Smith, Z. Xu, G. Gaspard, C.J. Hyde, W.W. Wits, I.A. Ashcroft, H. Chen, A.T. Clare, Powder Bed Fusion of nickel-based superalloys: A review, *Int. J. Mach. Tools Manuf.* 165 (2021) 103729. doi:10.1016/J.IJMACHTOOLS.2021.103729.
- [34] J.N.D. & J. C. Lippold, *Welding Metallurgy and Weldability of Nickel-Base Alloys*, *J. Chem. Inf. Model.* 53 (2009) 456. doi:10.1017/CBO9781107415324.004.
- [35] R.C. Reed, *The Superalloys fundamentals and applications*, *Superalloys Fundam. Appl.* 9780521859 (2006) 1–372. doi:10.1017/CBO9780511541285.
- [36] J. Chander, *Hardening Mechanism and Corrosion Resistance of Nickel-Base Alloys: A*

- Review, *Can. Metall. Q.* 3 (1964) 57–77. doi:10.1179/cmq.1964.3.1.57.
- [37] B. Geddes, H. Leon, X. Huang, *Superalloys: Alloying and Performance*, 2010. doi:10.1016/B978-0-7020-2797-0.00001-1.
- [38] H.K.D.H. Bhadeshia, *Nickel Based Superalloys*, Univ. Cambridge. (2012) 1–9. [www.msm.cam.ac.uk/phase-trans/2003/Superalloys/superalloys.html](http://www.msm.cam.ac.uk/phase-trans/2003/Superalloys/superalloys.html) 9/9.
- [39] L.N. Carter, Selective laser melting of nickel superalloys for high temperature applications, *Sch. Metall. Mater.* (2013) 298. <http://etheses.bham.ac.uk/4410/2/Carter13PhD.pdf> 5Cn<http://etheses.bham.ac.uk/4410/>.
- [40] H.Y. Bor, C.N. Wei, R.R. Jeng, P.Y. Ko, Elucidating the effects of solution and double ageing treatment on the mechanical properties and toughness of MAR-M247 superalloy at high temperature, *Mater. Chem. Phys.* 109 (2008) 334–341. doi:10.1016/J.MATCHEMPHYS.2007.11.041.
- [41] H.E. Huang, C.H. Koo, Effect of solution-treatment on microstructure and mechanical properties of cast fine-grain CM 247 LC superalloy, *Mater. Trans.* 45 (2004) 1360–1366. doi:10.2320/matertrans.45.1360.
- [42] J. Mao, K.M. Chang, W. Yang, D.U. Furrer, K. Ray, S.P. Vaze, Cooling precipitation and strengthening study in powder metallurgy superalloy Rene88DT, *Mater. Sci. Eng. A.* 332 (2002) 318–329. doi:10.1016/S0921-5093(01)01758-0.
- [43] R. Eksergian, Aircraft gas turbines, *J. Franklin Inst.* 264 (1957) 254–255. doi:10.1016/0016-0032(57)90996-1.
- [44] T.G. Gallmeyer, S. Moorthy, B.B. Kappes, M.J. Mills, B. Amin-Ahmadi, A.P. Stebner, Knowledge of process-structure-property relationships to engineer better heat treatments for laser powder bed fusion additive manufactured Inconel 718, *Addit. Manuf.* 31 (2020) 100977. doi:10.1016/J.ADDMA.2019.100977.
- [45] Y.C. Lin, H. Yang, L. Li, Effects of solutionizing cooling processing on  $\gamma''$  (Ni<sub>3</sub>Nb) phase and work hardening characteristics of a Ni-Fe-Cr-base superalloy, *Vacuum.* 144 (2017) 86–93. doi:10.1016/j.vacuum.2017.07.025.
- [46] J. Belan, GCP and TCP Phases Presented in Nickel-base Superalloys, *Mater. Today Proc.* 3 (2016) 936–941. doi:10.1016/j.matpr.2016.03.024.
- [47] G. Bi, C.N. Sun, H. chi Chen, F.L. Ng, C.C.K. Ma, Microstructure and tensile properties of superalloy IN100 fabricated by micro-laser aided additive manufacturing, *Mater. Des.* 60

- (2014) 401–408. doi:10.1016/j.matdes.2014.04.020.
- [48] S. Tin, T.M. Pollock, W.T. King, Carbon Additions and Grain Defect Formation in High Refractory Nickel-Base Single Crystal Superalloys, (2016). doi:10.7449/2000/Superalloys.
- [49] S.S. Handa, Precipitation of Carbides in a Ni-based Superalloy, Masters Degree Proj. University (2014) 1–33.
- [50] L. Wang, G. Xie, J. Zhang, L.H. Lou, On the role of carbides during the recrystallization of a directionally solidified nickel-base superalloy, 55 (2006) 457–460. doi:10.1016/j.scriptamat.2006.05.013.
- [51] Q. Li, S. Tian, H. Yu, N. Tian, Y. Su, Y. Li, Effects of carbides and its evolution on creep properties of a directionally solidified nickel-based superalloy, Mater. Sci. Eng. A. 633 (2015) 20–27. doi:10.1016/j.msea.2015.02.056.
- [52] M. Aliofkhazraei, Superalloys, 2015.
- [53] S. Kou, Welding Metallurgy, 2nd Editio, A John Wiley & Sons, Inc., 2003.
- [54] B. Seiser, R. Drautz, D.G. Pettifor, TCP phase predictions in Ni-based superalloys: Structure maps revisited, Acta Mater. 59 (2011) 749–763. doi:10.1016/j.actamat.2010.10.013.
- [55] M. Bonvalet, T. Philippe, X. Sauvage, D. Blavette, Modeling of precipitation kinetics in multicomponent systems: Application to model superalloys, Acta Mater. 100 (2015) 169–177. doi:10.1016/j.actamat.2015.08.041.
- [56] K.S. Kim, S. Yang, M.S. Kim, K.A. Lee, Effect of post heat-treatment on the microstructure and high-temperature oxidation behavior of precipitation hardened IN738LC superalloy fabricated by selective laser melting, J. Mater. Sci. Technol. 76 (2021) 95–103. doi:10.1016/j.jmst.2020.11.013.
- [57] C. Joseph, C. Persson, M. Hörnqvist Colliander, Influence of heat treatment on the microstructure and tensile properties of Ni-base superalloy Haynes 282, Mater. Sci. Eng. A. 679 (2017) 520–530. doi:https://doi.org/10.1016/j.msea.2016.10.048.
- [58] T. Etter, Reduction in mechanical anisotropy through high temperature heat treatment of Hastelloy X processed by Selective Laser Melting ( SLM ) Reduction in m echanical a nisotropy through h igh t emperature h eat t reatment of Hastelloy X p rocessed by Selective, Mater. Sci. Eng. (2015). doi:10.1088/1757-899X/82/1/012097.
- [59] H.T. Kim, S.S. Chun, X.X. Yao, Y. Fang, J. Choi, Gamma prime ( $\gamma'$ ) precipitating and

- ageing behaviours in two newly developed nickel-base superalloys, *J. Mater. Sci.* 32 (1997) 4917–4923. doi:10.1023/A:1018672107071.
- [60] H.E. Lippard, C.E. Campbell, T. Björklind, U. Borggren, P. Kellgren, V.P. Dravid, G.B. Olson, Microsegregation behavior during solidification and homogenization of AerMet100 steel, *Metall. Mater. Trans. B Process Metall. Mater. Process. Sci.* 29 (1998) 205–210. doi:10.1007/s11663-998-0023-0.
- [61] S.A. Hosseini, K.Z. Madar, S.M. Abbasi, Effect of homogenization heat treatments on the cast structure and tensile properties of nickel-base superalloy ATI 718Plus in the presence of boron and zirconium additions, *Mater. Sci. Eng. A.* 689 (2017) 103–114. doi:10.1016/j.msea.2017.02.047.
- [62] A.R.P. Singh, Mechanisms of ordered gamma prime precipitate in nickel base superalloys, (2011) 1–154.
- [63] D.A. Porter, K.E. Easterling, *Phase Transformations in Metals and Alloys*, 1992. doi:10.1007/978-1-4899-3051-4.
- [64] R.E. Smallman, A.H.W. Ngan, *Physical Metallurgy and Advanced Materials*, 2007.
- [65] A.R.P. Singh, S. Nag, S. Chattopadhyay, Y. Ren, J. Tiley, G.B. Viswanathan, H.L. Fraser, R. Banerjee, Mechanisms related to different generations of  $\gamma'$  precipitation during continuous cooling of a nickel base superalloy, *Acta Mater.* 61 (2013) 280–293. doi:10.1016/j.actamat.2012.09.058.
- [66] X. Wu, Y. Li, M. Huang, W. Liu, Z. Hou, Precipitation kinetics of ordered  $\gamma'$  phase and microstructure evolution in a Ni[ $\gamma$ ]Al alloy, *Mater. Chem. Phys.* 182 (2016) 125–132. doi:10.1016/j.matchemphys.2016.07.013.
- [67] R.A. Ricks, A.J. Porter, R.C. Ecob, The growth of  $\gamma'$  precipitates in nickel-base superalloys, *Acta Metall.* 31 (1983) 43–53. doi:10.1016/0001-6160(83)90062-7.
- [68] J.Y. Hwang, S. Nag, A.R.P. Singh, R. Srinivasan, J. Tiley, G.B. Viswanathan, H.L. Fraser, R. Banerjee, Compositional Variations between Different Generations of  $\gamma'$  Precipitates Forming during Continuous Cooling of a Commercial Nickel-Base Superalloy, *Metall. Mater. Trans. A.* 40 (2009) 3059. doi:10.1007/s11661-009-0075-z.
- [69] S.S. Babu, M.K. Miller, J.M. Vitek, S.A. David, Characterization of the microstructure evolution in a nickel base superalloy during continuous cooling conditions, *Acta Mater.* 49 (2001) 4149–4160. doi:10.1016/S1359-6454(01)00314-7.

- [70] E. Balikci, D. Erdeniz, Multimodal precipitation in the superalloy IN738LC, *Metall. Mater. Trans. A Phys. Metall. Mater. Sci.* 41 (2010) 1391–1398. doi:10.1007/s11661-010-0241-3.
- [71] P. Strunz, M. Petrevec, J. Polák, U. Gasser, G. Farkas, Formation and Dissolution of  $\gamma'$  Precipitates in IN792 Superalloy at Elevated Temperatures, *Metals (Basel)*. 6 (2016) 37. doi:10.3390/met6020037.
- [72] F. Masoumi, M. Jahazi, D. Shahriari, J. Cormier, Coarsening and dissolution of  $\gamma'$  precipitates during solution treatment of AD730<sup>TM</sup> Ni-based superalloy: Mechanisms and kinetics models, *J. Alloys Compd.* 658 (2016) 981–995. doi:10.1016/j.jallcom.2015.11.002.
- [73] J.S. Van Sluytman, T.M. Pollock, Optimal precipitate shapes in nickel-base  $\gamma$ - $\gamma'$  alloys, *Acta Mater.* 60 (2012) 1771–1783. doi:10.1016/J.ACTAMAT.2011.12.008.
- [74] R.R. Unocic, L. Kovarik, C. Shen, P.M. Sarosi, Y. Wang, J. Li, S. Ghosh, M.J. Mills, Deformation mechanisms in ni-base disk superalloys at higher temperatures, *Proc. Int. Symp. Superalloys*. (2008) 377–385. doi:10.7449/2008/superalloys\_2008\_377\_385.
- [75] R.W. Kozar, A. Suzuki, W.W. Milligan, J.J. Schirra, M.F. Savage, T.M. Pollock, Strengthening mechanisms in polycrystalline multimodal nickel-base superalloys, *Metall. Mater. Trans. A Phys. Metall. Mater. Sci.* 40 (2009) 1588–1603. doi:10.1007/s11661-009-9858-5.
- [76] Mechanical metallurgy - Dieter\_ George Ellwood.pdf, (n.d.).
- [77] A.J. Goodfellow, Strengthening mechanisms in polycrystalline nickel-based superalloys, *Mater. Sci. Technol. (United Kingdom)*. 34 (2018) 1793–1808. doi:10.1080/02670836.2018.1461594.
- [78] E.I. Galindo-Nava, L.D. Connor, C.M.F. Rae, On the prediction of the yield stress of unimodal and multimodal  $\gamma'$  Nickel-base superalloys, *Acta Mater.* 98 (2015) 377–390. doi:10.1016/j.actamat.2015.07.048.
- [79] Q. Fang, L. Li, J. Li, H. Wu, Z. Huang, B. Liu, Y. Liu, P.K. Liaw, A statistical theory of probability-dependent precipitation strengthening in metals and alloys, *J. Mech. Phys. Solids*. 122 (2019) 177–189. doi:10.1016/j.jmps.2018.09.010.
- [80] G. Wang, L. Huang, P. Zhao, X. Zhan, Z. Qin, W. He, F. Liu, Y. Nie, Effect of Heat Treatment on Microstructure and Mechanical Properties of ODS Nickel-Based Superalloy via Strengthening Mechanism, *Jom*. 72 (2020) 3279–3287. doi:10.1007/s11837-020-04220-6.

- [81] A. Gypen, L.A. , Deruyettere, Multi-component solid solution hardening, *J. Mater. Sci.* 12 (1977) 1028–1033.
- [82] A. Gypen, L.A. , Deruyettere, Multi-component solid solution hardening Part 2 Agreement with experimental results, *J. Mater. Sci.* 12 (1977).
- [83] H.A. Roth, C.L. Davis, R.C. Thomson, Modeling solid solution strengthening in nickel alloys, *Metall. Mater. Trans. A.* 28 (1997) 1329–1335. doi:10.1007/s11661-997-0268-2.
- [84] D. Raynor, J.M. Silcock, Strengthening Mechanisms in  $\gamma'$  Precipitating Alloys, *Met. Sci. J.* 4 (1970) 121–130. doi:10.1179/msc.1970.4.1.121.
- [85] B. Reppich, Some new aspects concerning particle hardening mechanisms in  $\gamma'$  precipitating Ni-base alloys-I. Theoretical concept, *Acta Metall.* 30 (1982) 87–94. doi:10.1016/0001-6160(82)90048-7.
- [86] M. Heilmaier, U. Leetz, B. Reppich, Order strengthening in the cast nickel-based superalloy IN 100 at room temperature, *Mater. Sci. Eng. A* TA - TT -. 319–321 (2001) 375–378. doi:10.1016/S0921-5093(01)00989-3 LK -  
<https://mcgill.on.worldcat.org/oclc/4648063576>.
- [87] M. Preuss, M., Quinta da Fonseca, J., Grant, B., Knoche, E., Moat, R., Daymond, The effect of  $\gamma'$  particle size on the deformation mechanism in an advanced polycrystalline nickel-base superalloy, in: *Superalloys 2008 (Eleventh Int. Symp., 2008: pp. 405–414*.
- [88] E.M. Francis, B.M.B. Grant, J.Q. da Fonseca, P.J. Phillips, M.J. Mills, M.R. Daymond, M. Preuss, High-temperature deformation mechanisms in a polycrystalline nickel-base superalloy studied by neutron diffraction and electron microscopy, *Acta Mater.* 74 (2014) 18–29. doi:10.1016/J.ACTAMAT.2014.04.028.
- [89] R. Kayacan, R. Varol, O. Kimilli, The effects of pre- and post-weld heat treatment variables on the strain-age cracking in welded Rene 41 components, *Mater. Res. Bull.* 39 (2004) 2171–2186. doi:10.1016/j.materresbull.2004.08.003.
- [90] B.S. Yilbas, Characterization of laser-treated Rene 41 surface due to B<sub>4</sub>C and SiC particles at surface prior to laser treatment, *Surf. Interface Anal.* 46 (2014) 30–35. doi:10.1002/sia.5342.
- [91] Q.L. Pan, B. Li, Y. Wang, Y.W. Zhang, Z.M. Yin, Characterization of hot deformation behavior of Ni-base superalloy Rene'41 using processing map, *Mater. Sci. Eng. A.* 585 (2013) 371–378. doi:10.1016/j.msea.2013.07.066.

- [92] D. Tali, H. Gasan, M. Gulesen, S. Gurgen, M. Cemal, Turning Operation of Nickel Based Superalloy Rene 41, (2017) 9–11.
- [93] M.N. Gussev, N. Sridharan, M. Norfolk, K.A. Terrani, S.S. Babu, Materials Science & Engineering A Effect of post weld heat treatment on the 6061 aluminum alloy produced by ultrasonic additive manufacturing ☆, Mater. Sci. Eng. A. 684 (2017) 606–616. doi:10.1016/j.msea.2016.12.083.
- [94] J. Li, H.M. Wang, H.B. Tang, Effect of heat treatment on microstructure and mechanical properties of laser melting deposited Ni-base superalloy Rene’41, Mater. Sci. Eng. A. 550 (2012) 97–102. doi:10.1016/j.msea.2012.04.037.
- [95] S. Crump, Discontinuous Grain Boundaries of Forged René 41 Approval Page, (2012).
- [96] N. D’Souza, M. Lekstrom, H.B. Dong, An analysis of measurement of solute segregation in Ni-base superalloys using X-ray spectroscopy, Mater. Sci. Eng. A. 490 (2008) 258–265. doi:10.1016/j.msea.2008.01.025.
- [97] H. Chandler, Heat Treater’s Guide: Practices and Procedures for Nonferrous Alloys, ASM International, 1996. [https://books.google.ca/books?id=\\_iUd4RskarMC](https://books.google.ca/books?id=_iUd4RskarMC).
- [98] george F. vander voort, Atlas of Time-Temperature Diagrams for Nonferrous Alloys ( Materials Data Series ) By George F ., n.d.
- [99] M. Schwartz, R. Ciocoiu, D. Gheorghe, G. Jula, I. Ciucă, Preliminary research for using Rene 41 in confectioning extrusion dies, 90 (2015) 95–106. doi:10.2495/MC150091.
- [100] J. Li, H.M. Wang, Microstructure and mechanical properties of rapid directionally solidified Ni-base superalloy Rene’41 by laser melting deposition manufacturing, Mater. Sci. Eng. A. 527 (2010) 4823–4829. doi:10.1016/j.msea.2010.04.062.
- [101] H.E. Collins, Relative Stability of Carbide and Intermetallic Phases in Nickel-Base Superalloys, (2012) 171–198. doi:10.7449/1968/superalloys\_1968\_171\_198.
- [102] Heat Treaters Guide: Nonferrous Aloys, 721 (1800) 59–75.
- [103] The Elevated-Temperature Properties of Selected Superalloys, Elev. Prop. Sel. Superalloys. (2015). doi:10.1520/ds7s1-eb.
- [104] G. Atxaga, A.M. Irisarri, Creep Behavior of a Cast Rene 41 Superalloy, n.d.
- [105] S.M. Richard, A Study on the Strain Age Crack Sensitivity of Rene 41, (1968). doi:10.1021/jz3014425.
- [106] J.E. Franklin, W.F. Savage, Stress Relaxation and Strain-Age Cracking in Rene 41

- Weldments, Weld. J. 53 (1974) 380s-387s.  
[http://aws.perusion.com/wj/supplement/WJ\\_1974\\_09\\_s380.pdf](http://aws.perusion.com/wj/supplement/WJ_1974_09_s380.pdf).
- [107] S. Tosto, Diffusion processes and weldability of hot-pressed RENE' 41 superalloy, *Metallography*. 17 (1984) 89–102. doi:10.1016/0026-0800(84)90007-7.
- [108] S. Wang, *Welding and Repair of Single Crystal Ni-based Superalloys*, (2005).
- [109] H.-S. Wang, C.-Y. Huang, K.-S. Ho, S.-J. Deng, Microstructure Evolution of Laser Repair Welded René 77 Nickel-Based Superalloy Cast, *Mater. Trans.* 52 (2011) 2197–2204. doi:10.2320/matertrans.m2011264.
- [110] M. Zielinska, J. Sieniawski, Gajecka, Criterion for selection the optimal physical and chemical properties of cobalt aluminate powder used in investment casting process, *Arch. Foundry Eng.* (2009).
- [111] H.Y. Bor, C.N. Wei, A.C. Yeh, W. Bin He, H. Sen Wang, C.M. Kuo, Heat treatment effects on the high temperature mechanical behavior of directionally solidified MAR-M247 superalloy, 8th Pacific Rim Int. Congr. Adv. Mater. Process. 2013, PRICM 8. 1 (2013) 379–386. doi:10.1007/978-3-319-48764-9\_46.
- [112] J.R. (Joseph R.. Davis, A.S.M.I.H. Committee., *Heat-resistant materials LK* - <https://mcgill.on.worldcat.org/oclc/37353908>, ASM International, Materials Park, Ohio SE - v, 591 pages : illustrations ; 29 cm., 1997.
- [113] M. Zielinska, J. Sieniawski, Surface modification and its influence on the microstructure and creep resistance of nickel based superalloy René 77, *Arch. Metall. Mater.* 58 (2013) 95–98. doi:10.2478/v10172-012-0157-6.
- [114] S.D. Antolovich, E. Rosa, *Low Cycle Fatigue of Rene 77 at Elevated Temperatures*, 47 (1981) 47–57.
- [115] J.A.N. Sieniawski, Selection of heat treatment and aluminizing sequence for Rene 77 superalloy, n.d.
- [116] M. Zielińska, J. Sieniawski, M. Poręba, Microstructure and mechanical properties of high temperature creep resisting superalloy René 77 modified CoAl<sub>2</sub>O<sub>4</sub>, *Arch. Mater.* 28 (2007) 629–632.
- [117] MetalTek René 77 Centri-Vac Nickel Cobalt Based Alloy, (n.d.). <http://www.matweb.com/search/datasheet.aspx?matguid=10c55bc1e84542adb8c6c3fd39837390&ckck=1> (accessed February 2, 2021).

- [118] S. Grades, Rene 77, (n.d.). <https://www.steel-grades.com/Steel-Grades/High-Alloy/Rene-77.html>.
- [119] R.G. Ding, O.A. Ojo, M.C. Chaturvedi, Laser beam weld-metal microstructure in a yttrium modified directionally solidified Ni3Al-base alloy, *Intermetallics*. 15 (2007) 1504–1510. doi:10.1016/J.INTERMET.2007.05.008.
- [120] N. Guo, M.C. Leu, Additive manufacturing: Technology, applications and research needs, *Front. Mech. Eng.* 8 (2013) 215–243. doi:10.1007/s11465-013-0248-8.
- [121] N.J. Harrison, I. Todd, K. Mumtaz, Reduction of micro-cracking in nickel superalloys processed by Selective Laser Melting: A fundamental alloy design approach, *Acta Mater.* 94 (2015) 59–68. doi:10.1016/j.actamat.2015.04.035.
- [122] X. Wang, L.N. Carter, B. Pang, M.M. Attallah, M.H. Loretto, Microstructure and yield strength of SLM-fabricated CM247LC Ni-Superalloy, *Acta Mater.* 128 (2017) 87–95. doi:10.1016/j.actamat.2017.02.007.
- [123] M.M. Attallah, R. Jennings, X. Wang, L.N. Carter, Additive manufacturing of Ni-based superalloys: The outstanding issues, *MRS Bull.* 41 (2016) 758–764. doi:10.1557/mrs.2016.211.
- [124] Y.T. Tang, C. Panwisawas, J.N. Ghousoub, Y. Gong, J.W.G. Clark, A.A.N. Németh, D.G. McCartney, R.C. Reed, Alloys-by-design: Application to new superalloys for additive manufacturing, *Acta Mater.* 202 (2021) 417–436. doi:10.1016/j.actamat.2020.09.023.
- [125] H. Wang, X. Zhang, G.B. Wang, J. Shen, G.Q. Zhang, Y.P. Li, M. Yan, Selective laser melting of the hard-to-weld IN738LC superalloy: Efforts to mitigate defects and the resultant microstructural and mechanical properties, *J. Alloys Compd.* 807 (2019). doi:10.1016/j.jallcom.2019.151662.
- [126] I. Lopez-Galilea, B. Ruttert, J. He, T. Hammerschmidt, R. Drautz, B. Gault, W. Theisen, Additive manufacturing of CMSX-4 Ni-base superalloy by Selective Laser Melting: Influence of processing parameters and heat treatment, *Addit. Manuf.* (2019) 100874. doi:10.1016/J.ADDMA.2019.100874.
- [127] T. Böllighaus, H. Herold, C. Cross, J.C. Lippold, *Hot Cracking Phenomena in Wels II*, 2008. doi:10.1017/CBO9781107415324.004.
- [128] J.L. Caron, J.W. Sowards, *Weldability of Nickel-Base Alloys*, 2014. doi:10.1016/B978-0-08-096532-1.00615-4.

- [129] S. Kou, Solidification and liquation cracking issues in welding, *Jom.* 55 (2003) 37–42. doi:10.1007/s11837-003-0137-4.
- [130] J. Zhang, Hot Tearing in Directionally Solidified Ni-Based Superalloys, *Superalloys 2004*. (2004) 727–733. doi:\url{10.7449/2004/Superalloys{\textunderscore }2004{\textunderscore }727{\textunderscore }733}.
- [131] O.A. Ojo, Intergranular liquation cracking in heat affected zone of a welded nickel based superalloy in as cast condition, *Mater. Sci. Technol.* 23 (2007) 1149–1155. doi:10.1179/174328407X213323.
- [132] O.A. Ojo, F. Tancret, Clarification on “Thermo-Calc and Dictra simulation of constitutional liquation of gamma prime ( $\gamma'$ ) during welding of Ni-base superalloys,” *Comput. Mater. Sci.* 45 (2009) 388–389. doi:10.1016/j.commatsci.2008.10.014.
- [133] P. Rong, N. Wang, L. Wang, R.N. Yang, W.J. Yao, The influence of grain boundary angle on the hot cracking of single crystal superalloy DD6, *J. Alloys Compd.* 676 (2016) 181–186. doi:10.1016/J.JALLCOM.2016.03.164.
- [134] E. Scheil, No Title, *Zeitschrift Für Met.* 34 (1942) 70–74.
- [135] D. Dye, O. Hunziker, R.C. Reed, Numerical analysis of the weldability of superalloys, *Acta Mater.* 49 (2001) 683–697. doi:https://doi.org/10.1016/S1359-6454(00)00361-X.
- [136] L.N. Carter, C. Martin, P.J. Withers, M.M. Attallah, The influence of the laser scan strategy on grain structure and cracking behaviour in SLM powder-bed fabricated nickel superalloy, *J. Alloys Compd.* 615 (2014) 338–347. doi:10.1016/j.jallcom.2014.06.172.
- [137] V. Kavooosi, S.M. Abbasi, S.M.G. Mirsaed, M. Mostafaei, Influence of cooling rate on the solidification behavior and microstructure of IN738LC superalloy, *J. Alloys Compd.* 680 (2016) 291–300. doi:10.1016/j.jallcom.2016.04.099.
- [138] M. Rappaz, J.M. Drezet, M. Gremaud, A new hot-tearing criterion, *Metall. Mater. Trans. A Phys. Metall. Mater. Sci.* 30 (1999) 449–455. doi:10.1007/s11661-999-0334-z.
- [139] N. Lu, Z. Lei, K. Hu, X. Yu, P. Li, J. Bi, S. Wu, Y. Chen, Hot cracking behavior and mechanism of a third-generation Ni-based single-crystal superalloy during directed energy deposition, *Addit. Manuf.* 34 (2020) 101228. doi:https://doi.org/10.1016/j.addma.2020.101228.
- [140] N. Wang, S. Mokadem, M. Rappaz, W. Kurz, Solidification cracking of superalloy single- and bi-crystals, *Acta Mater.* 52 (2004) 3173–3182. doi:10.1016/J.ACTAMAT.2004.03.047.

- [141] E. Chauvet, P. Kontis, E.A. Jäggle, B. Gault, D. Raabe, C. Tassin, J.J. Blandin, R. Dendievel, B. Vayre, S. Abed, G. Martin, Hot cracking mechanism affecting a non-weldable Ni-based superalloy produced by selective electron Beam Melting, *Acta Mater.* 142 (2018) 82–94. doi:10.1016/j.actamat.2017.09.047.
- [142] Z. Zhou, L. Huang, Y. Shang, Y. Li, L. Jiang, Q. Lei, Causes analysis on cracks in nickel-based single crystal superalloy fabricated by laser powder deposition additive manufacturing, *Mater. Des.* 160 (2018) 1238–1249. doi:10.1016/j.matdes.2018.10.042.
- [143] J.H. Boswell, D. Clark, W. Li, M.M. Attallah, Cracking during thermal post-processing of laser powder bed fabricated CM247LC Ni-superalloy, *Mater. Des.* 174 (2019) 107793. doi:10.1016/J.MATDES.2019.107793.
- [144] D. Zhang, A. Prasad, M.J. Bermingham, C.J. Todaro, M.J. Benoit, M.N. Patel, D. Qiu, D.H. StJohn, M. Qian, M.A. Easton, Grain Refinement of Alloys in Fusion-Based Additive Manufacturing Processes, *Metall. Mater. Trans. A Phys. Metall. Mater. Sci.* (2020). doi:10.1007/s11661-020-05880-4.
- [145] F. Yan, W. Xiong, E.J. Faierson, Grain structure control of additively manufactured metallic materials, *Materials (Basel)*. 10 (2017) 1260. doi:10.3390/ma10111260.
- [146] D. Tomus, P.A. Rometsch, M. Heilmaier, X. Wu, Effect of minor alloying elements on crack-formation characteristics of Hastelloy-X manufactured by selective laser melting, *Addit. Manuf.* 16 (2017) 65–72. doi:10.1016/j.addma.2017.05.006.
- [147] H. Gruber, E. Hryha, K. Lindgren, Y. Cao, M. Rashidi, L. Nyborg, The effect of boron and zirconium on the microcracking susceptibility of IN-738LC derivatives in laser powder bed fusion, *Appl. Surf. Sci.* 573 (2022) 151541. doi:10.1016/J.APSUSC.2021.151541.
- [148] L. Zhang, Y. Li, S. Zhang, Q. Zhang, Selective laser melting of IN738 superalloy with a low Mn+Si content: Effect of energy input on characteristics of molten pool, metallurgical defects, microstructures and mechanical properties, *Mater. Sci. Eng. A.* 826 (2021) 141985. doi:10.1016/J.MSEA.2021.141985.
- [149] P. Kontis, E. Chauvet, Z. Peng, J. He, A.K. da Silva, D. Raabe, C. Tassin, J.J. Blandin, S. Abed, R. Dendievel, B. Gault, G. Martin, Atomic-scale grain boundary engineering to overcome hot-cracking in additively-manufactured superalloys, *Acta Mater.* 177 (2019) 209–221. doi:10.1016/j.actamat.2019.07.041.
- [150] J. Xu, Y. Ding, Y. Gao, H. Wang, Y. Hu, D. Zhang, Grain refinement and crack inhibition

- of hard-to-weld Inconel 738 alloy by altering the scanning strategy during selective laser melting, *Mater. Des.* 209 (2021) 109940. doi:10.1016/J.MATDES.2021.109940.
- [151] Q. Han, Y. Gu, R. Setchi, F. Lacan, R. Johnston, S.L. Evans, S. Yang, Additive manufacturing of high-strength crack-free Ni-based Hastelloy X superalloy, *Addit. Manuf.* 30 (2019) 100919. doi:10.1016/j.addma.2019.100919.
- [152] L. Liu, T. Huang, Y. Xiong, A. Yang, Z. Zhao, R. Zhang, J. Li, Grain refinement of superalloy K4169 by addition of refiners: cast structure and refinement mechanisms, *Mater. Sci. Eng. A.* 394 (2005) 1–8. doi:10.1016/J.MSEA.2004.10.005.
- [153] G.P. Dinda, A.K. Dasgupta, J. Mazumder, Laser aided direct metal deposition of Inconel 625 superalloy: Microstructural evolution and thermal stability, *Mater. Sci. Eng. A.* 509 (2009) 98–104. doi:10.1016/j.msea.2009.01.009.
- [154] A. Basak, S. Das, Epitaxy and Microstructure Evolution in Metal Additive Manufacturing, *Annu. Rev. Mater. Res.* 46 (2016) 125–149. doi:10.1146/annurev-matsci-070115-031728.
- [155] S. Li, Q. Wei, Y. Shi, Z. Zhu, D. Zhang, Microstructure Characteristics of Inconel 625 Superalloy Manufactured by Selective Laser Melting, *J. Mater. Sci. Technol.* 31 (2015) 946–952. doi:10.1016/j.jmst.2014.09.020.
- [156] K. Kunze, T. Etter, J. Grässlin, V. Shklover, Texture, anisotropy in microstructure and mechanical properties of IN738LC alloy processed by selective laser melting (SLM), *Mater. Sci. Eng. A.* 620 (2014) 213–222. doi:10.1016/j.msea.2014.10.003.
- [157] D.J. Newell, R.P. O’Hara, G.R. Cobb, A.N. Palazotto, M.M. Kirka, L.W. Burggraf, J.A. Hess, Mitigation of scan strategy effects and material anisotropy through supersolvus annealing in LPBF IN718, *Mater. Sci. Eng. A.* 764 (2019) 138230. doi:10.1016/J.MSEA.2019.138230.
- [158] F. Geiger, K. Kunze, T. Etter, Tailoring the texture of IN738LC processed by selective laser melting (SLM) by specific scanning strategies, *Mater. Sci. Eng. A.* 661 (2016) 240–246. doi:10.1016/j.msea.2016.03.036.
- [159] Y. Tian, J.A. Muñoz-Lerma, M. Brochu, Nickel-based superalloy microstructure obtained by pulsed laser powder bed fusion, *Mater. Charact.* 131 (2017) 306–315. doi:10.1016/j.matchar.2017.07.024.
- [160] H.L. Wei, J. Mazumder, T. DebRoy, Evolution of solidification texture during additive manufacturing, *Sci. Rep.* 5 (2015) 1–7. doi:10.1038/srep16446.

- [161] Z. Liu, H. Qi, Effects of substrate crystallographic orientations on crystal growth and microstructure formation in laser powder deposition of nickel-based superalloy, *Acta Mater.* 87 (2015) 248–258. doi:10.1016/j.actamat.2014.12.046.
- [162] W. Kurz, R. Trivedi, Rapid solidification processing and microstructure formation, *Mater. Sci. Eng. A.* 179–180 (1994) 46–51. doi:10.1016/0921-5093(94)90162-7.
- [163] W. Kurz, B. Giovanola, R. Trivedi, Theory of microstructural development during rapid solidification, *Acta Metall.* 34 (1986) 823–830. doi:10.1016/0001-6160(86)90056-8.
- [164] H. Hyer, R. Newell, D. Matejczyk, S. Hsie, M. Anthony, L. Zhou, C. Kammerer, Y. Sohn, Microstructural Development in As Built and Heat Treated IN625 Component Additively Manufactured by Laser Powder Bed Fusion, *J. Phase Equilibria Diffus.* 42 (2021) 14–27. doi:10.1007/s11669-020-00855-9.
- [165] D.M. Stefanescu, R. Ruxanda, Fundamentals of Solidification, *Metallogr. Microstruct.* (2018) 71–92. doi:10.31399/asm.hb.v09.a0003724.
- [166] R. Acharya, R. Bansal, J.J. Gambone, M.A. Kaplan, G.E. Fuchs, N.G. Rudawski, S. Das, Additive Manufacturing and Characterization of René 80 Superalloy Processed Through Scanning Laser Epitaxy for Turbine Engine Hot-Section Component Repair, *Adv. Eng. Mater.* 17 (2015) 942–950. doi:10.1002/adem.201400589.
- [167] K. Moussaoui, W. Rubio, M. Mousseigne, T. Sultan, F. Rezai, Effects of Selective Laser Melting additive manufacturing parameters of Inconel 718 on porosity, microstructure and mechanical properties, *Mater. Sci. Eng. A.* 735 (2018) 182–190. doi:10.1016/J.MSEA.2018.08.037.
- [168] L. Rickenbacher, T. Etter, S. Hövel, K. Wegener, High temperature material properties of IN738LC processed by selective laser melting (SLM) technology, *Rapid Prototyp. J.* 19 (2013) 282–290. doi:10.1108/13552541311323281.
- [169] W. Philpott, M.A.E. Jepson, R.C. Thomson, Comparison of the effects of a conventional heat treatment between cast and selective laser melted IN939 alloy, *Adv. Mater. Technol. Foss. Power Plants - Proc. from 8th Int. Conf.* (2016) 735–746.
- [170] A.S. Shaikh, F. Schulz, K. Minet-Lallemand, E. Hryha, Microstructure and Mechanical Properties of Haynes 282 Superalloy Produced by Laser Powder Bed Fusion, *Mater. Today Commun.* (2021) 102038. doi:10.1016/j.mtcomm.2021.102038.
- [171] J. Xu, H. Gruber, R. Boyd, S. Jiang, R.L. Peng, J.J. Moverare, On the strengthening and

- embrittlement mechanisms of an additively manufactured Nickel-base superalloy, *Materialia*. 10 (2020) 100657. doi:<https://doi.org/10.1016/j.mtla.2020.100657>.
- [172] R. Muñoz-Moreno, V.D. Divya, S.L. Driver, O.M.D.M. Messé, T. Illston, S. Baker, M.A. Carpenter, H.J. Stone, Effect of heat treatment on the microstructure, texture and elastic anisotropy of the nickel-based superalloy CM247LC processed by selective laser melting, *Mater. Sci. Eng. A*. 674 (2016) 529–539. doi:[10.1016/j.msea.2016.06.075](https://doi.org/10.1016/j.msea.2016.06.075).
- [173] R. Acharya, J.A. Sharon, A. Staroselsky, Prediction of microstructure in laser powder bed fusion process, *Acta Mater.* 124 (2017) 360–371. doi:[10.1016/j.actamat.2016.11.018](https://doi.org/10.1016/j.actamat.2016.11.018).
- [174] F. Zhang, L.E. Levine, A.J. Allen, M.R. Stoudt, G. Lindwall, E.A. Lass, M.E. Williams, Y. Idell, C.E. Campbell, Effect of heat treatment on the microstructural evolution of a nickel-based superalloy additive-manufactured by laser powder bed fusion, *Acta Mater.* 152 (2018) 200–214. doi:[10.1016/j.actamat.2018.03.017](https://doi.org/10.1016/j.actamat.2018.03.017).
- [175] B. Graybill, M. Li, D. Malawey, C. Ma, J.M. Alvarado-Orozco, E. Martinez-Franco, Additive manufacturing of nickel-based superalloys, *ASME 2018 13th Int. Manuf. Sci. Eng. Conf. MSEC 2018*. 1 (2018). doi:[10.1115/MSEC2018-6666](https://doi.org/10.1115/MSEC2018-6666).
- [176] O. Adegoke, J. Andersson, H. Brodin, R. Pederson, Review of laser powder bed fusion of gamma-prime-strengthened nickel-based superalloys, *Metals (Basel)*. 10 (2020) 1–26. doi:[10.3390/met10080996](https://doi.org/10.3390/met10080996).
- [177] F. Hanning, A.K. Khan, J. Steffenburg-Nordenström, O. Ojo, J. Andersson, Investigation of the effect of short exposure in the temperature range of 750–950°C on the ductility of haynes® 282® by advanced microstructural characterization, *Metals (Basel)*. 9 (2019). doi:[10.3390/met9121357](https://doi.org/10.3390/met9121357).
- [178] C. Körner, M. Ramsperger, C. Meid, D. Bürger, P. Wollgramm, M. Bartsch, G. Eggeler, Microstructure and Mechanical Properties of CMSX-4 Single Crystals Prepared by Additive Manufacturing, *Metall. Mater. Trans. A Phys. Metall. Mater. Sci.* 49 (2018) 3781–3792. doi:[10.1007/s11661-018-4762-5](https://doi.org/10.1007/s11661-018-4762-5).
- [179] E. Chlebus, K. Gruber, B. Kuźnicka, J. Kurzac, T. Kurzynowski, Effect of heat treatment on the microstructure and mechanical properties of Inconel 718 processed by selective laser melting, *Mater. Sci. Eng. A*. 639 (2015) 647–655. doi:[10.1016/J.MSEA.2015.05.035](https://doi.org/10.1016/J.MSEA.2015.05.035).
- [180] I. Yadroitsev, M. Pavlov, P. Bertrand, I. Smurov, Mechanical properties of samples fabricated by selective laser melting, *14èmes Assises Eur. Du Prototypage Fabr. Rapide*.

625 (2009) 24–25.

- [181] D. Tomus, T. Jarvis, X. Wu, J. Mei, P. Rometsch, E. Hery, J.F. Rideau, S. Vaillant, Controlling the microstructure of Hastelloy-X components manufactured by Selective Laser Melting, in: *Phys. Procedia*, Elsevier B.V., 2013: pp. 823–827. doi:10.1016/j.phpro.2013.03.154.
- [182] A. Deshpande, S.D. Nath, S. Atre, K. Hsu, Effect of Post Processing Heat Treatment Routes on Microstructure and Mechanical Property Evolution of Haynes 282 Ni-Based Superalloy Fabricated with, (2020) 1–13.
- [183] P. Kanagarajah, F. Brenne, T. Niendorf, H.J. Maier, Inconel 939 processed by selective laser melting: Effect of microstructure and temperature on the mechanical properties under static and cyclic loading, *Mater. Sci. Eng. A.* 588 (2013) 188–195. doi:10.1016/j.msea.2013.09.025.
- [184] Y. Tian, A. Gontcharov, R. Gauvin, P. Lowden, M. Brochu, Effect of heat treatment on microstructure evolution and mechanical properties of Inconel 625 with 0.4 wt% boron modification fabricated by gas tungsten arc deposition, *Mater. Sci. Eng. A.* 684 (2017) 275–283. doi:10.1016/j.msea.2016.12.038.
- [185] M.E. Aydinöz, F. Brenne, M. Schaper, C. Schaak, W. Tillmann, J. Nellesen, T. Niendorf, On the microstructural and mechanical properties of post-treated additively manufactured Inconel 718 superalloy under quasi-static and cyclic loading, *Mater. Sci. Eng. A.* 669 (2016) 246–258. doi:10.1016/j.msea.2016.05.089.

## **Chapter 3: Microstructure and Mechanical Properties of Rene 41 Alloy Manufactured by Laser Powder Bed Fusion**

---

This chapter demonstrates that the use of LPBF is possible as a processing technique to fabricate bulk R41 parts. The solidification microstructure of LPBF fabricated R41 alloy and its evolution after the application of the standard heat treatment is investigated in detail. This chapter covers effect of the heat treatment and building direction on the room temperature mechanical properties of this alloy in relation with the microstructure. The microstructure and mechanical properties obtained after LPBF were compared with other processing methods. The knowledge obtained in this chapter can be used to identify the specific processing conditions and microstructure that would lead to a crack-free part as well as to obtain mechanical properties satisfying the specifications. Additionally, it could provide insight on the process-structure-property relationship for different processing routes.

This chapter has been published as: S.E. Atabay, O. Sanchez-Mata, J.A. Muñiz-Lerma, R. Gauvin, M. Brochu, Microstructure and mechanical properties of Rene 41 alloy manufactured by laser powder bed fusion, Mater. Sci. Eng. A. 773 (2020).

### 3.1. Abstract

Precipitation hardenable Ni-based superalloy Rene 41, considered to have moderate weldability, was produced by laser powder bed fusion (LPBF). Crack-free and dense parts were obtained directly from processing. Parts were characterized in both as-built condition and after aging heat treatment. In the as-deposited condition, scanning electron microscopy and electron back scattered diffraction analysis revealed a fine columnar dendritic microstructure with a preferred orientation along  $\langle 100 \rangle$ . Transmission electron microscopy analysis revealed the absence of  $\gamma'$  precipitates in the as fabricated state. After heat treatment, the columnar grain morphology was maintained and formation of distinct carbide particles at the grain and cell boundaries were observed along with the precipitation of fine and homogeneously distributed  $\gamma'$ . The size of these  $\gamma'$  precipitates were measured as 8 to 30 nm which is smaller compared to the reported values in the literature. Significant increase in the microhardness value from 347 HV to 548 HV is observed after the heat treatment. Increased room temperature yield and ultimate tensile strength values reaching 857 and 1165 MPa were measured for the samples built parallel to the base plate in the as built state. These values increased to 1263 and 1580 MPa after the heat treatment, ascribed to the presence of fine  $\gamma'$  precipitates. Fractography analysis revealed that failure occurred in a ductile manner for both as fabricated and heat-treated samples.

### 3.2. Introduction

Nickel-base superalloys are widely used high temperature materials in aerospace and power plant applications due to their high resistance to fatigue, creep and environmental degradation at temperatures of 1000°C and beyond [1]. These properties mainly achieved by precipitation of secondary phases such as  $\gamma'$ ,  $\gamma''$ [2][3]. Rene 41 (named thereafter R41) is a precipitation strengthened Ni-based superalloy developed in the mid 1950's. It possesses an excellent combination of corrosion and oxidation resistance along with high mechanical and microstructural stability at temperatures up to 980 °C [4,5]. Due to these properties, R41 has been used widely in hot section parts of jet aircraft engines and divergent seal and flap components, exhaust nozzles in military turbine engines [6–8]. Although presence of  $\gamma'$  makes R41 a suitable candidate for high strength and high temperature applications, this alloy has a limited usage due to its cracking tendency during processing [9]. The Al and Ti content classify R41 as an alloy having moderate

weldability from the welding metallurgy definition [10]. Strain age cracking in the heat affected zone and/or in the base metal is reported as a primary problem during welding and post-weld heat treatment [11]. Therefore, developing the processability of this alloy using new manufacturing techniques would be of great economical and practical interest.

Laser powder-bed fusion (LPBF) process, one of the main metal additive manufacturing (AM) processes, involves selective melting and solidification of powders by the aid of a rastered laser along a defined path [11,12]. LPBF offers a design flexibility by allowing production of complex metallic parts with reduced material waste, production cost and time. Owing to these unique advantages over conventional production techniques such as casting and forging, LPBF is finding more and more applications in aerospace, automobile and nuclear industries [13–15]

Due to high residual stresses encountered during LPBF, cracking is frequently observed during processing of Ni-based superalloys [16,17]. From that reason, literature on LPBF of Ni-based superalloys is mainly focused on alloys IN 718 [18–20] and IN 625 [21], due to their low cracking susceptibility. A variety of Ni-based superalloys that are prone to cracking were also studied by LPBF such as, high C-Hastelloy X [22,23], CM247LC [24,25] IN 738 [26,27]. From this list, only limited studies reported the production of crack free parts in high C-Hastelloy X [22] and IN 738 [26]. These demonstrations suggest the feasibility to fabricate difficult to weld alloys with LPBF, if tight control of process parameters and chemical composition of the alloy is implied [28]. Additionally, the high cooling rates achieved during LPBF processing yield finer microstructural features compared to conventional processing techniques [11,28], which should have a positive impact on the mechanical properties [28].

Although there is some literature on laser surface melting and laser melt deposition [9,29–31], no open literature on LPBF of R41 alloy was found. In that context, processability of R41 with LPBF is reported in this paper. For this purpose, parts were produced via LPBF and characterized in terms of microstructure (SEM, EBSD, TEM) and mechanical properties (tensile properties, hardness) in both the as fabricated and precipitation hardened condition.

### **3.3. Experimental Procedure**

Commercially available argon gas atomized R41 powders provided by TLS Technik, Germany, with the given composition listed in Table 3.1 were used in this study. Particle size distribution

(PSD) of the powder was measured using LA-920 Horiba laser particle size analyzer. Morphology of the powder was characterized with Hitachi 3500 scanning electron microscope (SEM). To characterize the flowability of the powder, cohesive index (CI) measurements were conducted using Granudrum.

Table 3.1. Chemical composition of the R41 powder.

Element	Al	Cr	Co	Ti	Fe	Mn	Mo	Si	C	Ni
Wt. %	1.57	19.0	10.94	3.12	2.96	0.01	9.78	0.02	0.08	Bal.

A Renishaw AM400 LPBF system equipped with a pulse Nd:YAG laser having maximum power capacity of 400W was used to fabricate the samples used in this study. The process was conducted under Ar atmosphere to prevent oxidation of the parts. Cubes having dimensions of 1cm x 1cm x 1cm was fabricated for microstructural characterization. For mechanical testing 10 mm x 10 mm x 55 mm bars were fabricated in horizontal (X) direction and 10 mm x 10 mm x 42 mm bars were fabricated using a reduced build volume chamber in the vertical (Z) direction. The standard precipitation hardening heat treatment for R41 alloy was studied. It consists of a solutionizing at 1065 °C for 4 hours than air cooling to room temperature followed by aging at 760 °C for 16 hours and air cooling to room temperature [32]. Heat treatment was conducted under Ar atmosphere to prevent any compositional changes due to oxidation.

Samples fabricated by LPBF were removed from the build plate and sectioned along the build direction for microstructural examination. Samples were prepared using standard metallographic preparation techniques and electro-etching was performed in a solution of 12 ml H<sub>3</sub>PO<sub>4</sub>, 40 ml HNO<sub>3</sub>, 48 ml H<sub>2</sub>SO<sub>4</sub> at 6 V for 5 s to reveal the microstructure [20]. Nikon light optical microscope equipped with a Clemex Vision System was used for optical imaging of the polished cross-sections. Fifteen micrographs from different parts of the sample were analyzed using image analysis software Image J [33] to calculate the relative density of the as fabricated parts. Hitachi 3500 SEM equipped with an energy dispersive spectrometer (EDS) was used for detailed microstructural analysis. Primary dendrite arm spacing (PDAS) of the as-fabricated samples was measured using the line intercept method in Image J software. Five different regions along the build direction were analyzed for these measurements. Grain morphology and texture were

analyzed by electron backscattered diffraction (EBSD) system installed on the Hitachi SU3500 SEM. The operating conditions were 15 kV and 2 $\mu$ m step size. Aztec data acquisition software combined with the HKL Channel 5 data processing software was used for the EBSD data analysis. Hitachi SU9000 STEM equipped with EDS was used for high magnification imaging and elemental analysis. For transmission electron microscopy (TEM), 70  $\mu$ m thick discs with 3mm diameter were prepared. The discs were then jet-polished for electron transparency using a perchloric acid/ methanol solution (ratio 1:3) at -30 °C with 25 V voltage. TEM analysis were conducted on a FEI Tecnai G2 F20 200 kV Cryo-STEM, located in Facility for Electron Microscopy Research at McGill University.

Microhardness measurements were conducted via a CM-100AT Clark Microhardness Indenter using 200 g load for 10s. Fifteen independent measurements were done for each sample and averaged. Round tensile test bars having a reduced cross-section of 3mm diameter and 12 mm gauge length were machined from the LPBF fabricated bars according to ASTM E8 / E8M - 16a [34]. SATEC Systems tensile machine 60UD with 250 kN load cell was used for room temperature tensile testing with a speed of 0.015 min<sup>-1</sup> up to yield, and 0.05 min<sup>-1</sup> afterwards. Strain measurements were conducted with an INSTRON AVE 2 non-contacting extensometer. Four samples were tested for each condition. Fractography analysis were conducted on the tested samples under SEM.

## **3.4. Results & Discussion**

### **3.4.1 Powder Characterization**

Powder particles were examined under SEM prior to processing to investigate their size, shape, morphology, and microstructure. As shown in Figure 3.1(a) majority of the powder particles have spherical morphology with presence of small irregularities, and satellites attached to powder particles. Higher magnification observations in Figure 3.1(b) revealed a surface dendritic microstructure on the powder particles.

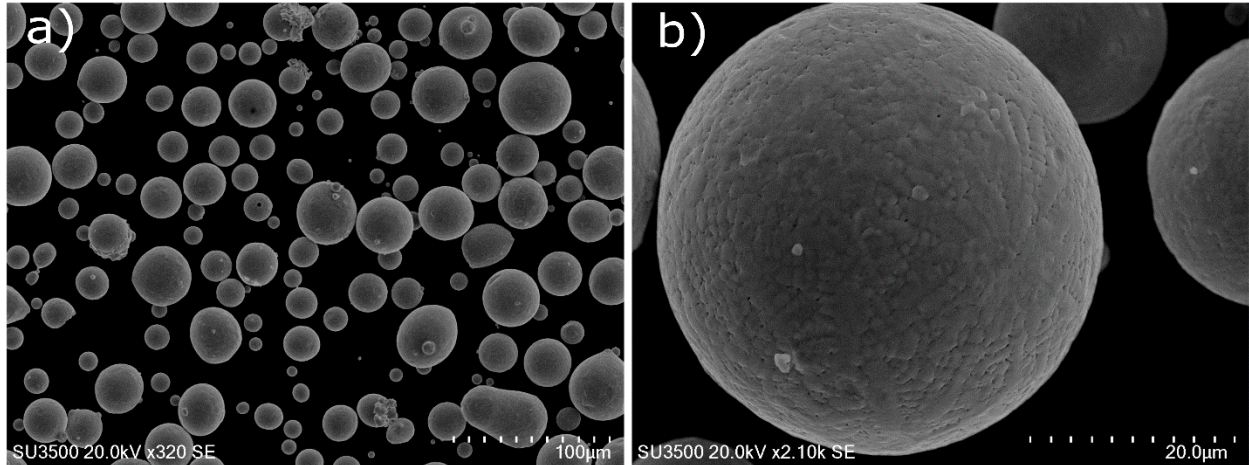


Figure 3. 1. SEM micrograph showing (a) size and shape (b) morphology of the R41 powder.

Figure 3.2(a) shows that the PSD of the powder has Gaussian distribution with  $D_{10}$ ,  $D_{50}$  and  $D_{90}$  particle diameters of 13, 25 and 43  $\mu\text{m}$ , respectively. Powder flowability analysis was conducted with the rotating drum and the CI value as a function of rotation speed shown in Figure 3.2(b). Measured values ranged between 22-25 for a rotating speed up to 14 rpm and were higher for higher rotating speeds. Literature has shown that powder with lower cohesive index possesses better flowability [35]. Humbeeck et. al reported that a CI of 25 is the threshold value of CI for a powder to be successfully spread for powder bed processing [35,36]. As such, recoater speed was adjusted to a value below the converted 14 rpm rotational speed for R41 powder, to maximize the possibility of having high quality spread layers.

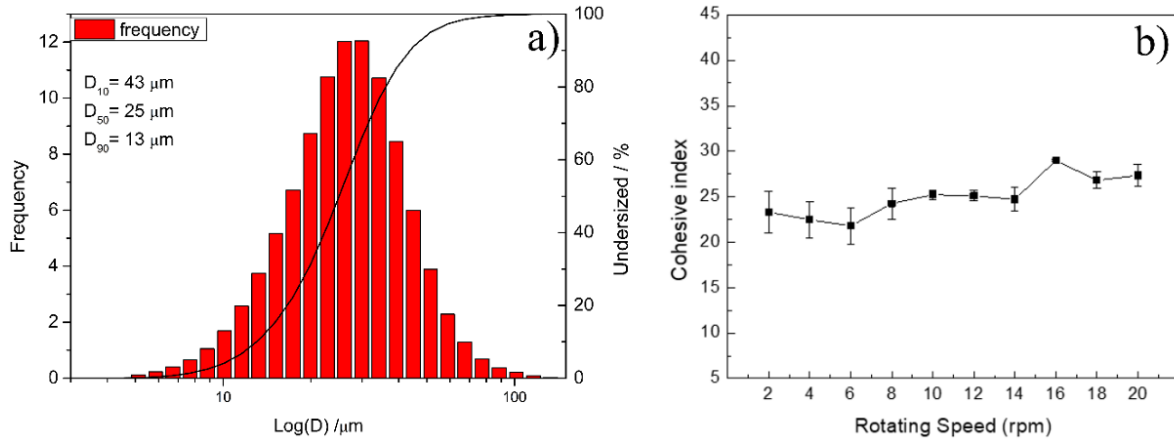


Figure 3. 2. (a) particle size distribution (b) cohesive index of R41 powder.

### 3.4.2 Microstructural Characterization of the As-fabricated Samples

Figure 3.3 shows a mosaic of representative optical micrographs of an as polished cross-section of an as fabricated sample. No cracks were observed throughout the sample cross-section. Relative density of the sample was measured as  $99.98 \pm 0.01\%$  via optical image analysis.

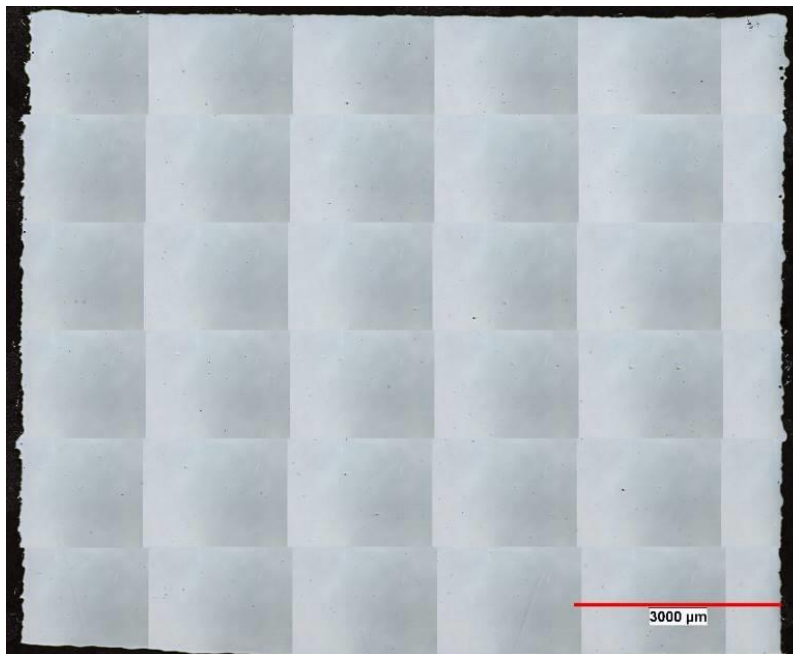


Figure 3. 3. Optical micrograph of as polished cross-section of the LPBF fabricated sample.

Figure 3.4 shows the EBSD orientation maps and pole figures taken from the cross-section imaged in Figure 3.3. The pole figures in Figure 3.4 revealed a cube texture. Grain boundaries were denoted with black lines in the orientation maps (for misorientation  $> 15^\circ$ ). The EBSD orientation map of Figure 3.5 shows columnar  $\gamma$  grains parallel to the build direction across several layers. In the present case, the substrate acted as a heat sink and created a large heat flux parallel to the build direction causing grains to grow along the direction of highest thermal gradient [23,37]. The grains in the new deposited layer grow on the same crystallographic orientation with the  $\gamma$  grains in the previous layers due to epitaxial solidification. Partial re-melting of the previous layers in LPBF process facilitates the grain growth from an existing grain, which acts as a nuclei for crystal growth in the same orientation [38,39]. Longitudinal axis of the grains is oriented along  $\langle 100 \rangle$  direction. This preferential growth was also reported by other researchers for different Ni-based superalloys processed by LPBF [25,38] and for cubic crystals as the  $\langle 100 \rangle$  direction is known as the preferred growth direction [40].

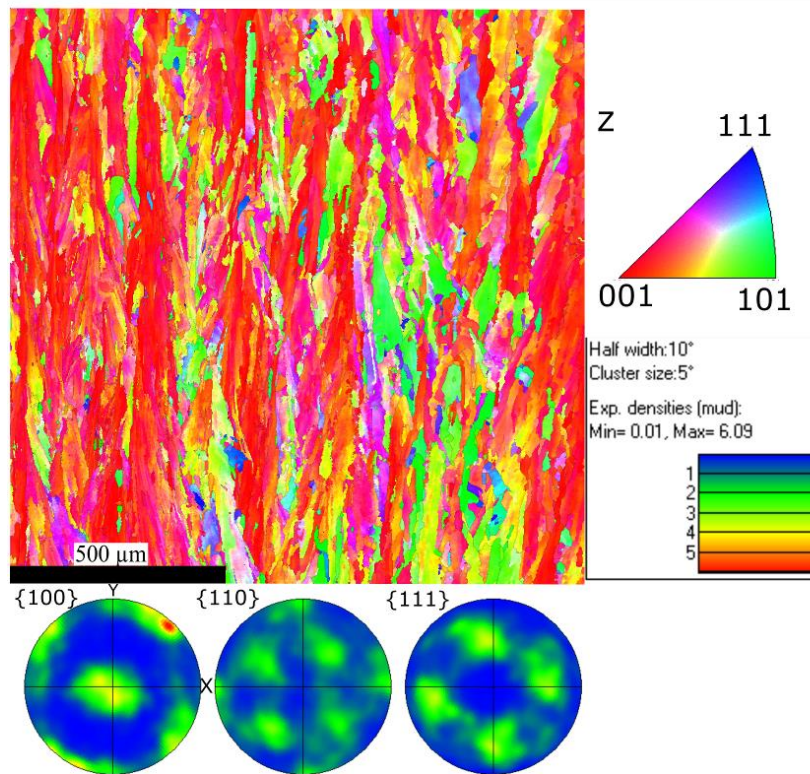


Figure 3. 4. EBSD analysis of the as fabricated R41 parts.

Microstructure of the as fabricated R41 samples were investigated under SEM after etching and a representative micrograph is shown in Figure 3.5. Molten pool boundaries were clearly visible in the as fabricated state. SEM micrograph in Figure 3.5 also shows the dendritic sub-grain morphology with extremely small secondary arms. The dendritic structure grows perpendicular to the melt pool boundaries which is also the direction of highest temperature gradient. Formation of this columnar dendritic microstructure during LPBF fabricated was reported before for various Ni-based superalloys such as IN738 [41], IN718 [42]. Size and morphology of the microstructure formed during solidification is controlled by the interaction of two main parameters at solidification front interface: the growth rate  $R$  (mm/s) and the temperature gradient  $G$  (K/mm). A lower  $G/R$  ratio favors equiaxed dendrite growth while it shifts to the columnar morphology with higher values of  $G/R$  [42]. Typical values for  $G$  and  $R$  were reported as  $10^6$  K/m and 0.4 m/s respectively for solidification conditions in laser surface treatment which usually leads to columnar grain growth [43–45]. These solidification conditions are similar to the ones reported for LPBF. Therefore, high thermal gradient encountered during LPBF process leads to the formation of columnar dendritic microstructure with undergrown secondary dendrite arms [46].

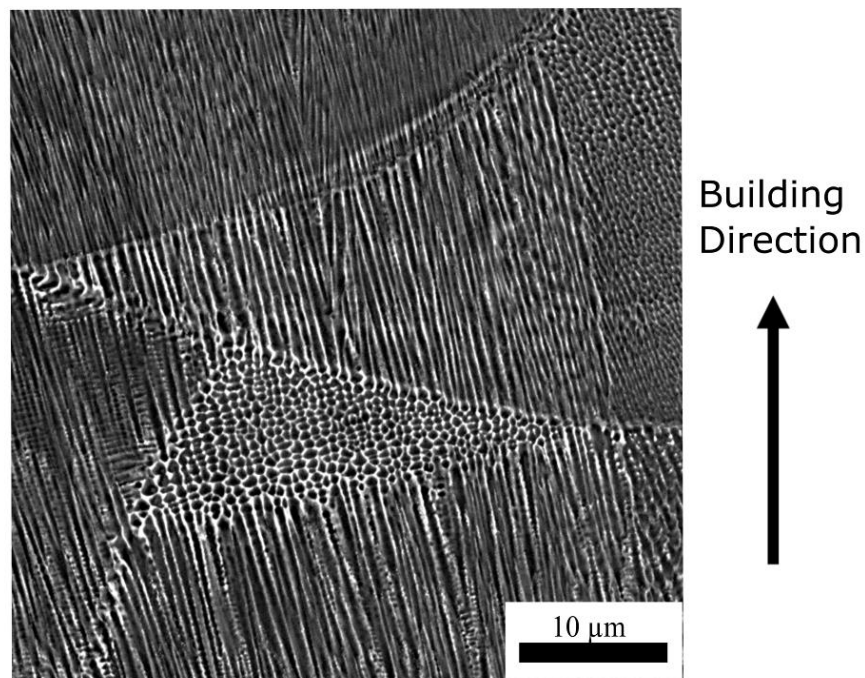


Figure 3. 5. SEM micrograph of the R41 parts fabricated by LPBF.

Average PDAS was measured as  $0.51 \pm 0.17 \mu\text{m}$  and corresponding cooling rate was calculated using Equation 3.1, where  $\varepsilon$  represents the cooling rate,  $a$  and  $b$  are the material constants. Specifically, for Ni-based superalloys  $a = 50 \mu\text{m}(\text{K/s})$  and  $b = 1/3$  [47].

$$PDAS = a\varepsilon^{-b} \quad (3.1)$$

Solidification rates observed in AM are generally in the order of  $10^5$ -  $10^6 \text{C}^\circ/\text{s}$  [21,47]. Obtained PDAS value for LPBF manufactured R41 corresponds to a cooling rate of  $9.7 \times 10^5 \text{K/s}$ . Similar values for primary dendrite arm spacing were previously reported for IN625 [47] and HX [22,23] when processed by LPBF. PDAS values reported for R41 processed by laser melt deposition (LMD) was approximately 35 microns which is two orders of magnitude larger than the present study [9]. Size of the microstructural features are determined by the cooling rate during solidification [1,28,30]. Finer microstructural features achieved in LPBF process can be explained by the higher cooling rates obtained due to much smaller laser beam diameter and thinner layer thickness compared to LMD [48].

Presence of  $\gamma'$  precipitates was not observable in as-built samples under SEM. TEM analysis were conducted to further investigate the possibility of  $\gamma'$  precipitation during solidification and following thermal gyrations. Bright field (BF) TEM micrograph collected from an area containing several cells is presented in Figure 3.6 with the corresponding selected area electron diffraction (SAED) pattern in the insert. No  $\gamma'$  precipitates were detected in the BF-TEM micrograph in the as-built sample. This is further supported by the SAED pattern along [210] zone axis shown in the insert. Indexing of the diffraction patterns solely demonstrate the presence of  $\gamma$  phase with FCC crystal structure. Time temperature cracking diagram for a mill annealed R41 alloy shows that critical cooling rate for precipitation of  $\gamma'$  phase is approximately 3 K/s which is 5 orders of magnitude slower compared to the cooling rate obtained in LPBF [32]. These results show that due to high cooling rates encountered in LPBF,  $\gamma'$  precipitation was inhibited during solidification or further thermal cycling.

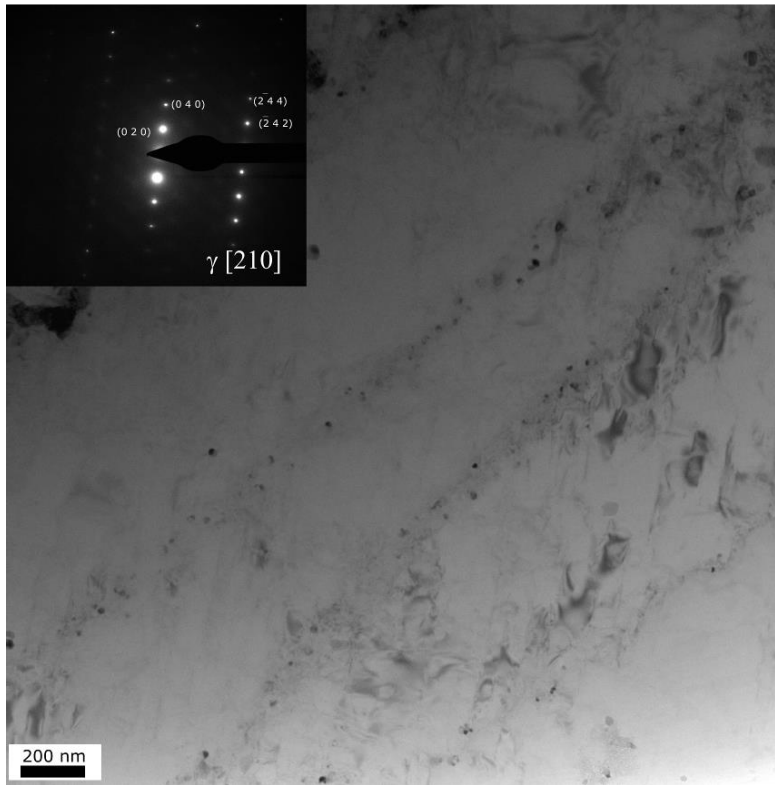


Figure 3. 6. BF TEM image and corresponding SAED pattern of the as-fabricated samples.

### 3.4.3 Microstructural Characterization of the Heat-Treated Samples

In the welding literature R41 was reported as a strain age cracking alloy during post weld heat treatment when improper heating rate is used [11,49]. In the current study, cracking was not observed in the samples after heat treatment and is attributed to the fine microstructural features obtained from LPBF process. Average diameter of the columnar grains was measured as  $12.3 \pm 11.0 \mu\text{m}$  in the as fabricated condition and  $14.2 \pm 12.3 \mu\text{m}$  after the heat treatment which corresponds to ASTM grain size #9.5 and #9 respectively. Parts with finer grain size are known to have higher resistance to strain age cracking during welding compared to the ones with coarser grains [1]. It is reported that R41 sheets having ASTM grain size #7 has higher strain age cracking resistance compared to the ones having ASTM grain size #1 [50].

SEM analysis was conducted on the samples after the precipitation hardening and micrographs are presented in Figure 3.7. Melt pool boundaries observed in the as fabricated condition in Figure 3.5 disappeared during the heat treatment cycle. The columnar grain structure was still visible in the SEM micrograph. EBSD analysis of the heat-treated samples also supports that the columnar grain

structure was maintained as shown in Figure 3.8. EBSD orientation maps shows that  $\gamma$  grains are still mostly oriented along the  $\langle 100 \rangle$  direction and the cube texture is maintained as shown in the pole figures presented in Figure 3.8. Peak intensity of the texture was 5.2 multiples of uniform density (MUD). This value was 6.1 MUD for the as-fabricated samples. Although the texture was maintained after the heat treatment it is found to be slightly weaker compared to the as-fabricated state.

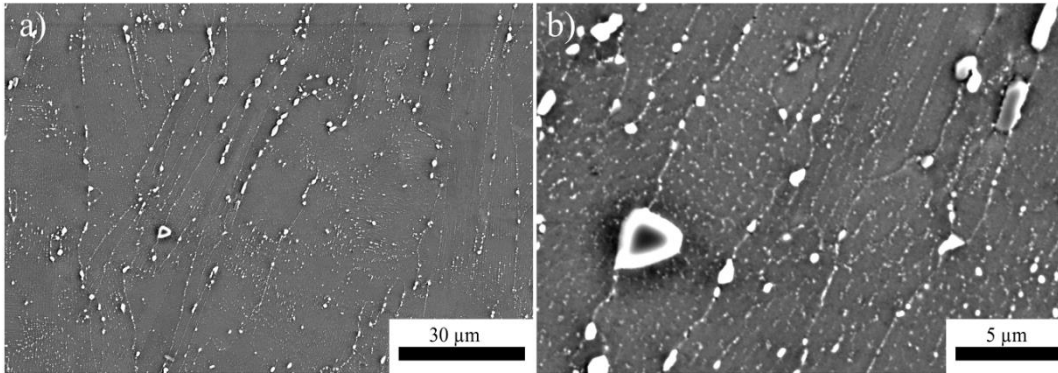


Figure 3. 7. (a) Lower magnification (b) higher magnification SEM image of the R41 parts after heat treatment.

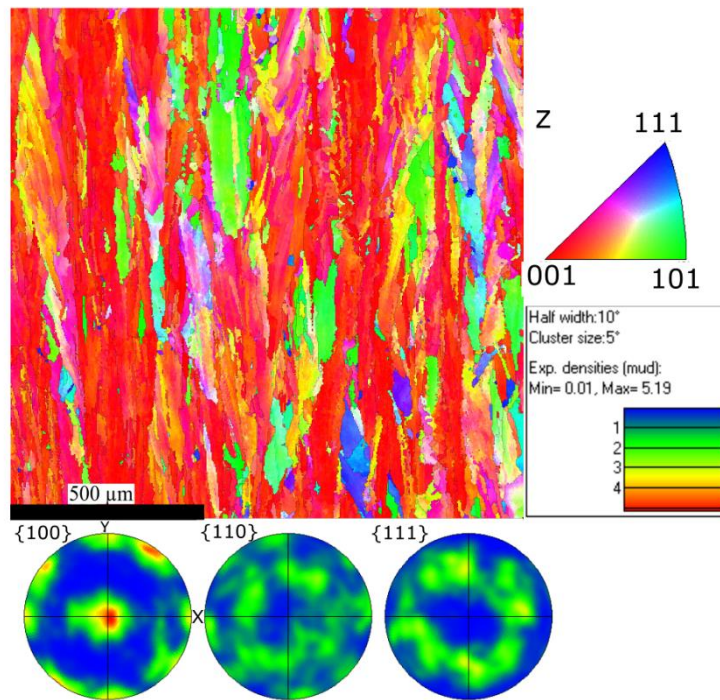


Figure 3. 8. EBSD analysis of the heat-treated R41 parts.

Although the grain structure and texture were maintained, heat treatment cycle resulted in the formation and growth of precipitates both at the grain and cell boundaries as depicted in Figure 3.7(b). The size of the precipitates that are located at the grain boundaries were measured as 0.5-2.5  $\mu\text{m}$ . EDS elemental maps were acquired from an area covering couple of cells to understand the elemental distribution of these phases formed after heat treatment. Elemental maps in Figure 3.9 shows that these precipitates are rich in Mo and Co. Whereas, local enrichment in Al and Ti is observed within the intercellular region suggesting formation of  $\gamma'$  precipitates in these regions. Due to its low segregation coefficient, Mo segregates in the inter-dendritic region during solidification [1,8]. Li et al. reported the presence of MC type carbides in the as deposited R41 samples [9]. MC carbides, which are rich in Mo and Ti, known to be stable at lower temperatures and they transform into secondary carbides  $\text{M}_{23}\text{C}_6$  and/or  $\text{M}_6\text{C}$  at higher temperatures [51]. Among these secondary carbides  $\text{M}_{23}\text{C}_6$  is rich in Cr whereas  $\text{M}_6\text{C}$  type carbides are rich in Mo and Co. Presence of  $\text{M}_{23}\text{C}_6$  and  $\text{M}_6\text{C}$  type secondary carbides were reported for R41 exhaust nozzle flap samples after post weld heat treatment [11]. Therefore, it can be said that enrichment of Mo and Co observed in the elemental analysis of the cell boundary precipitates suggests presence of  $\text{M}_6\text{C}$  carbides.

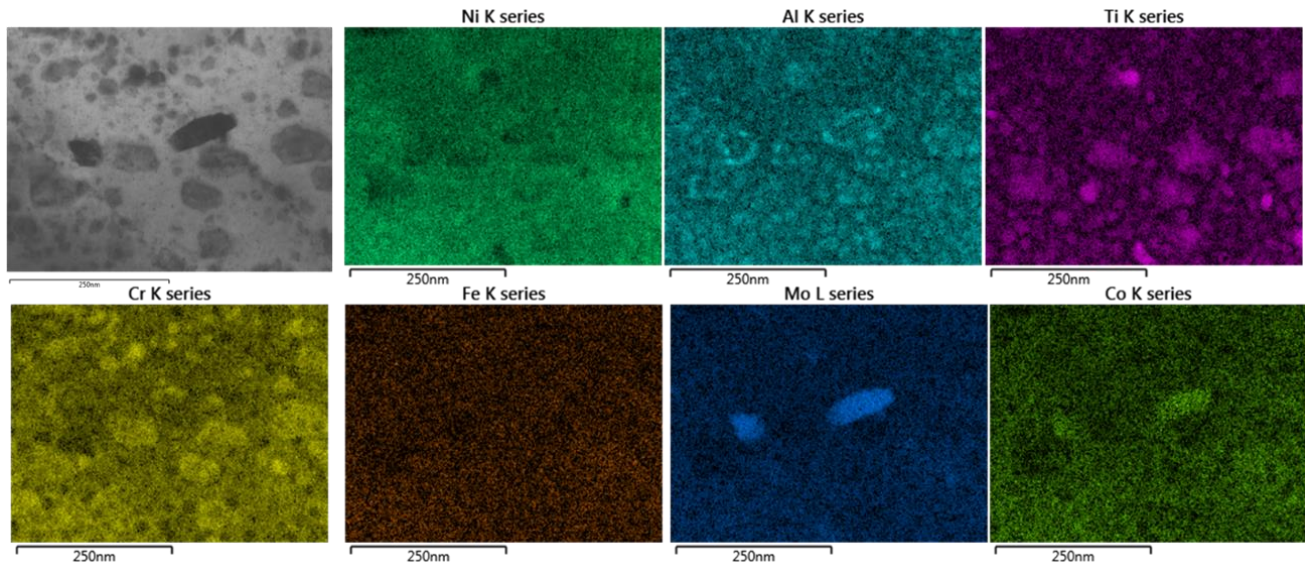


Figure 3. 9. EDS elemental maps of R41 after heat treatment.

TEM analyses were conducted on the heat-treated samples for further characterization of the precipitation evolution. Figure 3.10 shows a BF-TEM image taken from an area covering couple of cells. Homogeneously distributed small precipitates in the intercellular region are clearly visible along with the larger precipitates at the cell boundaries. The size of carbide particles at the cell boundaries were measured as 100-300 nm which is relatively smaller compared to the ones at the grain boundaries. Indexing of the SAED collected from the cell boundary precipitates in Figure 3.10(c) along [100] zone axis show that these discrete particles have  $E9_3$  crystal structure of  $M_6C$  carbides which is in consistence with the elemental analysis in Figure 3.9. Therefore, both compositional and crystallographic analysis proves that  $M_6C$  carbides forms at the cell boundaries after solutionizing and aging heat treatment.

Small precipitates observed in the intercellular area were also observed in more detail. Higher magnification micrographs were collected from those regions and shown in Figure 3.10(b). SAED pattern were also collected from these precipitates and the results are also shown as an inset figure in Figure 3.10(a). The diffraction pattern along [100] zone axis shows the presence of  $L_{12}$  crystal structure of  $\gamma'$  precipitates. Proving that Al and Ti enrichment observed in the EDS maps are due to presence of  $\gamma'$  particles in the intercellular region. Hence,  $\gamma'$  precipitation is observed during heat treatment. The size of this  $\gamma'$  precipitates found to be ranging between 8-30 nm. The  $\gamma'$  precipitates obtained in this study is significantly smaller and their size distribution is narrower compared to the reported values in the literature for different superalloys. Divya et. al. reported that for LPBF manufactured CM247LC alloy after heat treatment  $\gamma'$  sizes were ranging between 50-500 nm [24,52] while a value of  $486 \pm 28$  nm was reported for IN738 alloy [26]. The volume fraction of the  $\gamma'$  precipitates was measured as  $32.5 \pm 7$  % by image analysis. The volume fraction of the precipitates measured in this study is statistically similar to the reported equilibrium volume fraction of 27% [53].

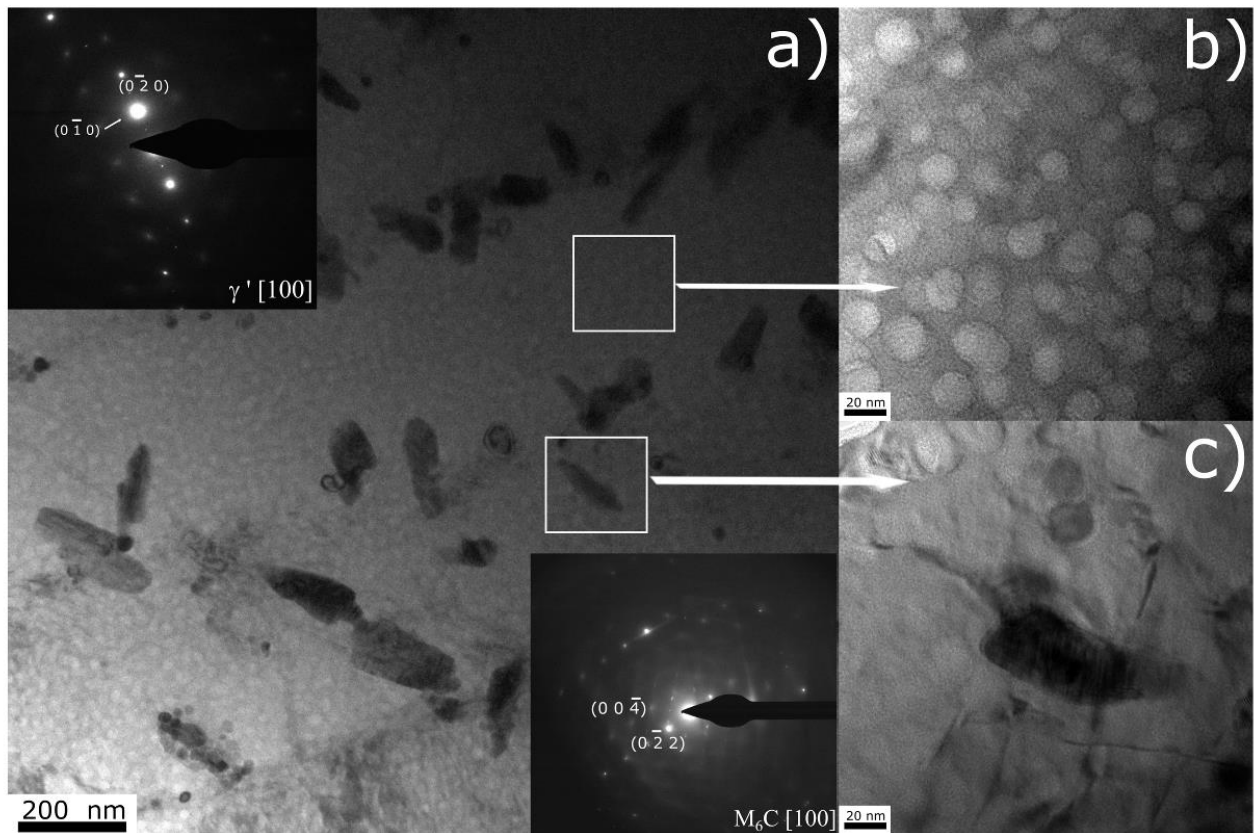


Figure 3. 10. BF TEM images of (a) the heat-treated sample and SAED patterns of (b)  $\gamma'$  precipitates in the intercellular area and (c)  $M_6C$  carbides on cell boundaries.

### 3.4.4. Mechanical Properties

Hardness and room temperature tensile properties of the samples were measured both in as build and heat-treated conditions. Summary of the LPBF mechanical properties along with the mechanical properties reported in literature for different processing conditions are given in Table 3.2. An average hardness value of  $347 \pm 10$  HV was measured for the as built sample in X direction and this value was increased 58% after solutionizing and aging heat treatment. Obtained hardness value after the heat treatment was significantly higher compared to the as fabricated state and found to be well above the typical range for a heat-treated wrought alloy [54].

Figure 3.11 shows tensile stress and elongation of the LPBF fabricated parts in as fabricated and heat-treated state. The curves are superimposed implying that mechanical properties are consistent within the batch of samples tested. A significant increase in strength and a decrease in elongation is observed after the heat treatment for both X and Z build directions. Moreover, one can also see

that as fabricated samples undergone necking after reaching ultimate tensile strength (UTS), while heat-treated samples fractured after strain hardening independent of the building direction. As depicted in Table 3.2 room temperature yield strength (YS) and UTS values in the as built samples were  $857 \pm 3$  MPa and  $1165 \pm 6$  MPa for the horizontal samples,  $729 \pm 14$  MPa and  $1040 \pm 12$  MPa for the vertical samples. When room temperature strength values are compared for different building directions in the as fabricated state, it is observed that obtained YS and UTS values samples build along Z direction are about 128 MPa and 125 MPa lower respectively compared to the samples build along X direction. This difference can be explained by the presence of molten pool boundaries perpendicular to the deformation direction in the vertical samples. YS and UTS values for the heat-treated parts were measured as  $1263 \pm 25$  MPa and  $1580 \pm 12$  MPa for horizontal samples,  $1163 \pm 38$  MPa and  $1480 \pm 27$  MPa for the vertical samples. Heat treatment resulted a significant increase in both YS and UTS independent of the build direction of the sample. This increase can be correlated with the precipitation of  $\gamma'$  during the heat treatment. Both YS and UTS values of horizontal samples are about 100 MPa higher compared to vertical ones after the heat treatment. It is shown in Figure 3.7 that molten pool boundaries dissolved during the heat treatment, which can explain the decrease in the anisotropy in the mechanical properties.

Measured elongation at fracture was 41% for samples build along Z direction and 24% for samples build along X direction in the as fabricated parts. The anisotropy in the elongation can be associated with columnar grain structure of the samples. Ductility of the vertical samples is 16% higher compared to the horizontal ones, due to lower number of grain boundaries perpendicular to the loading direction. The elongation value dropped to 14% and 11% for horizontal and vertical samples respectively after heat treatment. This reduction can be correlated with the significant increase in the tensile strength of the parts. Introduction of brittle  $\gamma'$  precipitates into  $\gamma$  matrix resulted the decrease in the ductility of the as fabricated parts. YS and UTS values for a wrought R41 alloy after the same heat treatment cycle was applied was reported as  $1043 \pm 27$  MPa and  $1270 \pm 27$  MPa in the specifications [54]. It is shown that LPBF manufactured R41 alloy has higher YS and UTS compared to a wrought part after the same heat treatment cycle. Although the strength value is considerably higher, elongation of the heat-treated parts is still comparable to the wrought and heat-treated parts. Li et.al. reported that the standard heat treatment suggested for wrought R41 alloy has failed to meet the minimum allowable specifications in terms of strength and

elongation in LMD parts due to coalescence of  $\gamma'$  precipitates and subsequent loss of coherency between  $\gamma$ - $\gamma'$  [29]. However, in the case of LPBF obtained results are well above the specifications. Mechanical properties after heat treatment are highly dependent on the formation of carbides and/or  $\gamma'$  phase along with the size, distribution and morphology of these phases [1]. Carbides can be both detrimental or beneficial in terms of mechanical properties. Fine discrete carbide particles found to improve strength by acting as a barrier for dislocation motion while a continuous film of carbides found to have the opposite effect since, they act as a crack initiation site and a crack propagation path [51]. Formation of  $M_6C$  carbides were observed both in the cell boundaries and grain boundaries, with a size ranging between 100 nm to 2.5  $\mu\text{m}$ , as discrete particles. Hence, they can act as a grain boundary strengthener by preventing grain boundary sliding. R41 is a precipitation strengthened alloy and precipitation of  $\gamma'$  is the main mechanism of strengthening for this alloy. During deformation at room temperature,  $\gamma'$  shearing dislocations was reported as the main strengthening mechanism [1,55]. Therefore, formation of extremely fine homogeneously distributed  $\gamma'$  precipitates is the main reason for achieving room temperature tensile properties well above the specifications.

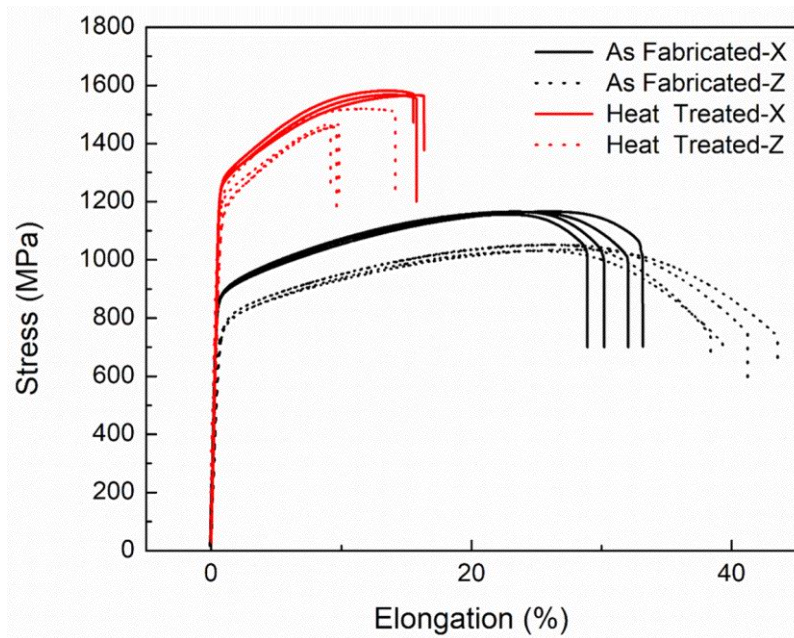


Figure 3. 11. Tensile stress strain diagram of R41 alloy in as fabricated and heat-treated condition.

Table 3.2. Summary of the mechanical properties of R41 alloy for different processing conditions.

Condition	0.2%YS (MPa)	UTS (MPa)	Elongation (%)	Hardness (HV)
<b>LPBF-X</b>	857 ± 3	1165 ± 6	24 ± 2	347 ± 10
<b>LPBF + HT-X</b>	1263 ± 25	1580 ± 12	14 ± 4	548 ± 19
<b>LPBF-Z</b>	729 ± 14	1040 ± 12	41 ± 2	-
<b>LPBF + HT-Z</b>	1163 ± 38	1480 ± 27	11 ± 2	-
<b>Wrought +HT [49]</b>	1043 ± 27	1270 ± 27	13 ± 2	380 - 460

Figure 3.12 shows the fracture surfaces of the LPBF manufactured R41 bars after tensile fracture in the as fabricated and heat-treated conditions. No porosity or any other defects such as un-melted powder or lack of fusion porosity is observed on the fracture surfaces of both samples. Heat treated samples fractured without neck formation while necking was observed for the as fabricated samples, proving that as fabricated samples undergone more plastic deformation before fracture. These observations are also in good correlation with the stress-strain data in Figure 3.11. Low magnification SEM micrographs in Figure 3.12(a) and (b) show that heat treated samples have a relatively flat fracture surface compared to the as fabricated ones. In this sample crack propagation follows the grain boundaries resulting formation of this flat fracture surface. In higher magnification observations in Figure 3.12(c) and (d) dimples are observed for both conditions suggesting the fracture occurred in a ductile manner. Size of the dimples were measured as  $0.4 \pm 0.1 \mu\text{m}$  from the fracture surface of both samples. This value is matching with the measured PDAS thus, dimples are thought to be originating from fracture of individual dendrites. The high magnification SEM image in Figure 3.12(d) shows presence of micro-voids with size of  $1.4 \pm 0.5 \mu\text{m}$  at grain boundaries. Size of these micro-voids are similar to the size of grain boundary carbide particles observed in Figure 3.7. Therefore, it can be said that cracks are initiated from the large carbide particles at the grain boundaries in the heat-treated samples. Measured elongation of the tensile samples was decreased from 24% to 14 % after heat treatment. Therefore, information obtained from the fracture surfaces are in consistence with the room temperature tensile tests.

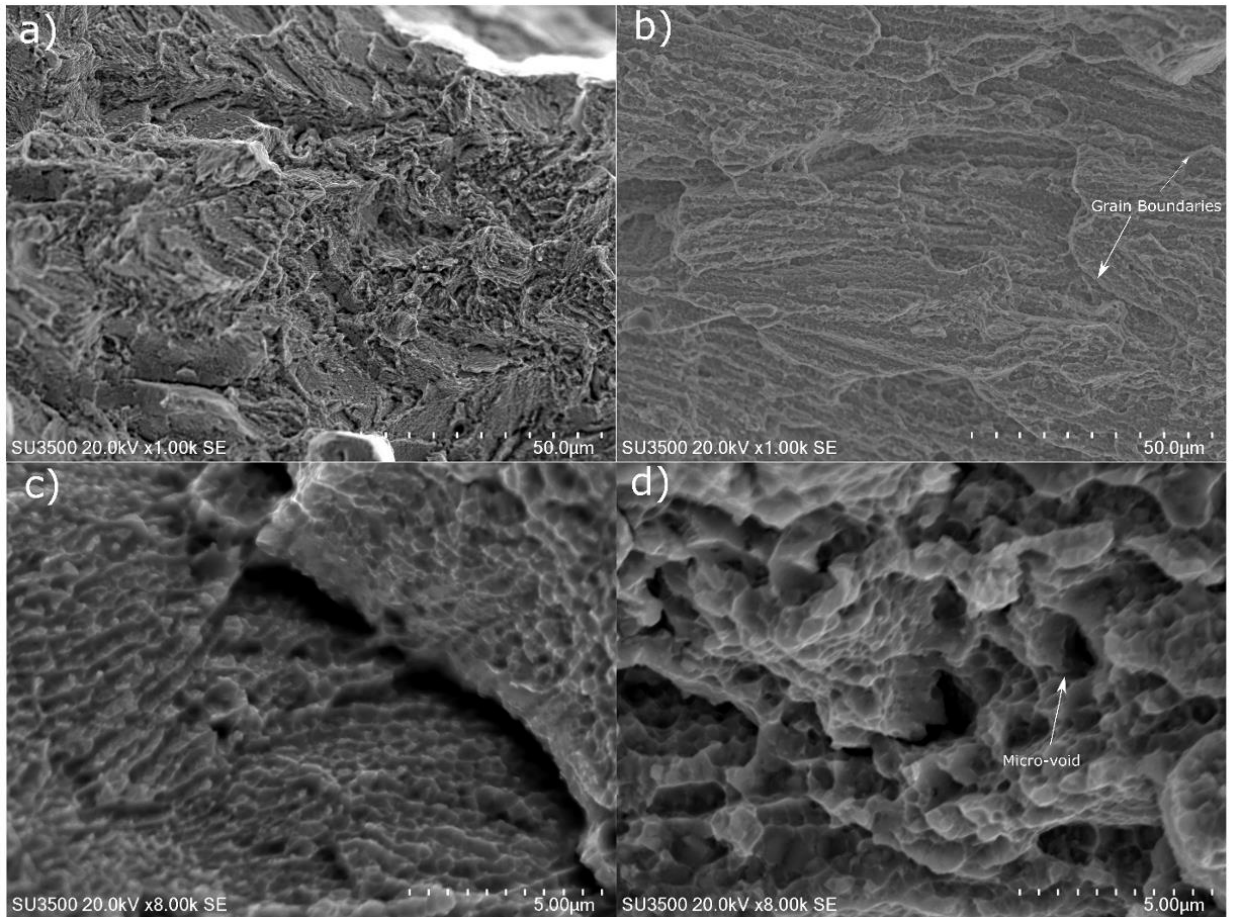


Figure 3. 12. Tensile fracture surface of (a), (c) as fabricated (b), (d) heat treated R41 samples.

### 3.5. Conclusion

In this study, high density crack free R41 parts were fabricated via LPBF for the first time in literature. Microstructure and room temperature mechanical properties were investigated in as fabricated state and after subsequent heat treatment. SEM and EBSD analysis revealed presence of fine columnar dendritic microstructure with a preferred orientation of  $\langle 100 \rangle$ . Formation of  $\gamma'$  precipitates were not observed under TEM in the as fabricated state. Crack free structure and columnar grain morphology along the build direction were sustained after the heat treatment. Formation of distinct Mo-enriched carbide particles were observed at the grain and cell boundaries along with the precipitation of extremely fine and homogeneously distributed  $\gamma'$  precipitates after the heat treatment. Size of  $\gamma'$  precipitates were measured as 8-30 nm which is considerably smaller compared to the values reported in literature. Room temperature yield and ultimate tensile strength

values measured for the samples build horizontally were found to be ~100 MPa higher compared to the samples build vertically. Presence of the molten pool boundaries perpendicular to the loading direction caused this slight reduction in tensile properties for the vertical samples. Elongation of the vertical samples found to be 15 percent higher compared to horizontal ones due to the orientation of columnar grains parallel to the building direction. Significant increase in room temperature yield and tensile strengths was observed due to precipitation of  $\gamma'$  after solutionizing and aging heat treatment for both building directions. Obtained tensile properties after heat treatment were well above the specification for a wrought alloy. Although precipitation of  $\gamma'$  resulted a reduction in the elongation of the heat-treated samples caused by the strengthening of the matrix, the measured elongation values still meet the standards. Therefore, it can be concluded that standard heat treatment suggested for wrought R41 alloy is sufficient to obtain room temperature strength and elongation properties that meets the specifications for an LPBF fabricated R41 part. Although, measured elongation value after heat treatment was lower compared to the as fabricated state, fractography analysis revealed tensile fracture occurred in a ductile manner for both conditions.

### **3.6. Acknowledgement**

The authors would like to thank the generous research support by the Natural Sciences and Engineering Research Council (NSERC) of Canada (NSERC Project Number: NETGP 494158 – 16). The authors would also like to acknowledge McGill Engineering Doctoral Award (MEDA) granted to Ms. Atabay. We also thank Nicolas Brodusch in Mining and Materials Engineering Department and David Liu at the Facility for Electron Microscopy Research of McGill University for help in microscope operation and data collection.

### **3.7. References**

- [1] J.N.D.& J. C.Lippold, Welding Metallurgy and Weldability of Nickel-Base Alloys, J. Chem. Inf. Model. 53 (2009) 456. doi:10.1017/CBO9781107415324.004.
- [2] K. Chen, J. Dong, Z. Yao, T. Ni, M. Wang, Creep performance and damage mechanism for Allvac 718Plus superalloy, Mater. Sci. Eng. A. 738 (2018) 308–322. doi:10.1016/J.MSEA.2018.09.088.

- [3] H. Zhang, C. Li, Y. Liu, Q. Guo, Y. Huang, H. Li, J. Yu, Effect of hot deformation on  $\gamma''$  and  $\delta$  phase precipitation of Inconel 718 alloy during deformation&isothermal treatment, *J. Alloys Compd.* 716 (2017) 65–72. doi:10.1016/J.JALLCOM.2017.05.042.
- [4] S. Crump, Discontinuous Grain Boundaries of Forged René 41 Approval Page, (2012).
- [5] M. Schwartz, R. Ciocoiu, D. Gheorghe, G. Jula, I. Ciucă, Preliminary research for using Rene 41 in confectioning extrusion dies, 90 (2015) 95–106. doi:10.2495/MC150091.
- [6] Q. Li, S. Tian, H. Yu, N. Tian, Y. Su, Y. Li, Effects of carbides and its evolution on creep properties of a directionally solidified nickel-based superalloy, *Mater. Sci. Eng. A.* 633 (2015) 20–27. doi:10.1016/j.msea.2015.02.056.
- [7] B. Seiser, R. Drautz, D.G. Pettifor, TCP phase predictions in Ni-based superalloys: Structure maps revisited, *Acta Mater.* 59 (2011) 749–763. doi:10.1016/j.actamat.2010.10.013.
- [8] Q.L. Pan, B. Li, Y. Wang, Y.W. Zhang, Z.M. Yin, Characterization of hot deformation behavior of Ni-base superalloy Rene’41 using processing map, *Mater. Sci. Eng. A.* 585 (2013) 371–378. doi:10.1016/j.msea.2013.07.066.
- [9] J. Li, H.M. Wang, Microstructure and mechanical properties of rapid directionally solidified Ni-base superalloy Rene’41 by laser melting deposition manufacturing, *Mater. Sci. Eng. A.* 527 (2010) 4823–4829. doi:10.1016/j.msea.2010.04.062.
- [10] M.M. Attallah, R. Jennings, X. Wang, L.N. Carter, Additive manufacturing of Ni-based superalloys: The outstanding issues, *MRS Bull.* 41 (2016) 758–764. doi:10.1557/mrs.2016.211.
- [11] R. Kayacan, R. Varol, O. Kimilli, The effects of pre- and post-weld heat treatment variables on the strain-age cracking in welded Rene 41 components, *Mater. Res. Bull.* 39 (2004) 2171–2186. doi:10.1016/j.materresbull.2004.08.003.
- [12] D. Herzog, V. Seyda, E. Wycisk, C. Emmelmann, Additive manufacturing of metals, *Acta Mater.* 117 (2016) 371–392. doi:10.1016/j.actamat.2016.07.019.
- [13] W.E. Frazier, Metal additive manufacturing: A review, *J. Mater. Eng. Perform.* 23 (2014) 1917–1928. doi:10.1007/s11665-014-0958-z.
- [14] Y. Ding, M. Trask, S. Chou, A. Walker, M. Brochu, Microstructure and mechanical property considerations in additive manufacturing of aluminum alloys, (2017) 745–751. doi:10.1557/mrs.2016.214.

- [15] A. Nesma, Additive manufacture of an aluminium alloy : processing , microstructure , and mechanical properties., (2016) 293.
- [16] L.N. Carter, M.M. Attallah, R.C. Reed, Laser powder bed fabrication of nickel-base superalloys: influence of parameters; characterisation, quantification and mitigation of cracking, Proc. 12th Int. Symp. Superalloys, Champion, PA, 9–13 Sept. 2012. (2012) 577–586.
- [17] W.E. King, A.T. Anderson, R.M. Ferencz, N.E. Hodge, C. Kamath, S.A. Khairallah, A. Rubenchik, Laser powder bed fusion additive manufacturing of metals; physics, computational, and materials challenges, Appl. Phys. Rev. 2 (2015). doi:10.1063/1.4937809.
- [18] Y. Gao, D. Zhang, M. Cao, R. Chen, Z. Feng, R. Poprawe, J.H. Schleifenbaum, S. Ziegler, Effect of  $\delta$  phase on high temperature mechanical performances of Inconel 718 fabricated with SLM process, Mater. Sci. Eng. A. 767 (2019) 138327. doi:10.1016/J.MSEA.2019.138327.
- [19] H.E. Helmer, C. Körner, R.F. Singer, Additive manufacturing of nickel-based superalloy Inconel 718 by selective electron beam melting: Processing window and microstructure, J. Mater. Res. 29 (2014) 1987–1996. doi:10.1557/jmr.2014.192.
- [20] Y. Tian, J.A. Muñoz-Lerma, M. Brochu, Nickel-based superalloy microstructure obtained by pulsed laser powder bed fusion, Mater. Charact. 131 (2017) 306–315. doi:10.1016/j.matchar.2017.07.024.
- [21] F. Zhang, L.E. Levine, A.J. Allen, M.R. Stoudt, G. Lindwall, E.A. Lass, M.E. Williams, Y. Idell, C.E. Campbell, Effect of heat treatment on the microstructural evolution of a nickel-based superalloy additive-manufactured by laser powder bed fusion, Acta Mater. 152 (2018) 200–214. doi:10.1016/j.actamat.2018.03.017.
- [22] O. Sanchez-Mata, X. Wang, J.A. Muñoz-Lerma, M. Attarian Shandiz, R. Gauvin, M. Brochu, Fabrication of Crack-Free Nickel-Based Superalloy Considered Non-Weldable during Laser Powder Bed Fusion, Materials (Basel). 11 (2018). doi:10.3390/ma11081288.
- [23] N.J. Harrison, I. Todd, K. Mumtaz, Reduction of micro-cracking in nickel superalloys processed by Selective Laser Melting: A fundamental alloy design approach, Acta Mater. 94 (2015) 59–68. doi:10.1016/j.actamat.2015.04.035.
- [24] V.D. Divya, R. Muñoz-Moreno, O.M.D.M. Messé, J.S. Barnard, S. Baker, T. Illston, H.J.

- Stone, Microstructure of selective laser melted CM247LC nickel-based superalloy and its evolution through heat treatment, *Mater. Charact.* 114 (2016) 62–74. doi:10.1016/j.matchar.2016.02.004.
- [25] X. Wang, L.N. Carter, B. Pang, M.M. Attallah, M.H. Loretto, Microstructure and yield strength of SLM-fabricated CM247LC Ni-Superalloy, *Acta Mater.* 128 (2017) 87–95. doi:10.1016/j.actamat.2017.02.007.
- [26] J.A. Muñiz-Lerma, Y. Tian, X. Wang, R. Gauvin, M. Brochu, Microstructure evolution of Inconel 738 fabricated by pulsed laser powder bed fusion, *Prog. Addit. Manuf.* (2018). doi:10.1007/s40964-018-0062-2.
- [27] F. Geiger, K. Kunze, T. Etter, Tailoring the texture of IN738LC processed by selective laser melting (SLM) by specific scanning strategies, *Mater. Sci. Eng. A.* 661 (2016) 240–246. doi:10.1016/j.msea.2016.03.036.
- [28] T. DebRoy, H.L. Wei, J.S. Zuback, T. Mukherjee, J.W. Elmer, J.O. Milewski, A.M. Beese, A. Wilson-Heid, A. De, W. Zhang, Additive manufacturing of metallic components – Process, structure and properties, *Prog. Mater. Sci.* 92 (2018) 112–224. doi:10.1016/j.pmatsci.2017.10.001.
- [29] J. Li, H.M. Wang, H.B. Tang, Effect of heat treatment on microstructure and mechanical properties of laser melting deposited Ni-base superalloy Rene’41, *Mater. Sci. Eng. A.* 550 (2012) 97–102. doi:10.1016/j.msea.2012.04.037.
- [30] A. Formenti, A. Eliasson, H. Fredriksson, On the dendritic growth and microsegregation in Ni-base superalloys In718, In625 and In939, *High Temp. Mater. Process.* 24 (2005) 221–238. doi:10.1515/HTMP.2005.24.4.221.
- [31] B.S. Yilbas, Characterization of laser-treated Rene 41 surface due to B<sub>4</sub>C and SiC particles at surface prior to laser treatment, *Surf. Interface Anal.* 46 (2014) 30–35. doi:10.1002/sia.5342.
- [32] H. Chandler, *Heat Treater’s Guide: Practices and Procedures for Nonferrous Alloys*, ASM International, 1996. [https://books.google.ca/books?id=\\_iUd4RskarMC](https://books.google.ca/books?id=_iUd4RskarMC).
- [33] C.A. Schneider, W.S. Rasband, K.W. Eliceiri, NIH Image to ImageJ: 25 years of image analysis, *Nat. Methods.* 9 (2012) 671–675. doi:10.1038/nmeth.2089.
- [34] A. Gros, M. Hartung, T. Kirsten, E. Rahm, GOMMA results for OAEI 2012, *CEUR Workshop Proc.* 946 (2012) 133–140. doi:10.1520/E0008.

- [35] J. Van Humbeeck, G. Lumay, J. Schrooten, G. Yablokova, F. Boschini, R. Cloots, J. Luyten, M. Speirs, J.-P. Kruth, Rheological behavior of  $\beta$ -Ti and NiTi powders produced by atomization for SLM production of open porous orthopedic implants, *Powder Technol.* 283 (2015) 199–209. doi:10.1016/j.powtec.2015.05.015.
- [36] A.B. Spierings, M. Voegtlin, T. Bauer, K. Wegener, Powder flowability characterisation methodology for powder-bed-based metal additive manufacturing, *Prog. Addit. Manuf.* 1 (2016) 9–20. doi:10.1007/s40964-015-0001-4.
- [37] V. Martinez, A.D. Neely, G. Ren, A. Smart, A.I. of M.R. <London>, *High Value Manufacturing*, 2008.
- [38] G.P. Dinda, A.K. Dasgupta, J. Mazumder, Laser aided direct metal deposition of Inconel 625 superalloy: Microstructural evolution and thermal stability, *Mater. Sci. Eng. A.* 509 (2009) 98–104. doi:10.1016/j.msea.2009.01.009.
- [39] A. Basak, S. Das, *Epitaxy and Microstructure Evolution in Metal Additive Manufacturing*, *Annu. Rev. Mater. Res.* 46 (2016) 125–149. doi:10.1146/annurev-matsci-070115-031728.
- [40] L.L. Parimi, R.G. A., D. Clark, M.M. Attallah, Microstructural and texture development in direct laser fabricated IN718, *Mater. Charact.* 89 (2014) 102–111. doi:10.1016/J.MATCHAR.2013.12.012.
- [41] M. Cloots, K. Kunze, P.J. Uggowitzer, K. Wegener, Microstructural characteristics of the nickel-based alloy IN738LC and the cobalt-based alloy Mar-M509 produced by selective laser melting, *Mater. Sci. Eng. A.* 658 (2016) 68–76. doi:10.1016/J.MSEA.2016.01.058.
- [42] N. Nadammal, S. Cabeza, T. Mishurova, T. Thiede, A. Kromm, C. Seyfert, L. Farahbod, C. Haberland, J.A. Schneider, P.D. Portella, G. Bruno, Effect of hatch length on the development of microstructure, texture and residual stresses in selective laser melted superalloy Inconel 718, *Mater. Des.* 134 (2017) 139–150. doi:10.1016/j.matdes.2017.08.049.
- [43] W. Kurz, B. Giovanola, R. Trivedi, Theory of microstructural development during rapid solidification, *Acta Metall.* 34 (1986) 823–830. doi:10.1016/0001-6160(86)90056-8.
- [44] M. Gremaud, M. Carrard, W. Kurz, The microstructure of rapidly solidified Al-Fe alloys subjected to laser surface treatment, *Acta Metall. Mater.* 38 (1990) 2587–2599. doi:10.1016/0956-7151(90)90271-H.
- [45] M. Carrard, M. Gremaud, M. Zimmermann, W. Kurz, About the banded structure in rapidly

- solidified dendritic and eutectic alloys, *Acta Metall. Mater.* 40 (1992) 983–996. doi:10.1016/0956-7151(92)90076-Q.
- [46] H.L. Wei, J. Mazumder, T. DebRoy, Evolution of solidification texture during additive manufacturing, *Sci. Rep.* 5 (2015) 1–7. doi:10.1038/srep16446.
- [47] S. Li, Q. Wei, Y. Shi, Z. Zhu, D. Zhang, Microstructure Characteristics of Inconel 625 Superalloy Manufactured by Selective Laser Melting, *J. Mater. Sci. Technol.* 31 (2015) 946–952. doi:10.1016/J.JMST.2014.09.020.
- [48] V.A. Wills, D.G. McCartney, A comparative study of solidification features in nickel-base superalloys: microstructural evolution and microsegregation, *Mater. Sci. Eng. A.* 145 (1991) 223–232. doi:10.1016/0921-5093(91)90252-I.
- [49] S. Kou, *WELDING METALLURGY*, 2nd Editio, A JOHN WILEY & SONS, INC., 2003.
- [50] S.M. Richard, A Study on the Strain Age Crack Sensitivity of Rene 41, (1968). doi:10.1021/jz3014425.
- [51] S.S. Handa, Precipitation of Carbides in a Ni-based Superalloy, Masters Degree Proj. University (2014) 1–33.
- [52] R. Muñoz-Moreno, V.D. Divya, S.L. Driver, O.M.D.M. Messé, T. Illston, S. Baker, M.A. Carpenter, H.J. Stone, Effect of heat treatment on the microstructure, texture and elastic anisotropy of the nickel-based superalloy CM247LC processed by selective laser melting, *Mater. Sci. Eng. A.* 674 (2016) 529–539. doi:10.1016/j.msea.2016.06.075.
- [53] L.M. Pike, Development of a fabricable gamma-prime ( $\gamma'$ ) strengthened superalloy, *Proc. Int. Symp. Superalloys.* (2008) 191–200. doi:10.7449/2008/superalloys\_2008\_191\_200.
- [54] The Elevated-Temperature Properties of Selected Superalloys, *Elev. Prop. Sel. Superalloys.* (2015). doi:10.1520/ds7s1-eb.
- [55] R. Acharya, S. Das, Additive Manufacturing of IN100 Superalloy Through Scanning Laser Epitaxy for Turbine Engine Hot-Section Component Repair: Process Development, Modeling, Microstructural Characterization, and Process Control, *Metall. Mater. Trans. A Phys. Metall. Mater. Sci.* 46 (2015) 3864–3875. doi:10.1007/s11661-015-2912-6.

## **Chapter 4: Effect of Heat Treatment on the Microstructure and Elevated Temperature Tensile Properties of Rene 41 Alloy Produced by Laser Powder Bed Fusion**

---

The previous chapter discussed the microstructural evolution and room temperature mechanical properties of LPBF fabricated R41 and the effect of standard heat treatment on these properties. The microstructure of the LPBF fabricated sample was significantly different from a wrought sample hence, the standard heat treatment applied to wrought parts resulted in a different microstructure. In this chapter, microstructural modifications of the LPBF fabricated R41 as a function of different heat treatments were investigated. It has proven that it is possible to modify the grain morphology and size and distribution of the  $\gamma'$  precipitates and carbides by modifying the heat treatment. The elevated temperature deformation behaviors for each heat treatment were investigated and related to the microstructure. The knowledge gained in this chapter can be used to design post-processing heat treatment routes for LPBF fabricated Ni-base superalloys for specific elevated temperature properties.

This chapter has been published as: S.E. Atabay, O. Sanchez-Mata, J.A. Muñiz-Lerma, M. Brochu, Effect of heat treatment on the microstructure and elevated temperature tensile properties of Rene 41 alloy produced by laser powder bed fusion, *J. Alloys Compd.* (2020)

## 4.1. Abstract

The microstructure and elevated temperature mechanical properties of a precipitation hardenable Nickel based superalloy, Rene 41, fabricated by laser powder bed fusion followed by two different heat treatment regimes were studied. The as built (AB) microstructure consists of  $\gamma$  columnar grains aligned in  $\langle 100 \rangle$  direction. No  $\gamma'$  precipitates were observed in the AB condition. Following to a sub-solvus solutionizing and aging heat treatment, the AB grain morphology was maintained. The development of fine  $\gamma'$  precipitates within the grains along with the discrete carbide particles on the grain boundaries occurred. Heat treatment above the solvus temperature of  $\gamma'$  resulted in the formation of a random equiaxed grain morphology. The  $\gamma'$  and carbide precipitation was also observed in this heat treatment regime, but their distribution and morphology were different. Uniaxial tensile tests were conducted at 760 °C. Average yield strength values for AB, sub-solvus and super-solvus heat treated alloys were 879, 824 and 855 MPa respectively. The three tested conditions showed similar strength values that are comparable with a wrought alloy at the testing temperature. However, the elongation and deformation behaviors were different for each condition. Sub-solvus heat treatment led to the highest elongation at break with 22% whereas super-solvus heat treatment resulted in the highest work hardening rate during deformation.

## 4.2. Introduction

Laser powder bed fusion (LPBF) is one of the main metal additive manufacturing (AM) processes, which involves localized melting and solidification of a powder bed, according to a defined raster path, in a layer wise manner [1,2]. LPBF process allows the fabrication of complex geometries with reduced material waste, production cost and time. These unique advantages over conventional processing techniques have driven significant research into application of LPBF in many areas such as aero-engine and nuclear components [3,4]. Nickel-based superalloys are prime candidate in such applications due to the unique balance of properties during high temperature service [5,6]. These alloys derive their strength from solid solution strengthening of the  $\gamma$  matrix along with the precipitation of  $\gamma'$  phase within the grains, and from grain boundary carbides [7,8]. Extensive research has been conducted on the structure/mechanical property relationship and suggests that the carbide morphology is important for the creep properties, the size, morphology and distribution of the  $\gamma'$  particles affects the strength significantly, whereas grain size and morphology

have a significant influence on the strength and ductility of the alloy [7,9,10]. Microstructural constituents, distribution and morphology of the different phases in nickel-based superalloys are mainly controlled by heat treatment. Consequently, influence of heat treatment on the mechanical properties has been extensively studied for materials produced by conventional production techniques [11–13]. However, the microstructure of the LPBF fabricated parts have been shown to be significantly different [14].

Columnar grains epitaxially grown along the building direction have been frequently reported for LPBF fabricated parts [15–17]. This grain morphology is similar to that of directionally solidified material. However, the extremely high heating and cooling rates involved during LPBF leads to significantly finer solidification microstructure [18,19]. Additionally, high residual stresses have been observed in Ni-based LPBF constructs due to repetitive heating and cooling cycles [20,21]. Hence, post processing heat treatments are required to relieve the residual stresses and to form the strengthening  $\gamma'$  precipitates. Since the as-built microstructure of the LPBF fabricated parts are significantly different compared to the conventional production techniques, a knowledge gap exists in terms of microstructural response during the heat treatment. Thus, study of the post processing heat treatment of LPBF fabricated parts has significant importance to attain improved elevated temperature mechanical performance.

Rene 41 (R41) is a precipitation hardenable nickel-based superalloy developed during 1950s as a high strength, high temperature material [22,23]. It possesses an excellent combination of corrosion and oxidation resistance, mechanical performance and microstructural stability at temperatures up to 980°C. It has been used mostly in exhaust nozzles in military turbine engines, hot section parts of jet aircraft engines and divergent seal and flap components [24,25]. Despite the good high temperature properties, it has limited usage due to its cracking tendency during production. Strain age cracking in the heat affected zone and/or in the base metal has been commonly reported during welding and post-weld heat treatments [22,26]. Although literature on R41 is mostly focused on conventional fabrication techniques such as welding and forging [22,24,27], crack free fabrication of this alloy by LPBF was previously reported [28]. It was observed that microstructure of the as-fabricated samples consisted of only  $\gamma$  phase. Hence, a post processing heat treatment was required to reach superior mechanical properties through the  $\gamma'$  precipitation. Conventionally a sub-solvus heat treatment is applied to R41 parts which consist of

solutionizing at a temperature below the solvus temperature of the  $\gamma'$  phase followed by an age hardening heat treatment [29]. Although, standard sub-solvus heat treatment yielded good mechanical performance at room temperature for LPBF fabricated R41 bars, a knowledge gap exists governing the relationship between heat treatment and the LPBF microstructure, and the corresponding elevated temperature mechanical properties response.

In this study, microstructure and elevated temperature mechanical properties of LPBF fabricated R41 alloy was investigated in as built, after sub-solvus and super-solvus heat treatments. Development of the grain morphology and texture along with the size, morphology and distribution of carbides and  $\gamma'$  phases has been studied for all three conditions. Mechanical properties under tensile loading at 760°C were tested and correlated with the obtained microstructures as a result of different heat treatment regimes.

### 4.3. Experimental Procedure

Argon gas atomized R41 powder provided by TLS Technik, Germany with a composition shown in Table 4.1 was used in this study. The powder particles were mostly spherical with presence of few satellites and irregularities as shown in Figure 4.1(a). Particle size distribution (PSD) was characterized by LA-920 Horiba laser particle size analyzer and the results are presented in Figure 4.1(b). The  $D_{10}$ ,  $D_{50}$  and  $D_{90}$  were measured as 13, 25 and 43  $\mu\text{m}$ , respectively.

Table 4.1. Chemical composition of the R41 powder according to certificate of conformity of the manufacturer.

Element	Al	Cr	Co	Ti	Fe	Mn	Mo	Si	C	Ni
wt%	1.57	19.00	10.94	3.12	2.96	0.01	9.78	0.02	0.08	Bal.

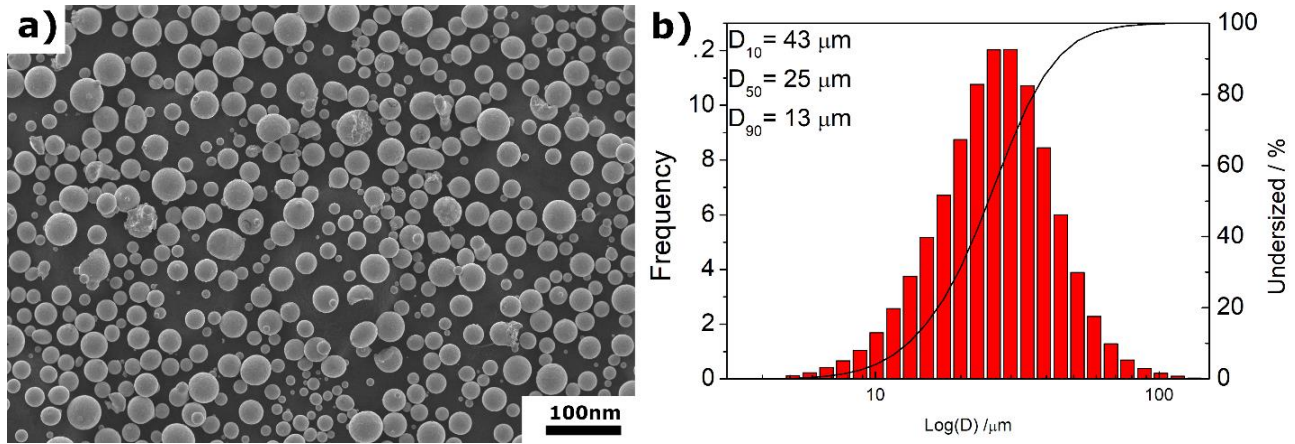


Figure 4. 1. (a) Morphology (b) PSD of the R41 powder.

Specimens used in this study were fabricated using a Renishaw AM400 machine equipped with a reduced build volume chamber. LPBF process was conducted under Ar atmosphere with oxygen levels lower than 300 ppm. Two different sample geometries (cubes and bars) were fabricated on a stainless-steel plate. Cubes having 10 x 10 x 10 mm were used for microstructural analysis and bars of 10 x 10 x 55 mm with their length along the building direction were prepared for elevated temperature tensile testing. In order to understand the effect of the solutionizing temperature, samples were then subjected to 2 different heat treatment cycles. Solutionizing temperatures were selected to cover temperatures below and above the  $\gamma'$  solvus temperature range,  $T_{\gamma'} = 1071\text{--}1082 \text{ }^\circ\text{C}$  [29]. The sub-solvus heat treatment (HT1) consists of solutionizing the samples at  $1065 \text{ }^\circ\text{C}$  for 4 h followed by air cooling. Afterwards samples were subjected to an aging heat treatment at  $760 \text{ }^\circ\text{C}$  for 16 h and air cooled to room temperature. In the super-solvus heat treatment (HT2), the samples were solutionized at  $1200 \text{ }^\circ\text{C}$  for 4 h then air cooled to room temperature followed by the same aging treatment at  $760 \text{ }^\circ\text{C}$  for 16 h. All heat treatments were conducted under Ar atmosphere to prevent any compositional change from oxidation.

Cube samples for each of the 3 following conditions AB, HT1 and HT2 were sectioned, mounted and ground up to 600 grits SiC paper. The samples were then polished using 9, 3 and  $1 \mu\text{m}$  diamond suspension followed by a final polishing using a  $0.05 \mu\text{m}$  colloidal silica suspension.

Grain morphology and texture analysis of the samples were studied using a Hitachi SU3500 scanning electron microscope (SEM) equipped with an electron back scattered diffraction (EBSD) detector. The operating conditions were 15 kV and  $2 \mu\text{m}$  step size. Aztec data acquisition software

combined with the HKL Channel 5 data processing software was used to analyze the raw data obtained from the EBSD. Pole figures of the {100}, {110} and {111} planes were obtained from the EBSD data using a half width of 10° and a cluster size of 5°, and the resultant intensities were presented as multiples of uniform density (MUD). Hitachi SU8000 STEM equipped with energy dispersive spectrometer (EDS) was used for further microstructural characterization at high magnifications. Five micrographs collected from different regions of the samples were analyzed using image analysis software Image J [30] to determine the size and fraction of the  $\gamma'$  precipitates and carbide particles.

For elevated temperature tensile testing, round bars having a reduced cross-section of 4 mm diameter and 16 mm gauge length were machined from the LPBF fabricated bars according to ASTM E8 / E8M - 16a [31]. Tensile testing was conducted at 760 °C with a strain rate of 0.005 mm/mm/min up to yield and 0.05 mm/mm/min until the fracture. Two samples were tested in AB condition and 3 samples were tested for each of the HT1 and HT2 conditions.

Tested samples from each condition were mounted and prepared using the same metallographic techniques for post-fracture analysis. Hitachi SU3500 SEM equipped with EDS was used for the microstructural characterization of the tested cross-sections. Post-fracture EBSD analysis was carried out near the fracture locations to understand the deformation behavior. The step size used for the deformed samples was 1  $\mu\text{m}$ . Fracture surfaces of the samples were also analyzed for each three conditions using SEM.

## **4.4. Results and Discussion**

### **4.4.1. Microstructure**

The microstructure of the samples for all three conditions were observed under SEM. Micrographs taken under back scattered electron (BSE) contrast are shown in Figure 4.2. AB condition revealed a dendritic sub-grain structure with primary dendrite arm spacing of  $0.51 \pm 0.17 \mu\text{m}$  and extremely small secondary dendrite arms as seen in Figure 4.2(a). This type of microstructure was extensively reported for variety of superalloys [32,33]. Presence of molten pool boundaries are also clearly visible in the AB condition. The dendritic growth follows the direction of highest temperature gradient which is perpendicular to the molten pool boundaries. As depicted in the higher

magnification micrograph of the AB sample in Figure 4.2(b), no  $\gamma'$  precipitation occurred during fabrication. High cooling rates achieved in LPBF prevented precipitation of  $\gamma'$  in R41 during the LPBF process. Authors also reported that previously for this alloy [28].

Dissolution of the molten pool boundaries were observed after the samples were subjected to heat treatment. The SEM micrograph of the HT1 condition shown in Figure 4.2(c) still depicts the cellular sub-grain structure previously observed in the AB condition. Formation of fine bright particles were observed along the cell and grain boundaries. Qualitative EDS and TEM diffraction analysis showed that these particles are Mo rich  $M_6C$  carbides [28]. EDS linescan analysis shown in Figure 4.3(a) also shows that those carbide particles are enriched in Mo.

The columnar sub-grain structure observed in the AB and HT1 conditions was replaced by an equiaxed structure upon HT2. Similar to the HT1 molten pool boundaries were also not visible in this condition. The bright carbide particles on the cell boundaries of HT1 condition were not present around the equiaxed grains of the HT2 condition, as shown in Figure 4.2(e). However, a thin carbide film decorating the grain boundaries is clearly visible at higher magnification, as shown in Figure 4.2(f). Therefore, carbide formation was still observed in the HT2 condition, but with a different morphology compared to the HT1. EDS analysis in Figure 4.3(b) reveals that composition of the film like carbides is different compared to the carbide phase of HT1 condition. As depicted, the linescan suggests that the carbide film in the HT2 condition is enriched in Cr and Mo, depleted in Ni, Ti and Co. High composition of Cr indicates that observed carbides in the HT2 condition are  $M_{23}C_6$  carbides which are stable at a lower temperature compared to the  $M_6C$  carbides [34].

The size of the discrete carbide particles in HT1 condition was measured as  $527 \pm 252$  nm, whereas a thin grain boundary film-like carbide structure of HT2 condition showed a thickness of  $187 \pm 81$  nm. It is well known that refractory metals such as Mo, segregates at the inter-dendritic region during solidification due to their low partition coefficient [5,24]. Formation MC carbides enriched in Mo and Ti during solidification were indeed previously reported for this alloy [35]. MC carbides are stable at low temperatures and transforms into  $M_6C$  or  $M_{23}C_6$  carbides, when the alloy is exposed to higher temperatures [34]. Therefore, formation of  $M_6C$ , observed in HT1 condition, is expected when the samples are heated up to the solutionizing temperature. These  $M_6C$  carbides were formed as discrete particles while heating up to the solutionizing temperature of  $1065^\circ\text{C}$  and

those carbide particles further grown during holding at that temperature and following aging heat treatment. When the temperature is raised above 1150 °C,  $M_6C$  carbides starts to dissolve [29]. The HT2 condition involves solutionizing the samples at 1200 °C, which is above the dissolution temperature of the  $M_6C$  carbides. Hence, the Mo rich discrete carbide particles dissolved during the super-solvus solutionizing and reformed as a Mo and Cr rich thin film while cooling to aging temperature or during the aging heat treatment.

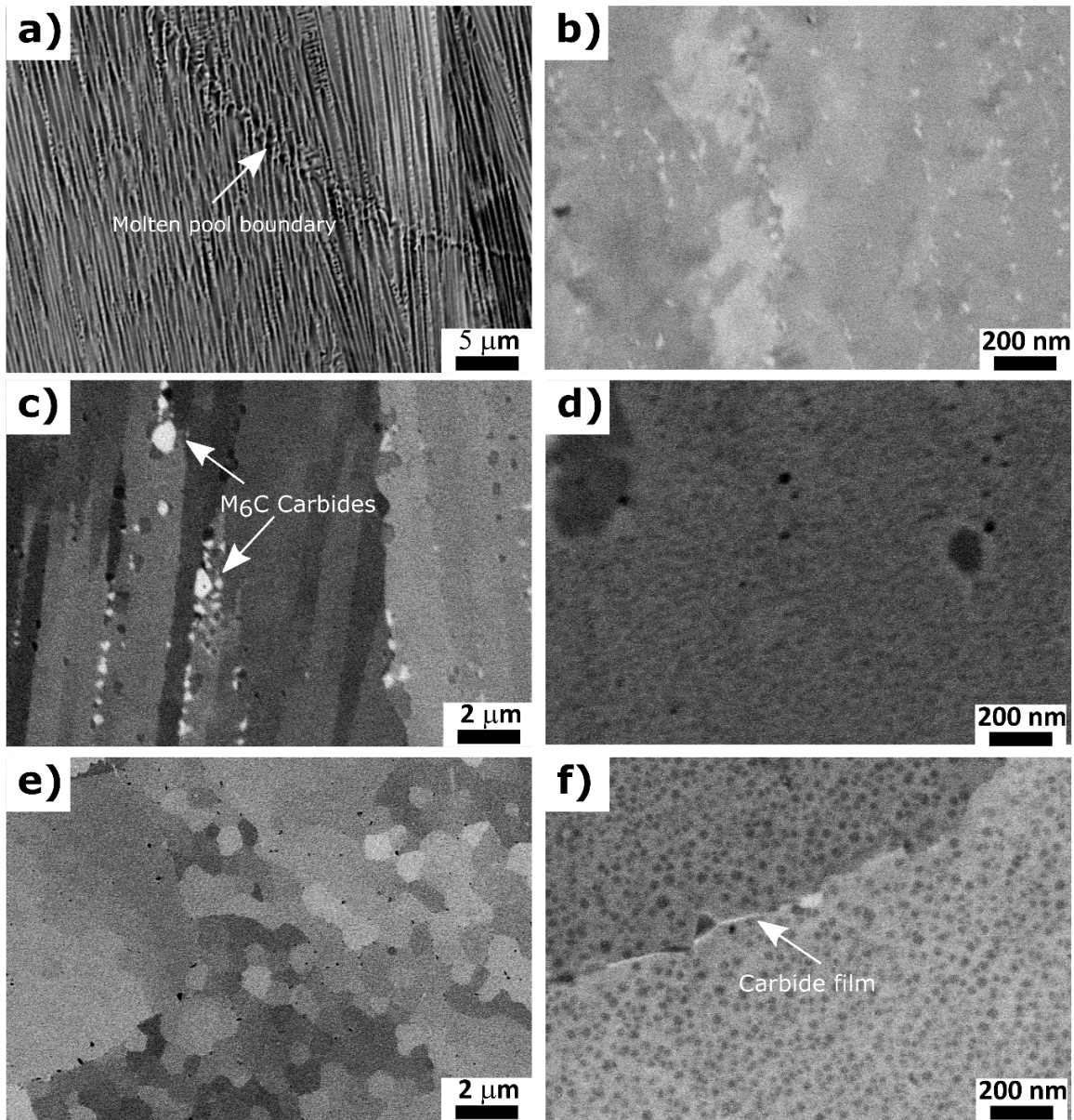


Figure 4. 2. SEM micrographs of the R41 samples in (a) and (b) AB; (c) and (d) HT1; (e) and (f) HT2 condition.

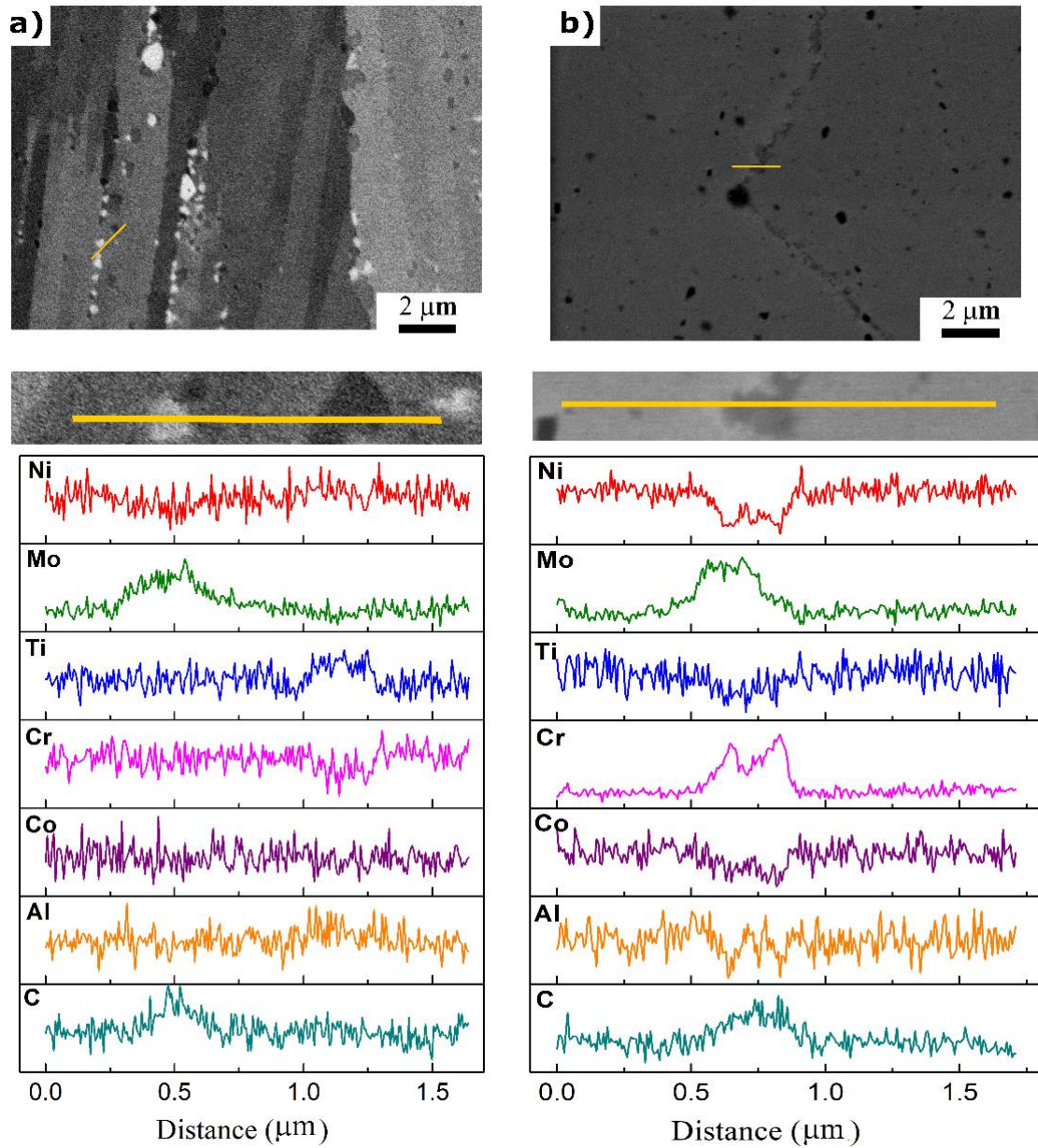


Figure 4. 3. SEM micrographs and corresponding EDS linescan analysis of R41 samples in (a) HT1, (b) HT2 conditions.

In addition to the carbide particles, formation of  $\gamma'$  precipitates were observed after both heat treatments. High magnification micrograph of the HT1 sample in Figure 4.2(d) depicts presence of cuboidal dark grey  $\gamma'$  precipitates with sizes ranging between 120-450 nm on the cell boundaries along with the secondary spherical  $\gamma'$  precipitates within the cells, with an average size of  $18 \pm 5$  nm. In the case of HT2 condition average particle size of spherical  $\gamma'$  precipitates was measured as

44 ± 15 nm. Size distribution of the  $\gamma'$  precipitates in both conditions was obtained by image analysis using line intercept method is presented in Fig. 4. As observed in Figure 4.4(a), the HT1 cycle resulted in a bimodal size distribution. The presence of the primary  $\gamma'$  shows that  $\gamma'$  precipitation occurred during the heating up to the solutionizing temperature and they continue growing during the 4-hour sub-solvus solutionizing heat treatment. When the sample is air cooled and heated up to the aging temperature, the precipitation of secondary  $\gamma'$ , with a significantly smaller diameter, occurred. In contrast, the precipitates in HT2 condition have a unimodal distribution, as shown in Figure 4.4(b). This difference in size distribution emerges from the super-solvus solutionizing heat treatment involved in the HT2 condition. The primary  $\gamma'$  formed during the heating completely dissolved during the super-solvus solutionizing heat treatment and all the precipitates observed in the microstructure are formed in the second step of the heat treatment. The average size of the precipitates in the HT2 condition is also found to be statistically larger compared to the secondary  $\gamma'$  particles in HT1. Growth of the  $\gamma'$  precipitates is limited by the diffusion of available Al and Ti in the matrix [36,37]. The EDS linescan analysis of HT1 condition in Figure 4.3(a) shows that the primary  $\gamma'$  particles are enriched in Ti. Hence, presence of larger primary  $\gamma'$  particles resulted a reduced availability of Al and Ti in solution, which limits the growth potential of the secondary  $\gamma'$  precipitates in the HT1 condition.

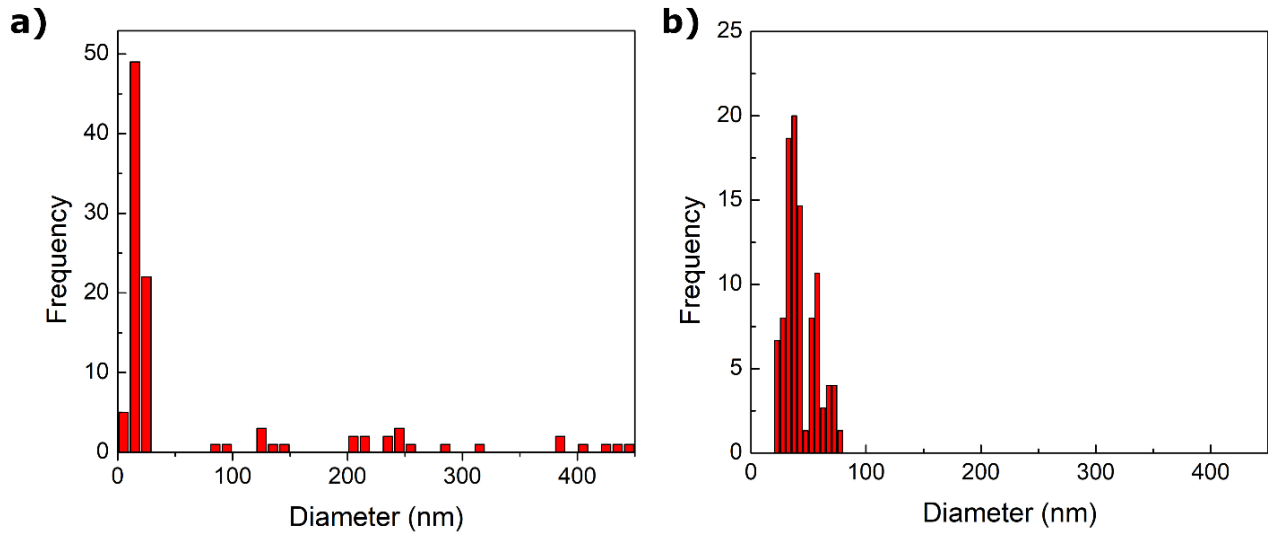


Figure 4. 4.  $\gamma'$  precipitates size distribution upon (a) HT1 and (b) HT2 conditions.

#### 4.4.2. Grain Morphology and Texture

EBSD analysis was carried out to understand the effect of different heat treatment cycles on grain morphology and texture. Figure 4.5 presents IPF orientation maps along with the corresponding pole figures obtained from the respective cross-sections. Grain boundaries were denoted with black lines in the orientation maps for misorientations  $> 15^\circ$ . The orientation map of the AB sample of Figure 4.5(a) shows the expected columnar grains parallel to the building direction. Epitaxial growth of  $\gamma$  grains across several layers during LPBF fabrication was reported before for R41 and other Ni-based superalloys [28,38,39]. The AB condition revealed a strong cube texture with a peak intensity of 5.74 mud predominantly oriented along  $\langle 100 \rangle$  direction. Columnar morphology of the grains oriented along  $\langle 100 \rangle$  direction was maintained in the HT1 condition as shown in Figure 4.5(b). The strong  $\langle 100 \rangle$  cube texture was also observed for this sample with an increased maximum intensity value of 7.54 mud. When a super-solvus solutionizing treatment was tested, it was observed that the equiaxed grains replaced the columnar grains of the AB condition. IPF orientation map and corresponding pole figures in Figure 4.5(c) depicts that the equiaxed grains have no apparent preferential crystallographic orientation upon HT2.

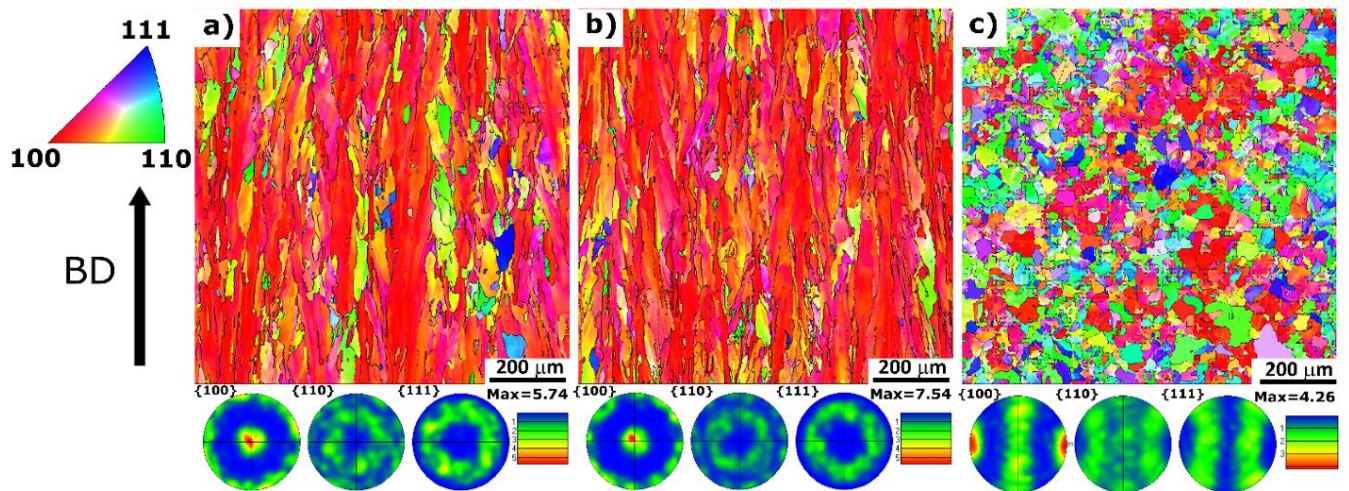


Figure 4. 5. IPF orientation maps and the corresponding pole figures for (a)AB, (b)HT1 and (c)HT2 conditions.

Regions of 1000 by 1000 $\mu\text{m}$  of the IPF orientation maps were used to calculate the diameter and aspect ratio of the grains. The graphs showing the 10<sup>th</sup>, 50<sup>th</sup> and 90<sup>th</sup> percentiles for each condition are shown in Fig.6. Line intercept method was used to measure the grain diameter. It can be seen that 90% of the grains in the AB condition have a diameter below 70 $\mu\text{m}$  and a slight increase in D90 to 75 $\mu\text{m}$  was observed after HT1 conditions. The equiaxed grains formed in HT2 condition has shown smaller grain size compared to the AB and HT1 conditions. The aspect ratio, which represents the length over width ratio of the fitted ellipses to the grains, was also evaluated. Higher values of aspect ratio correspond to a columnar-type grain whereas a value of 1 represents a perfectly equiaxed grain structure. The aspect ratio analysis shown in Figure 4.6(b) confirms that the grain morphology has not change significantly after the HT1 cycle. Slight increase in the aspect ratio values observed for HT1 condition represents an increase in the intensity of the texture which is in agreement with the pole figures in Figure 4.5(b). The lower grain aspect ratio values calculated for HT2 condition strengthens the development of equiaxed grains. These findings suggest that sub-solvus solutionizing heat treatment in HT1 condition allowed coalescence of the AB cell colonies while, super-solvus heat treatment in HT2 condition resulted in static recrystallization leading to formation of smaller equiaxed grains.

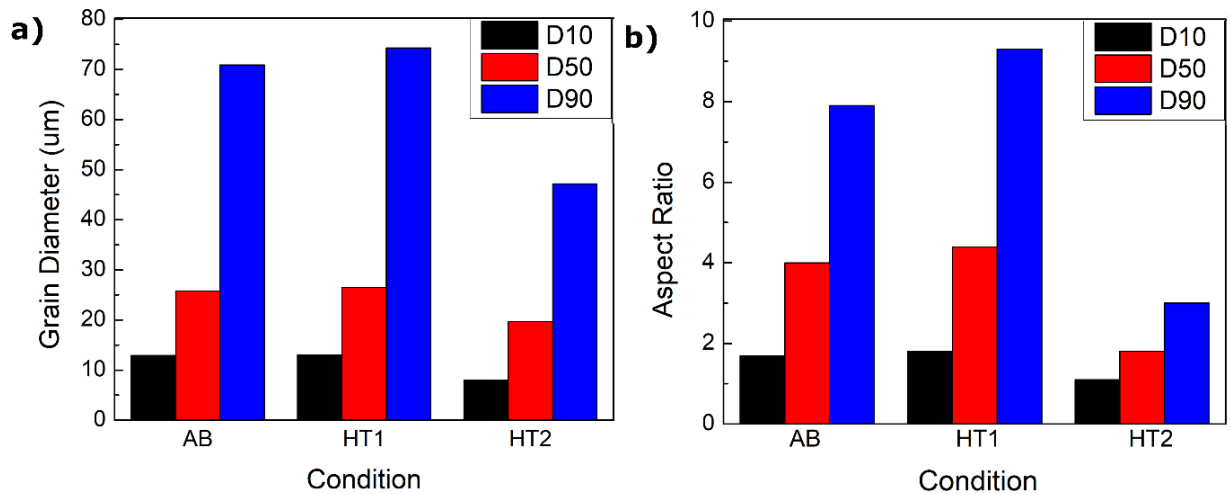


Figure 4. 6. (a) Diameter, (b) aspect ratio of the grains in AB, HT1 and HT2 conditions.

Figure 4.7 shows the classification of grains according to their internal average misorientations for the samples in each 3 conditions calculated by the Channel5 EBSD analysis software. In terms of nomenclature for the current analysis, when the internal average misorientation of the grains

exceeds  $15^\circ$ , they are classified as deformed, when this value is below  $2^\circ$ , they are classified as recrystallized and all the grains with an average misorientation in between  $2$ - $15^\circ$  are considered as sub-structured. As shown in Figure 4.7(a) and (d) 75% of the columnar grains in the AB condition are sub-structured with low angle grain boundaries. Fraction of the grains having high misorientations above  $15^\circ$  was calculated as 25% for the AB condition and increased to 45 and 60% for HT1 and HT2 conditions respectively. Precipitation of  $\gamma'$  is known to induce strain to the matrix due to lattice mismatch and an increase in the induced strain is observed as the particle size gets larger [5,7]. Therefore, increase in the local misorientation of these 2 conditions can be explained by the formation of  $\gamma'$  precipitates within the sub-grains during the heat treatment. The difference between the misorientation values of HT1 and HT2 conditions can also be attributed to the larger size of secondary  $\gamma'$  particles observed in the HT2 condition. As shown in Figure 4.7(c) and (d), approximately 25% of the analyzed grains in the HT2 condition, were new strain free grains with low misorientation. Therefore, partial recrystallization of the grain structure in AB condition is observed during solutionizing at  $1200^\circ\text{C}$  for 4 hours. It is well documented that the recrystallization process is driven by the stored energy within the material [40]. In the case of LPBF, this process is driven by the large strain energy stored in the microstructure as a result of iterative rapid heating and cooling. Recrystallization phenomenon is commonly reported for variety of LPBF fabricated superalloys during the post processing heat treatments [41,42]. In contrast, no evidence of recrystallization was observed for the HT1 condition. Although, recrystallization phenomenon has been extensively studied during the past few decades available information regarding the recrystallization in complex superalloy systems are mostly focused on wrought and powder metallurgy alloys. In most of these studies it has been reported that presence of  $\gamma'$  precipitates or carbide particles can retard the nucleation of recrystallization and migration of recrystallized grain boundaries [43,44]. This suggests that presence of undissolved carbide particles and  $\gamma'$  precipitates during the heat treatment in HT1 condition prevented the recrystallization by grain boundary pinning [45].

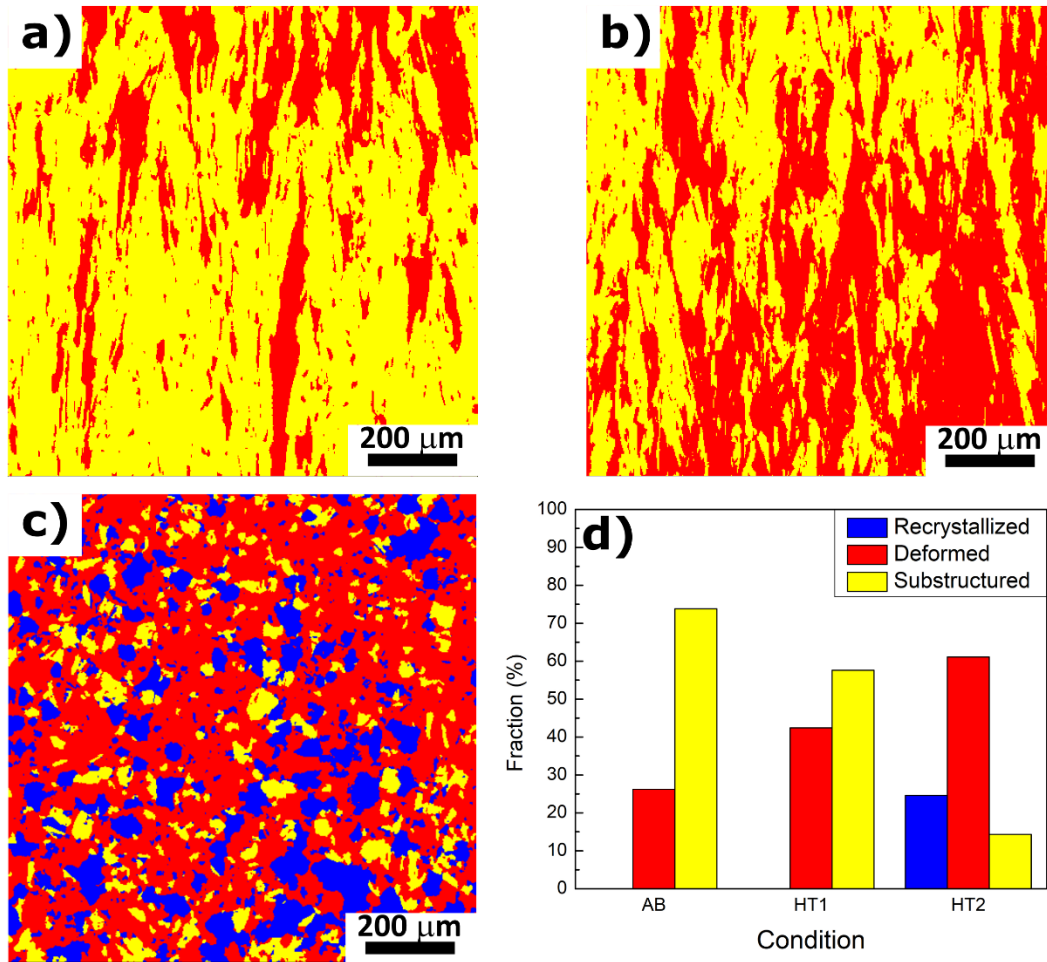


Figure 4. 7. Recrystallized grain distribution in (a) AB, (b) HT1, (c) HT2 conditions. (d) Fraction of recrystallized grains in all conditions.

#### 4.4.3. Elevated Temperature Tensile Properties

Figure 4.8(a) shows the yield strength (YS) and ultimate tensile strength (UTS) values for the three conditions. The average tensile YS and UTS of the AB condition at 760 °C are 879 and 1020 MPa, respectively. When the samples were subjected to the 2 different heat treatments, no significant change was observed in their elevated temperature strengths. The YS and UTS values were 824 and 986 MPa for HT1, and 855 and 1003 MPa for HT2, respectively. All three conditions tested for LPBF manufactured R41 alloy had comparable YS and UTS values with a wrought alloy, subjected to HT1 at 760 °C ( YS: 700-839 MPa , UTS : 805-1074 MPa) [46].

Nickel based superalloys mainly gain their strengths from 3 different mechanisms; grain boundary strengthening, solid solution strengthening and precipitation strengthening [47–49]. Since  $\gamma'$  precipitates are not present in the AB condition, precipitation strengthening is not operative. Hence, these samples gain their strength only from grain boundary and solid solution strengthening. Grain boundary strengthening has been attributed to the presence of high angle grain boundaries acting as a barrier to dislocation motion and it is well known to be inversely proportional to the grain size according to Hall-Petch relation. When the average grain diameters for all conditions are considered, the grain size of the AB condition is slightly larger than the HT2 and smaller than the HT1 condition. Although the difference in grain size is small it can be said that the contribution of grain boundary strengthening to the strength in AB condition would be higher than the HT1 and lower than the HT2 condition.

Theoretical modelling of solid solution strengthening according to the model proposed by Gypen and Deruyetere [50,51] was studied by several researchers [9,47,52]. According to those studies, strengthening coefficients of Mo and Ti are the highest, meaning those elements provide the highest solid solution strengthening to the  $\gamma$  matrix. Chemical composition of the  $\gamma$  matrix obtained by quantitative EDS analysis is listed in Table 4.2. EDS analysis showed that AB condition has the highest Mo content in the  $\gamma$  phase whereas HT1 condition has the lowest. The difference in Mo content of the matrix can be explained by the presence of Mo-rich carbides in both HT1 and HT2 conditions. Additionally, Ti content of the HT1 condition was found to be lower compared to the other two conditions. This can be attributed to the presence of large primary  $\gamma'$  precipitates in the HT1 condition. As mentioned in section 4.4.1. these precipitates are enriched in Ti, causing the depletion observed in the  $\gamma$  matrix. Thus, strengthening by solid solution would be the highest in the AB condition and lowest in the HT1 condition.

Precipitation hardening is an active strengthening mechanism only for the HT1 and HT2 conditions. Variety of different strengthening mechanism were identified for precipitation strengthened alloys including particle cutting by weakly or strongly coupled dislocations and Orowan looping [47,48,53]. It is generally accepted that the deformation mechanism is closely related with the  $\gamma'$  particle size distribution. Systems containing high volume fraction of fine  $\gamma'$  particles are mostly strengthened by particle cutting and large precipitates are bypassed by Orowan looping mechanism. It should be also noted that Orowan looping is rarely reported for

polycrystalline superalloys having  $\gamma'$  particles size less than 400 nm [49,54]. Size of most  $\gamma'$  precipitates both in HT1 and HT2 conditions were less than 70 nm as shown in Figure 4.4. Therefore, most plausible strengthening mechanism for those conditions is particle cutting by dislocations.

Although, all of the mentioned strengthening mechanisms play an important role on the final tensile properties, in a complex system like this it is very difficult to differentiate their individual contributions to the overall strength value. It should be noted that, AB samples have similar strength values to the heat-treated samples at 760°C even without the contribution of precipitation strengthening mechanism. On the contrary, at room temperature a significant increase was observed in the tensile YS and UTS after the samples were subjected to the standard heat treatment [28]. It can be said that the higher contribution of solid solution strengthening in the AB condition has provided the strength lost due to lack of  $\gamma'$  precipitation during high temperature tensile deformation.

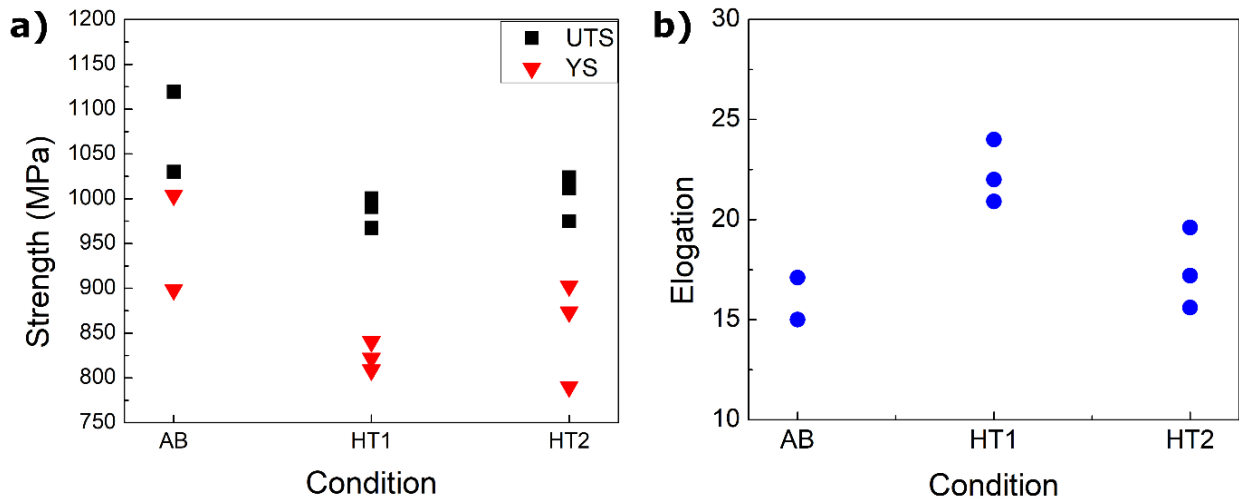


Figure 4. 8. Tensile properties of R41 @ 760C in different conditions; (a) UTS and YS, (b) elongation.

Table 4.2. Composition of the  $\gamma$  matrix for AB, HT1 and HT2 conditions

	<b>Cr</b>	<b>Co</b>	<b>Ti</b>	<b>Al</b>	<b>Fe</b>	<b>Mo</b>
<b>AB</b>	17.3 $\pm$ 0.6	10.9 $\pm$ 0.5	3.1 $\pm$ 0.1	1.4 $\pm$ 0.1	2.8 $\pm$ 0.2	9.2 $\pm$ 0.4
<b>HT1</b>	18.2 $\pm$ 0.4	11.43 $\pm$ 0.7	2.6 $\pm$ 0.2	1.28 $\pm$ 0.5	2.83 $\pm$ 0.1	8.1 $\pm$ 0.2
<b>HT2</b>	17.6 $\pm$ 0.4	10.7 $\pm$ 0.6	3.2 $\pm$ 0.9	1.4 $\pm$ 0.1	2.7 $\pm$ 0.2	8.8 $\pm$ 0.3

Although, all three conditions had similar strength values, their tensile elongation behaviors at 760°C were different as shown in Figure 4.8(b). The measured elongation at fracture for the AB condition was 16 %. When the samples were subjected to the super-solvus HT2 cycle, an elongation value of 17 % was observed, which is statistically similar to the AB condition. The HT1 samples had the highest elongation, reaching 22 %. Therefore, the sub-solvus HT1 condition was found an attractive route to improve the elevated temperature ductility without sacrificing the strength. Even though the mechanism is not fully understood, typically, a loss of ductility at intermediate temperatures (500°C -900°C) is reported for variety of superalloys [55], which is opposite to the results obtained in this study. A minimum in the ductility value was reported for wrought equiaxed R41 alloys at 760°C when subjected to the standard heat treatment (HT1) [46]. One of the proposed mechanisms for this drop of ductility is grain boundary shearing or sliding [5,55]. It is observed that as the temperature increases, grain boundary shearing becomes possible. Grain boundary triple junctions or directional changes acts as a stress concentration site and results in a reduced ductility due to fast crack propagation [5,55]. However, this effect was not observed for the LPBF samples and subjected to HT1. The elongation value obtained at 760°C was twice the value obtained at room temperature [28]. Studies on ductility dip cracking of superalloys revealed that if the microstructure consists of straight grain boundaries decorated with discrete carbide particles, the samples possess higher resistance to grain boundary sliding [5]. Therefore, the observed microstructure in the HT1 sample prevented the ductility drop at 760°C observed in the wrought parts. Although the ductility of the HT1 condition is the highest, it should be noted that all three LPBF R41 samples had comparable or superior elongation at 760°C compared to the reported values for the wrought counterparts that are ranging between 4 - 16 % [46].

#### 4.4.4. Hot Deformation Behavior

Representative true stress / true strain curves at 760°C are presented in Figure 4.9(a) for the three conditions to compare their hot deformation behavior. The shapes of the true stress-strain diagrams suggest that the sample in each condition exhibits a different deformation behavior at 760°C. The true stress-strain curve of the AB condition shows 2 stages during deformation. During the first stage of deformation, the sample reached a peak stress value at low strains, which is followed by a steady state deformation until failure in the second stage. It is well known that the increase in stress during the initial stage of deformation is associated with the work hardening from the generation and multiplication of dislocation in the sample [56]. Dynamic recovery and recrystallization is reported as the main dynamic softening mechanism during hot deformation of Ni-based superalloys [57,58]. The high deformation temperatures cause an increase in the mobility of dislocation and activate the dislocation climb and cross-slip mechanisms [59]. As a result, dynamic recovery takes place and balances the work hardening and provides steady state deformation until fracture.

In the case of HT1, the initial work hardening was again observed until a peak stress is reached, followed by a reduction in strength and finally by a steady state deformation behavior. This particular shape of the true stress-strain curve is characteristic to dynamic recrystallization (DRX) phenomenon. In this condition, dynamic recovery is weak to balance the work hardening since both dislocation motion and grain boundary mobility is limited by to presence of  $\gamma'$  precipitates and carbide particles. Once the accumulated dislocation density exceeds a critical strain limit, new strain free grains nucleate at the pre-existing grain boundaries. These DRX grains can annihilate dislocations causing a reduction in strength. When the DRX and work hardening reached equilibrium, a steady state deformation behavior was observed [56,60,61]. Post-mortem EBSD analysis, from the neck region, were conducted to prove the occurrence of dynamic recrystallization during deformation of the HT1 samples. The IPF map along with the Kernel Average Misorientation (KAM) map are shown in Figure 4.9(b). The IPF maps obtained from the tested cross-section showed presence of small equiaxed grains that have a different crystallographic orientation compared to the deformed columnar grains. KAM maps were generated to describe the dislocation density in the grains. Higher degree of misorientation indicates higher dislocation density within the grain. It is found that the observed equiaxed grains

have lower misorientation proving that they have undergone less deformation compared to the others. Therefore, during high temperature testing of HT1 samples, DRX takes place by the nucleation and growth of strain free grains resulting softening during deformation. It is reported that refinement of microstructure by DRX followed by deformation of those newly nucleated grains improves the plastic deformation capacity of the material [59]. Therefore, in addition to the grain morphology, DRX is believed to be a strong contributor for the observed highest ductility.

True high temperature stress-strain curve for the HT2 samples shows a continuous work hardening after the initial stage of deformation. The equiaxed grain morphology combined with the fine  $\gamma'$  precipitates provided the work hardening ability for these samples. It is seen that the microstructure observed after the HT2 cycle prevents DRX, hence the dynamic softening during plastic deformation. After this stage a plastic instability region according to Considere's criterion is observed until the fracture [62]. Necking is initiated once the slope of the true stress-strain curve (work hardening rate) is equal to the UTS.

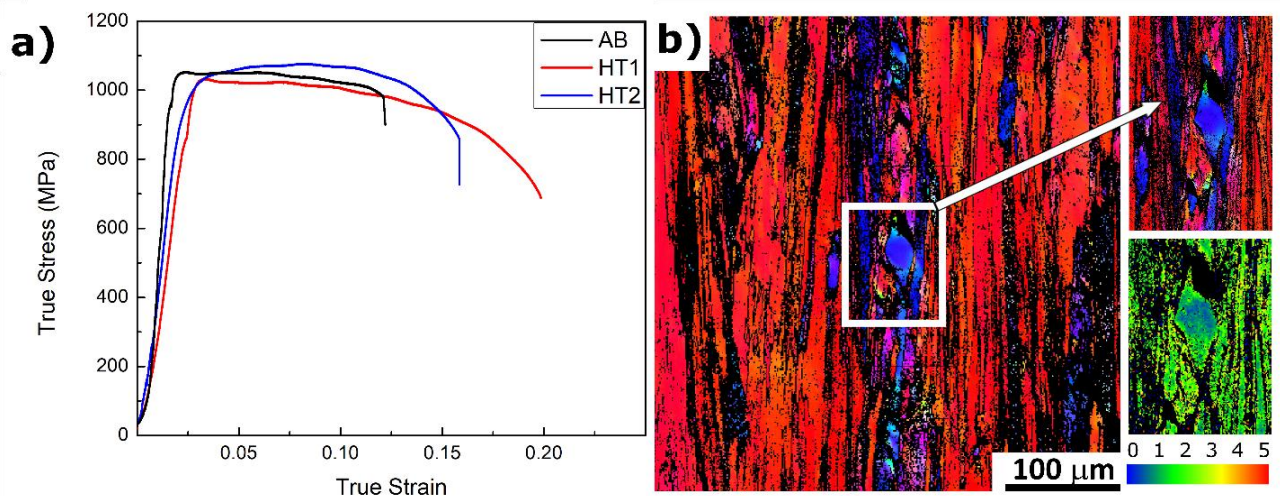


Figure 4. 9. (a) True stress-true strain curve for R41 samples at 760°C, (b) IPF orientation map of HT1 condition near fracture surface along with the misorientation map.

#### 4.4.5. Fractography

Post-mortem analysis of the fracture surfaces was conducted in order to understand the effect of the heat treatment on the elevated temperature fracture behavior. Cross-sections of the tested

samples and fracture surfaces of the samples were examined under SEM for all three conditions and results are shown in Figures 4.10, 4.11 and 4.12, respectively.

Fractography of the AB condition shown in Figure 4.10(a) depict that, all the microcracks are localized along the molten pool boundaries and are perpendicular to the tensile loading direction. It is known that solidification start at the edge of the molten pool and thermal gradient and solid liquid interface growth rate changes along the molten pool [63]. Rapid solidification along the molten pool boundaries known to result a local change in the solidification features such, as cell size and solute distribution creating a mechanically weak region [64]. It is thus believed that the molten pool boundaries in the AB condition acted as a crack initiation and propagation site which explains the observed lower ductility compared to the other samples. Fig.10(b) depicts that fracture followed a transgranular path and higher magnification SEM micrograph in Figure 4.10(c) shows the presence of river markings along with small amounts of dimple colonies on the fracture surface. River markings are characteristic features of cleavage type of fracture while dimples are observed in the case of ductile fracture. The mixed mode transgranular fracture surface observed in the AB condition is also in agreement with the limited elongation measured in the elevated temperature tensile tests.

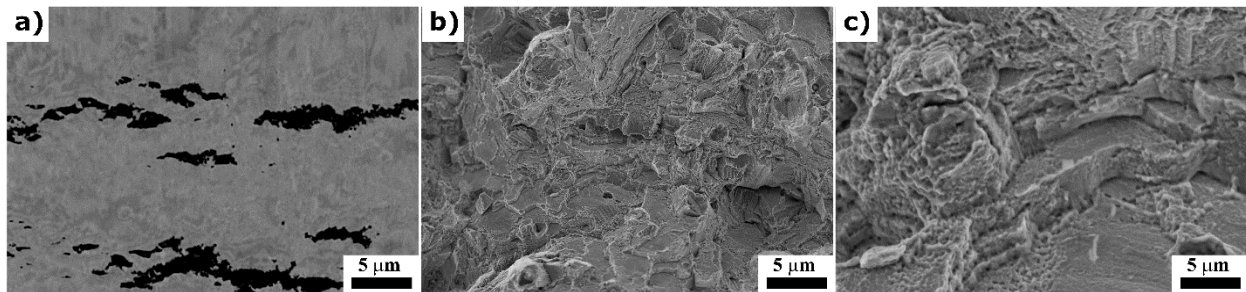


Figure 4. 10. SEM micrographs (a) near fracture region, (b) and (c) fracture surface of the AB condition.

As opposed to the AB condition, for the HT1 samples, micro-voids shown in Figure 4.11(a) are localized along the cell boundaries and around the carbide particles. Although, decohesion at the carbide cell boundary interface is observed, the discrete nature of the carbides prevented the crack propagation in the HT1 condition. Due to the observed columnar sub-grain morphology, all the voids and micro-cracks are lying parallel to the loading direction resulting the superior elongation achieved in this condition. Similar to the AB condition, fracture occurred in a transgranular manner

in the HT1 condition. The surface shown in Figure 4.11(b) consists of homogeneously distributed deep dimples and microvoids with sizes similar to the observed carbide particles. This observation also suggests that decohesion occurred around the carbide particles yet, the fracture occurred in a completely ductile manner.

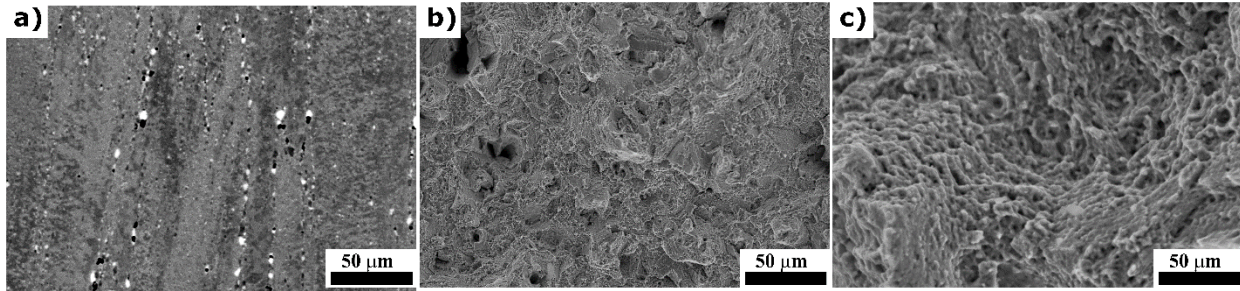


Figure 4. 11. SEM micrographs (a) near fracture region, (b) and (c) fracture surface of the HT1 condition.

In the HT2 condition, the voids are localized along the grain boundaries similar to the HT1 condition and microcracks are mainly located along the grain boundaries. Due to the equiaxed morphology of the grains, the presence of microcracks both perpendicular and parallel to the loading direction is observed as shown in Figure 4.12(a). Microstructure of the HT2 condition showed thin carbide films along the boundaries of these grains. It is well known that film-like morphology of carbide is unwanted in the superalloys since it causes embrittlement [5,7,65]. Thus, the lower elongation at fracture observed in the HT2 condition can be explained with the presence of this discontinuous thin film of carbides and increased number of grain boundaries perpendicular to the loading direction due to the equiaxed grain morphology. As depicted in Figure 4.12(b), intergranular fracture was observed in the HT2 condition. These results prove that fracture behavior is directly affected by the grain boundary carbide morphology. The film like carbide morphology observed along the grain boundaries of the HT2 condition acted as a crack initiation and propagation site, transforming the fracture mode from transgranular to intergranular. Although, HT2 condition has a similar elongation at fracture with the AB condition, the fracture surface micrograph of Figure 4.12(c) indicates that this condition also fractured in a ductile manner. However, the dimples observed in this condition are shallower compared to the ones in the HT1 condition. This implies that HT2 condition has lower ductility which is agreement with the results obtained from elevated temperature tensile testing.

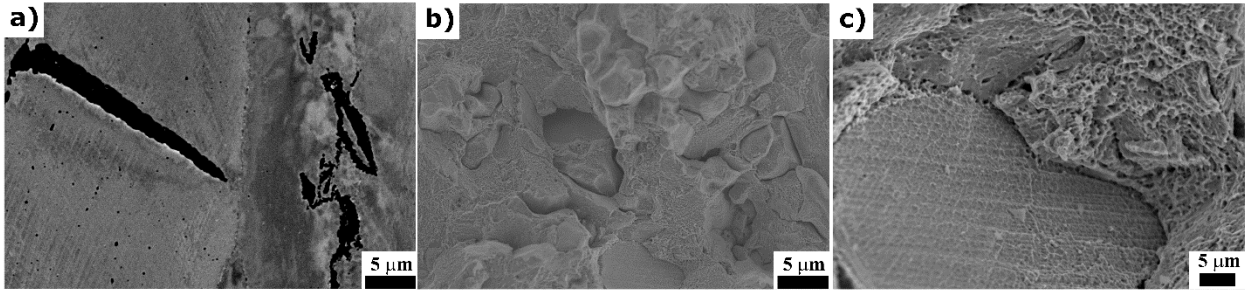


Figure 4. 12.SEM micrographs (a) near fracture region, (b) and (c) fracture surface of the HT2 condition.

## 4.5. Conclusion

In this study, the microstructure and elevated temperature tensile properties of LPBF fabricated R41 alloy were investigated in as-built (AB), sub-solvus heat treated (HT1) and super-solvus heat treated (HT2) conditions. Change in the microstructure resulting from the applied different heat treatments and its effects on the tensile deformation behavior at 760°C are discussed. The main conclusions can be summarized as follows:

1. The AB condition exhibits a columnar dendritic sub-grain structure without presence of  $\gamma'$  precipitates. This columnar structure is preserved in the HT1 condition. Formation of fine  $\gamma'$  precipitates having a bimodal distribution along with the discrete grain boundary carbide particles is observed after the applied sub-solvus heat treatment. When the samples are subjected to a super-solvus heat treatment columnar sub-grain morphology was transformed to an equiaxed one. Microstructure of the HT2 condition consists of a unimodal distribution of fine  $\gamma'$  precipitates and film-like grain boundary carbides.
2. EBSD analysis revealed a columnar grain morphology along the  $\langle 100 \rangle$  direction for the AB condition. This columnar grain morphology is preserved in the HT1 condition. However, a slight increase in the grain size and texture intensity is observed due to rearrangement and coalescence of cellular sub-grain structure. The heat treatment regime in HT2 condition resulted formation of equiaxed grains with finer grain size by static recrystallization. It is found that, presence of undissolved discrete carbide particles and  $\gamma'$  precipitates prevented the recrystallization by pinning the grain boundaries, during the sub-solvus heat treatment in HT1 condition.

3. All three of the tested conditions showed similar YS and UTS values at 760°C that are on par with the wrought and heat-treated alloys reported in literature. However, their elongations and fracture behaviors showed distinct differences. Presence of the molten pool boundaries has limited the elongation in the AB condition. It is seen that the samples in the AB condition had limited ductility at the testing temperature and failure started locally at the molten pool boundaries. HT1 condition has the highest elongation among all the others and it is also well above the values reported in literature. Columnar grain morphology observed in the HT1 condition provided the improved ductility without sacrificing the strength. In the case of HT2 condition thin carbide films on the grain boundaries acted as a crack initiation and propagation site resulting a transgranular ductile fracture.
4. All conditions also exhibited different elevated temperature deformation behaviors. Work hardening is observed in the HT2 condition after yield whereas HT1 condition showed softening and steady state deformation. EBSD analysis of the tested samples revealed that this difference in the flow curves are caused by the dynamic recrystallization phenomenon taking place during deformation of the HT2 condition.

#### **4.6. Acknowledgement**

The authors would like to thank the generous research support by the Natural Sciences and Engineering Research Council (NSERC) of Canada (NSERC Project Number: NETGP 494158 – 16). The authors would also like to acknowledge McGill Engineering Doctoral Award (MEDA) granted to Ms. Atabay.

#### **4.7. References**

- [1] D. Herzog, V. Seyda, E. Wycisk, C. Emmelmann, Additive manufacturing of metals, *Acta Mater.* 117 (2016) 371–392. doi:10.1016/j.actamat.2016.07.019.
- [2] T. DebRoy, H.L. Wei, J.S. Zuback, T. Mukherjee, J.W. Elmer, J.O. Milewski, A.M. Beese, A. Wilson-Heid, A. De, W. Zhang, Additive manufacturing of metallic components – Process, structure and properties, *Prog. Mater. Sci.* 92 (2018) 112–224. doi:10.1016/j.pmatsci.2017.10.001.
- [3] C.Y. Yap, C.K. Chua, Z.L. Dong, Z.H. Liu, D.Q. Zhang, L.E. Loh, S.L. Sing, C.Y. Yap,

- C.K. Chua, Z.L. Dong, Z.H. Liu, D.Q. Zhang, L.E. Loh, Review of selective laser melting : Materials and applications APPLIED PHYSICS REVIEWS — FOCUSED REVIEW Review of selective laser melting: Materials and applications, 041101 (2016). doi:10.1063/1.4935926.
- [4] F. Froes, R. Boyer, Additive manufacturing for the aerospace industry, (2019). <https://search.ebscohost.com/login.aspx?direct=true&scope=site&db=nlebk&db=nlabk&AN=1805939>.
- [5] J.N.D.& J. C.Lippold, Welding Metallurgy and Weldability of Nickel-Base Alloys, J. Chem. Inf. Model. 53 (2009) 456. doi:10.1017/CBO9781107415324.004.
- [6] H.K.D.H. Bhadeshia, Nickel Based Superalloys, Univ. Cambridge. (2012) 1–9. [www.msm.cam.ac.uk/phase-trans/2003/Superalloys/superalloys.html](http://www.msm.cam.ac.uk/phase-trans/2003/Superalloys/superalloys.html) 9/9.
- [7] R.C. Reed, The Superalloys fundamentals and applications, Superalloys Fundam. Appl. 9780521859 (2006) 1–372. doi:10.1017/CBO9780511541285.
- [8] J. Chander, Hardening Mechanism and Corrosion Resistance of Nickel-Base Alloys: A Review, Can. Metall. Q. 3 (1964) 57–77. doi:10.1179/cmq.1964.3.1.57.
- [9] C. Joseph, C. Persson, M. Hörnqvist Colliander, Influence of heat treatment on the microstructure and tensile properties of Ni-base superalloy Haynes 282, Mater. Sci. Eng. A. 679 (2017) 520–530. doi:<https://doi.org/10.1016/j.msea.2016.10.048>.
- [10] J. Mao, K.M. Chang, W. Yang, D.U. Furrer, K. Ray, S.P. Vaze, Cooling precipitation and strengthening study in powder metallurgy superalloy Rene88DT, Mater. Sci. Eng. A. 332 (2002) 318–329. doi:10.1016/S0921-5093(01)01758-0.
- [11] H.Y. Bor, C.N. Wei, A.C. Yeh, W. Bin He, H. Sen Wang, C.M. Kuo, Heat treatment effects on the high temperature mechanical behavior of directionally solidified MAR-M247 superalloy, 8th Pacific Rim Int. Congr. Adv. Mater. Process. 2013, PRICM 8. 1 (2013) 379–386. doi:10.1007/978-3-319-48764-9\_46.
- [12] H.E. Huang, C.H. Koo, Effect of solution-treatment on microstructure and mechanical properties of cast fine-grain CM 247 LC superalloy, Mater. Trans. 45 (2004) 1360–1366. doi:10.2320/matertrans.45.1360.
- [13] S. Xu, J.I. Dickson, A.K. Koul, Grain Growth and Carbide Precipitation in Superalloy , 29 (1998) 2687–2695.
- [14] D. Gu, Laser Additive Manufacturing (AM): Classification, Processing Philosophy, and

- Metallurgical Mechanisms, 2015. doi:10.1007/978-3-662-46089-4\_2.
- [15] S. Li, Q. Wei, Y. Shi, Z. Zhu, D. Zhang, Microstructure Characteristics of Inconel 625 Superalloy Manufactured by Selective Laser Melting, *J. Mater. Sci. Technol.* 31 (2015) 946–952. doi:10.1016/J.JMST.2014.09.020.
- [16] T. Vilaro, C. Colin, J.D. Bartout, L. Nazé, M. Sennour, Microstructural and mechanical approaches of the selective laser melting process applied to a nickel-base superalloy, *Mater. Sci. Eng. A.* 534 (2012) 446–451. doi:10.1016/j.msea.2011.11.092.
- [17] H.L. Wei, J. Mazumder, T. DebRoy, Evolution of solidification texture during additive manufacturing, *Sci. Rep.* 5 (2015) 1–7. doi:10.1038/srep16446.
- [18] J.A. Muñoz-Lerma, Y. Tian, X. Wang, R. Gauvin, M. Brochu, Microstructure evolution of Inconel 738 fabricated by pulsed laser powder bed fusion, *Prog. Addit. Manuf.* (2018). doi:10.1007/s40964-018-0062-2.
- [19] V.A. Wills, D.G. McCartney, A comparative study of solidification features in nickel-base superalloys: microstructural evolution and microsegregation, *Mater. Sci. Eng. A.* 145 (1991) 223–232. doi:10.1016/0921-5093(91)90252-I.
- [20] N.J. Harrison, I. Todd, K. Mumtaz, Reduction of micro-cracking in nickel superalloys processed by Selective Laser Melting: A fundamental alloy design approach, *Acta Mater.* 94 (2015) 59–68. doi:10.1016/j.actamat.2015.04.035.
- [21] G. Marchese, G. Basile, E. Bassini, A. Aversa, M. Lombardi, D. Ugues, P. Fino, S. Biamino, Study of the microstructure and cracking mechanisms of hastelloy X produced by laser powder bed fusion, *Materials (Basel)*. 11 (2018). doi:10.3390/ma11010106.
- [22] R. Kayacan, R. Varol, O. Kimilli, The effects of pre- and post-weld heat treatment variables on the strain-age cracking in welded Rene 41 components, *Mater. Res. Bull.* 39 (2004) 2171–2186. doi:10.1016/j.materresbull.2004.08.003.
- [23] B.S. Yilbas, Characterization of laser-treated Rene 41 surface due to B<sub>4</sub>C and SiC particles at surface prior to laser treatment, *Surf. Interface Anal.* 46 (2014) 30–35. doi:10.1002/sia.5342.
- [24] Q.L. Pan, B. Li, Y. Wang, Y.W. Zhang, Z.M. Yin, Characterization of hot deformation behavior of Ni-base superalloy Rene 41 using processing map, *Mater. Sci. Eng. A.* 585 (2013) 371–378. doi:10.1016/j.msea.2013.07.066.
- [25] D. Tali, H. Gasan, M. Gulesen, S. Gurgun, M. Cemal, Turning Operation Of Nickel Based

- Superalloy Rene 41, (2017) 9–11.
- [26] J.E. Franklin, W.F. Savage, Stress Relaxation and Strain-Age Cracking in Rene 41 Weldments, *Weld. J.* 53 (1974) 380s-387s. [http://aws.perusion.com/wj/supplement/WJ\\_1974\\_09\\_s380.pdf](http://aws.perusion.com/wj/supplement/WJ_1974_09_s380.pdf).
- [27] S. Tosto, Diffusion processes and weldability of hot-pressed RENE' 41 superalloy, *Metallography*. 17 (1984) 89–102. doi:10.1016/0026-0800(84)90007-7.
- [28] S.E. Atabay, O. Sanchez-Mata, J.A. Muñiz-Lerma, R. Gauvin, M. Brochu, Microstructure and mechanical properties of rene 41 alloy manufactured by laser powder bed fusion, *Mater. Sci. Eng. A*. 773 (2020) 138849. doi:10.1016/J.MSEA.2019.138849.
- [29] Heat Treaters Guide: Nonferrous Alloys, 721 (1800) 59–75.
- [30] C.A. Schneider, W.S. Rasband, K.W. Eliceiri, NIH Image to ImageJ: 25 years of image analysis, *Nat. Methods*. 9 (2012) 671–675. doi:10.1038/nmeth.2089.
- [31] A. Gros, M. Hartung, T. Kirsten, E. Rahm, GOMMA results for OAEI 2012, *CEUR Workshop Proc.* 946 (2012) 133–140. doi:10.1520/E0008.
- [32] M. Cloots, K. Kunze, P.J. Uggowitz, K. Wegener, Microstructural characteristics of the nickel-based alloy IN738LC and the cobalt-based alloy Mar-M509 produced by selective laser melting, *Mater. Sci. Eng. A*. 658 (2016) 68–76. doi:10.1016/J.MSEA.2016.01.058.
- [33] N. Nadammal, S. Cabeza, T. Mishurova, T. Thiede, A. Kromm, C. Seyfert, L. Farahbod, C. Haberland, J.A. Schneider, P.D. Portella, G. Bruno, Effect of hatch length on the development of microstructure, texture and residual stresses in selective laser melted superalloy Inconel 718, *Mater. Des.* 134 (2017) 139–150. doi:10.1016/j.matdes.2017.08.049.
- [34] S.S. Handa, Precipitation of Carbides in a Ni-based Superalloy, Masters Degree Proj. University (2014) 1–33.
- [35] J. Li, H.M. Wang, Microstructure and mechanical properties of rapid directionally solidified Ni-base superalloy Rene'41 by laser melting deposition manufacturing, *Mater. Sci. Eng. A*. 527 (2010) 4823–4829. doi:10.1016/j.msea.2010.04.062.
- [36] S. Meher, M.C. Carroll, T.M. Pollock, L.J. Carroll, Designing nickel base alloys for microstructural stability through low  $\gamma$ - $\gamma'$  interfacial energy and lattice misfit, *Mater. Des.* 140 (2018) 249–256. doi:10.1016/j.matdes.2017.11.065.
- [37] X. Wu, Y. Li, M. Huang, W. Liu, Z. Hou, Precipitation kinetics of ordered  $\gamma'$  phase and

- microstructure evolution in a Ni[ $\sigma$ ]Al alloy, *Mater. Chem. Phys.* 182 (2016) 125–132. doi:10.1016/j.matchemphys.2016.07.013.
- [38] S.E. Atabay, O. Sanchez-Mata, J.A. Muñiz-Lerma, R. Gauvin, M. Brochu, Microstructure and mechanical properties of rene 41 alloy manufactured by laser powder bed fusion, *Mater. Sci. Eng. A*. 773 (2020). doi:10.1016/j.msea.2019.138849.
- [39] A. Basak, S. Das, Microstructure of nickel-base superalloy MAR-M247 additively manufactured through scanning laser epitaxy (SLE), *J. Alloys Compd.* 705 (2017) 806–816. doi:10.1016/j.jallcom.2017.02.013.
- [40] M. Rollet, A. Humphreys, F. Rohrer, G.S. Hatherly, *Recrystallization and Related Annealing Phenomena*, 2nd ed., Pergamon, 2004.
- [41] T. Etter, Reduction in mechanical anisotropy through high temperature heat treatment of Hastelloy X processed by Selective Laser Melting ( SLM ) Reduction in mechanical anisotropy through high temperature heat treatment of Hastelloy X processed by Selective, *Mater. Sci. Eng.* (2015). doi:10.1088/1757-899X/82/1/012097.
- [42] Y.L. Hu, X. Lin, Y.L. Li, J. Wang, S.Y. Zhang, X.F. Lu, W.D. Huang, Effect of heat treatment on the microstructural evolution and mechanical properties of GH4099 additive-manufactured by directed energy deposition, *J. Alloys Compd.* 800 (2019) 163–173. doi:10.1016/J.JALLCOM.2019.05.348.
- [43] Z. Li, Q. Xu, B. Liu, Simulation and Experimental study of Recrystallization Kinetics of Nickel Based Single Crystal Superalloys, *Mater. Today Proc.* 2 (2015) S440–S452. doi:10.1016/j.matpr.2015.05.060.
- [44] L. Wang, G. Xie, J. Zhang, L.H. Lou, On the role of carbides during the recrystallization of a directionally solidified nickel-base superalloy, 55 (2006) 457–460. doi:10.1016/j.scriptamat.2006.05.013.
- [45] V.D. Divya, R. Muñoz-Moreno, O.M.D.M. Messé, J.S. Barnard, S. Baker, T. Illston, H.J. Stone, Microstructure of selective laser melted CM247LC nickel-based superalloy and its evolution through heat treatment, *Mater. Charact.* 114 (2016) 62–74. doi:10.1016/j.matchar.2016.02.004.
- [46] The Elevated-Temperature Properties of Selected Superalloys, *Elev. Prop. Sel. Superalloys.* (2015). doi:10.1520/ds7s1-eb.
- [47] R.W. Kozar, A. Suzuki, W.W. Milligan, J.J. Schirra, M.F. Savage, T.M. Pollock,

- Strengthening mechanisms in polycrystalline multimodal nickel-base superalloys, *Metall. Mater. Trans. A Phys. Metall. Mater. Sci.* 40 (2009) 1588–1603. doi:10.1007/s11661-009-9858-5.
- [48] E.M. Francis, B.M.B. Grant, J.Q. da Fonseca, P.J. Phillips, M.J. Mills, M.R. Daymond, M. Preuss, High-temperature deformation mechanisms in a polycrystalline nickel-base superalloy studied by neutron diffraction and electron microscopy, *Acta Mater.* 74 (2014) 18–29. doi:10.1016/J.ACTAMAT.2014.04.028.
- [49] M. Preuss, M., Quinta da Fonseca, J., Grant, B., Knoche, E., Moat, R., Daymond, The effect of  $\gamma'$  particle size on the deformation mechanism in an advanced polycrystalline nickel-base superalloy, in: *Superalloys 2008 (Eleventh Int. Symp., 2008: pp. 405–414.*
- [50] A. Gypen, L.A. , Deruyettere, Multi-component solid solution hardening, *J. Mater. Sci.* 12 (1977) 1028–1033.
- [51] A. Gypen, L.A. , Deruyettere, Multi-component solid solution hardening Part 2 Agreement with experimental results, *J. Mater. Sci.* 12 (1977).
- [52] H. Kou, W. Li, J. Ma, J. Shao, Y. Tao, X. Zhang, P. Geng, Y. Deng, Y. Li, X. Zhang, F. Peng, Theoretical prediction of the temperature-dependent yield strength of solid solution strengthening Nickel-based alloys, *Int. J. Mech. Sci.* 140 (2018) 83–92. doi:https://doi.org/10.1016/j.ijmecsci.2018.02.042.
- [53] L.M. Brown, R.K. Ham, Strengthening methods in crystals, *Appl. Sci. London.* 9 (1971).
- [54] M. Heilmaier, U. Leetz, B. Reppich, Order strengthening in the cast nickel-based superalloy IN 100 at room temperature, *Mater. Sci. Eng. A TA - TT -*. 319–321 (2001) 375–378. doi:10.1016/S0921-5093(01)00989-3 LK -  
https://mcgill.on.worldcat.org/oclc/4648063576.
- [55] L. Zheng, G. Schmitz, Y. Meng, R. Chellali, R. Schlesiger, L. Zheng, G. Schmitz, Y. Meng, R. Chellali, R. Schlesiger, Mechanism of Intermediate Temperature Embrittlement of Ni and Ni-based Superalloys Mechanism of Intermediate Temperature Embrittlement of Ni and Ni-based Superalloys, *Crit. Rev. Solid State Mater. Sci.* 43 (2012) 843–866. doi:10.1080/10408436.2011.613492.
- [56] Y.C. Lin, X.-Y. Wu, X.-M. Chen, J. Chen, D.-X. Wen, J.-L. Zhang, L.-T. Li, EBSD study of a hot deformed nickel-based superalloy, *J. Alloys Compd.* 640 (2015) 101–113. doi:10.1016/J.JALLCOM.2015.04.008.

- [57] D.X. Wen, Y.C. Lin, J. Chen, X.M. Chen, J.L. Zhang, Y.J. Liang, L.T. Li, Work-hardening behaviors of typical solution-treated and aged Ni-based superalloys during hot deformation, *J. Alloys Compd.* 618 (2015) 372–379. doi:10.1016/j.jallcom.2014.08.187.
- [58] X. Yuan, J. Hui, Z. Feng, W. Fan, W. Gao, C. Xue, Microstructure analysis of high-temperature deformation of Al-Cu alloy, *Mater. Res. Express.* 5 (2018). doi:10.1088/2053-1591/aacd41.
- [59] Y.C. Lin, J. Deng, Y.-Q. Jiang, D.-X. Wen, G. Liu, Hot tensile deformation behaviors and fracture characteristics of a typical Ni-based superalloy, *Mater. Des.* 55 (2014) 949–957. doi:https://doi.org/10.1016/j.matdes.2013.10.071.
- [60] A. Etaati, K. Dehghani, A study on hot deformation behavior of Ni-42.5Ti-7.5Cu alloy, *Mater. Chem. Phys.* 140 (2013) 208–215. doi:10.1016/J.MATCHEMPHYS.2013.03.022.
- [61] G.R. Ebrahimi, H. Keshmiri, A. Momeni, M. Mazinani, Dynamic recrystallization behavior of a superaustenitic stainless steel containing 16%Cr and 25%Ni, *Mater. Sci. Eng. A.* 528 (2011) 7488–7493. doi:10.1016/J.MSEA.2011.05.081.
- [62] P.W. Bridgman, *Studies in Large Plastic Flow and Fracture, with Special Emphasis on the Effects of Hydrostatic Pressure*, 1964.
- [63] W. Kurz, R. Trivedi, Rapid solidification processing and microstructure formation, *Mater. Sci. Eng. A.* 179–180 (1994) 46–51. doi:10.1016/0921-5093(94)90162-7.
- [64] S. Ghosh, L. Ma, L.E. Levine, R.E. Ricker, M.R. Stoudt, J.C. Heigel, J.E. Guyer, Single-Track Melt-Pool Measurements and Microstructures in Inconel 625, *Jom.* 70 (2018) 1011–1016. doi:10.1007/s11837-018-2771-x.
- [65] S. Kou, *WELDING METALLURGY*, 2nd Editio, A JOHN WILEY & SONS, INC., 2003.

## **Chapter 5: Microstructure and Mechanical Properties of Difficult to Weld Rene 77 Superalloy Produced by Laser Powder Bed Fusion**

---

Chapters 3 and 4 investigated the microstructure, heat treatment, room, and elevated temperature tensile deformation of the alloy R41, having moderate weldability. They provide a better understanding of the LPBF processing of precipitation hardenable Ni-base superalloys and design of property-oriented heat treatments for the unique microstructure of the LPBF parts. The gained knowledge has been transferred for LPBF processing of a difficult to weld alloy, R77, in this chapter. This chapter demonstrates that it is possible to fabricate crack-free, dense parts of a high  $\gamma'$  containing alloy just by process parameter modification. It is also possible to modify the existing standard heat treatments for the unique microstructure observed in LPBF to prevent cracking during heat treatment and to achieve the desired elevated temperature mechanical properties. This chapter also provides insight on the microstructural stability during short term exposures to elevated temperatures. The results showed that even though the microstructure of the alloy remains the same, thermally activated deformation mechanisms strongly affects the mechanical behavior of the parts.

This chapter has been published as: S.E. Atabay, O. Sanchez-Mata, J.A. Muñiz-Lerma, M. Brochu, Microstructure and mechanical properties of difficult to weld Rene 77 superalloy produced by laser powder bed fusion, Mater. Sci. Eng. A. 827 (2021).

## 5.1. Abstract

Fabrication of  $\gamma'$  precipitation strengthened nickel-based superalloys via laser powder bed fusion still remains a challenge. In this study, Rene 77, a high  $\gamma'$  containing superalloy that is considered as difficult to weld, was processed by laser powder bed fusion. Crack-free parts with high density were fabricated without any compositional modifications or preheating of the built plate. This defect-free structure was maintained upon solutionizing and aging heat treatment. The microstructure of the samples has been characterized in detail following the fabrication and after the heat treatment. Scanning electron microscopy analysis revealed that the as-built microstructure consists of columnar grains mainly aligned in the  $\langle 100 \rangle$  direction along with extremely fine  $\gamma'$  precipitates and spherical cell boundary carbides. The grain structure and texture were unaffected by the applied heat treatment due to the pinning effect exerted by the carbide particles. Development of a bimodal  $\gamma'$  distribution including cuboidal primary and spherical secondary precipitates was observed in the heat-treated sample. Additional carbide formation as a discontinuous grain boundary film was also seen. Tensile deformation behavior for both conditions was also tested at room temperature and 810 °C. Measured strength values for all test conditions were higher compared to a wrought and heat-treated alloy tested at room temperature. The as-built sample showed hardening and loss of ductility during elevated temperature testing due to  $\gamma'$  precipitation at the test temperature. The microstructure of the heat-treated sample was not altered during testing at 810 °C. However, improved elongation behavior and transition in fracture mode from cleavage to ductile fracture were observed due to microtwin formation at elevated temperatures.

## 5.2. Introduction

Nickel based superalloys are unique high temperature materials due to their resistance to mechanical and chemical degradation at temperatures up to 1000°C and beyond [1]. They have found a variety of applications in aircraft, marine and industrial gas turbines, rocket engines, nuclear reactors, and petrochemical equipment [2]. The high temperature properties of these alloys strongly depend on their composition and microstructural constituents [3]. Rene 77 (R77) is a precipitation hardened superalloy with high  $\gamma'$  volume fraction, designed to operate at a temperature between 730- 900 °C [4]. It is often used in hot gas turbine engine parts, such as vanes

blades and discs [5]. The properties of these nickel-based superalloy parts are determined by the microstructural features such as grain size and morphology, size and distribution of the  $\gamma'$  and carbide phases [6–8]. Control of the microstructure is crucial for the production of parts that fulfill the basic requirements for aerospace applications. Turbine blades made out of R77 having coarse and inhomogeneous grain structure were commonly reported for conventional casting [9,10]. It is reported that incorporation of the grain size control results in improved mechanical performance [9]. Control of the microstructure is possible through the control of solidification front velocity and cooling rate during solidification [11,12]. Therefore, the application of new processing techniques that would yield better microstructural control for the fabrication of high temperature parts would improve their service life as well as room and high temperature mechanical properties.

Laser Powder Bed Fusion (LPBF) is an attractive candidate as a processing route that offers design flexibility by allowing the production of complex metallic parts with reduced material waste, production cost, and time [13–15]. Additionally, LPBF makes it possible to obtain microstructures that are comparable to those of directionally solidified or single crystalline superalloys [16,17]. Despite all the advantages of LPBF, the process requires precise control over the process parameters to produce defect-free parts. A variety of parameters such as layer thickness, scan speed, laser raster path, hatch spacing, laser power, etc., as well as powder characteristics, should be carefully tailored to fabricate parts from advanced alloys to meet severe industrial requirements [18,19]. Another challenge in LPBF is the repetitive heating and cooling cycles that lead to high residual stresses, which at the end can cause cracking, especially for high  $\gamma'$  containing alloys [20]. Hence, the processability of these alloys by LPBF is limited and they are considered difficult to weld [21,22]. To date, LPBF processing of various crack susceptible alloys including Hastelloy X [20,23], CM247LC [24], IN738 [25] has been studied. Grange et.al reported minimization of cracking in IN738 and R77 alloys by controlling the molten pool dimensions and overlapping [26]. Modification of alloy composition or preheating the base plate were reported as effective ways to mitigate the cracking during LPBF fabrication of precipitation strengthened superalloys [27]. Engeli et.al reported the crack-free fabrication of IN738LC when the Si content kept lower than 0.02% [28]. Hagedorn et.al obtained crack-free MAR-M247 samples when the base plate was heated up to 1200 °C [29]. However, to the best of our knowledge, crack-free processing of a high  $\gamma'$  containing alloy by LPBF, without modifying the composition or the process, has never been reported before.

In the present study, a high  $\gamma'$  containing superalloy R77 was processed with LPBF, and crack-free parts were obtained. Density, microstructure, and tensile properties of the LPBF-fabricated R77 parts were investigated in as-built (AB) and heat-treated (HT) conditions. Grain morphology and texture, as well as the size, morphology, and distribution of carbides and  $\gamma'$  precipitates, were studied for both conditions. Tensile properties, deformation behaviors, and fracture morphologies were also investigated at room temperature and 810 °C.

### 5.3. Materials and Methods

Gas atomized R77 powder sourced from Praxair Surface Technologies, with the composition displayed in Table 5.1, was used in this study. As shown in Figure 5.1(a), the starting powder was mostly spherical in morphology with the presence of few irregularities and satellites attached to the powder particles. Particle size distribution (PSD) was measured by LA-920 Horiba laser particle size analyzer and the results are shown in Figure 5.1(b). The PSD analysis showed an asymmetrical normal distribution with  $D_{10}$ ,  $D_{50}$ , and  $D_{90}$  values of 19, 29, and 49  $\mu\text{m}$ , respectively.

Table 5.1. Chemical composition of the R77 powder as per the certificate of conformity.

Element	Al	Cr	Co	Mo	Ti	Si	C	Ni
wt.%	4.30	14.76	15.18	4.20	3.30	0.02	0.08	bal.

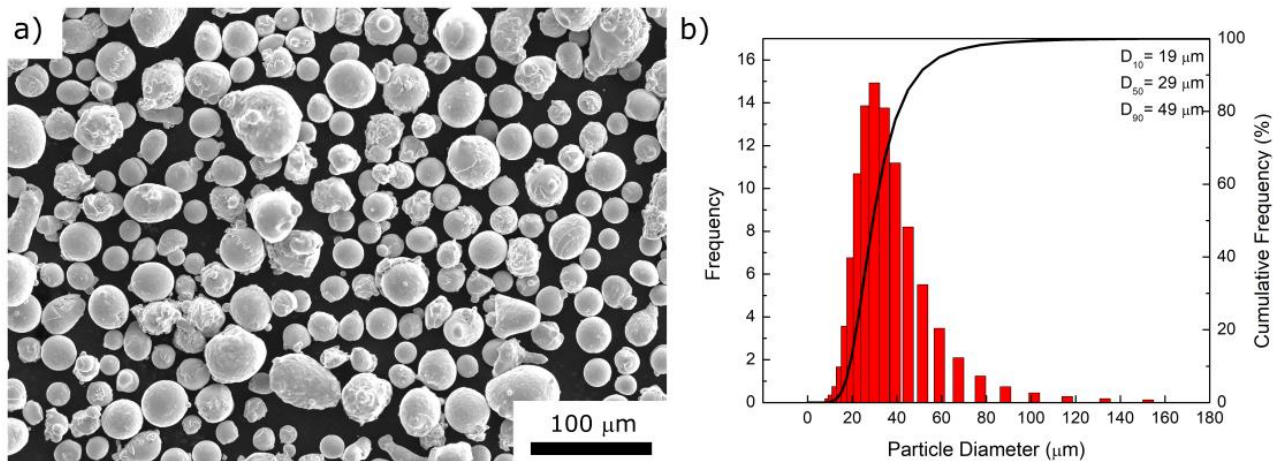


Figure 5. 1. (a) Morphology, (b) PSD of the starting R77 powder.

The samples used in this study were fabricated with a Renishaw AM400 LPBF system equipped with a reduced build volume chamber using an Nd: YAG laser with a maximum power output of 400W and a beam diameter at the focus of  $\sim 70$   $\mu\text{m}$ . The process was conducted under Ar gas atmosphere with  $\text{O}_2$  levels lower than 300 ppm. A bi-directional scanning strategy was used for the sample fabrication with an equivalent volumetric energy density of  $100 \text{ J/mm}^2$ . Two different geometries (cubes and bars) were fabricated on a stainless-steel build plate. Cubes with dimensions of  $10 \times 10 \times 10$  mm were used for microstructural analysis and bars of  $10 \times 10 \times 55$  mm with their long axis aligned with the building direction were prepared for room and elevated temperature tensile testing. After fabrication, the samples were subjected to a two-step sub-solvus precipitation hardening heat treatment (HT) which is a modified version of the standard heat treatment for R77 [30]. The samples were solutionized at  $1080$   $^\circ\text{C}$  for 4 h then air cooled to room temperature followed by an aging treatment at  $760$   $^\circ\text{C}$  for 24h. The HT was conducted under Ar atmosphere to prevent any compositional change due to oxidation.

The AB and HT cube samples were sectioned parallel to the building direction. Bulk densities of the samples were measured using the Archimedes method. Then the samples were then mounted, ground up to 600 grit SiC paper, and polished using 9, 3, and 1  $\mu\text{m}$  diamond suspension. Final polishing of the samples was done with a  $0.05$   $\mu\text{m}$  colloidal silica suspension on a Vibromet 2 polisher [31]. Nikon Epiphot 200 optical light microscope equipped with Clemex Vision system was used for the optical imaging of the polished cross-section. Fifteen micrographs from different parts of the samples were analyzed using image analysis software Image J [32] to calculate the relative optical density.

Texture and grain morphology of the samples were analyzed by electron backscattered diffraction (EBSD) using a Hitachi SU3500 scanning electron microscope (SEM). Operating conditions were 15 kV and 2  $\mu\text{m}$  step size. Raw data obtained from the EBSD analysis were analyzed using Aztec data analysis software combined with the HKL Channel 5 data processing software. Pole figures of the  $\{100\}$ ,  $\{110\}$  and  $\{111\}$  planes were extracted from the EBSD data using a half width of  $10^\circ$  and a cluster size of  $5^\circ$ . Electro-etching was performed in a 12 ml  $\text{H}_3\text{PO}_4$ , 40 ml  $\text{HNO}_3$ , 48 ml  $\text{H}_2\text{SO}_4$  at 6 V for 15 s to reveal the microstructure [33]. A Hitachi SU8000 STEM equipped with an energy dispersive spectrometer (EDS) was used for microstructural analysis. Five different regions on the samples were imaged and the obtained micrographs were analyzed using the line intercept method in Image J to determine the primary dendrite arm spacing (PDAS), along with the size and distribution

of the  $\gamma'$  precipitates. Approximately 100 measurements were conducted and averaged. For scanning transmission electron microscopy (STEM), approximately 50 to 70  $\mu\text{m}$  thick discs with 3mm diameter were prepared. The discs were then jet-polished for electron transparency using a perchloric acid/methanol solution (ratio 1:3) at  $-30\text{ }^\circ\text{C}$  with 25 V voltage. STEM imaging was also conducted in Hitachi SU8000 STEM.

Round bars with a reduced cross-section of 4 mm and a gauge length of 16mm were machined from the LPBF fabricated bars for tensile testing according to ASTM E8/E8M-16a [34]. Two samples for both AB and HT conditions were tested at room temperature (RT) according to ASTM E8/E8M-16a [34] and  $810\text{ }^\circ\text{C}$  according to ASTM E21-17 [35].  $810\text{ }^\circ\text{C}$  was selected as the testing temperature to prevent the issues related to the loss of oxidation resistance, at higher temperatures. The samples were tested with a strain rate of 0.005 mm/mm/min up to yield and 0.05 mm/mm/min until fracture. For the elevated temperature testing, the samples were soaked at the test temperature for 30 minutes prior to testing. The tested samples for each condition were mounted and their cross-sections were prepared using the same metallographic techniques for post-fracture analysis.

EBSD analysis was carried out near the fracture site of the tested samples to investigate the plastically deformed microstructures. Step sizes of 0.6 and 0.2  $\mu\text{m}$  were used for the post-fracture EBSD analysis. The Hitachi SU8000 SEM was used for the microstructural analysis of the tested samples after elevated temperature exposure. Fracture surfaces of the samples in each condition were also analyzed using SEM.

## **5.4. Results and Discussion**

### **5.4.1. Density**

The relative optical density of cube samples was measured through image analysis on as-polished micrographs. A representative micrograph of the cross-section of an as-fabricated cube is shown in Figure 5.2(a). The samples were fully dense with a relative density of  $99.96 \pm 0.03\%$ . To further demonstrate the absence of defects in the as-built condition higher magnification images of the top, middle, and bottom sections of the sample were also displayed in Figure 5.2(a), (b), and (c). The same procedure was performed on samples after HT and an optical density of  $99.94 \pm 0.06\%$  was measured. It is important to note that no cracks were observed throughout the samples' cross-sections for both the AB and HT conditions. Densities of the cube samples were also measured by

using the Archimedes method in order to assess the bulk density. Archimedean densities of the samples in AB and HT conditions were  $\sim 7.88$ , and  $\sim 7.89$   $\text{g/cm}^3$  respectively. These values are 99.6 and 99.8 % of the theoretical bulk density of the alloy ( $\sim 7.91$   $\text{g/cm}^3$ ) [36]. These results are also in good agreement with the measured optical densities.

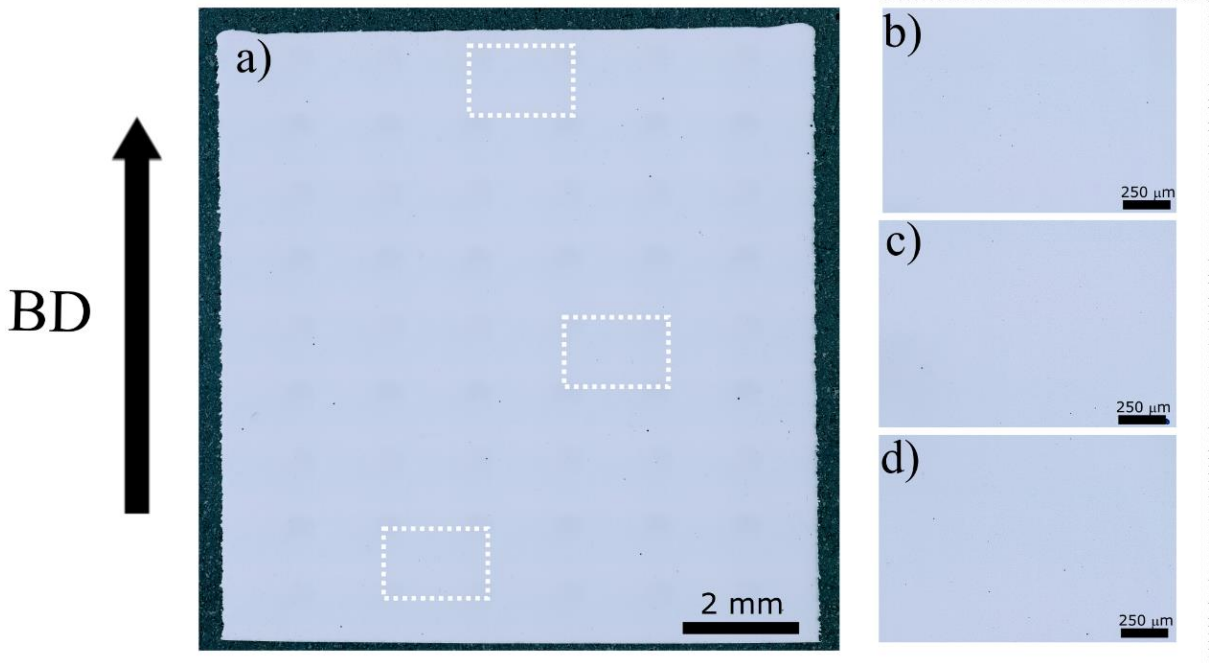


Figure 5. 2. As-polished micrograph of the (a) entire cross-section of the AB sample along with the higher magnification images from (b) top, (c) middle, and (d) bottom sections.

## 5.4.2. Microstructural Comparison of AB and HT Samples

### 5.4.2.1 Grain Morphology and Texture

EBSD analysis was conducted to investigate the crystallographic texture and grain morphology of the samples in the AB and HT conditions. IPF orientation maps along with the corresponding pole figures obtained from the respective cross-sections are presented in Figure 5.3. The grain boundaries are denoted as black lines in the orientation maps for misorientations greater than  $15^\circ$ . The IPF orientation map of the AB sample in Figure 5.3(a) reveals a columnar grain morphology that is parallel to the building direction. This type of grain morphology occurs due to the epitaxial growth of the  $\gamma$  grains across several layers during processing and is commonly reported for LPBF-

fabricated superalloys [37–39]. The corresponding pole figures of the AB sample indicate a strong cube texture, predominantly aligned along the  $\langle 100 \rangle$  direction. The orientation distribution of the grains was represented by the multiples of uniform density (MUD) and a maximum intensity value of 10.12 was observed. The diameter and aspect ratio of the grains were also measured from the 1 mm<sup>2</sup> region of the orientation maps. The line intercept method gave an average diameter of  $19.2 \pm 11.6 \mu\text{m}$  where 90 % of the measured grains had a diameter below 53  $\mu\text{m}$ . The aspect ratio was determined by taking the length over width ratio of the fitted ellipses to the grains. The average aspect ratio was calculated to be  $4.3 \pm 1.8$  which fit the columnar nature of the grains.

The columnar grain structure oriented along the  $\langle 100 \rangle$  direction was maintained after the solutionizing and aging HT, as depicted in Figure 5.3(b). The strong cube texture was still present with a similar maximum intensity value of 10.20 MUD. Similar to texture, grain size and shape quantifications for the HT sample were maintained. The average grain diameter was calculated as  $21.7 \pm 13.3 \mu\text{m}$  where the diameter of 90 % of the grains was smaller than 57  $\mu\text{m}$ . An average aspect ratio of  $4.3 \pm 2.0$  was calculated. Modification in the solidification grain morphology and texture is frequently observed during post processing heat treatment of the LPBF fabricated parts [40]. It is documented that large strain energy generated by the rapid heating and cooling cycles derives the grain growth or recrystallization of the grains [41]. However, in the present study, no noticeable grain growth or recrystallization of  $\gamma$  grains after the elevated temperature exposure was observed.

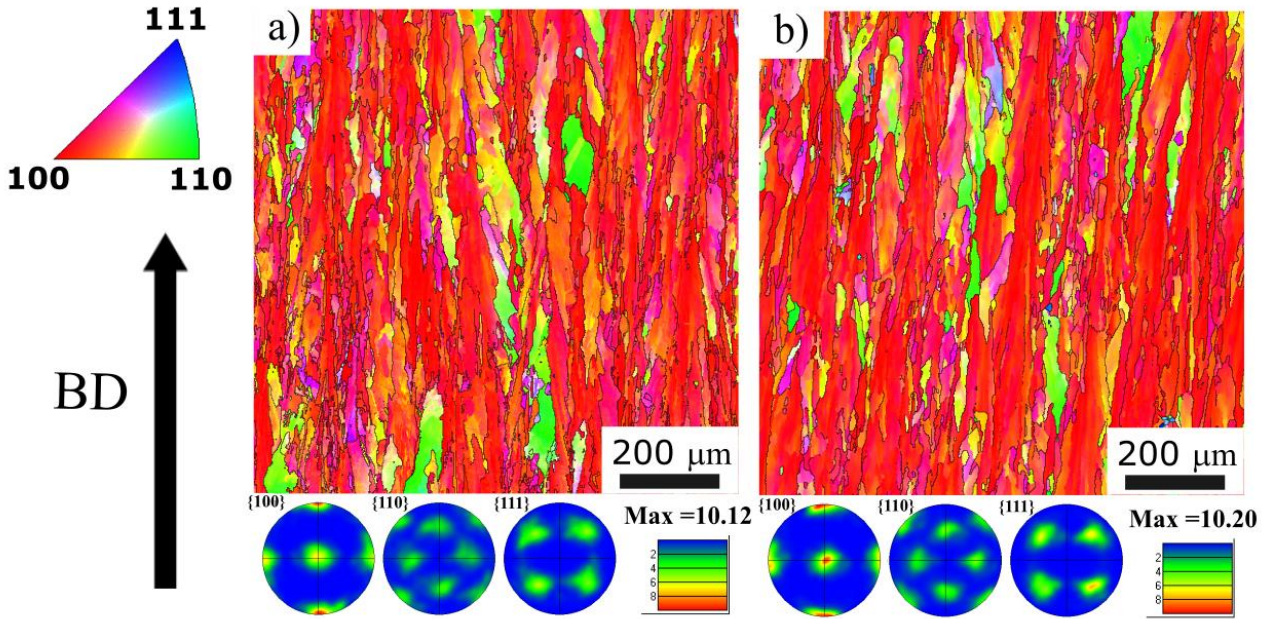


Figure 5. 3. IPF orientation maps and the corresponding pole figures for (a) AB and (b) HT samples.

#### 5.4.2.2. Characterization of the $\gamma'$ Precipitates

Detailed microstructural analysis for both AB and HT samples was conducted using SEM. Micrograph of the AB sample in Figure 5.4(a) shows a fine cellular solidification structure. It can be seen that cell growth is perpendicular to the bottom of the molten pool and parallel to the building direction, which is also the direction of the highest temperature gradient. Primary dendrite arm spacing (PDAS) was measured as  $0.45 \pm 0.14 \mu\text{m}$ , with no clear indication of secondary arms. This value of PDAS corresponds to a cooling rate of  $1.4 \times 10^6 \text{ }^\circ\text{C/s}$  during solidification, according to the equation;  $\text{PDAS} = \alpha \varepsilon^{-b}$  ( $\alpha = 50 \mu\text{m(K/s)}$  and  $b = 1/3$  for Ni-based superalloys) [38,42].

Closer examination of the AB microstructure in Figure 5.4(b) reveals the presence of nearly spherical  $\gamma'$  precipitates within the cellular structure. STEM image on the inset also clearly shows the presence of the spherical precipitates. The size of the  $\gamma'$  precipitates was measured using the line intercept method and their size distribution is displayed in Figure 5.4(c). The precipitates in the AB condition were extremely fine with a size below 12 nm. Although R77 is a high  $\gamma'$ -fraction alloy, precipitation and growth of the  $\gamma'$  precipitates were limited during fabrication due to short thermal cycles encountered in LPBF. The absence or very fine observable  $\gamma'$  precipitates below 50

nm was also reported previously for other LPBF -fabricated high  $\gamma'$  - fraction alloys such as CM247 [43] and IN738LC [44].

Upon heat treatment, the dissolution of molten pool boundaries was observed along with the growth and further precipitation of  $\gamma'$  precipitates (Figure 5.5(a)). Both the SEM micrograph and the precipitate size histogram of Figure 5.5(c) confirm the bimodal size distribution of  $\gamma'$ . The primary  $\gamma'$  was mostly cuboidal in shape with a size ranging between 200-550 nm. As the solutionizing heat treatment was conducted below the  $\gamma'$  solvus temperature, the precipitates observed in the AB condition grew along with the precipitation and growth of the new  $\gamma'$  particles resulting in the wide size distribution of the primary  $\gamma'$  precipitates in the HT samples. The following aging treatment resulted in the formation of fine secondary  $\gamma'$  precipitates with sizes smaller than 90 nm. The high magnification micrograph of the secondary  $\gamma'$  in Figure 5.5(b) shows the mostly spherical morphology of these precipitates.

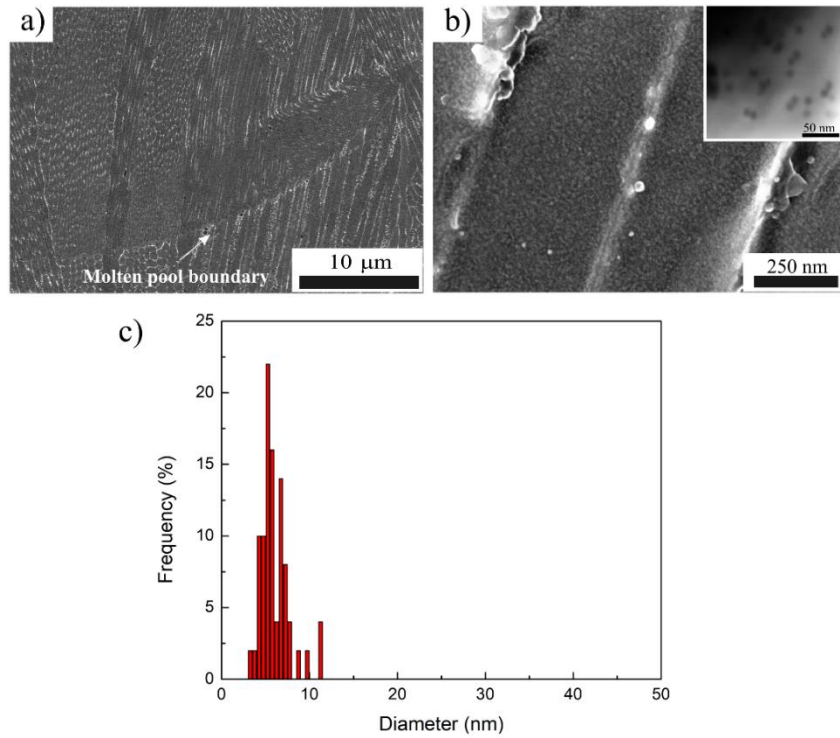


Figure 5. 4. (a) and (b) SEM micrographs; (c) size distribution of  $\gamma'$  precipitates in AB condition.

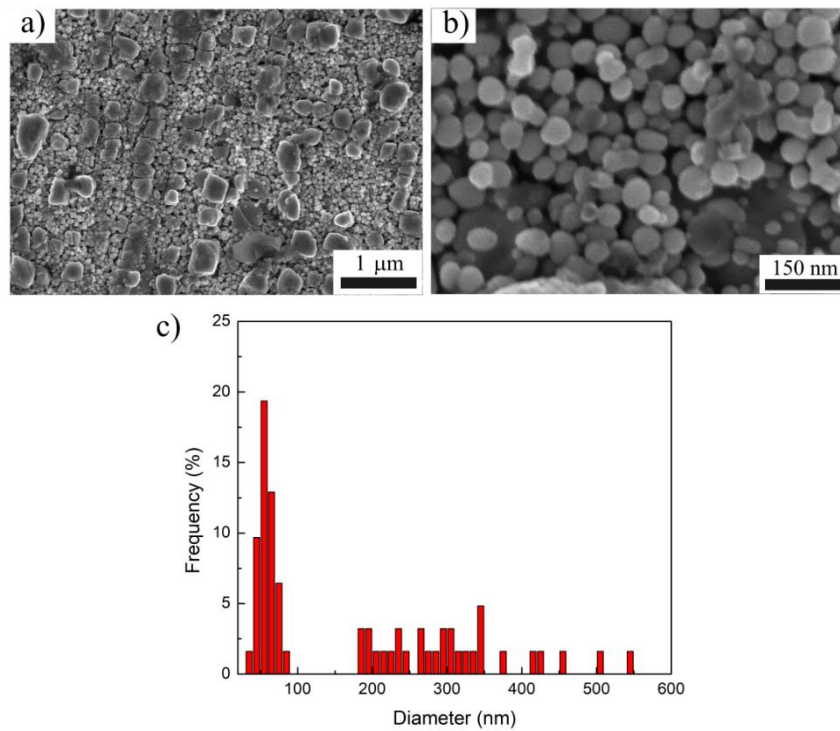


Figure 5. 5. (a) and (b) SEM micrographs; (c) size distribution of  $\gamma'$  precipitates in HT condition.

### 5.4.2.3. Characterization of the Carbides

The imaging of the microstructure under backscattered electron (BSE) contrast in Figure 5.6(a) showed the presence of dark particles with spherical morphology along the cell boundaries in the AB sample. The size of these fine discrete particles was measured as  $39 \pm 7$  nm. EDS line scan analysis conducted on these particles revealed that they are enriched in Ti and Mo, suggesting that these are (Ti, Mo)C particles (Figure 5.6(c)). These two elements are known to segregate in the liquid phase during solidification due to their partition coefficients [3,45]. Interaction of Ti and Mo with the carbon results in the formation of the MC carbides on the cell boundaries [46]. The formation of Ti-rich MC carbides during solidification was previously reported for a cast R77 alloy [5]. However, in the cast alloy, these carbides were large blocky particles in contrast to the fine spherical carbides observed in the LPBF microstructure. This difference in the carbide morphology can be attributed to the significantly higher cooling rates of the LPBF compared to casting. It is suggested that C is distributed over a larger grain boundary area due to the fine grain structure obtained in LPBF [47], resulting in the very fine and highly dispersed carbide morphology observed in the AB condition. MC carbides are known to be very stable at low temperatures but tend to dissociate into secondary carbides at higher temperatures by the following reaction [48]:

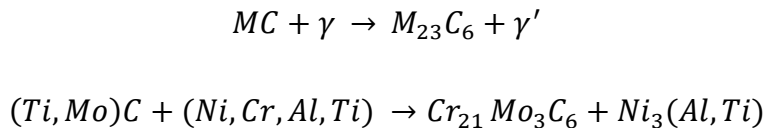


Figure 5.6(b) and (d) clearly reveal that such reactions took place during the heat treatment of R77 parts. The fine discrete carbide particles were still visible in the HT condition, and they are mostly rich in Ti. Therefore, it can be said that the Ti-rich MC carbides were stable through the heat treatment but have coarsened with their size increasing to  $61 \pm 6$  nm. Additionally, a discontinuous grain boundary film with an average thickness of  $82 \pm 18$  nm was detected in the HT structure. The EDS analysis shows that the grain boundary films are enriched in Cr, Mo, and C, which proves the formation of  $M_{23}C_6$  carbides via the aforementioned reactions.

Many studies report that the presence of carbide particles retards the recrystallization of grains or the migration of grain boundaries by grain boundary pinning [33,49,50]. As previously discussed, the solidification grain structure of the present samples remained after the HT. Hence, it could be

concluded that the presence of stable MC carbides along with the formation of  $M_{23}C_6$  carbides are the main reasons why the grain structure remained unchanged upon exposure to solutionizing and aging heat treatments at 1080 and 760 °C, respectively.

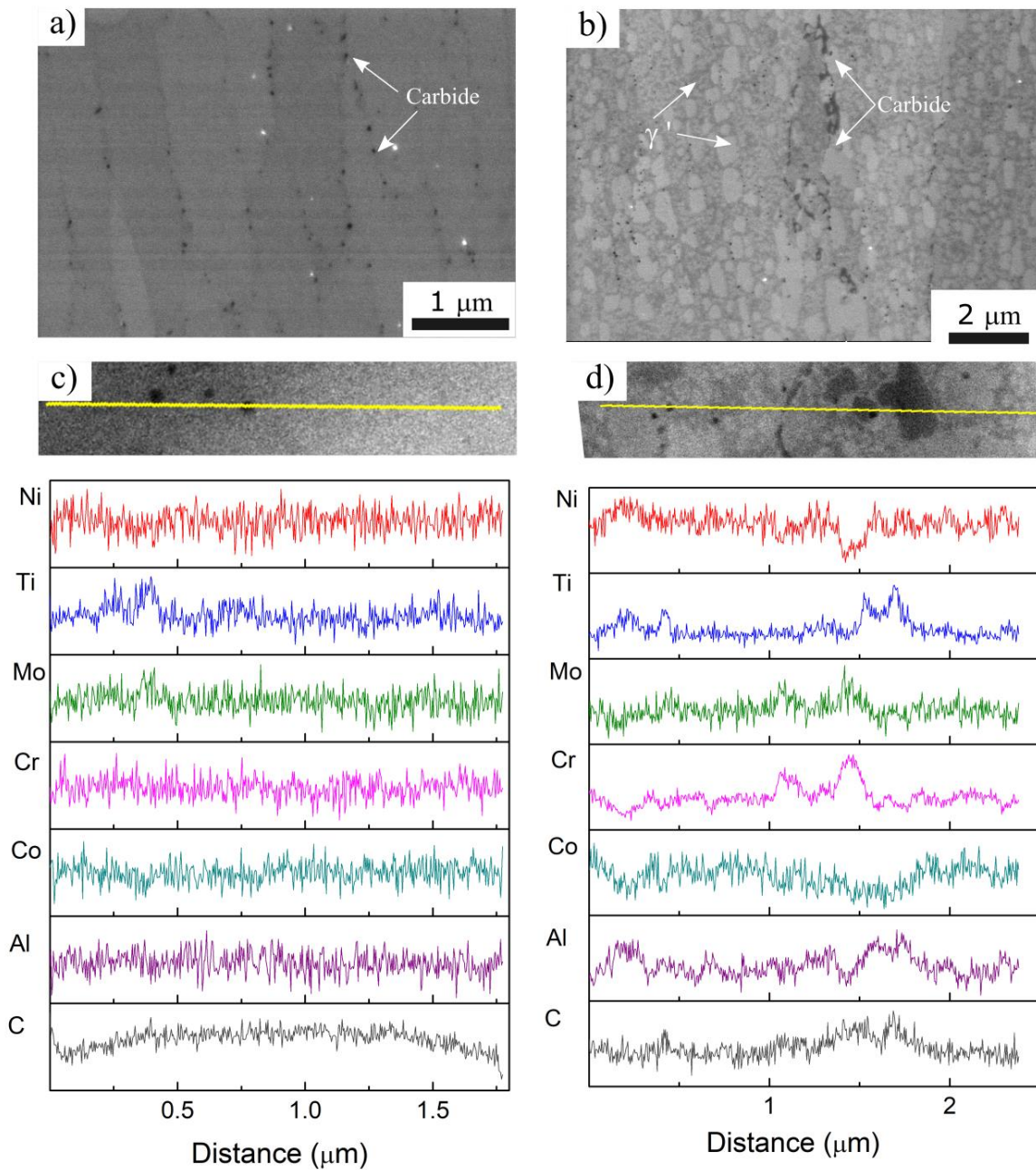


Figure 5. 6. SEM micrographs and corresponding EDS linescan analysis in (a) and (c) AB; (b) and (d) HT conditions.

### **5.4.3. Room Temperature Tensile Deformation Behavior**

#### **5.4.3.1. Room Temperature Tensile Properties**

Room temperature yield strength (YS), ultimate tensile strength (UTS), and elongation for the R77 samples in AB and HT conditions are presented in Figure 5.7(a) and (b). As shown, the AB samples exhibited an average YS, UTS, and elongation values of 723 MPa, 912 MPa, and 55%, respectively. When the samples were subjected to the HT, an increase of approximately 36 % in both YS and UTS values was observed along with an approximately 50% reduction in elongation. The measured average RT YS, UTS, and elongation values for the HT samples were 989 MPa, 1231 MPa, and 28 %, respectively. The minimum room temperature YS and UTS of 760 and 860 MPa reported for wrought R77 alloy subjected to a solutionizing and aging heat treatment were added as a black dashed line to Figure 5.7(a) and (b) for comparison [51]. Both AB and HT LPBF strength values are well above the comparative wrought UTS. In addition, three other, high  $\gamma'$  containing alloys fabricated by LPBF and tested in AB and HT conditions are shown in Figure 5.7 for further benchmarking. As shown in Figure 5.7(a), when subjected to HT, both YS and elongation of the R77 samples are higher compared to the other high  $\gamma'$  containing alloys. Furthermore, as shown in Figure 5.7(b), the UTS of R77 in AB condition is approximately 100 MPa higher compared to ABD850AM and 200 MPa lower compared to IN939 alloys. Although the strength values are similar, the elongation observed in the LPBF fabricated R77 is approximately two times higher compared to the other alloys.

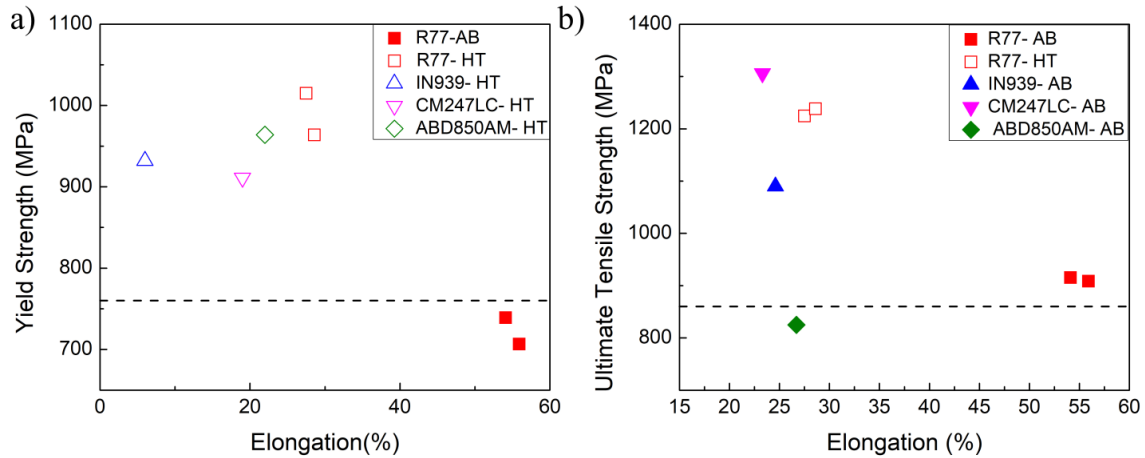


Figure 5. 7. (a) YS vs. elongation (b) UTS vs. elongation of R77 in AB and HT conditions and their comparisons to other high  $\gamma'$  containing alloys at RT [52].

Even though the AB samples microstructure contains only very fine (<12 nm)  $\gamma'$  particles, it was observed that their RT strength exceeded the strength of age hardened wrought parts, while retaining high elongation. This combined gain in strength and elongation was also previously reported for LPBF IN738LC alloy, the gain attributed to dislocation strengthening combined with the fine AB cellular microstructure [47]. It is reported that the AB structure is strengthened by the cell walls having extremely high dislocation densities impeding the dislocation movement. This large amount of dislocations and their heterogeneous distribution is believed to be a result of the rapid heating and cooling cycles involved in the LPBF process [53].

Grain boundary strengthening is also known as an active strengthening mechanism, especially during room temperature deformation [54]. It is well known that the presence of high angle grain boundaries acts as a barrier to dislocation motion and strengthens the material, this gain of strength is inversely proportional to the grain size [55]. However, for the present study, the results shown in section 3.2. suggested that the grain sizes of the AB and HT samples were similar; hence the contribution of grain boundary strengthening to the overall strength would be similar for these two conditions.

The significant increase in strength after HT can be explained by the difference in  $\gamma'$  size distribution and volume fraction of AB and HT samples. The effective mechanism of precipitation strengthening is dictated by the dislocation-particle interactions, which are directly dependent on the precipitate size. One of the main strengthening mechanisms is through the shearing of the  $\gamma'$

precipitates by a pair of dislocations. For small precipitates (less than approximately 20 nm), each dislocation composing the dislocation pair is located within a different precipitate. This situation is referred as weak pair coupling [54,55]. For the larger precipitates, the dislocation pair is found within the same particle, which is referred as strong pair coupling [54,55]. Kozar et.al. reported that the active mechanism changes from weak pair coupling to strong pair coupling as the size of the  $\gamma'$  precipitates increase. When the particle size is even larger (approximately more than 400nm), the stress required to shear the particles are greater than the stress required to bow between the precipitates [56]. In this case, the Orowan looping mechanism is observed. However, Preuss et al. suggested that Orowan looping is not commonly seen in polycrystalline Ni-based superalloys with  $\gamma'$  particle diameter less than 400 nm due to the small values of misfit or the complexity of the bi- or tri-modal  $\gamma'$  particle size distributions [56,57]. Hence the most plausible contribution of precipitation strengthening for the AB condition would be particle shearing by weak pair coupling as its microstructure consists of fine  $\gamma'$  precipitates that are smaller than 20 nm. On the other hand, the HT samples have a bimodal distribution of precipitates with a size range of 30-550 nm. Therefore, it could be said that both particle shearing and Orowan looping are possible strengthening mechanisms. It could be concluded that the change in the size distribution of the  $\gamma'$  precipitates during the HT resulted in a change in the active precipitation strengthening mechanism. Additionally, precipitation of the secondary  $\gamma'$  particles resulted in an increase in the fraction of  $\gamma'$ , meaning that contribution to the strengthening would be higher. This change in the strengthening mechanism and the  $\gamma'$  volume fraction led to an increase in the strength along with the decrease in the elongation observed in the HT samples.

#### **5.4.3.2. Room Temperature Deformation Behavior**

EBSD analysis was performed on the cross-sections of the tested samples near the fracture surface to better understand the deformation behavior. Figure 5.8 shows the EBSD analysis of the AB sample parallel to the loading direction (LD) after the room temperature testing. As seen in the IPF orientation map and corresponding IPF of Figure 5.8(a), the grains are mainly aligned along the  $\langle 100 \rangle$  and  $\langle 111 \rangle$  directions. Rotation of the crystal lattice by deformation is a commonly observed phenomenon in Ni-based superalloys [58]. Previous studies conducted on single crystalline samples showed that the FCC crystal deforms mainly by glide on the  $\{111\}\langle 011 \rangle$  or  $\{100\}\langle 011 \rangle$  slip systems [59]. Therefore, it could be hypothesized that the deformed grains

showed lattice rotation towards  $\langle 100 \rangle$  and  $\langle 111 \rangle$  directions depending on their initial orientations. The IPF orientation map and band contrast image of an enlarged region composed of grains of both  $\langle 100 \rangle$  and  $\langle 111 \rangle$  orientations are presented in Figure 5.8(b) and (c). Presence of parallel arrays of slip bands angled at approximately  $35^\circ$  along the tensile loading direction for the  $\langle 111 \rangle$  oriented grains and at  $45^\circ$  for the  $\langle 100 \rangle$  oriented grains, corresponding to  $\langle 110 \rangle$  slip orientation, were observed. These slip bands are found to be high strain regions and pointed out with arrows in the Kernel average misorientation (KAM) map of Figure 5.8(d). Additionally, EBSD analysis showed that these slip bands are mainly restricted within the cell, proving that the dislocation strengthening by the cell walls is an active strengthening mechanism during RT deformation of the AB sample.

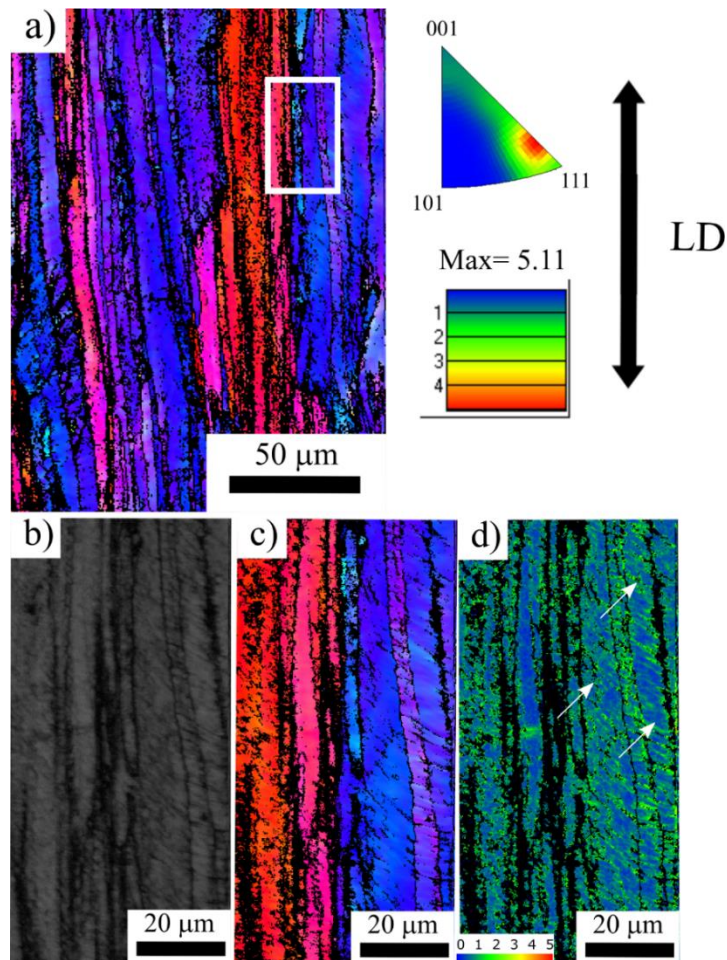


Figure 5. 8. EBSD analysis of the AB sample tested at RT (a) IPF orientation map and its corresponding inverse pole figure along the LD. (b) Band contrast, (c) IPF orientation map, and (d) misorientation map of the selected enlarged region highlighting the slip bands.

In the case of the HT R77 samples tested at RT, the EBSD analysis revealed that the deformed grain structure was again mainly aligned along the  $\langle 111 \rangle$  and  $\langle 100 \rangle$  directions, as shown in Figure 5.9(a). As opposed to the AB sample, slip band formation was not observed in the deformed microstructure of the HT sample. Band contrast image of Figure 5.9(b) shows the presence of dislocation structures lying within the cell boundaries of the grains that are mainly oriented along  $\langle 100 \rangle$  direction. The dislocation substructure appears as dark irregular stripes due to severe lattice distortion during tensile deformation. These highly distorted regions can also be seen in the corresponding IPF map of Figure 5.9(c) and of the KAM map of Figure 5.9(d) for these regions. The KAM map also shows that the strain within the cells was significantly less compared to the AB samples meaning that the HT sample has undergone less plastic deformation during tensile testing. Instead, the deformation in the HT sample was more localized in certain regions. These results are in agreement with the lower elongation of the HT sample compared to the AB sample and suggest that they exhibited different deformation behaviors. Previous research showed that RT deformation of precipitation strengthened superalloys mainly takes place by the formation of stacking faults (SF) or antiphase boundaries (APB) within the  $\gamma'$  by the partial dislocations [60,61]. Although the EBSD analysis showed the presence of dislocation lines in multiple slip directions, no evidence of the presence of SF and APB is visible within its resolution limits.

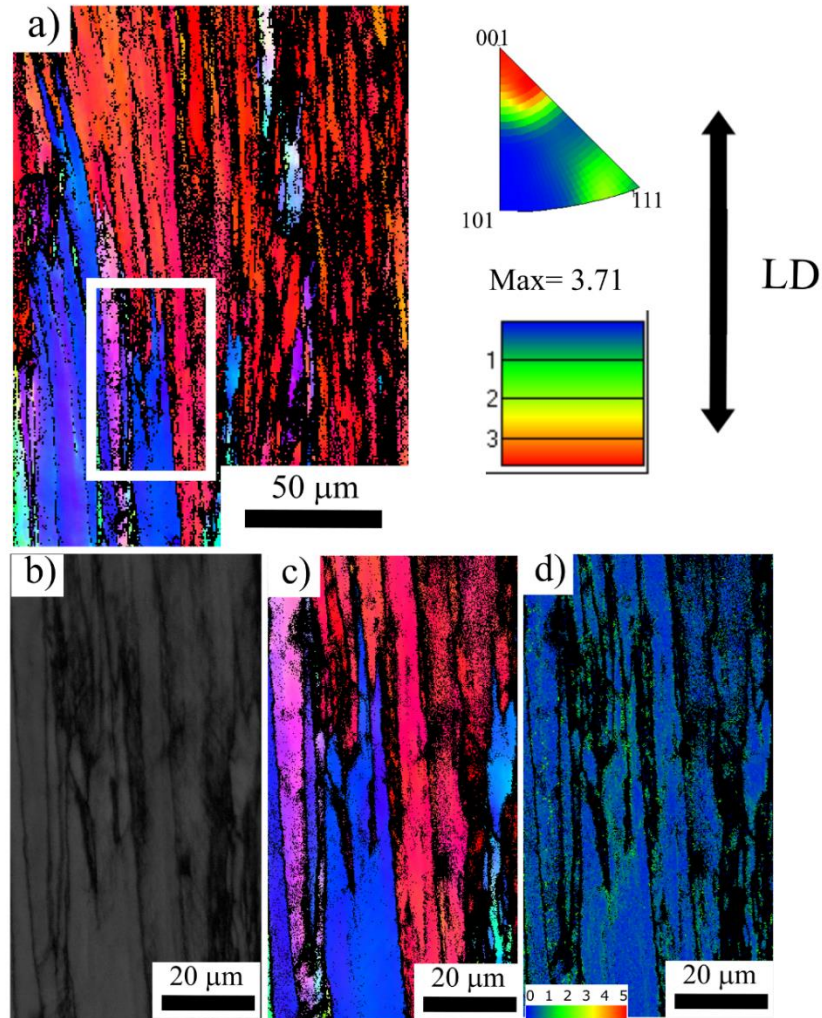


Figure 5. 9. EBSD analysis of the HT sample tested at RT (a) IPF orientation map and its corresponding inverse pole figure along the LD. (b) Band contrast, (c) IPF orientation map, and (d) misorientation map of the selected enlarged region.

#### 5.4.4. Elevated Temperature Tensile Deformation Behavior

##### 5.4.4.1. Microstructural Modifications During Elevated Temperature Testing

Microstructural characterization was conducted on the undeformed regions of the tested samples to investigate the effect of the elevated temperature exposure during testing on the  $\gamma'$  and carbide morphologies of the AB and HT samples. As shown in the SEM micrograph of the AB sample in Figure 5.10(a), the cellular substructure observed in the AB condition remained after the testing at

810°C. In addition, the presence of  $\gamma'$  precipitates with a unimodal size distribution ranging between 15-65 nm was observed. The volume fraction of these precipitates was measured as  $70 \pm 3$  %, suggesting that in addition to the growth of extremely fine precipitates observed in the AB condition, further precipitation of  $\gamma'$  occurred during the elevated temperature testing. In addition to the fine discrete particles observed at RT, coarser carbide particles were also visible on the cell boundaries in the polished micrograph of the AB sample of Figure 5.10(b). The size of these carbide particles was measured as  $63 \pm 3$  nm and their EDS analysis revealed that they were enriched in Cr, similar to the carbide particles formed after the HT. Therefore, it is believed that the elevated temperature exposure resulted in the formation of  $M_{23}C_6$  carbides as discrete particles on the cell boundaries, supporting that the temperature for the formation of  $M_{23}C_6$  carbides is below 810 °C for LPBF fabricated R77 alloy.

As opposed to the AB ones, the HT samples have not undergone significant microstructural modifications after testing at 810 °C. As seen in Figure 5.10(c), the microstructure of the HT sample after the elevated temperature exposure consists of spherical secondary and cuboidal primary  $\gamma'$  precipitates. Similar to the HT microstructure observed at RT, the size distribution of the secondary precipitates ranged between 20 – 95 nm while the primary precipitates had a size range of 200- 550 nm. These results show that the morphology and size distribution of the  $\gamma'$  precipitates were not altered during the testing at 810 °C. Both the discontinuous carbide film and discrete carbide particles were also maintained after testing, as shown in Figure 5.10(d). The average size of the discrete particles was measured as  $64 \pm 11$  nm and the thickness of the discontinuous film was  $81 \pm 17$  nm, which are statistically similar to the RT microstructure. Hence, the microstructure of the HT sample was stable during the short-term exposure to 810 °C.

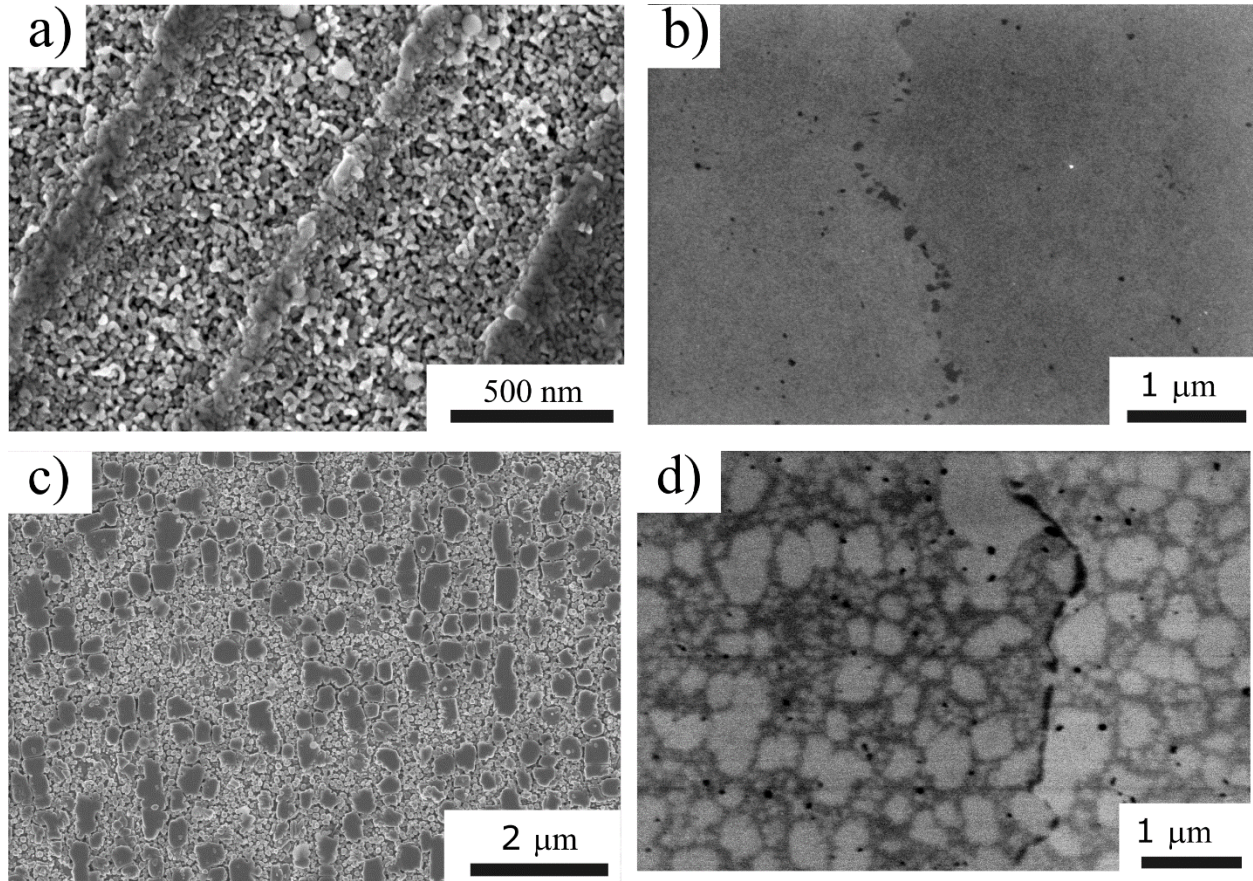


Figure 5. 10. SEM micrographs after testing at 810 °C in (a) and (b) AB, (c) and (d) HT conditions.

#### 5.4.4.2. Elevated Temperature Tensile Properties

The YS, UTS, and elongation of the R77 alloy both in AB and HT conditions was measured at 810°C. The results of the elevated temperature tensile test are shown in Figure 5.11, with an additional comparison with several other high  $\gamma'$  containing alloys in similar conditions. The average YS, UTS, and elongation values for the AB condition were 853 MPa, 956 MPa, and 15 %, respectively. In the HT condition, average YS, UTS, and elongation values of 800 MPa, 911 MPa, and 33% were measured. As depicted in Figure 5.11(a), the YS values observed for the HT sample are similar to the other alloys after being subjected to a similar heat treatment. However, the elevated temperature elongation of the R77 in HT condition was at least two times higher than the other high  $\gamma'$  containing alloys fabricated by LPBF.

**Fig 5.11(b)** reveals that the UTS of the R77 in AB condition is either higher or comparable with the CM247LC, IN939, and ABD850AM alloys. The AB R77 alloy also demonstrated a higher elevated temperature elongation at fracture compared to the other shown alloys in AB condition.

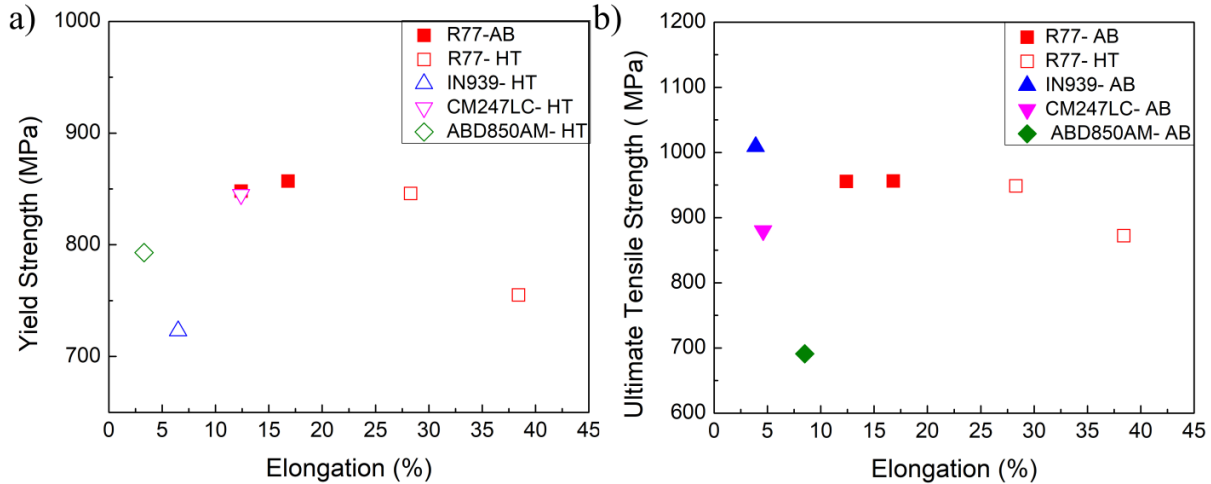


Figure 5. 11. (a) YS vs. elongation (b) UTS vs. elongation of R77 in AB and HT conditions and their comparisons to other high  $\gamma'$  containing alloys at 810 °C [52].

It is also worth discussing the difference in the tensile mechanical properties of the AB and HT samples when tested at RT and 810°C. Elevated temperature YS and UTS of the AB sample were found to be higher compared to the RT ones, whereas the elongation was significantly lower. On the contrary, HT samples had lower elevated temperature strength and higher elongation at break. The observed increase in the YS and UTS values, as well as the significant reduction in the elongation of the AB sample at 810 °C when compared to the RT testing, is attributed to the evolution of  $\gamma'$  during the elevated temperature testing.  $\gamma'$  precipitates with an average size of ~30 nm and a volume fraction of  $70 \pm 3$  % were observed after the elevated temperature exposure. This type of rapid hardening response and loss of ductility after such short soaking at elevated temperature was also reported for other precipitation hardenable superalloys [62].

No significant change in the  $\gamma'$  size distribution was observed for the HT sample after high temperature exposure. Therefore, the change in the observed strength and elongation at 810 °C indicates that a change in the deformation behavior has occurred during the elevated temperature testing. Details of the deformation mechanism will be further discussed hereinafter.

### 5.4.4.3. Elevated Temperature Deformation Behavior

EBSD analysis of the fractured AB sample after the elevated temperature deformation is displayed in Figure 5.12. The alignment of the grains in the orientation map and IPF in Figure 5.12(a) shows that the lattice rotation behavior at elevated temperature is similar to the RT deformation. Comparison of the degree of the rotation could not be made due to the circular geometry of the samples. The appearance of the parallel slip bands was again visible in the band contrast of Figure 5.12(b) and the IPF orientation map of Figure 5.12(c) for the magnified region. However, it is observed that these bands were lying along the length of multiple cells unlike the sample deformed at RT. Therefore, it could be inferred that slip transfer has occurred between the cells of the AB sample during the elevated temperature deformation and strengthening by dislocation walls on the cell boundaries was not an active mechanism at 810 °C. The KAM map in Figure 5.12(d) clearly shows that the stain is localized around the slip bands and a lower strain is observed between the bands, compared to the RT tested sample. Therefore, deformation was more localized in the sample tested at 810 °C. This change in the deformation behavior could be rationalized with the  $\gamma'$  precipitation during testing which in turn negatively affected the elongation at break in this sample. Additionally, the observed slip bands after the elevated temperature testing were wider compared to the RT one. The previous report for other Ni-based superalloys showed that the stress localization and the slip band width are related to the size of the  $\gamma'$  precipitates [63]. The wider slip bands observed in this sample could be explained by the larger size and volume fraction of the  $\gamma'$  precipitates and shows that multiple active glide planes were necessary to shear or overcome the precipitates.

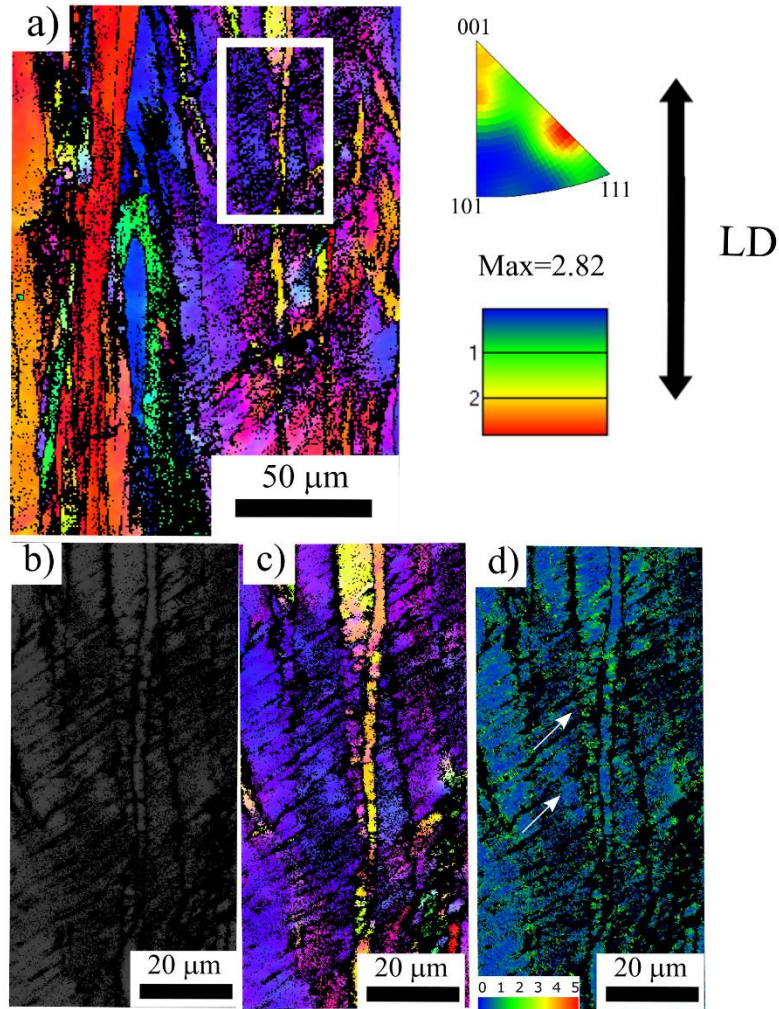


Figure 5. 12. EBSD analysis of the AB sample tested at 810°C (a) IPF orientation map and its corresponding inverse pole figure along the LD. (b) Band contrast, (c) IPF orientation map, and (d) misorientation map of the selected enlarged region highlighting the slip bands.

Results of EBSD analysis near the fracture surface analysis of the HT sample tested at 810 °C shown in Figure 5.13(a) revealed that the deformed grains are mainly rotated towards the  $\langle 111 \rangle$  and  $\langle 100 \rangle$  directions similar to the other three tested samples. The IPF orientation map and band contrast images of the highlighted region are shown in Figure 5.13(a) and (b), respectively. The formation of microtwins in the grains oriented along the  $\langle 111 \rangle$  orientation is clearly visible in the orientation map. Two different twin systems, oriented at approximately  $67^\circ$  from each other are detected. Misorientation profiles from each of these systems were taken and presented in Figure 5.13(e) and (f). As shown, the misorientation of each twin boundary from the  $\langle 111 \rangle$  oriented grain

is  $60^\circ$ , confirming that the observed traces are microtwins. This suggests that microtwinning is a thermally activated deformation mechanism for the LPBF fabricated R77 alloy tested at  $810^\circ\text{C}$ . Microtwinning is a mechanism that is mainly reported for intermediate or elevated temperature and low strain rate deformation of Ni-based superalloys [64]. Although the microtwins have a specific crystallographic orientation similar to deformation twins, it has been found that their formation mechanism is different [60]. The experimental and theoretical studies showed that microtwins are formed by diffusion assisted reordering of the ordered structure sheared by the  $a/6\langle 112 \rangle$  twinning partials. The dislocation partials operate on adjacent  $\{111\}$  glide planes shearing both  $\gamma$  and  $\gamma'$  phases. The thermally activated reordering process removes the wrong nearest neighbors at the complex stacking faults created by the twinning partials, resulting in the formation of microtwins [65,66]. In addition to the microtwin formation, a more homogeneous strain distribution was observed in the KAM map of this sample as shown in Figure 5.13(d) when compared to the RT tested one. Hence, the activation of the microtwinning mechanism during the elevated temperature testing of the HT sample leads to a more homogeneous deformation behavior compared to the RT one. The higher elongation of the HT sample at elevated temperature without significant loss in strength is ascribed to this behavior. Various contradictory claims have been made regarding the effect of microtwin formation on the elevated temperature mechanical properties of Ni-based superalloys. Kim et al reported a ductility minimum for wrought CM247LC, Haynes 230, Hastelloy X superalloys at a temperature range of  $760\text{-}860^\circ\text{C}$  due to microtwinning [67]. Similarly, embrittlement induced by the twin boundaries due to dislocation pile up was observed during creep deformation of a single crystalline alloy [65]. On the other hand, several researchers reported a simultaneous improvement in the elevated temperature tensile strength and elongation in Ni-Co based superalloys due to the formation of microtwins [60,68]. It is shown that the twin boundaries effectively interact with dislocations and stacking faults, impeding their movement. At the same time, they decrease the mean free path of dislocation slip. During the elevated temperature deformation of the HT R77 samples, no embrittlement was observed. Although there was a slight reduction in the tensile strength compared to the RT tested samples, the measured values were still higher than the RT strength for a wrought alloy. Therefore, it is believed that the microtwin formation improved the elevated temperature tensile properties of LPBF fabricated R77 alloy.

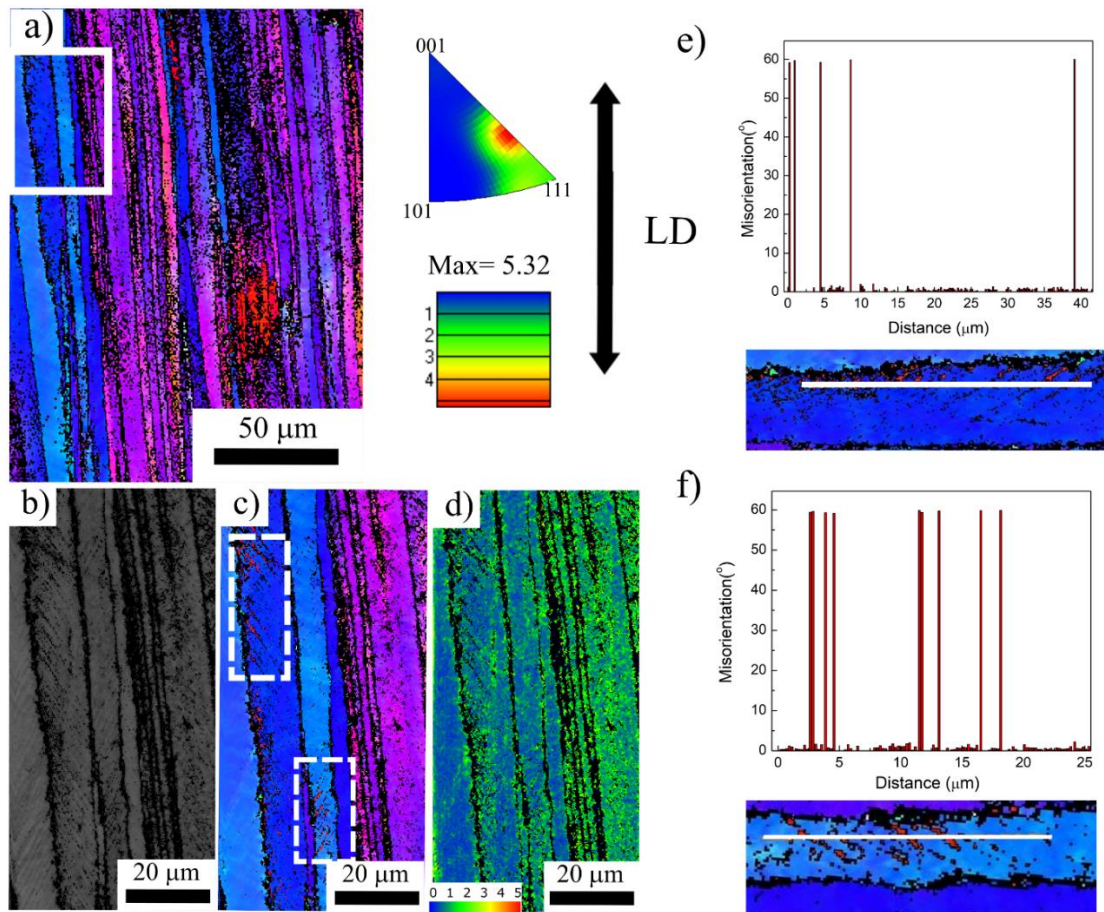


Figure 5. 13. EBSD analysis of the HT sample tested at 810°C (a) IPF orientation map and its corresponding inverse pole figure along the LD. (b) Band contrast, (c) IPF orientation map, and (d) misorientation map of the selected enlarged region. (e) and (f) misorientation profile of the twins highlighted in (c).

### 5.4.5. Fractography

Fracture surfaces of the tested samples were analyzed to understand their room and elevated temperature fracture behaviors. Representative SEM micrographs for each sample condition are shown in Figure 5.14, 5.15, 5.16, and 5.17.

From the low magnification fractograph on the AB sample tested at RT in Figure 5.14(a) it is recognizable that the sample has failed in a ductile manner and an obvious necking was also observable. The higher magnification micrograph in Figure 5.14(b) taken from the marked area from the Figure 5.14(a) depicts that the fracture followed a transgranular path during RT testing

of this sample. Large amount of dimple colonies homogeneously distributed throughout the fracture surface is clearly visible along with the small number of river markings in certain regions. River markings are characteristic features of cleavage fracture while dimples are characteristic of the ductile type of fracture. Higher magnification image of the fracture surface in Figure 5.14(c) reveals that dimples were also visible on the surfaces of the river markings. Hence, it could be interpreted that the nature of the fracture in the AB sample tested at RT was mainly ductile even though both cleavage and ductile fracture features were visible on the fracture surface. This is in good agreement with the observed high elongation value at fracture and the strain distribution of the deformed sample. Small spherical pores approximately of the size of the carbide particles observed in the microstructure of the AB sample can also be observed on the surface, suggesting decohesion at the carbide/cell boundary interface. The discrete nature of the carbides prevented the crack propagation along the boundaries resulting in the observed transgranular fracture morphology.

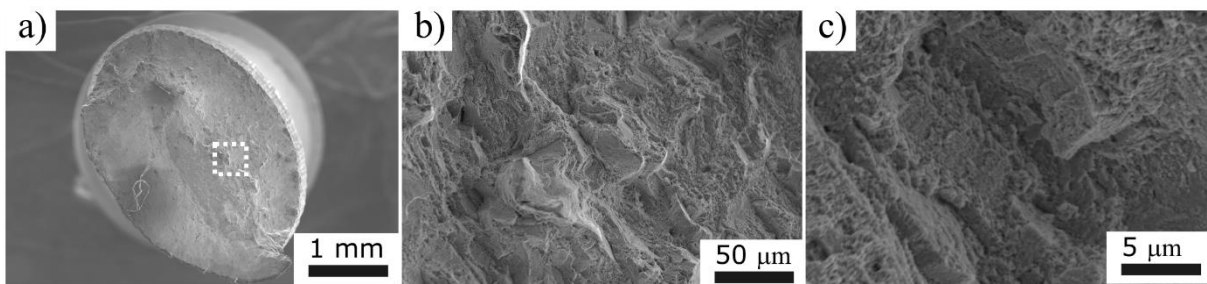


Figure 5. 14. (a), (b), and (c) The fracture surface of the AB sample, tested at RT.

The fractograph of the AB sample tested at 810 °C in Figure 5.15(a) reveals a flat fracture surface covered with square-shaped facets indicating that the nature of the fracture in this sample was cleavage. Although the fracture still follows a transgranular path, the type of fracture clearly changed during the elevated temperature tensile testing as shown in Figure 5.15(b). Large amount of river markings and cleavage facets with shallow dimple colonies can be observed on the fracture surface of the AB sample tested at 810 °C (Figure 5.15(c)). As previously mentioned, the precipitation of fine spherical  $\gamma'$  particles, was observed after the elevated temperature exposure of the AB sample, resulting in a localized deformation behavior along with a reduction in the measured elongation. The hardening response of this sample during testing lead to a shift in the fracture behavior towards cleavage. Additionally, small secondary cracks were observed on the

fracture surface of this sample. These cracks are caused by the crack propagation path resulting from the decohesion around the grain boundary carbides. Due to the discrete morphology of the carbides observed, the fracture mode remained transgranular.

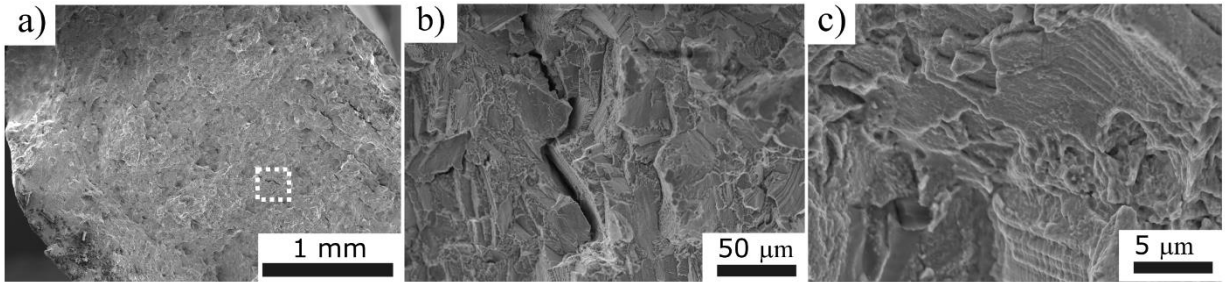


Figure 5. 15. (a), (b), and (c) The fracture surface of the AB sample, tested at 810 °C.

As shown in Figure 5.16(a) the HT sample tested at RT showed a zigzag fracture path without neck formation, indicating a cleavage type of fracture. Closer examination of the fracture surface in Figure 5.16(b) revealed a step like cleavage facet morphology throughout the sample. Additionally, shallow dimples were observed on the faces of these facets as shown in the higher magnification micrograph in Figure 5.16(c). This type of fracture behavior is not commonly observed in FCC alloys. It is mainly reported when there is intergranular segregation leading to environmentally assisted cracking or during fatigue deformation of Ni-based superalloys [69–71]. The EDS analysis is proved that neither of these could be the reason for the observed fracture behavior in this alloy. Zhang et.al reported a similar fracture behavior during RT tensile testing of CMSX-4 alloy [72]. It is suggested that the network slip morphologies are formed via activation of multiple slip systems, leading to the formation of dislocation walls at the  $\gamma$  channels. Further deformation creates stress concentration at points where the dislocation tangles are present. Finally, microcracks initiate at the sample surface and follow a path of intersecting slip bands leading to the formation of a faceted fracture surface with dimples on the faces of the facets. The highly deformed regions and dislocation tangles on the multiple directions observed in the EBSD analysis of the tested sample indicate that the suggested mechanism might be effective during the RT tensile deformation of the HT sample.

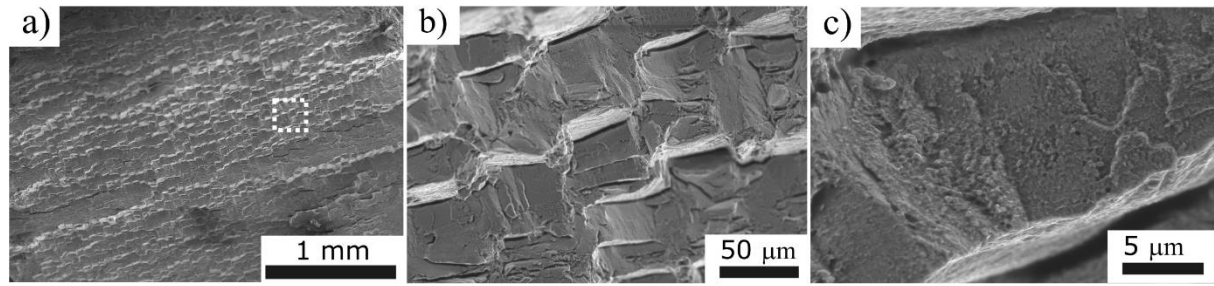


Figure 5. 16. (a), (b), and (c) The fracture surface of the HT sample, tested at RT.

When tested at 810 °C, the HT sample exhibited a completely ductile behavior with neck formation as shown in Figure 5.17(a). The fracture surface of this sample exhibits a network of large dimples connected by finer dimples and no features indicating cleavage fracture as depicted in Figure 5.17(a), and (b). The distribution of the dimples shows that the sample has deformed uniformly throughout the cross-section leading to a transgranular ductile fracture. This is in agreement with the homogenous distribution of the strain seen in the deformed sample. Some evidence of secondary cracking was also observed in this sample, similarly to the AB sample tested at elevated temperature. However, the overall morphology of the fracture surface was consistent with the ductile fracture. Although the elongation at break was only slightly higher compared to the RT tested sample, it is clear that deformation by microtwinning, activated at elevated temperature, resulted in a sharp change of the fracture behavior from cleavage to a completely ductile one.

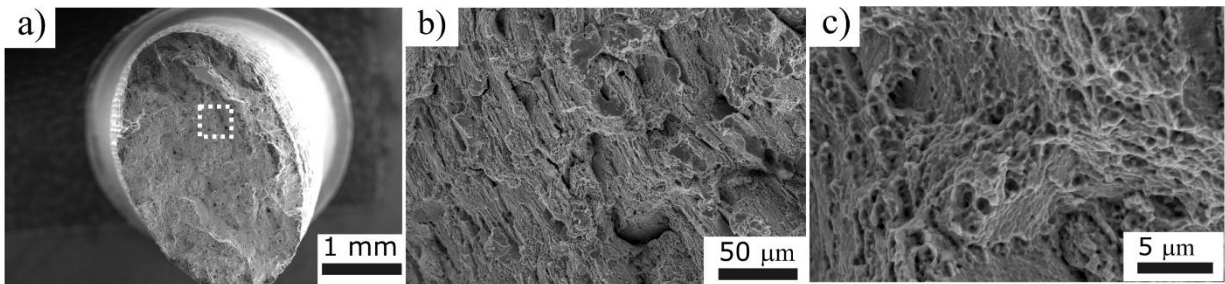


Figure 5. 17. (a), (b), and (c) The fracture surface of the HT sample, tested at 810 °C.

## 5.5. Conclusion

Current study includes the fabrication of crack free, dense parts of R77, a superalloy considered as difficult to weld, by LPBF. Fabricated samples were subjected to a sub-solvus solutionizing and aging heat treatment during which their crack free state was maintained. Microstructure and tensile

deformation behavior of the as fabricated and heat-treated samples were investigated at room temperature and 810 °C. The following conclusions can be drawn:

1. The sample in AB condition exhibits a columnar grain morphology with cellular grain structure. Columnar grains were mainly aligned along the  $\langle 100 \rangle$  direction. The grain structure of the AB sample was found to be stable at elevated temperatures and maintained after the applied heat treatment.
2. The presence of fine  $\gamma'$  precipitates with a unimodal distribution was observed within the cells of the AB sample, along with the fine discrete carbide particles on the cell boundaries. Heat treatment resulted in a bimodal distribution of  $\gamma'$  precipitates consisting of cuboidal primary and spherical secondary particles. In addition to the coarsening of carbides in the AB condition, the formation of a discontinuous film of Cr rich carbides was observed in the HT condition.
3. The microstructure of the HT sample has not altered during the elevated temperature tensile testing whereas growth and additional precipitation of  $\gamma'$  precipitates have occurred in the AB condition.
4. All of the tested conditions exhibited UTS and YS values above the minimum recommendations of the room temperature strength values for a wrought heat-treated R77 alloy.
5. The microstructural change of the AB sample during the elevated temperature testing resulted in an increase in the hardness and strength as well as a significant drop in the elongation. The hardening response at 810 °C led to a more localized deformation behavior and cleavage type of fracture.
6. The microstructure was maintained in the HT condition, however, samples tested at different temperatures exhibited completely different deformation behaviors. Localized highly deformed regions were observed in the sample tested at RT as well as a faceted cleavage type of fracture surface. The thermally activated microtwinning mechanism during elevated temperature testing improved the ductility of the HT sample without a significant loss in strength. This deformation mechanism resulted in a more uniform deformation and completely ductile fracture behavior.

## 5.6. Acknowledgment

The authors would like to thank the generous research support by the Natural Sciences and Engineering Research Council (NSERC) of Canada (NSERC Project Number: NETGP 494158 – 16). The authors would also like to acknowledge McGill Engineering Doctoral Award (MEDA) granted to Ms. Atabay.

## 5.7. References

- [1] R.C. Reed, The Superalloys fundamentals and applications, *Superalloys Fundam. Appl.* 9780521859 (2006) 1–372. doi:10.1017/CBO9780511541285.
- [2] M. Aliofkhaeaei, *Superalloys*, 2015.
- [3] J.N.D. & J. C. Lippold, *Welding Metallurgy and Weldability of Nickel-Base Alloys*, *J. Chem. Inf. Model.* 53 (2009) 456. doi:10.1017/CBO9781107415324.004.
- [4] S. Wang, *Welding and Repair of Single Crystal Ni-based Superalloys*, (2005).
- [5] H.-S. Wang, C.-Y. Huang, K.-S. Ho, S.-J. Deng, *Microstructure Evolution of Laser Repair Welded René 77 Nickel-Based Superalloy Cast*, *Mater. Trans.* 52 (2011) 2197–2204. doi:10.2320/matertrans.m2011264.
- [6] J. Chander, *Hardening Mechanism and Corrosion Resistance of Nickel-Base Alloys: A Review*, *Can. Metall. Q.* 3 (1964) 57–77. doi:10.1179/cm.1964.3.1.57.
- [7] H.Y. Bor, C.N. Wei, A.C. Yeh, W. Bin He, H. Sen Wang, C.M. Kuo, *Heat treatment effects on the high temperature mechanical behavior of directionally solidified MAR-M247 superalloy*, *8th Pacific Rim Int. Congr. Adv. Mater. Process.* 2013, *PRICM 8.* 1 (2013) 379–386. doi:10.1007/978-3-319-48764-9\_46.
- [8] H.E. Huang, C.H. Koo, *Effect of solution-treatment on microstructure and mechanical properties of cast fine-grain CM 247 LC superalloy*, *Mater. Trans.* 45 (2004) 1360–1366. doi:10.2320/matertrans.45.1360.
- [9] M. Zielińska, J. Sieniawski, M. Poręba, *Microstructure and mechanical properties of high temperature creep resisting superalloy René 77 modified CoAl<sub>2</sub>O<sub>4</sub>*, *Arch. Mater.* 28 (2007) 629–632.
- [10] M. Zielinska, J. Sieniawski, *Surface modification and its influence on the microstructure and creep resistance of nickel based superalloy René 77*, *Arch. Metall. Mater.* 58 (2013)

- 95–98. doi:10.2478/v10172-012-0157-6.
- [11] W. Kurz, D.J. Fisher, Dendrite growth at the limit of stability: tip radius and spacing, *Acta Metall.* 29 (1981) 11–20. doi:10.1016/0001-6160(81)90082-1.
- [12] S. Kou, *Welding Metallurgy*, 2nd Editio, A John Wiley & Sons, Inc., 2003.
- [13] M. Brandt, ed., *Laser Additive Manufacturing Materials, Design, Technologies, and Applications*, Woodhead Publishing, n.d.
- [14] S.S. Babu, R. Goodridge, *Additive manufacturing*, 2015. doi:10.1179/0267083615Z.000000000929.
- [15] D. Herzog, V. Seyda, E. Wycisk, C. Emmelmann, Additive manufacturing of metals, *Acta Mater.* 117 (2016) 371–392. doi:10.1016/j.actamat.2016.07.019.
- [16] N. Nadammal, S. Cabeza, T. Mishurova, T. Thiede, A. Kromm, C. Seyfert, L. Farahbod, C. Haberland, J.A. Schneider, P.D. Portella, G. Bruno, Effect of hatch length on the development of microstructure, texture and residual stresses in selective laser melted superalloy Inconel 718, *Mater. Des.* 134 (2017) 139–150. doi:10.1016/j.matdes.2017.08.049.
- [17] O. Sanchez-Mata, X. Wang, J.A. Muñiz-Lerma, S.E. Atabay, M. Attarian Shandiz, M. Brochu, Dependence of mechanical properties on crystallographic orientation in nickel-based superalloy Hastelloy X fabricated by laser powder bed fusion, *J. Alloys Compd.* 865 (2021) 158868. doi:10.1016/j.jallcom.2021.158868.
- [18] W.E. Frazier, Metal additive manufacturing: A review, *J. Mater. Eng. Perform.* 23 (2014) 1917–1928. doi:10.1007/s11665-014-0958-z.
- [19] T. DebRoy, H.L. Wei, J.S. Zuback, T. Mukherjee, J.W. Elmer, J.O. Milewski, A.M. Beese, A. Wilson-Heid, A. De, W. Zhang, Additive manufacturing of metallic components – Process, structure and properties, *Prog. Mater. Sci.* 92 (2018) 112–224. doi:10.1016/j.pmatsci.2017.10.001.
- [20] N.J. Harrison, I. Todd, K. Mumtaz, Reduction of micro-cracking in nickel superalloys processed by Selective Laser Melting: A fundamental alloy design approach, *Acta Mater.* 94 (2015) 59–68. doi:10.1016/j.actamat.2015.04.035.
- [21] H. Wang, X. Zhang, G.B. Wang, J. Shen, G.Q. Zhang, Y.P. Li, M. Yan, Selective laser melting of the hard-to-weld IN738LC superalloy: Efforts to mitigate defects and the resultant microstructural and mechanical properties, *J. Alloys Compd.* 807 (2019).

- doi:10.1016/j.jallcom.2019.151662.
- [22] M.M. Attallah, R. Jennings, X. Wang, L.N. Carter, Additive manufacturing of Ni-based superalloys: The outstanding issues, *MRS Bull.* 41 (2016) 758–764. doi:10.1557/mrs.2016.211.
- [23] O. Sanchez-Mata, X. Wang, J.A. Muñoz-Lerma, M. Attarian Shandiz, R. Gauvin, M. Brochu, Fabrication of Crack-Free Nickel-Based Superalloy Considered Non-Weldable during Laser Powder Bed Fusion, *Materials (Basel)*. 11 (2018). doi:10.3390/ma11081288.
- [24] L.N. Carter, Selective laser melting of nickel superalloys for high temperature applications, *Sch. Metall. Mater.* (2013) 298. <http://theses.bham.ac.uk/4410/2/Carter13PhD.pdf%5Cnhttp://theses.bham.ac.uk/4410/>.
- [25] J.A. Muñoz-Lerma, Y. Tian, X. Wang, R. Gauvin, M. Brochu, Microstructure evolution of Inconel 738 fabricated by pulsed laser powder bed fusion, *Prog. Addit. Manuf.* (2018). doi:10.1007/s40964-018-0062-2.
- [26] D. Grange, Fusion laser sélective de pièces en Inconel 738 et René 77 : vers une maîtrise de la fissuration au cours du procédé pour les superalliages à haute fraction de précipités  $\gamma'$ , 2020. <http://www.theses.fr/2020UPSLM029/document>.
- [27] S. Griffiths, H. Ghasemi Tabasi, T. Ivas, X. Maeder, A. De Luca, K. Zweiacker, R. Wróbel, J. Jhabvala, R.E. Logé, C. Leinenbach, Combining alloy and process modification for micro-crack mitigation in an additively manufactured Ni-base superalloy, *Addit. Manuf.* 36 (2020). doi:10.1016/j.addma.2020.101443.
- [28] R. Engeli, T. Etter, S. Hövel, K. Wegener, Processability of different IN738LC powder batches by selective laser melting, *J. Mater. Process. Technol.* 229 (2016) 484–491. doi:10.1016/j.jmatprotec.2015.09.046.
- [29] Y. Hagedorn, J. Risse, N. Pirch, W. Meiners, R. Poprawe, K. Wissenbach, Processing of nickel based superalloy MAR M-247 by means of High-Temperature Selective Laser Melting (HT-SLT), in: 2013.
- [30] J.R. (Joseph R.. Davis, A.S.M.I.H. Committee., Heat-resistant materials LK - <https://mcgill.on.worldcat.org/oclc/37353908>, ASM International, Materials Park, Ohio SE - v, 591 pages : illustrations ; 29 cm., 1997.
- [31] G.F.V. Voort, Metallography of superalloys, *Ind. Heat.* 70 (2003) 40.
- [32] C.A. Schneider, W.S. Rasband, K.W. Eliceiri, NIH Image to ImageJ: 25 years of image

- analysis, *Nat. Methods*. 9 (2012) 671–675. doi:10.1038/nmeth.2089.
- [33] S.E. Atabay, O. Sanchez-Mata, J.A. Muñoz-Lerma, M. Brochu, Effect of heat treatment on the microstructure and elevated temperature tensile properties of Rene 41 alloy produced by laser powder bed fusion, *J. Alloys Compd.* (2020). doi:10.1016/j.jallcom.2020.157645.
- [34] A. International, *Standard Test Methods for Tension Testing of Metallic Materials*, (2018). doi:10.1520/E0008.
- [35] A. International, *ASTM E21-17, Standard Test Methods for Elevated Temperature Tension Tests of Metallic Materials*, (2017). doi:10.1520/E0021-17.
- [36] C.M. Corporation, *Vacuum Alloys*, (n.d.). <https://cannonmuskegon.com/products/vacuum-alloys/>.
- [37] Q. Jia, D. Gu, Selective laser melting additive manufacturing of Inconel 718 superalloy parts: Densification, microstructure and properties, *J. Alloys Compd.* 585 (2014) 713–721. doi:10.1016/j.jallcom.2013.09.171.
- [38] S.E. Atabay, O. Sanchez-Mata, J.A. Muñoz-Lerma, R. Gauvin, M. Brochu, Microstructure and mechanical properties of rene 41 alloy manufactured by laser powder bed fusion, *Mater. Sci. Eng. A*. 773 (2020). doi:10.1016/j.msea.2019.138849.
- [39] A. Basak, S. Das, Microstructure of nickel-base superalloy MAR-M247 additively manufactured through scanning laser epitaxy (SLE), *J. Alloys Compd.* 705 (2017) 806–816. doi:10.1016/j.jallcom.2017.02.013.
- [40] T. Etter, Reduction in mechanical anisotropy through high temperature heat treatment of Hastelloy X processed by Selective Laser Melting ( SLM ) Reduction in mechanical anisotropy through high temperature heat treatment of Hastelloy X processed by Selective, *Mater. Sci. Eng.* (2015). doi:10.1088/1757-899X/82/1/012097.
- [41] R. Muñoz-Moreno, V.D. Divya, S.L. Driver, O.M.D.M. Messé, T. Illston, S. Baker, M.A. Carpenter, H.J. Stone, Effect of heat treatment on the microstructure, texture and elastic anisotropy of the nickel-based superalloy CM247LC processed by selective laser melting, *Mater. Sci. Eng. A*. 674 (2016) 529–539. doi:10.1016/j.msea.2016.06.075.
- [42] S. Li, Q. Wei, Y. Shi, Z. Zhu, D. Zhang, Microstructure Characteristics of Inconel 625 Superalloy Manufactured by Selective Laser Melting, *J. Mater. Sci. Technol.* 31 (2015) 946–952. doi:10.1016/j.jmst.2014.09.020.
- [43] V.D. Divya, R. Muñoz-Moreno, O.M.D.M. Messé, J.S. Barnard, S. Baker, T. Illston, H.J.

- Stone, Microstructure of selective laser melted CM247LC nickel-based superalloy and its evolution through heat treatment, *Mater. Charact.* 114 (2016) 62–74. doi:10.1016/j.matchar.2016.02.004.
- [44] K. Kunze, T. Etter, J. Grässlin, V. Shklover, Texture, anisotropy in microstructure and mechanical properties of IN738LC alloy processed by selective laser melting (SLM), *Mater. Sci. Eng. A.* 620 (2014) 213–222. doi:10.1016/j.msea.2014.10.003.
- [45] M. Technological, Segregation During Solidification, (1992) 175–184. doi:10.7449/1992/Superalloys\_1992\_175\_184.
- [46] H.E. Collins, Relative Stability of Carbide and Intermetallic Phases in Nickel-Base Superalloys, (2012) 171–198. doi:10.7449/1968/superalloys\_1968\_171\_198.
- [47] A.S. Shaikh, F. Schulz, K. Minet-Lallemand, E. Hryha, Microstructure and Mechanical Properties of Haynes 282 Superalloy Produced by Laser Powder Bed Fusion, *Mater. Today Commun.* (2021) 102038. doi:10.1016/j.mtcomm.2021.102038.
- [48] S.S. Handa, Precipitation of Carbides in a Ni-based Superalloy, Masters Degree Proj. University (2014) 1–33.
- [49] Z. Li, Q. Xu, B. Liu, Simulation and Experimental study of Recrystallization Kinetics of Nickel Based Single Crystal Superalloys, *Mater. Today Proc.* 2 (2015) S440–S452. doi:10.1016/j.matpr.2015.05.060.
- [50] L. Wang, G. Xie, J. Zhang, L.H. Lou, On the role of carbides during the recrystallization of a directionally solidified nickel-base superalloy, 55 (2006) 457–460. doi:10.1016/j.scriptamat.2006.05.013.
- [51] MetalTek RENE ® 77 Centri-Vac Nickel Cobalt Based Alloy, (n.d.). <http://www.matweb.com/search/datasheet.aspx?matguid=10c55bc1e84542adb8c6c3fd39837390&ckck=1> (accessed February 2, 2021).
- [52] Y.T. Tang, C. Panwisawas, J.N. Ghoussoub, Y. Gong, J.W.G. Clark, A.A.N. Németh, D.G. McCartney, R.C. Reed, Alloys-by-design: Application to new superalloys for additive manufacturing, *Acta Mater.* 202 (2021) 417–436. doi:10.1016/j.actamat.2020.09.023.
- [53] J. Xu, H. Gruber, R. Boyd, S. Jiang, R.L. Peng, J.J. Moverare, On the strengthening and embrittlement mechanisms of an additively manufactured Nickel-base superalloy, *Materialia.* 10 (2020) 100657. doi:https://doi.org/10.1016/j.mtla.2020.100657.
- [54] A.J. Goodfellow, Strengthening mechanisms in polycrystalline nickel-based superalloys,

- Mater. Sci. Technol. (United Kingdom). 34 (2018) 1793–1808. doi:10.1080/02670836.2018.1461594.
- [55] R.W. Kozar, A. Suzuki, W.W. Milligan, J.J. Schirra, M.F. Savage, T.M. Pollock, Strengthening mechanisms in polycrystalline multimodal nickel-base superalloys, *Metall. Mater. Trans. A Phys. Metall. Mater. Sci.* 40 (2009) 1588–1603. doi:10.1007/s11661-009-9858-5.
- [56] D. Raynor, J.M. Silcock, Strengthening Mechanisms in  $\gamma'$  Precipitating Alloys, *Met. Sci. J.* 4 (1970) 121–130. doi:10.1179/msc.1970.4.1.121.
- [57] M. Preuss, M., Quinta da Fonseca, J., Grant, B., Knoche, E., Moat, R., Daymond, The effect of  $\gamma'$  particle size on the deformation mechanism in an advanced polycrystalline nickel-base superalloy, in: *Superalloys 2008 (Eleventh Int. Symp., 2008: pp. 405–414.*
- [58] L. Tian, J. Chen, C. Xu, C. Ma, Deformation localization in a single crystal nickel-based superalloy oriented for multiple slip, *Mater. Charact.* 115 (2016) 55–60. doi:10.1016/j.matchar.2016.03.019.
- [59] M.G. Ardakani, R.N. Ghosh, V. Brien, B.A. Shollock, M. McLean, Implications of dislocation micromechanisms for changes in orientation and shape of single crystal superalloys, *Scr. Mater.* 39 (1998) 465–472. doi:10.1016/S1359-6462(98)00223-1.
- [60] H. Xu, Z.J. Zhang, P. Zhang, C.Y. Cui, T. Jin, Z.F. Zhang, The synchronous improvement of strength and plasticity (SISP) in new Ni-Co based disc superalloys by controlling stacking fault energy, *Sci. Rep.* 7 (2017) 1–11. doi:10.1038/s41598-017-07884-4.
- [61] H. Long, Y. Liu, D. Kong, H. Wei, Y. Chen, S. Mao, Shearing mechanisms of stacking fault and anti-phase-boundary forming dislocation pairs in the  $\gamma'$  phase in Ni-based single crystal superalloy, *J. Alloys Compd.* 724 (2017) 287–295. doi:10.1016/j.jallcom.2017.07.020.
- [62] F. Hanning, A.K. Khan, J. Steffenburg-Nordenström, O. Ojo, J. Andersson, Investigation of the effect of short exposure in the temperature range of 750–950°C on the ductility of haynes® 282® by advanced microstructural characterization, *Metals (Basel)*. 9 (2019). doi:10.3390/met9121357.
- [63] A. Harte, M. Atkinson, A. Smith, C. Drouven, S. Zaefferer, J. Quinta da Fonseca, M. Preuss, The effect of solid solution and gamma prime on the deformation modes in Ni-based superalloys, *Acta Mater.* 194 (2020) 257–275. doi:10.1016/j.actamat.2020.04.004.
- [64] R.R. Unocic, L. Kovarik, C. Shen, P.M. Sarosi, Y. Wang, J. Li, S. Ghosh, M.J. Mills,

- Deformation mechanisms in ni-base disk superalloys at higher temperatures, *Proc. Int. Symp. Superalloys*. (2008) 377–385. doi:10.7449/2008/superalloys\_2008\_377\_385.
- [65] D. Barba, E. Alabort, S. Pedrazzini, D.M. Collins, A.J. Wilkinson, P.A.J. Bagot, M.P. Moody, C. Atkinson, A. Jérusalem, R.C. Reed, On the microtwinning mechanism in a single crystal superalloy, *Acta Mater.* 135 (2017) 314–329. doi:10.1016/j.actamat.2017.05.072.
- [66] L. Kovarik, R.R. Unocic, J. Li, P. Sarosi, C. Shen, Y. Wang, M.J. Mills, Microtwinning and other shearing mechanisms at intermediate temperatures in Ni-based superalloys, *Prog. Mater. Sci.* 54 (2009) 839–873. doi:10.1016/j.pmatsci.2009.03.010.
- [67] I.S. Kim, B.G. Choi, H.U. Hong, Y.S. Yoo, C.Y. Jo, Anomalous deformation behavior and twin formation of Ni-base superalloys at the intermediate temperatures, *Mater. Sci. Eng. A.* 528 (2011) 7149–7155. doi:10.1016/j.msea.2011.05.083.
- [68] Y. Yuan, Y.F. Gu, T. Osada, Z.H. Zhong, T. Yokokawa, H. Harada, A new method to strengthen turbine disc superalloys at service temperatures, *Scr. Mater.* 66 (2012) 884–889. doi:10.1016/j.scriptamat.2012.01.025.
- [69] J.S. Wang, A new type of brittle fracture in a fcc metal bicrystal with intergranular segregation, *J. Mater. Res.* 3 (1988) 16–28. doi:10.1557/JMR.1988.0016.
- [70] M. Tiryakioğlu, J. Campbell, C. Nyahumwa, Fracture surface facets and fatigue life potential of castings, *Metall. Mater. Trans. B Process Metall. Mater. Process. Sci.* 42 (2011) 1098–1103. doi:10.1007/s11663-011-9577-3.
- [71] F. Weng, Y. Liu, Y. Chew, X. Yao, S. Sui, C. Tan, F.L. Ng, G. Bi, IN100 Ni-based superalloy fabricated by micro-laser aided additive manufacturing: Correlation of the microstructure and fracture mechanism, *Mater. Sci. Eng. A.* 788 (2020) 139467. doi:10.1016/j.msea.2020.139467.
- [72] H. Zhang, P. Li, X. Gong, T. Wang, L. Li, Y. Liu, Q. Wang, Tensile properties, strain rate sensitivity and failure mechanism of single crystal superalloys CMSX-4, *Mater. Sci. Eng. A.* 782 (2020) 139105. doi:10.1016/j.msea.2020.139105.

# Chapter 6: General Discussion

---

## 6.1. Introduction

Ni-based superalloys are widely used for high-temperature applications due to their microstructural and mechanical stability at elevated temperatures as well as their oxidation and corrosion resistance [1–3]. When Ni-base superalloys contain additions of Al, Ti, and/or Nb to form the strengthening precipitates, i.e.  $\gamma'$  ( $\text{Ni}_3\text{Al}$ ,  $\text{Ni}_3\text{Ti}$ ) or  $\gamma''$  ( $\text{Ni}_3\text{Nb}$ ) after the appropriate heat treatment, they are classified as precipitation-hardened alloys [1,4]. Rene 41 (R41) and Rene 77 (R77) are two precipitation hardened superalloys having different Al and Ti levels hence, different  $\gamma'$  precipitates fractions. They are both designed to operate at high temperatures for hot section parts of turbine engines. The average equilibrium volume fraction of  $\gamma'$  precipitates reported for R41 is 27% [5]. Due to its higher Al and Ti content, R77 is an alloy with high  $\gamma'$  volume fraction ( $\sim >50\%$ ) [6–9]. Conventionally parts of R77 and R41 are fabricated by casting or forging followed by joining by welding when needed. During these conventional processing routes, cracking was reported for both alloys limiting their processing and applications [9–14]. Depending on their cracking susceptibility, R41 is considered fairly weldable and R77 is considered difficult to weld from the welding literature. Therefore, the utilization of a new processing technique that enables control over manufacturing microstructure would broaden the application of these alloys.

Laser powder bed fusion (LPBF) is an attractive alternative as a production technique as it offers more and new design flexibility over conventional manufacturing techniques. Additionally, LPBF allows microstructural control that enables the production of parts having unique microstructural features and superior mechanical properties compared to the conventional methods [15,16]. However, the number of precipitation-hardened Ni-base superalloys that can be successfully fabricated by LPBF is only limited to a few due to their cracking susceptibility. The high residual stressed parts encounter during the LPBF process results in cracking especially in the alloys with high  $\gamma'$  volume fraction [17,18]. A large number of precipitation-hardened alloys having superior elevated temperature performance are overlooked on the LPBF side due to their susceptibility to cracking and the lack of knowledge on the evolution of microstructural and mechanical properties upon and after post-processing.

Prior to this study, LPBF processing of neither R41 nor R77 was reported. Even though many studies exist on the processing of cracking susceptible alloys by LPBF, they usually rely on compositional modifications, preheating the base plate, or post-processing such as hot isostatic pressing (HIP) to mitigate or eliminate cracking [19–22]. Elimination of cracking just by process parameter optimization was not reported. Thus, a fundamental and systematic study was carried out to study the potential of fabrication of these two precipitation-hardened alloys, having different cracking susceptibilities. Moreover, the effect of different heat treatments on the room and elevated temperature tensile properties were investigated to fill the above-mentioned knowledge gaps.

## **6.2. Laser Powder Bed Fusion of R41**

The study first focuses on the LPBF processability and microstructural development of R41, an alloy having moderate weldability. By applying LPBF process parameter control, crack-free dense parts of R41 were fabricated. The results presented in Chapter 3 enabled an understanding of the formation of the microstructural features during the LPBF process. The formation of the grain structure and  $\gamma'$  precipitation kinetics of R41 as a result of the experienced cooling rates were properly discussed. The obtained results led to the conclusion that the use of LPBF as a processing route is feasible for R41 alloy even though the obtained microstructure was different compared to the conventionally fabricated parts. Additionally, the application of heat treatment was required as the  $\gamma'$  precipitation was suppressed during solidification.

Strain age cracking of R41 was reported during welding and post-weld heat treatment [10]. The susceptibility of the LPBF parts to solid-state cracking was assessed by the application of post-processing heat treatment. The resistance of the LPBF parts to strain age cracking was associated with the fine grain structure resulting from the high cooling rates in LPBF. The change in the microstructure, once an LPBF part was subjected to the standard heat treatment established for wrought parts was also investigated in detail. An understanding of the stability of the grain structure during elevated temperature exposure was acquired from the resulting microstructure. One thing to note here is that when the standard heat treatment was applied to the unique microstructure obtained after LPBF, the volume fraction of  $\gamma'$  was similar to the reported equilibrium value yet the size of the precipitates was smaller [5]. Thus, the present study is of great

value in terms of understanding the effect of standard post-processing heat treatments on the LPBF microstructure.

A comprehensive understanding of the room temperature tensile properties of the parts as a function of the observed microstructure was developed. The changes in the strength and elongation behavior were correlated with the precipitation of the  $\gamma'$  and carbide particles observed after the heat treatment. One thing worth noting here is that the standard heat treatment suggested for wrought parts can be used for the LPBF fabricated R41 parts. Application of this heat treatment would be sufficient to obtain room temperature tensile properties meeting the specification for this alloy.

The building direction was also identified as an important process parameter affecting the room temperature tensile properties of the LPBF processed R41 parts. The alignment of the columnar grain structure with the loading direction significantly affected the elongation of the parts. Yet once the samples were subjected to the heat treatment, a similar elongation value was observed, independent on the building direction.

### **6.3. Post-processing Heat Treatment of R41 and Its Effects on Elevated Temperature Properties**

In the previous section, feasibility of the effectiveness of a heat treatment optimized for conventional processing techniques was assessed during room temperature deformation. Although the standard sub-solvus heat treatment yielded good mechanical performance at room temperature for LPBF fabricated R41 bars, a knowledge gap exists governing the relationship between heat treatment and the LPBF microstructure, and the corresponding elevated temperature mechanical properties response. This part of the study aims to develop an understanding of the effect of solutionizing temperature on the evolution of the unique microstructure of the LPBF parts along with the resulting elevated temperature tensile deformation behaviors.

The results in Chapter 4 have proven that it is possible to modify the grain structure, size distribution, and morphology of the  $\gamma'$  precipitates along with the type and morphology of the carbide particles by the application of different heat treatments. The  $\gamma'$  precipitates and cell boundary carbides were identified as the main phases providing the grain stability at elevated

temperatures. Dissolution of these phases was found to be resulting in the recrystallization of the columnar grain morphology obtained after LPBF. Hence, this study provides insight into the effect of the solutionizing heat treatment temperature on the grain morphology of the parts. It proves that it is possible to completely modify for the microstructure to meet application-specific requirements. It is reported that a unimodal  $\gamma'$  distribution would lead to higher strength whereas a bimodal distribution may lead to better creep resistance [23]. Hence, different size distributions of  $\gamma'$  precipitates are required for different applications. This study is of great value in terms of designing a heat treatment for an LPBF part to obtain a specific size distribution of the  $\gamma'$  precipitates. For the conventionally fabricated microstructures, it is not always possible to fully dissolve the primary  $\gamma'$  precipitates. However, as the precipitation is suppressed during LPBF, utilization of the super-solvus heat treatment for 4 hours was proven sufficient to obtain a unimodal distribution. This study also provides significant information on the effect of solutionizing temperature and cooling rate on the type and morphology of the carbides. It is found that the extremely fast cooling rates of the LPBF lead to discrete carbide morphologies. Even though, the transformation of these carbides occurred during sub-solvus heat treatment, their morphology was still spherical and discrete. On the other hand, once they are completely in solution, they form with a different composition and morphology due to the difference between the LPBF processing and air cooling after heat treatment. Therefore, the selection of the solutionizing heat treatment is very important in terms of carbide phase transformations as well.

The results demonstrated that the tensile strength of the LPBF fabricated R41 parts was not significantly affected by the observed changes in the microstructure. However, the deformation behavior was strictly dependent on the microstructural features. It was found that even in the as-built state, the LPBF fabricated samples had comparable elevated temperature strength with wrought and heat-treated counterparts. However, the presence of molten pool boundaries perpendicular to the tensile loading direction was detrimental for the elongation. Once more, the necessity of the heat treatment for the samples after LPBF processing was demonstrated. Moreover, the difference in the grain morphology and  $\gamma'$  size distribution led to a difference in the deformation behavior of the two heat-treated parts. Thus, this study provides a detailed understanding of the elevated temperature deformation behavior in relation to the observed microstructure. The super-solvus heat treatment showed superior strain hardening compared to the

other tested conditions whereas sub-solvus heat treatment resulted in improved elongation due to the combined contribution of grain orientation and dynamic recrystallization.

The main findings of this section are that it is possible to control the final microstructure of the LPBF fabricated parts by modifying the post-processing heat treatment. The findings will also provide valuable insight on the design of a heat treatment for the LPBF microstructure for specific elevated temperature deformation behavior.

#### **6.4. Laser Powder Bed Fusion of R77**

Finally, the study aims to transfer and extend the knowledge gained from LPBF processing of an alloy with moderate weldability, to process a difficult to weld superalloy, R77. Crack-free dense parts of R77 were successfully fabricated by LPBF without compositional modification or HIPing for the first time in literature. This study demonstrates that it is feasible to use LPBF to fabricate parts from high  $\gamma'$  containing, difficult to weld alloys. Additionally, the results provide insight on the  $\gamma'$  precipitation kinetics as a function of Al and Ti content. Even though the calculated cooling rates for LPBF fabricated R77 were higher compared to the R41, precipitation of  $\gamma'$  was not completely suppressed. However, their growth was still limited by the observed cooling rates.

The room temperature tensile test results revealed that the strength value observed for the as-fabricated sample was comparable to a wrought and heat-treated counterpart. This phenomenon is attributed to the fine solidification microstructure of the LPBF sample as well as the dislocation strengthening provided by the repetitive heating and cooling cycles. All the mechanical data was compared with other high  $\gamma'$  containing alloys which also provides information on the composition-microstructure-property relationship in LPBF processed superalloys. Even though the as-fabricated microstructure showed sufficient strength at room temperature, it underwent hardening during elevated temperature testing. This hardening response was related to the precipitation of  $\gamma'$  during testing. Hence, it was demonstrated that the as-fabricated microstructure was not stable even for short-term exposure to elevated temperatures.

The study also aimed to understand the transferability of the knowledge on the post-processing heat treatment on LPBF fabricated superalloys. The knowledge gained from the previous section was used to modify the existing standard heat treatment for wrought R77 parts. Application of the modified heat treatment to the LPBF fabricated parts demonstrated its feasibility to maintain the

crack-free structure of the sample. Additionally, these results proved that similar microstructural modifications were observed for R41 and R77 upon application of the sub-solvus heat treatments. For both alloys, sub-solvus heat treatment resulted in the preservation of the solidification grain structure along with a bimodal  $\gamma'$  distribution. However, the resulting  $\gamma'$  volume fractions were different as a result of their compositional differences. Furthermore, the study also provides insight into the stability of the heat-treated microstructure after short-term exposure to 810 °C.

Upon application of the modified heat treatment, the obtained room temperature strength for the LPBF fabricated parts was significantly higher compared to their wrought counterparts. Hence, the study demonstrated that the modification of the existing heat treatments for the LPBF microstructure is feasible to improve the room temperature tensile strength. In comparison to the other high  $\gamma'$  containing LPBF fabricated and heat-treated parts, R77 showed very similar strength yet higher elongation. These results are of significant importance to provide additional proof on the crack-free structure of the R77 samples in the current study. Moreover, the elongation was further improved during testing at 810°C without compromising strength. Considering the stability of the microstructure after the heat treatment, the change in the elongation value was associated with the change in the deformation behavior at elevated temperatures. The study is of great importance to show that the deformation behavior of the Ni-base superalloys is subjected to change with temperature, even though the microstructure remains the same.

Overall, this thesis presented the LPBF processing of two different precipitation-hardened alloys having different weldabilities. It is proven that it is possible to successfully fabricate conventionally available Ni-base superalloys with LPBF even though the processing window is narrow. The possibility of designing or modifying heat treatments for the solidification microstructure of LPBF and the resulting room and elevated temperature mechanical properties in relation to the corresponding microstructures were also demonstrated.

## 6.5. References

- [1] J.N.D.& J. C.Lippold, Welding Metallurgy and Weldability of Nickel-Base Alloys, J. Chem. Inf. Model. 53 (2009) 456. doi:10.1017/CBO9781107415324.004.
- [2] R.C. Reed, The Superalloys fundamentals and applications, Superalloys Fundam. Appl. 9780521859 (2006) 1–372. doi:10.1017/CBO9780511541285.

- [3] J. Chander, Hardening Mechanism and Corrosion Resistance of Nickel-Base Alloys: A Review, *Can. Metall. Q.* 3 (1964) 57–77. doi:10.1179/cmq.1964.3.1.57.
- [4] B. Geddes, H. Leon, X. Huang, *Superalloys: Alloying and Performance*, 2010. doi:10.1016/B978-0-7020-2797-0.00001-1.
- [5] L.M. Pike, Development of a fabricable gamma-prime ( $\gamma'$ ) strengthened superalloy, *Proc. Int. Symp. Superalloys.* (2008) 191–200. doi:10.7449/2008/superalloys\_2008\_191\_200.
- [6] Q.L. Pan, B. Li, Y. Wang, Y.W. Zhang, Z.M. Yin, Characterization of hot deformation behavior of Ni-base superalloy Rene'41 using processing map, *Mater. Sci. Eng. A.* 585 (2013) 371–378. doi:10.1016/j.msea.2013.07.066.
- [7] D. Tali, H. Gasan, M. Gulesen, S. Gurgun, M. Cemal, Turning Operation of Nickel Based Superalloy Rene 41, (2017) 9–11.
- [8] S. Wang, *Welding and Repair of Single Crystal Ni-based Superalloys*, (2005).
- [9] H.-S. Wang, C.-Y. Huang, K.-S. Ho, S.-J. Deng, Microstructure Evolution of Laser Repair Welded René 77 Nickel-Based Superalloy Cast, *Mater. Trans.* 52 (2011) 2197–2204. doi:10.2320/matertrans.m2011264.
- [10] R. Kayacan, R. Varol, O. Kimilli, The effects of pre- and post-weld heat treatment variables on the strain-age cracking in welded Rene 41 components, *Mater. Res. Bull.* 39 (2004) 2171–2186. doi:10.1016/j.materresbull.2004.08.003.
- [11] M.M. Attallah, R. Jennings, X. Wang, L.N. Carter, Additive manufacturing of Ni-based superalloys: The outstanding issues, *MRS Bull.* 41 (2016) 758–764. doi:10.1557/mrs.2016.211.
- [12] R.G. Ding, O.A. Ojo, M.C. Chaturvedi, Laser beam weld-metal microstructure in a yttrium modified directionally solidified Ni3Al-base alloy, *Intermetallics.* 15 (2007) 1504–1510. doi:10.1016/J.INTERMET.2007.05.008.
- [13] M. Zielińska, J. Sieniawski, M. Poręba, Microstructure and mechanical properties of high temperature creep resisting superalloy René 77 modified CoAl<sub>2</sub>O<sub>4</sub>, *Arch. Mater.* 28 (2007) 629–632.
- [14] M. Zielinska, J. Sieniawski, Surface modification and its influence on the microstructure and creep resistance of nickel based superalloy René 77, *Arch. Metall. Mater.* 58 (2013) 95–98. doi:10.2478/v10172-012-0157-6.
- [15] D. Herzog, V. Seyda, E. Wycisk, C. Emmelmann, Additive manufacturing of metals, *Acta*

- Mater. 117 (2016) 371–392. doi:10.1016/j.actamat.2016.07.019.
- [16] W.E. Frazier, Metal additive manufacturing: A review, *J. Mater. Eng. Perform.* 23 (2014) 1917–1928. doi:10.1007/s11665-014-0958-z.
- [17] L.N. Carter, M.M. Attallah, R.C. Reed, Laser powder bed fabrication of nickel-base superalloys: influence of parameters; characterisation, quantification and mitigation of cracking, *Proc. 12th Int. Symp. Superalloys, Champion, PA, 9–13 Sept. 2012.* (2012) 577–586. doi:10.1002/9781118516430.ch64.
- [18] W.E. King, A.T. Anderson, R.M. Ferencz, N.E. Hodge, C. Kamath, S.A. Khairallah, A. Rubenchik, Laser powder bed fusion additive manufacturing of metals; physics, computational, and materials challenges, *Appl. Phys. Rev.* 2 (2015). doi:10.1063/1.4937809.
- [19] S. Griffiths, H. Ghasemi Tabasi, T. Ivas, X. Maeder, A. De Luca, K. Zweiacker, R. Wróbel, J. Jhabvala, R.E. Logé, C. Leinenbach, Combining alloy and process modification for micro-crack mitigation in an additively manufactured Ni-base superalloy, *Addit. Manuf.* 36 (2020) 101443. doi:10.1016/J.ADDMA.2020.101443.
- [20] R. Engeli, T. Etter, S. Hövel, K. Wegener, Processability of different IN738LC powder batches by selective laser melting, *J. Mater. Process. Technol.* 229 (2016) 484–491. doi:10.1016/j.jmatprotec.2015.09.046.
- [21] Y. Hagedorn, J. Risse, N. Pirch, W. Meiners, R. Poprawe, K. Wissenbach, Processing of nickel based superalloy MAR M-247 by means of High-Temperature Selective Laser Melting (HT-SLT), in: 2013.
- [22] K. Kunze, T. Etter, J. Grässlin, V. Shklover, Texture, anisotropy in microstructure and mechanical properties of IN738LC alloy processed by selective laser melting (SLM), *Mater. Sci. Eng. A.* 620 (2014) 213–222. doi:10.1016/j.msea.2014.10.003.
- [23] L.N. Carter, Selective laser melting of nickel superalloys for high temperature applications, *Sch. Metall. Mater.* (2013) 298. [http://theses.bham.ac.uk/4410/2/Carter13PhD.pdf%5Cnhttp://theses.bham.ac.uk/4410/.](http://theses.bham.ac.uk/4410/2/Carter13PhD.pdf%5Cnhttp://theses.bham.ac.uk/4410/)

## Chapter 7: Conclusion

---

This study systematically investigated the microstructural development and mechanical properties of precipitation-hardened Ni-base superalloys after LPBF processing and post-processing heat treatments. Specifically, the processability of an alloy with moderate weldability and the effect of standard heat treatment on the LPBF microstructure and room temperature mechanical properties were studied in Chapter 3. Chapter 4 focused on the effect of different heat treatment cycles on the microstructural development of LPBF fabricated R41 and their effects on the elevated temperature deformation behavior. Finally, the knowledge gained from a moderately weldable alloy has been used to process R77, an alloy known as difficult to weld. LPBF processing of R77 and its microstructural change was studied in Chapter 5. Additionally, room and elevated temperature deformation behaviors of as built and heat-treated samples was investigated. The main conclusions drawn can be summarized as follows:

1. High density, crack-free parts of R41 was successfully fabricated by LPBF. Microstructure and room temperature tensile properties were investigated after fabrication and its subjected to the standard heat treatment. The microstructure of the as-fabricated sample consists of fine columnar grains mainly aligned in  $\langle 100 \rangle$  direction with a cellular sub-grain morphology.  $\gamma'$  precipitation was suppressed due to the cooling rates encountered in LPBF. When the samples were subjected to the standard heat treatment, grain morphology was maintained and precipitation of fine  $\gamma'$  precipitates along with Mo-rich carbides were observed. The size of the precipitates was found to be considerably smaller compared to values reported in the literature. Room temperature mechanical properties of the samples were investigated by using microhardness measurements and tensile testing. Two different build orientations were tested in each condition to see the effect of the building direction. For both directions, heat treatment led to a significant increase in strength and hardness along with a loss in elongation. Tensile properties of each direction were also meeting the specifications for a wrought and heat-treated alloy. It is found that vertically built samples had slightly lower strength in the as-built condition due to the presence of molten pool boundaries perpendicular to the loading direction. The elongation of these samples was also significantly higher as a result of the alignment of

columnar grains along the loading direction. Finally, fractography analysis revealed that even though different elongation values were observed all samples fractured in a ductile manner.

2. In addition to the previously studied standard, sub-solvus heat treatment a modified heat treatment was applied to the LPBF fabricated R41 samples. Microstructural modification as a result of each heat treatment along with the resulting tensile properties at 760 °C was studied for each of the three conditions. Contrary to the as built and standard heat-treated sample, when super-solvus heat treatment was applied, recrystallization was observed. The grain morphology of this sample was equiaxed with random orientation. The morphology of the carbide particles and  $\gamma'$  precipitates were also different for each heat treatment. The sub-solvus heat treatment resulted in a bimodal distribution of  $\gamma'$  whereas the super-solvus one showed a unimodal distribution. The carbides in the sub-solvus heat treatment were discrete spherical ones enriched in Mo. Super-solvus heat treatment resulted in the formation of a film like Cr rich  $M_{23}C_6$  carbides. These differences in the microstructures resulted in similar tensile strength values at 760 °C yet the observed deformation behaviors showed distinct differences. The samples in the as-built condition had limited ductility due to the presence of molten pool boundaries perpendicular to the testing direction. It is found that failure started locally at these boundaries and resulted in the low elongation at break. The samples had the highest elongation after the sub-solvus heat treatment. Observed elongation values were also significantly higher compared to their wrought counterparts. The improved elongation without sacrificing the strength is associated with the presence of columnar grains aligned with the loading direction. For the super-solvus heat-treated samples the film-like morphology of the carbides acted as a crack initiation and propagation site and resulted in a transgranular ductile fracture. Their deformation behaviors were also significantly different. Super-solvus heat treatment resulted in work hardening during elevated temperature deformation. Whereas the sub-solvus heat-treated sample showed a steady-state deformation behavior caused by the dynamic recrystallization phenomenon taking place.
3. The knowledge gained on the processing and heat treatment design was successfully transferred to process a difficult to weld alloy. Crack-free parts of R77 were fabricated by LPBF just by modifying the process parameters. Standard heat treatment applied to the cast alloys was modified for the LPBF microstructure and the crack-free structure of the part was maintained during the applied heat treatment. The microstructure of as fabricated and heat-

treated samples was investigated in detail and resulting tensile properties were tested at room temperature and 810 °C. Similar to R41, R77 also showed columnar grain morphology aligned in  $\langle 100 \rangle$  direction. However, this time  $\gamma'$  prime precipitation kinetics was so fast that even the LPBF cooling rates could not suppress it. The as-built microstructure consists of extremely fine spherical  $\gamma'$  precipitates and Mo- and Ti- enriched spherical carbide particles at the cell boundaries. Modified sub-solvus heat treatment resulted in a bimodal  $\gamma'$  distribution with cuboidal primary and spherical secondary precipitates as well as the formation of a discrete film like  $M_{23}C_6$  carbides while the grain morphology remained unchanged. Each testing condition showed strength values above the minimum recommended values for a wrought and heat-treated alloy. Even though the strength of the as-built condition was comparable to a heat-treated wrought counterpart it is found that the microstructure obtained after LPBF was not stable during elevated temperature exposure even for a short time. Hence these samples experienced hardening and a significant loss in the ductility during elevated temperature testing resulting from the excessive precipitation of  $\gamma'$ . The heat-treated microstructure showed elevated temperature stability but still, a change in the deformation behavior was observed between the room temperature and elevated temperature testing. When tested at room temperature localized deformation and a brittle faceted fracture were observed. Whereas during elevated temperature testing improved ductility, without a significant loss in strength was observed due to the thermally activated microtwinning mechanism. As a result, a more uniform deformation and a completely ductile failure were observed.

## Chapter 8: Contributions to the Original Knowledge

---

The contributions to the original knowledge achieved during the course of this study are summarized as follows:

1. This study, for the first time reported in the literature achieved, crack free fabrication by LPBF of R41 and R77 without any compositional modifications or preheating the base plate.
2. The understanding of the solidification microstructure and mechanical property development of R41 and R77 manufactured by LPBF was produced.
3. The thermal post-processing of an LPBF fabricated R41 alloy was studied for the first time, and it was determined that conventional HT are compatible with the AB LPBF microstructure.
4. This study, for the first time, proposed a new heat treatment schedule for the difficult to weld alloy R77 and achieved a crack free structure after the heat treatment cycle.
5. For the first time in literature, room, and elevated temperature tensile properties of LPBF fabricated R41 and R77 alloys were measured both in as built and heat treated conditions.